AMERICAN UNIVERSITY OF BEIRUT

EFFECT OF PLASMA DENSITY FLUCTUATIONS ON THE LOWER HYBRID POWER SPECTRUM

by

MERVAT AKRAM MADI

A dissertation
submitted in partial fulfillment of the requirements
for the degree of Doctor of Philosophy
to the Department of Electrical and Computer Engineering
of the Faculty of Engineering and Architecture
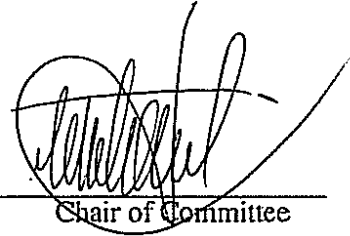at the American University of Beirut

Beirut, Lebanon
April 2015

AMERICAN UNIVERSITY OF BEIRUT

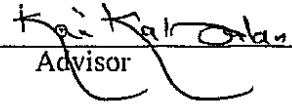EFFECT OF PLASMA DENSITY FLUCTUATIONS ON THE
LOWER HYBRID POWER SPECTRUM

by

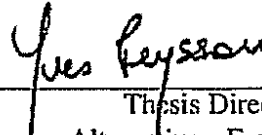MERVAT AKRAM MADI

Approved by :

_____
Dr. Hassan A Artail, Professor   Chair of Committee
AUB - Department Electrical and Computer Engineering

_____
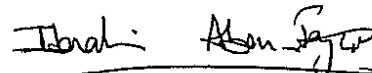Dr. Karim Y Kabalan, Professor   Advisor
AUB - Department Electrical and Computer Engineering
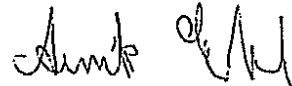

_____
Dr. Yves Peysson, Professor   Thesis Director
CEA - Commissariat à l'Energie Atomique et aux Energies Alternatives, France

_____
Dr. Ibrahim Abou Faycal, Associate Professor   Member of Committee
AUB - Department Electrical and Computer Engineering

_____
Dr. Annika Ekedahl, Professor   Member of Committee
CEA - Commissariat à l'Energie Atomique et aux Energies Alternatives, France

Date of dissertation defense: April 22, 2015

AMERICAN UNIVERSITY OF BEIRUT

THESIS, DISSERTATION, PROJECT RELEASE FORM

Student Name : _____ *Madi* _____ *Mervat* _____ *Akram* _____
               Last   First   Middle

○ Master's Thesis   ○ Master's Project   ✓ Doctoral Dissertation

✓   I authorize the American University of Beirut to: (a) reproduce hard or electronic copies of my thesis, dissertation, or project; (b) include such copies in the archives and digital repositories of the University; and (c) make freely available such copies to third parties for research or educational purposes.

☐   I authorize the American University of Beirut, **three years after the date of submitting my thesis, dissertation, or project**, to: (a) reproduce hard or electronic copies of it; (b) include such copies in the archives and digital repositories of the University; and (c) make freely available such copies to third parties for research or educational purposes.

_____   7/May/2015

Signature   Date

COLLABORATION BETWEEN AUB AND CEA STATEMENT

This thesis is done under an agreement of collaboration between The American University of Beirut and CEA, Cadarche. Mervat Madi has conducted her thesis under the supervision of Yves Peysson in CEA/IRFM institue in Cadarache for almost three years all the period from April 2012 till June 2014.

ACKNOWLEDGEMENTS

An Abstract of the Dissertation of

Mervat Akram Madi   for   Doctor of Philosophy
                                         Major: Electrical and Computer Engineering

Title: Effect of Plasma Density Fluctuations on The lower Hybrid Power Spectrum

Radiofrequency waves at the Lower Hybrid (LH) frequency are widely used in tokamak plasmas for driving a large fraction of the toroidal current. Consequently, evolution of the LH wave inside the plasma has been an important research subject. LH wave transfers energy to electrons by kinetic resonance via Landau damping. Landau damping takes places most efficiently for electrons at parallel velocities $4v_{the} > v_{\parallel} > 2.5v_{the}$ (v_{the} is the electron thermal velocity). However, the particles number as a function of $v_{\parallel}$ is a Maxwellian distribution function in which electrons that satisfy Landau damping condition occupy the tail and hence are very few which creates the spectral gap problem.

On the other hand, it has been heuristically validated that RF power spectrum emitted by LH launchers should couple to a wide range electrons for $n_{\parallel L}$[1] that exceeds $\sim$ $5.5/\sqrt{T_e[keV]}$, so that the spectral gap is filled. It has been noticed that if a perturbed power spectrum with fluctuation rate faster then fast electron slowing time is fed into the present models of plasma, it would come up with answers that explain all phenomena inside plasma and reproduce realistically what observations are up to. This study suggests a plausible mechanism for filling the LH spectral gap, that starting with standard theory, a deeper investigation would allow to redo the calculations with new perspective regarding density fluctuations and turbulence in the SOL. Using COMSOL Multiphysics, it is shown that parallel to magnetic field line density fluctuations in front the LH antenna, with parallel wavelength in the order of the LH wavelength modify the power spectrum at the separatrix by diffraction, such that experimental observations in wide spectral gap regimes at Tore Supra are successfully reproduced.

---

[1] $n_{\parallel L}$ is the LH wave refractive index along the magnetic field at which values the electrons damp the wave by the phenomenon known as Landau damping.

TABLE OF CONTENTS

Appendix

ILLUSTRATIONS

TABLES

CHAPTER I

INTRODUCTION

This thesis report aims at exploring a new physical mechanism that interprets the efficient absorption of an RF wave at the lower hybrid (LH) frequency in existing tokamak plasmas, in particular in presence of a large spectral gap regime.

First, a LH wave is used in tokamaks to drive a current along the toroidal direction for sustaining a steady-state operation or for current profile control. In this thesis, a derivation of the coupling theory calculation is done to show the characteristics of the LH wave coupling and propagation in the plasma edge i.e in the region bounded by the tokamak walls and is separated from the plasma core via the last closed magnetic field line (separatrix). Experimental efforts have shown an efficient absorption of the LH wave inside the plasma at all temperature plasmas. However, in general there is a difference between the launched LH parallel refractive index and that at which the wave is absorbed, which is known as the spectral gap problem. [1] In particular, in low temperature plasmas usually accompanied by high densities, there is a large difference which is not bridged in modeling efforts (large spectral gap regime). It was suggested that in this case, the LH power spectrum should be bridged at the plasma edge. Moreover, this suggestion has been successfully applied in current drive simulations for Tore Supra French tokamak in CEA, France. These simulations have successfully reproduced experimental results for a specific heuristic model of the power spectrum known by the tail model [7].

This study shows a numerical model of the antenna-plasma as a whole system constructed in a finite element solver COMSOL Multiphysics® which is an appropriate solver for Maxwell equations. Possible effect of density fluctuations in the parallel to magnetic field lines direction is investigated. A thin perturbation layer is modeled in front the LH antenna with time scale of the slowing down time of fast electrons. Diffraction effect results in a significant broadening in the power spectrum that propagates through the perturbed layer. Moreover, the power spectrum is perturbed randomly upon using a random fluctuation phase. More exlipilcity the pdf of the power spectrum shows that more than 50 % of the power is transfered to satellite lobes that extend as a tail at higher values of the refractive index $n_\parallel$ in consistence with the suggested model mentioned above. Only parallel fluctuations with a wavelength in the vicinity of the LH wavelength significantly modify the LH power spectrum as it passes through the fluctuating layer.

Details are given in the thesis chapters as follows: Chapter two is an introduction to Fusion energy and its main features including plasma drift motion, heating, current drive importance, and non-inductive current drive methods. Chapter three shows the LH coupling theory and derivation of all calculations that lead to distinguish the LH wave branches, the corresponding cut-off densities, $n_\parallel$ power spectrum calculation, plasma surface admittance, and radiated power of the electromagnetic modes. The LH antenna sys-

---

[1]Here parallel direction is along the magnetic field lines.

tem and the relevant codes used in current drive calculations are presented in Chapter four, while the spectral gap problem and the investigation of density fluctuations in the plasma edge are discussed in Chapter five. The model constructed in COMSOL Multiphysics® is thoroughly explained in Chapter six, in particular the importance of meshing and wave damping at the boundaries is highlighted. Moreover, a density perturbation layer is introduced in front a fully active multijunction (FAM) like antenna. Detailed parametric study on the role played by fluctuations in the plasma and the consequences on spectral properties is shown and discussed in Chapter seven. Finally, the conclusion is summarized in Chapter eight.

CHAPTER II

FUSION

A. Introduction

The fossil fuels are increasing the CO_2 levels in the atmosphere; thus contributing to the global warming since CO_2 absorbs the infrared radiation emitted by the earth and releases it back [8]. Alternative power resources have not been efficient enough to replace the fossil fuels. For example, renewables have low power density and need huge storage capacity due to their dependence on natural factors. In addition, fission was not accepted by the public in some countries due to nuclear waste, and as fossil fuels, fission resources are limited and would be available only for another 80 years. Therefore, there is a need to find another way to provide the increasing demand for power without augmenting the environmental risks and before natural resources used today are completely exhausted.

Fusion is a promising clean source of energy that produces large amounts of power compared to other sources with safe conditions and for a long term use. Unlike renewables, fusion is independent of weather conditions and does not require large surface areas. Note that the fuel mass used in fusion to generate 1 U of power is 4 times that of fission and 10^7 times that of fossil fuels. Moreover, fusion resources are abundant in nature since it mainly uses hydrogen isotopes like deuterium which is available in sea water. Hence fusion energy is economically competitive and environment friendly. However, fusion imposes a main challenge as it imitates a sun on earth. Indeed, in order to bring two light positively charged ions such as deuterium and tritium to fuse and thus release a large amount of energy ($17.6\,MeV$), they should be heated to very large temperatures.

Since 1930's when the first fusion experiments took place, fusion has been under development [9]. In 1946 the fusion apparatus has evolved first as a bottle; however, the first toroidal device known as tokamak had been set by Russian physicists in 1961 where the name Tokamak is an acronym of the Russian phrase 'toroïdalnaïa kamera s magnitnymi katushkami' which in English means 'toroidal chamber with magnetic coils'. Despite the international endeavor to achieve fusion, it still needs more decades to arrive at a power plant. Tireless efforts are being exerted internationally in particular on the technological level which renders fusion as an extremely challenging mission for the human kind at the present time.

Fusion is not easy to achieve due to Coulomb force of repulsion though it is minimized by choosing light ions of deuterium and tritium. In fact, an energy of $0.1\,MeV$ is needed to overcome the repulsion force between deuterium and tritium nuclei which is equivalent to a temperature of $3 \times 10^9\,K$. In order to confine the highly energetic particles for achieving fusion, two main modes are being considered; magnetic confinement (MCF)

for which a magnetic field is tuned in space so that the particles follow the magnetic field lines, and inertial confinement (ICF) which uses the inertia of the gas to overcome natural expansion at thermonuclear temperatures.

The most promising machine called tokamak is developed for MCF and has a donut shape, though other magnetic configurations are also considered for MCF which are the stellarators and reversed field pinch. The tokamak is an axisymmetric toroidal device that confines hot and dense plasma ($T \simeq 10\,KeV$, $n \simeq 10^{21}\,m^{-3}$). A large magnetic field ($\sim 5\,T$) is applied, so that highly energetic charged particles (electrons and ions) are accelerated along magnetic field lines around the tokamak by Lorentz force. Besides confinement of the charged particles, the tokamak geometry enlarges the trajectories followed by the ions and thus the fusion cross section area[1] is increased which raises the probability of the fusion reaction. Note that the enclosed charged particles satisfy both conditions of being quasi neutral in net charge and dense enough to behave in a collective manner and thus form a plasma. Fig. 1 shows the high temperature and density required for fusion reaction to take place in comparison between different naturally and artificially existing plasmas.

The fusion reaction in which one deuterium and one tritium fuse, produces one alpha particle, one neutron and large amount of energy as given in the following reaction

$$ {}^{2}_{1}D^{+} + {}^{3}_{1}T^{+} \rightarrow {}^{4}_{2}He^{+2}\,(3.5MeV) + n\,(14.1MeV) \tag{1} $$
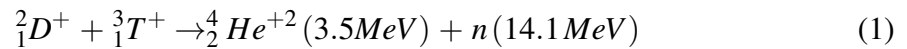
where the produced energy is due to a mass difference 4 per thousand which is $3.1 \times 10^{-29}\,kg$ and is transformed into energy ($17.6MeV$) released as kinetic energy, according to Einstein relation, $\Delta E = \Delta mc^2$. Neutrons have the advantage of being able to escape the magnetic field and hit the heating pads in the tokamak walls. Kinetic energy of the neutrons is thus transferred to water pipes placed next to the pads, and consequently the water becomes steam that drives turbines of a power plant. The α particles having high kinetic energy contribute to heat the plasma and thus sustain ignition.

Other fusion reactions that replace tritium with deuterium or helium are also possible, but are more difficult to achieve. While deuterium extracted from sea water is accessible, cheap and nonradioactive, tritium doesn't exist in large amounts on earth and is a radioactive material with a short half life of 12 years. Hence the need to regenerate tritium inside the tokamak as energetic neutrons produced from the fusion reaction hit the wall where lithium (Li) is embedded to give tritium according to the following reactions

---

[1]Particles lost as they travel distance ds is dn/ds= $\sigma\,n_D\,n_T$ where σ (m^{-4}) is the reaction cross section and n_D , n_T are the deuterium and tritium densities. Fusion reaction probability is proportional to σ, in particular, the average fusion rate coefficient is given by $<\sigma(v)v>$, where v is the relative velocity of the reacting particles and averaging is done over the particles velocity distribution. Only small fraction of highly energetic particles is lost through fusion while about 8000 times more are particles are scattered by collisions for a $10\,KeV$ reactor, that's why beam target fusion doesn't release net energy.
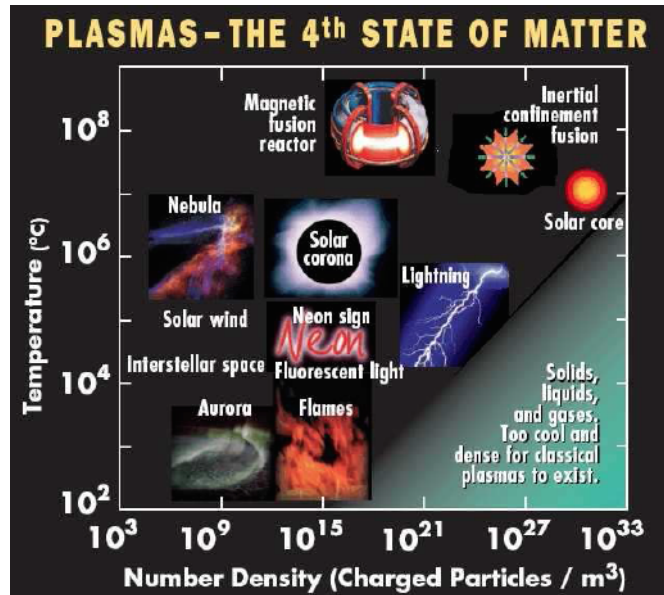
Figure 1: Different temperature and density conditions of plasma that exist naturally, constituting more than 99% of the universe, and artificially such as plasmas that satisfy the conditions for fusion reactions to occur in magnetic confinement and inertial confinement regimes. Copyright 1996 Contemporary Physics Education Project.

$$^{6}Li + n \rightarrow \,^{4}_{2}He(2.05\,MeV) + T(2.73\,MeV) \tag{2}$$

$$^{7}Li + n \rightarrow \,^{4}_{2}He + T + n - 2.47\,MeV \tag{3}$$
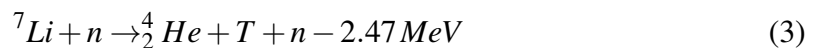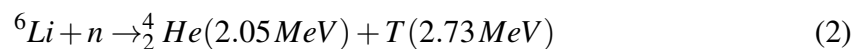
where lithium is abundant in nature and easy to extract.

B. ITER

On 2005 it was decided to build a large scale international tokamak called ITER (a Latin word meaning "the way") in Cadarache, South of France with the contribution of 7 members which are the European Union, U.S., Russia, India, China, Japan and South Korea, in order to test the first fusion machine as a preparatory step for a fusion reactor. Cutting edge technologies are being developed for the first time to assemble the ITER tokamak which is $11\,m$ high and $19\,m$ wide.

Confining a 150 million degree celsius plasma i.e at temperature larger than that of the sun[2], demands massive magnetic coils to provide strong toroidal magnetic field, a sophisticated feedback control system, complicated diagnostics and heating and current

---

[2] $T(sun) = 15 \times 10^{6}\,{}^{o}C$
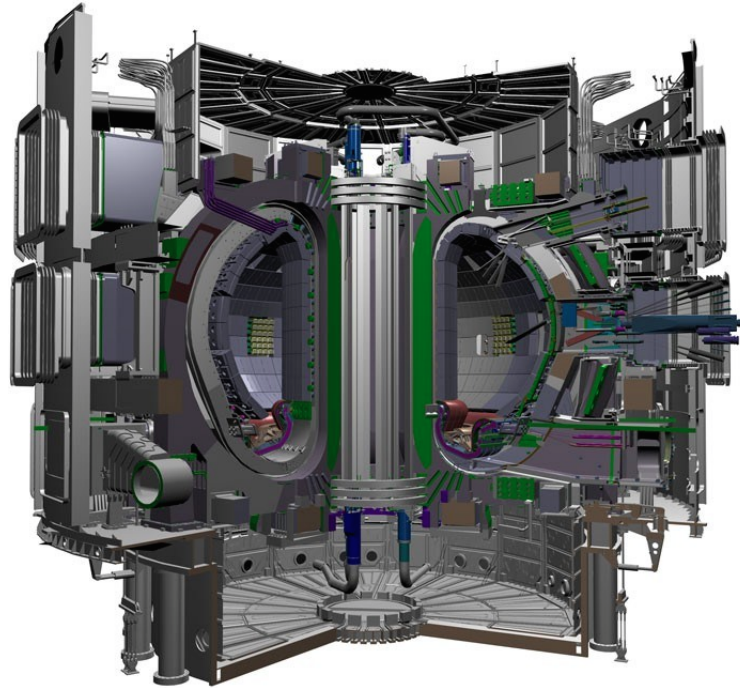
Figure 2: ITER tokamak composed of the central torus that encloses the plasma and the external vessel composed of the magnetic coils and devices such as diagnostics and different apparatus used for heating and feed back control. Special ports are designed in the tokamak wall to allow control of the plasma.

drive methods. Moreover, the materials used in the first wall that faces the plasma has to show high tolerance to high heat flux coming from the plasma with minimum erosion probability to avoid diluting the plasma and thus losing energy by radiation. First plasma is expected to be tested in ITER by 2023, and the first fuel plasma ignition[3] is planned to take place in 2029 [10].

C. Lawson Criterion and β limit

Power density is given by

$$p_{OH} + p_{ext} + p_\alpha + p_{rad} \tag{4}$$

where ohmic heating given by $p_{OH} = \eta j^2$ is provided by the solenoid at the first stage of operation, while the remaining terms correspond to the external heating methods such as electromagnetic waves, the α particle heating, and the heat loss by radiation assuming ideal operation where there is negligible particle loss into the plasma facing components (PFC). Since p_{OH} is negligible with respect to p_α,

$$p_{ext} = p_{fus}/Q = 5p_\alpha/Q \tag{5}$$

---

[3]Ignition of plasma fuel is the process in which the right conditions for fusion reaction are met, such that the produced energy contribute to the heating of colder plasma and thus the system becomes self sustained

where Q is the power enhancement factor i.e is the ratio of thermonuclear power produced to the heating power supplied and is important to measure how close is the tokamak from being a reactor.

Lawson criterion provides a rough estimate of the quantities needed to have a net gain in energy produced from a fusion reaction. Besides energy produced from fusion, energy is released and lost though thermal and radiation processes, thus equilibrating consumed and produced energy leads to the lawson criterion which defines a lower limit of the fusion product $nT\tau_E$,

$$nT\tau_E > 3 \times 10^{21} \, KeV \, s \, m^{-3}$$

where n is the density of the ions, T is the temperature and τ_E is the energy confinement time defined as the time needed for a plasma to cool down in absence of additional heating. Thus for $n = 10^{21} \, m^{-3}$, and $T = 30 \, KeV$, $\tau_E = 1s$; however longer confinement times are certainly needed so that the number of start up times is reduced and therefore a fusion reactor can serve longer especially that it needs 25 work years for a reactor to compensate its cost. The energy confinement time for ITER as extrapolated from JET (Joint European Tokamak) results is 3s where 1s was achieved in JET in 1988 [11].

Note that density is proportional to the number of ions which raises the fusion probability; however, a density rise leads to an increase in the kinetic pressure $<p>$ and thus results in plasma instabilities due to the tendency of the plasma to expand and cool down where the magnetic field forces the ions to stay confined. Scientists have come up with the notion of the β limit which sets a limit for the fusion power output and is given by

$$\beta = <p> / <B/2\mu_0> \tag{6}$$

where $<p>$ is the mean kinetic pressure ($p = nT$), and $B/2\mu_0$ is the magnetic pressure $<B>$ being the mean magnetic field and μ_0 the permeability in vacuum. $\beta = 1$ is the ideal value since it minimizes the magnetic pressure, however achieved $\beta's$ are maximum 0.4 or 40% due to plasma instabilities. β is used as a rough economic estimate of the fusion efficiency where a minimum of $\beta = 0.05$ is needed in a reactor. Moreover, normalized β given by

$$\beta_N = \beta \frac{aB}{I_p} \tag{7}$$

is used as an operational limit where a is the minor radius and I_p is the plasma current. The higher β_N ($\beta_N > 3.5$), the higher risk of plasma disruption.

The tokamak
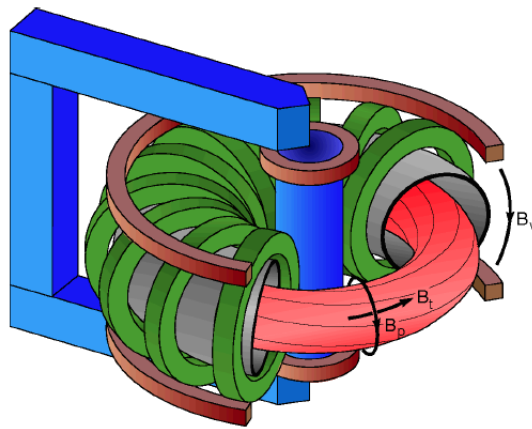
Figure 3: Toroidal magnetic coils (green) create the toroidal magnetic field B_t and the Solenoid in the center of the tokamak (blue) induce a toroidal current that creates poloidal magnetic field.

D. Confinement Modes

1. Inertial confinement

Another type of confinement is the inertial confinement (ICF) which is still being explored [12, 13]. Simply speaking, a frozen pellet of D-T is bombarded directly by laser or indirectly by X-rays in pulses of $1-10\ \mu s$ in order to initiate the burning process of the mixture so that it continues burning till all the fuel is consumed. This requires unattainable amount of injected energy. However, compressing the D-T ice at a density of $0.2 g/m^3$ by 1000 times reduces energy consumption by 10^6 which renders the input energy feasible.

2. Magnetic confinement

A strong magnetic field confines the plasma and thus keeps it away from the tokamak walls according to the relation $j \times B = \nabla p$, where j is the current and p is the pressure knowing that ∇p is in the radial direction. Ions and electrons of the plasma gyrate around the magnetic field lines that extend in helical orbits around the tokamak. Due to Lorentz force charged particles undergo radial acceleration along magnetic field lines with a thermal Larmor radius[4] of $\cong 4\,mm$ for deuterium ions and $\cong 0.07\,mm$ for electrons assuming a $5\,T$ magnetic field and a temperature of $10\,keV$, [14, 15]. In case of having

---

[4]Larmor radius is the radius of the orbit that the particle follows around the field line

a purely toroidal magnetic field, particle drifts caused by variation of magnetic field in direction and magnitude cause vertical polarization of the plasma leading to particle loss. Therefore, a poloidal magnetic field component is added resulting in a helical magnetic geometry, which allows the charged particles to change vertical position as they flow along the magnetic field line and thus undergo opposite vertical forces that ultimately cancel each other. Magnetic field lines and coils are illustrated in Fig. 3.

a. Magnetic field

Tokamaks have both toroidal and poloidal magnetic fields which form helical nested flux surfaces. Toroidal magnetic field is maintained by the toroidal magnetic coils that are placed around the tokamak, while poloidal magnetic field is supplied by poloidal coils along with a toroidal plasma current. The plasma current is partly provided by the bootstrap current generated inside the plasma due to pressure gradient. However, additional current is driven via external sources such as electron cyclotron (EC) waves and lower hybrid (LH) waves.

b. Particle drifts

The plasma is in principle confined to the magnetic field lines; however the plasma movement across the field lines towards the walls is inevitable due to particle drifts. In particular, the region enclosed between the material walls and the last closed field lines known as the scrape-off layer (SOL), is subject to several types of particle drifts. A summary of the particle drifts in the SOL shall be given below where parallel and perpendicular directions are those parallel and perpendicular to the magnetic field lines respectively.

1. $\mathbf{E} \times \mathbf{B}$ drift is due to electric field arising perpendicular to the magnetic field lines where the particle velocity is given by :

$$v_{E \times B} = \frac{E \times B}{B^2} \tag{8}$$

2. ∇B drift is due to magnetic field gradient where the particle velocity is given by :

$$v_{\nabla B} = \frac{v_\perp m}{2qB^3} B \times \nabla B \tag{9}$$

3. Diamagnetic drift is due to plasma pressure gradient along poloidal and radial directions and the particles where the particles velocity is given by :

$$v_{\nabla P} = \frac{B \times \nabla P}{enB^2}. \tag{10}$$
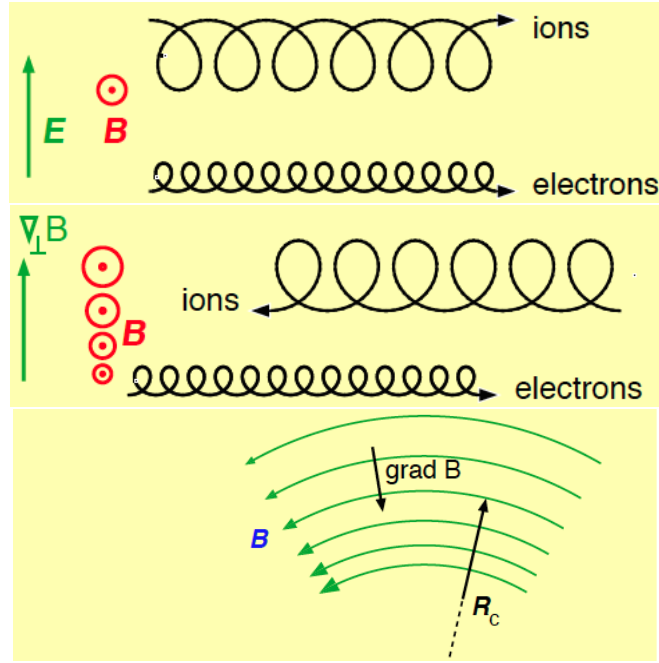
Figure 4: ExB, $\nabla_\perp B$ and B curvature drifts (from top to bottom).

In addition to the above drifts that exist in the SOL, the polarization drift generated by the electric field time derivative exists in the plasma but with a negligible effect in the SOL [16] and is given by :

$$v_{pol} = \frac{m}{qB^2} \frac{dE_\perp}{dt}.$$ (11)

E. Plasma heating

Heating the plasma is achieved through several methods. In addition to Ohmic heating, the basic heating method, RF and micro waves and neutral beam injection are used as shown in Fig. 6.

1. Ohmic heating

Ohmic heating is the original method used to heat up the plasma. Since the plasma is a charged medium with a resistivity ρ, it acts as an electrical wire, thus the flow of a current I with a density j through it dissipates energy [5] into the plasma and

---

[5]The volume power density dissipation by Ohm's law is equivalent to ρj^2.
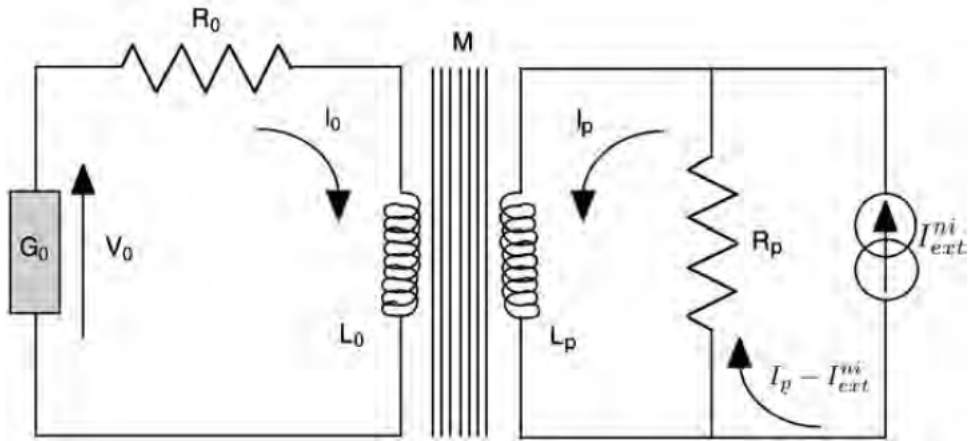
Figure 5: Transformer concept in plasma with solenoid being the primary circuit (left) and the plasma forming the secondary circuit (right).

consequently heats it. This current is induced by the solenoid placed at the tokamak center, via the transformer effect which was experimentally validated in Tore Supra [17] and is given by the simple inductance formula

$$\frac{d\Phi_M}{dt} = R_0 L_0 \frac{dI_0}{dt} = -R_p \frac{L_0}{M}(I_p - I_{ext}^{ni}) \tag{12}$$

where

R_0, I and L_0 are the resistance, current and inductance in the primary circuit of the transformer

M is the mutual inductance

R_p, I_p and I_{ext}^{ni} are the plasma resistance, plasma current and non-inductive current respectively.

Fig. 5 shows the transformer sketch of the plasma with solenoid being the primary circuit and the plasma forming the secondary circuit. Note that a steady state operation is given by a zero inductive current for a long time while a more strict constraint is having a zero loop voltage in the plasma [18].
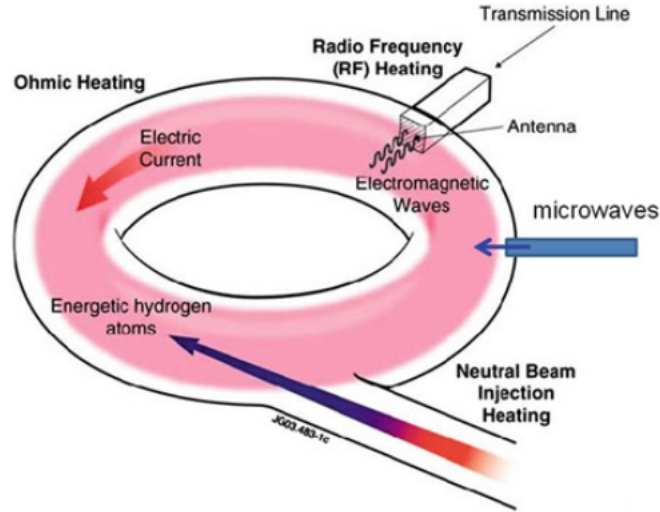
Figure 6: Heating Methods in ITER

2. *Wave heating*

a. ICRF

Magnetosonic waves in the ion cyclotron range of frequencies (ICRF) $\sim 10\,MHz$ interact resonantly with ions and heat them thus providing an efficient tool for heating the plasma [19, 20]. Plasma heating by IC waves has become well developed to be used as a heating auxiliary method in ITER [21, 22]. With an antenna composed of short-circuited current straps protected by a Faraday screen (see Fig. 7) designed in accordance with desirable sheath conditions [23], the IC wave understanding has rapidly evolved; however, research is still in progress to understand the IC wave interaction with the plasma edge and the walls. IC waves easily propagate to the plasma center with a strong perpendicular electric field well adapted to the transfer of energy from the wave to the ions and a weak parallel electric field [24]. Direct coupling with electrons takes place at the IC frequency while coupling to ions takes place at the IC frequency harmonics according to the resonance condition:

$$\omega + p\omega_{cs} + k_{\parallel}v_{\parallel s} = 0 \tag{13}$$

where $p = 0$ for electrons and $p \geq 1$ for ions, s corresponds to the species, and ω_{ci} is the ion or electron cyclotron frequency for $s = i$ or $s = e$ respectively.
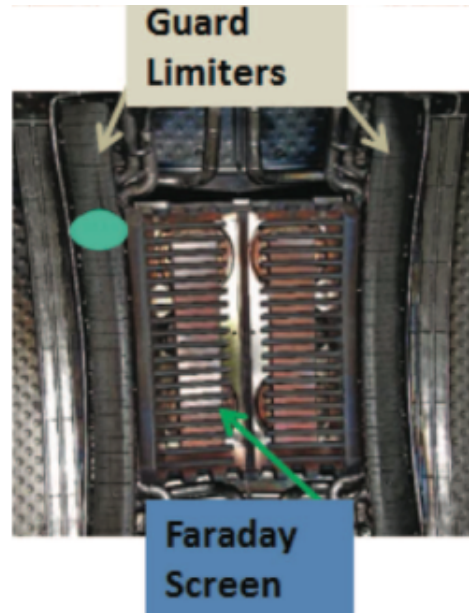
Figure 7: ICRH antenna

b. ECRH

Electron cyclotron (EC) wave is an electromagnetic wave used for heating and for current drive in tokamak plasmas. EC wave propagates in vacuum and thus the launching antenna does not have to be in contact with the plasma which facilitates maintenance. Moreover the beam diameter can be focused such that all power could be deposed in as small as $10 \, cm^3$ volume. For a magnetic field $[3-6] \, T$, the EC frequency is in the range $[84-170] \, GHz$ where the wavelength is few mms. [6] The EC wave resonates with electrons at the EC frequency or its harmonics and thus transfer energy and momentum to the electrons

$$\omega = \frac{p}{\gamma} \omega_{ce} + k_{\|} v_{\|e} \tag{14}$$

where γ is the usual relativistic factor $\gamma = (1 - v^2/c^2)^{1/2}$. The main result of EC resonance is to increase the perpendicular energy of resonant electrons, however an efficient current drive can take place [25, 26] as discussed in Sec. 2..

3. Particle heating

Particles heating is mainly achieved by neutral beam injection (NBI). Plasma is injected by very energetic particles that transfer heat to ions and electrons as they collide

---

[6]The electrons gyrate around the magnetic field lines at EC frequency given by $f_{ce} = eB/(2\pi m)$ where e and m are the electron charge and mass respectively.

with them. In order to escape the magnetic field lines, neutral particles are used so that they can reach at the plasma core where they lose their energy.

4. Alpha particle heating

Alpha particle heating is a main source of energy for sustaining the plasma and is one of the main issues to be addressed in ITER. As alpha particles are released from fusion reaction at very high energies, most of them orbit along the field lines and collide with other particles thus heating the plasma as they slow down. The main drawback of alpha particle heating is the formation of helium ash that needs to be exhausted immediately to avoid radiation and dilution of the deuterium-tritium mixture thus preserving the available fuel energy for continuous ignition. In the meantime, confining the alpha particles inside the plasma core so that they do not end by radial transport at the tokamak walls constitutes an additional challenge for plasmas physicists.

F. Non-inductive current drive

A poloidal magnetic field, B_p, is required to cancel vertical particle drifts in toroidal configurations. This field is provided by a driving a toroidal current inside the plasma. Basically, an ohmic toroidal current is generated by induction via the transformer effect; however, the transformer is inherently pulsed ($V = L\,dI/dt$) while a steady state operation[7] is necessary for an economically feasible power plant. In addition, the plasma resistivity is inversely proportional to temperature ($\rho \sim T^{-3/2}$), hence as the plasma temperature increases, current drive efficiency $\gamma = J/P$ decreases since it is less sustained by collisions where J and P represent current density and power density input respectively.

According to Fisch's theory of current drive [25, 27], $\triangle J/\triangle P(v_\parallel \gg v_{the}) \propto v_\parallel^2$ where $v_\parallel$ is the toroidal velocity and v_{the} is the thermal velocity of electrons, $v_{the} = \sqrt{T_e/m_e}$ (T_e and m_e are the electron temperature and mass respectively). Therefore increasing the toroidal velocity of electrons and ions drives current at high plasma temperatures. As the plasma current is directly related to the plasma confinement time ($\tau_E \propto J/\sqrt{P_{ext}}$) and is an essential component of magnetic confinement; the development of non-inductive current drive methods has become imperative in tokamaks [25, 28].

First, it was observed that due to pressure gradients a bootstrap current is self generated in the plasma [29]. In a high confinement mode (H-mode) plasma, a transport barrier that confines heat and particles is formed. It is characterized by pressure gradient at the region between the plasma core and the plasma edge known as the "pedestal" .

---

[7]A steady state discharge is the state in which the plasma continues running after switching off the transformer (characterized by a pulsed operation) for a long time.

While the current density profile in inductive regime (ohmic regime) is monotone with a maximum at the center, an enhanced current outside the plasma core sustains the transport barrier and thus enhances confinement. The current profile at the pedestal could be controlled via injecting fast particles or electromagnetic waves. Electromagnetic waves have shown efficient coupling to the plasma and include waves in the ion cyclotron, lower hybrid and electron cyclotron range of frequencies which are in the order of $10\,Mhz$, $1\,GHz$, and $100\,GHz$ respectively, where only LH waves are used to drive current off-axis.

1. Bootstrap current

Bootstrap current is internally generated in the plasma parallel to the magnetic field lines due to density (pressure) gradients [30, 31]. Banana orbits resulting from magnetic field inhomogeneity (mirror force) trap electrons along the magnetic field lines as shown in Fig. 8. The radial density gradient results in a difference between co-current and counter-current trapped particles, thus a banana current given by

$$j_b = T \frac{\varepsilon^{3/2}}{B_p} dn/dr \tag{15}$$

is generated, where ε is the safety factor given by $\varepsilon = a/R$, where (a, R) are the minor and major radii of the tokamak.

The bootstrap current is created by pitch angle scattering due to collisions between trapped particles and the much denser passing particles leading to an amplification of the banana current. The bootstrap current is given by

$$j_{BS} = \frac{1}{\varepsilon} j_b. \tag{16}$$

A high fraction of bootstrap current is needed for a high gain in tokamak operation [31], with $I_b/I_p \propto \varepsilon^{1/2} \beta_p$ where β_p is the poloidal component of β given by

$$\beta_p = <p> / <B_p/2\mu_0> \tag{17}$$

. While bootstrap current can achieve up to 80% (obtained in JT60 [32]) of the total current needed to confine the plasma, auxiliary methods are needed to supply additional current, which in addition provide a tool for adjusting the current density profile which allows to mitigate turbulence and thus improves confinement.

2. Neutral beam injection

Fast atoms are injected into the plasma bulk while they escape the strong magnetic field being neutral [25, 33]. The atoms injected at high speeds get ionized inside the

$$B \propto 1/R$$
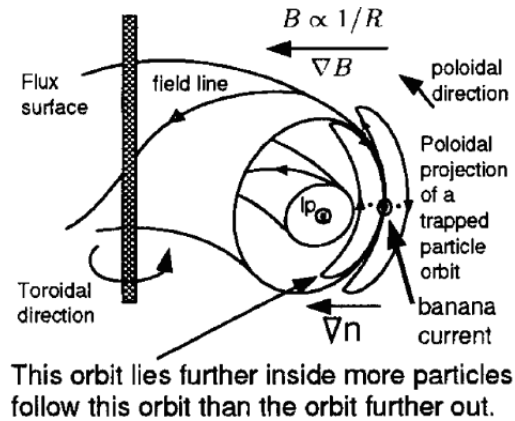
Figure 8: Bootstrap current
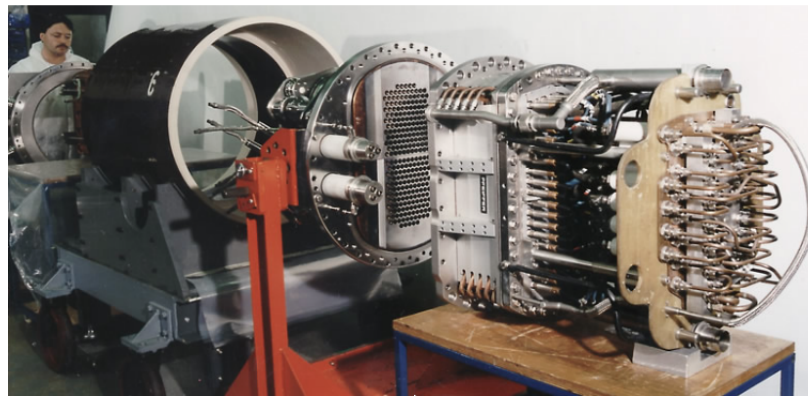
Figure 9: One assembly of the sixteen ion sources in Jet NBI system [1]

plasma which results in a series of ion-ion, ion-electron and electron-electron collisions and hence transfer momentum and energy to the plasma. Neutral beam injection (NBI) is used to drive currentdue to the fact that electrons undergo more collisions with ions moving along a certain direction which creates current in the opposite one. The major draw back of NBI is that injecting neutral beams at high energies is technically difficult. Neutral beams are produced by first creating positively charged ions which are accelerated to high speeds by applying strong electric field and then neutralized before entering the plasma as shown in Fig. 9. However, not all ions are neutralized thus an electromagnet is used to deflect them. Moreover, for ITER very high energetic beams are required which increases dramatically the lost ions and thus decrease the efficiency of the NBI source. Since, it is more difficult to make an electron attach to a positive ion moving at high speed than it is to cause an ion to lose an electron, another approach would be to generate negative ions and then accelarate them to high speeds and then remove the extra electron from them. A new facility called SNIF (small negative ion facility) is investigating a negative ion source for NBI [34].

G. Generation of current drive via electromagnetic waves

RF waves could be used to tailor the current density profile in contrary to the NBI which drives current in a wider radial extent. Lower hybrid (LH), electron cyclotron (EC) waves were developed for or current drive (CD) as shown in recent review on TS experiments of additional RF systems[20].

1. Lower hybrid waves

Lower hybrid (LH) waves are launched at $\sim 1 GHz$ radio frequencies into the tokamak chamber to drive current in the plasma core due to the electrostatic slow branch of the wave [35]. Wave plasma coupling is mainly affected by the electron density in front the antennas which should be above a cut-off value $n_{e,c} = \omega_{pe}^2 m_e / 4\pi e^2$. The LH wave is launched via antennas composed of phased waveguides arrays as shown in Fig. 23. The LH fast phase velocities accelerate fast electrons via longitudinal Landau damping [36] thus pulling a fast electron tail from the Maxwellian distribution. They have been efficiently used to drive toroidal current which allowed to achieve in 1996 a $1000\,s$ non-inductive discharge in Tore Supra tokamak [37], $1\,h$ non-inductive discharge in TRIAM 1M [38], and to maintain a quasi steady state discharge in JET [39]. Moreover, LH waves are employed in tailoring the current density profile and thus will help control the q-profile[8] in ITER [40, 41]. Since 1980, theoretical studies and modeling of the LH wave physics has been addressing the LH spectral gap problem defined as the difference between the nominal parallel phase velocity $v_{\parallel 0}$ of the launched wave and the parallel velocity at which the electrons absorb the wave $v_{\parallel L}$. This report is dedicated to the spectral gap problem of the LH wave, in particular a new mechanism is suggested and modeled. [7].

2. ECCD

Electron cyclotron current drive (ECCD) is applied in several tokamak plasmas [25, 26]. It could successfully achieve a full non-inductive discharge at the TCV tokamak. ECCD is basically due to the effect of collisionality change with energy and the fact that electrons with same sign of $v_{\parallel}$ absorb the EC waves as explained by Fisch-Boozer [42]. The EC frequency is dependent on the radial position position of the electrons due to the magnetic field radial dependence ($f_{ce} \propto B$) thus tuning the EC frequency targets specific areas inside the plasma; Consequently the EC wave is a tool for feedback control [43, 44]. For example, EC wave shall be employed in ITER to drive current in the mag-

---

[8]q-profile is determined from the radial safety factor variation and plays an important role in stabilizing the plasma.
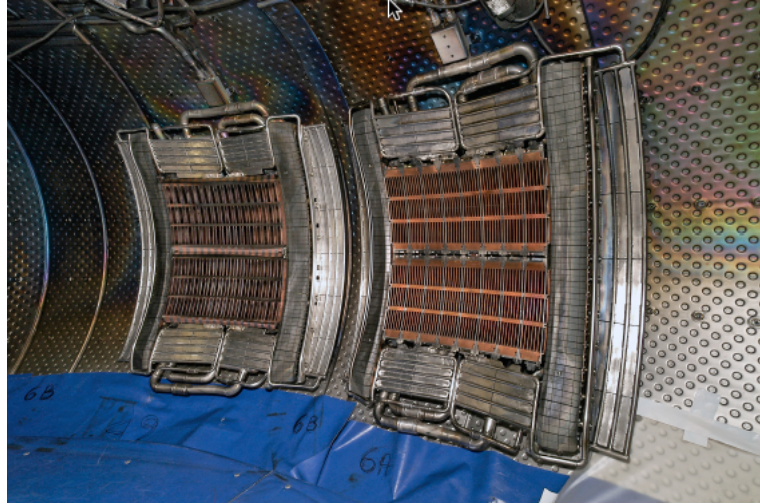
Figure 10: Front view of the FAM and PAM antennas facing the plasma in Tore Supra tokamak

netic island O-point to substitute for the bootstrap current [9] and thus stabilize neoclassical tearing modes (NTM's). Other MHD instabilities such as saw-teeth oscillations are also controlled by the EC waves.

---

[9]In a magnetic island the pressure becomes flattened while a bootstrap current is created by the pressure gradient.

CHAPTER III

LH WAVE COUPLING THEORY

A. Introduction

Radio frequency waves at the Lower Hybrid (LH)[1] frequency are widely used in tokamak plasmas for driving a large fraction of the toroidal current. The high current drive efficiency achieved experimentally make them particularly attractive for controlling the current density profile in the plasma (MHD stability, energy confinement, etc) with a limited fraction of recycled fusion power. For this purpose, it is considered in the fusion tokamak demonstrator ITER [45, 46, 41, 47].

Current drive modeling is carried out by calculating self-consistently the wave field (Maxwell equation) with the resonant particle dynamics (Fokker-Planck equation) inside the plasma. The LH wave propagation is described by a ray tracing (WKB approximation), initial conditions being described by the power spectrum at the separatrix (which is the first magnetic flux surface where the field lines are closed (FCFL)) of the toroidal MHD magnetic equilibrium. Numerous studies suggest that the launched power spectrum could be a critical parameter for understanding the wave propagation in the plasma and its self-consistent absorption by wave-particle interaction. Since recent measurements have shown that the electron density fluctuations level in front of the LH antenna could be very high (100%), it is important to assess their possible contribution to a broadening of the power spectrum used as initial conditions of the ray tracing [48, 49]. So far, as a preliminary step towards the full description of the LH physics at the plasma edge with fluctuations, theoretical developments have been performed assuming a quiescent plasma in the scrape-off layer (SOL) lying between the antenna port to the separatrix. The standard theory is re-derived in order to highlight possible limitations of the model and to detail where fluctuations could play a role. The efficiency of HF phased waveguide arrays in coupling to plasma was first proposed in [50], and the standard theory was well developed in [51, 52]. Since the effect of density at the launcher-plasma interface is a key factor, it was addressed in [53] and thereafter experimental verification was achieved as reported in [54].

First, the derivation of the propagating modes in plasma results in two differential equations in E_y and E_z. Plasma parameters are calculated and consequently, the two equations in E_y and E_z are decoupled resulting in two independently propagating waves which are the fast wave and the slow wave respectively. Slow wave is chosen for lower hybrid current drive due to its efficiency in coupling to electrons in the parallel direction and for having lower cut-off frequency. Thus the antenna is designed to launch slow wave only. Subsequently, the antenna dimensions are studied to investigate the excited

---

[1]Lower Hybrid frequency is defined by $\omega_{c,i}^2 \ll \omega^2 \ll \omega_{c,e}^2$, where $\omega_{c,i}$ and $\omega_{c,e}$ are the ion and electron cyclotron frequencies in the order of 100 MHz and 100 GHz respectively.

propagating and evanescent eigenmodes. Due to the continuity of the fields, the wave field represented as superposition of eigenmodes is matched to the field inside plasma, serving as a boundary condition for solving for the electric field at the antenna-plasma interface. Thereafter the n_z spectrum of the excited wave is calculated for the simple case of considering only the fundamental *TEM* mode and neglecting reflections. Then the plasma surface admittance is calculated at the antenna plasma interface to be able to calculate the power spectrum in n_z. Afterwards the multipole theory is developed such that the incident and reflected modes are presented as vectors to simplify calculations. Also the magnetic field is expressed in terms of the admittance matrices and the electric field, which allows expressing all incident and reflected fields in terms of the incident and reflected electric potential at the various ports of the waveguide. The Fourier transform of the electric field along the direction parallel to the magnetic field along with Parseval's theorem are used to obtain the power spectrum in n_z. The obtained formula show the effect of the waveguides' number, their dimensions, and the phasing between them in achieving either plasma heating or CD.

B. Electric Field Solutions Inside Plasma

The question of wave propagation and coupling to plasma in the layer that lies between the antenna and the first closed field line (FCFL) shall be addressed.

Some assumptions are taken to simplify the calculations.

- Consider a slab geometry in which the toroidal static magnetic field is in the z direction, the poloidal dimension is the y axis, and the density gradient is assumed to be along the radial direction x being the direction of inhomogeneity. Thus the plasma is considered homogenous in both y and z directions. The problem is considered as 2 dimensional (Fig. 11), thus the wave front is parallel to $0y$ axis which is the dimension that doesn't introduce any inhomogeneity to the problem and hence it is completely ignored.

- The antenna is taken as infinite in the y direction so there is no variation along $0y$ ($\partial/\partial y = 0$). Consequently, $k_y = 0$. This is justified since the antenna size in the y direction is $6 - 20$ times more than that in the z direction (Fig. 12) [55].

- Time dependence has the harmonic form $e^{i\omega t}$ where ω is the frequency excited by the RF source ($\omega = 2\pi f$ where f has a fixed value of $3.7\,GHz$ in Tore Supra LH wave launchers).

- Cold plasma approximation ($\lambda \gg \lambda_D$) [2] i.e thermal effects do not have any signif-

---

[2]λ_D is the radius of the Debye sphere. The Debye sphere is formed by the electrons that shield a positive ion charge under Coulomb force. Hence, the plasma is considered quasi neutral only on radial scales greater than λ_D. $\lambda_D = (\varepsilon_0 T/ne^2)^{1/2} = v_{th,e}/\omega_{pe} = 2.35 \times 10^5 \times \sqrt{T_e/n}$ (T_e in keV) where $v_{th,e} = (T_e/m_e)^{1/2}$ is the
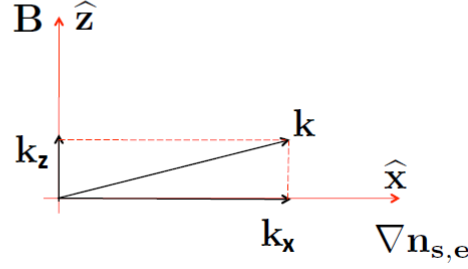
Figure 11: Slab Geometry

icant influence on wave coupling to the plasma where at the plasma edge [3] $\lambda_{LH} \cong$ $8\,cm$ and $\lambda_D \cong 0.1\,mm$ and $\lambda_D \cong 0.1\,mm$. Note that in cold plasma $v_{th,e} \ll v_\phi = \omega/k$, where v_ϕ is the phase velocity of the wave. Moreover, the plasma temperature increases as its distance from the wall increases and reaches $10\,KeV$ in the bulk, that's why the approximations used depend on the plasma position.

- Wentzel-Kramers-Brillouin approximation (WKB) since $k \gg |\nabla n/n|$ i.e. the density changes slowly with respect to the wavelength (k is the wave vector length and n is the density, where $|\nabla n/n|$ is considered as scale length). More precisely, if the density at antenna mouth is less than or equal to the cut-off density or equivalently, if the wave angular frequency ω is greater than ω_{pe}, the wave undergoes strong reflection and is evanescent in which case WKB fails. However, WKB approximation is valid since the wave is launched in an over dense regime that is away from cut-off while x is the only direction of inhomogeneity [56]. Thus the wave solution would be a superposition of harmonic waves having the form $A(x)e^{-i(k_x(x)x+k_zz)}$. (k_x, k_y, and k_z are the components of the wave vector and k_y was replaced by zero.) .

- The direction of the magnetic field is almost parallel to the z direction since we assume a high safety factor q ranging between 3 and 10 as done in most tokamak plasmas [4]. Thus $n_z \simeq n_\parallel$, where $n_\parallel$ is the component of the refractive index vector along the static magnetic field.

- The density profile could be approximated as linearly increasing between the antenna and the FCFL, and zero in the region between the wall and the antenna port [54, 53]. Fig. 13 shows the considered density profile.

---

thermal velocity of the electrons and $\omega_{pe} = (ne^2/\varepsilon_0 m_e)^{1/2}$ is the angular frequency of plasma oscillations. In scrape off layer, $T_e = 100\,eV$ is taken with $n_e = (5.1-9) \times 10^{17} m^{-3}$, which gives $\lambda_D = (0.078-0.14)\,mm$. n_e is taken greater than $3n_c$ where $n_c = 1.7 \times 10^{17}\,m^{-3}$ is the cut-off density since the antenna is placed beyond the cut-off region.

[3]λ_{LH} is the vacuum wavelength at $3.7\,GHz$ frequency which is the LH wave frequency used in Tore Supra tokamak which is small compared to the plasma dimension in large tokamaks.

[4]$q = d\phi/d\theta$, measures the winding of the magnetic field lines, where ϕ is the toroidal angle, and θ is the poloidal angle. Hence for a magnetic field line to complete one poloidal turn, it needs q toroidal turns.
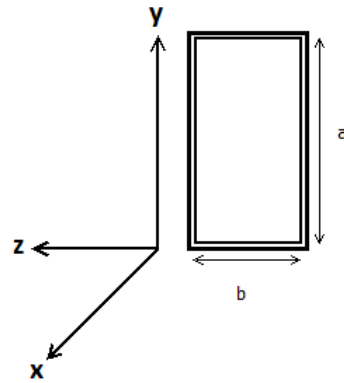
Figure 12: Two dimensional model of a waveguide
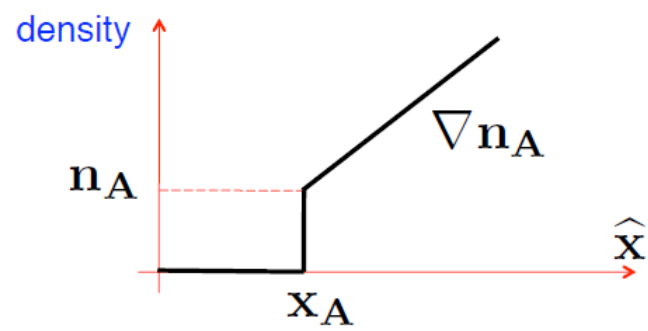
Figure 13: Density profile

As the LH wave is launched into the plasma, the electric field E, magnetic field H, and current density J could be expressed in terms of plasma parameters.

Consider a general form of the E, H, and J fields as: $A(\xi)\exp+i(\omega t - k_z z - k_x x)$ where $\xi = k_0 x$ [5] is a normalization to the LH wave length, and $A(\xi)$ is slowly varying in x with respect to the wavelength. This form conforms with WKB approximation for a plane wave launched into plasma having density inhomogeneity along x direction only. Thereby $\partial/\partial z$ can be replaced by $-ik_z$.

After applying Fourier transform in time, Faraday's and Ampere's laws of Maxwell's equations are:

$$\nabla \times E = -i\omega\mu_0 H \tag{18}$$

$$\nabla \times H = J + i\omega\varepsilon_0 E \tag{19}$$

The characteristics of the cold plasma are identified by the local conductivity tensor $\overline{\overline{\sigma}}$ defined as: $J(r) = \overline{\overline{\sigma}}(r)E(r)$, which is deduced from Lorentz force[6]. Then Eq. 19 becomes

$$\nabla \times H = (\overline{\overline{\sigma}} + i\omega\varepsilon_0 I)E = (i\omega\varepsilon_0)\overline{\overline{\varepsilon}}E \tag{20}$$

where I is the identity matrix and $\overline{\overline{\varepsilon}}$ is the dielectric tensor given by,

$$\overline{\overline{\varepsilon}} = I - \frac{i}{\omega\varepsilon_0}\overline{\overline{\sigma}} = \begin{bmatrix} S & iD & 0 \\ -iD & S & 0 \\ 0 & 0 & P \end{bmatrix} \tag{21}$$

with S, P, and D follow Stix notation

$$S = 1 + \frac{\omega_{pe}^2}{\omega_{ce}^2 - \omega^2} + \sum_s \frac{\omega_{ps}^2}{\omega_{c,s}^2 - \omega^2} \tag{22}$$

$$P = 1 - \left(\frac{\omega_{pe}}{\omega}\right)^2 - \sum_s \left(\frac{\omega_{ps}}{\omega}\right)^2 \tag{23}$$

$$D = \frac{\omega_{pe}^2 \omega_{ce}}{\omega(\omega^2 - \omega_{ce}^2)} + \sum_s \frac{\omega_{ps}^2 \omega_{cs}}{\omega(\omega^2 - \omega_{cs}^2)} \tag{24}$$

---

[5]$k_0 = \omega/c = 2 \times pi/\lambda_0 = 77.453\,rad/m$ where λ_0 is the wavelength in vacuum.
[6]Lorentz force equation: $mv = q(E + v \times B)$.

In the lower hybrid range of frequencies[7], S and D in Eqs. 22 and 24 can be simplified as

$$S \cong 1 + \frac{\omega_{pe}^2}{\omega_{ce}^2} - \frac{\omega_{ps}^2}{\omega^2} \tag{25}$$

$$D \cong -\frac{\omega_{pe}^2}{\omega \omega_{ce}^2}. \tag{26}$$

At this point, the electric field equation(s) would be recovered in view of the plasma characteristics. Eq. 18 gives

$$\frac{\partial}{\partial x} E_y - \frac{\partial}{\partial y} E_x = -i\omega\mu_0 H_z \tag{27}$$

$$\frac{\partial}{\partial x} E_z - \frac{\partial}{\partial z} E_x = +i\omega\mu_0 H_y \tag{28}$$

$$\frac{\partial}{\partial y} E_z - \frac{\partial}{\partial z} E_y = -i\omega\mu_0 H_x \tag{29}$$

Consider $Y_0 = \sqrt{\varepsilon_0/\mu_0} = Z_0^{-1}$, where Y_0 is the wave admittance in vacuum and Z_0 is the wave impedance. Using the relation $\partial/\partial x = k_0 \times \partial/\partial\xi$, Eq. 27 becomes,

$$\frac{\partial}{\partial\xi} E_y = \frac{-i\omega\mu_0}{k_0} H_z = -i\sqrt{\frac{\mu_0}{\varepsilon_0}} H_z = -iZ_0 H_z. \tag{30}$$

Also rearranging Eq. 28 gives,

$$\frac{\partial}{\partial\xi} E_z = \frac{+i\omega\mu_0}{k_0} H_y - i\frac{k_z}{k_0} E_x = i\sqrt{\frac{\mu_0}{\varepsilon_0}} H_y + \frac{k_z}{k_0} E_x = iZ_0 H_y - in_z E_x. \tag{31}$$

Eq. 29 simplifies to

---

[7] $\omega_{LH}^{-1} = \sqrt{((\omega_{cs}\omega_{ce})^{-1} + \omega_{ps}^{-2})}$.

For a hydrogen plasma :

$\omega_{c,s} = Z_s eB/m_s \cong 3.35 \times 10^8 rad/s = 53.3 MHz$

$\omega_{c,e} = eB/m_e \cong 0.615 \times 10^{12} rad/s = 97.99 GHz$

where $Z_s = 1$, is the atomic charge.

$$\frac{\partial}{\partial z}E_y = i\omega\mu_0 H_x \Leftrightarrow H_x = -n_z Y_0 E_y. \tag{32}$$

Note that $\omega = ck_0 = k_0/\sqrt{\varepsilon_0\mu_0} = k_0 Z_0/\mu_0 = k_0/(Y_0\mu_0) = k_0 Y_0/\varepsilon_0$ and $n_z = k_z/k_0$.

Let's investigate the components of Eq. 20 when Eq. 21 is substituted in it,

$$\frac{\partial}{\partial x}H_y - \frac{\partial}{\partial y}H_x = i\omega\varepsilon_0(PE_z) \Leftrightarrow \frac{\partial}{\partial \xi}H_y = iY_0 PE_z \tag{33}$$

$$\frac{\partial}{\partial x}H_z - \frac{\partial}{\partial z}H_x = -i\omega\varepsilon_0(-iDE_x + SE_y)$$

$$\Leftrightarrow \frac{\partial}{\partial \xi}H_z = -iY_0 SE_y - Y_0 DE_x - in_z H_x \tag{34}$$

$$\frac{\partial}{\partial y}H_z - \frac{\partial}{\partial z}H_y = i\omega\varepsilon_0(SE_x + iDE_y) \Leftrightarrow E_x = \frac{1}{S}(-iDE_y + n_z Z_0 H_y) \tag{35}$$

Since the electric and magnetic fields are expressed in terms of E_z and E_y, the second order differential equations in E_z and E_y can be deduced. Eqs. 30 and 34 give,

$$\frac{\partial^2}{\partial \xi^2}E_y = -iZ_0(-iY_0 SE_y - Y_0 DE_x - in_z H_x)$$

and when applying Eq. 32

$$\frac{\partial^2}{\partial \xi^2}E_y = -iZ_0(-iY_0 SE_y - Y_0 DE_x - in_z(-n_z Y_0 E_y))$$

$$\frac{\partial^2}{\partial \xi^2}E_y = (-S + n_z^2)E_y + iDE_x. \tag{36}$$

The electromagnetic dispersion relation for slab geometry as shown in Appendix B is given by

$$\overline{\overline{D}}.E = 0, \tag{37}$$

where $\overline{\overline{D}}$ satisfies the equation

$$\overline{\overline{D}} = k \times k \times \mathbb{I} + \frac{\omega^2}{c^2}(\mathbb{I} + \frac{i}{\omega\varepsilon_0}\overline{\overline{\sigma}}).$$

Which gives due to applying WKB,

$$\bar{\bar{D}} = \begin{bmatrix} S - n_z^2 & iD & n_z n_x \\ -iD & S - n^2 & 0 \\ n_z n_x & 0 & P - n_x^2 \end{bmatrix}.$$

Eq. 37 implies that

$$(S - n_z^2)E_x + iDE_y + n_z n_x E_z = 0$$

i.e

$$E_x = \frac{1}{n_z^2 - S}(iDE_y + n_z n_x E_z). \tag{38}$$

Thus Eq. 36 becomes

$$\frac{\partial^2}{\partial \xi^2}E_y = (n_z^2 - S)E_y + iD\left(\frac{1}{n_z^2 - S}(iDE_y + n_z n_x E_z)\right).$$

Therefore

$$\frac{\partial^2}{\partial \xi^2}E_y = (n_z^2 - S - \frac{D^2}{n_z^2 - S})E_y + \frac{iDn_z n_x}{n_z^2 - S}E_z. \tag{39}$$

Similarly for E_z, Eqs. 31 and 33 give

$$\frac{\partial^2}{\partial \xi^2}E_z = \frac{\partial}{\partial \xi}(iZ_0 H_y - in_z E_x)$$

$$\frac{\partial^2}{\partial \xi^2}E_z = iZ_0(iY_0 P E_z) - in_z \frac{\partial}{\partial \xi}E_x.$$

Now substituting Eq. 35, gives

$$\frac{\partial^2}{\partial \xi^2}E_z = -PE_z - \frac{n_z D}{S}(\frac{\partial}{\partial \xi}E_y) - i\frac{n_z^2}{S}Z_0(\frac{\partial}{\partial \xi}H_y)$$

Eqs. 30 and 33 give

$$\frac{\partial^2}{\partial \xi^2}E_z = -PE_z - \frac{n_z D}{S}(-iZ_0 H_z) - i\frac{n_z^2}{S}Z_0(iY_0 P E_z)$$

$$\frac{\partial^2}{\partial \xi^2}E_z = \frac{P}{S}(n_z^2 - S)E_z - \frac{n_z D(-iZ_0)}{S}H_z.$$

Hence

$$\frac{\partial^2}{\partial \xi^2} E_z = \frac{P}{S}(n_z^2 - S)E_z + \frac{in_z D}{S}E_y. \tag{40}$$

Having $D \simeq 0^8$ in the SOL as shown in Appendix B, Eqs. 39 and 40 are decoupled. Eq. 39 gives

$$\frac{\partial^2}{\partial \xi^2} E_y = (n_z^2 - S)E_y, \tag{41}$$

also Eq. 40 gives

$$\frac{\partial^2}{\partial \xi^2} E_z = \frac{P}{S}(n_z^2 - S)E_z. \tag{42}$$

Having E_y and E_z as two independent variables, two wave branches are obtained by solving for $A(\xi)$,

$$A(\xi) = e^{-ik_x x} = e^{-in_x \xi}$$

using Eqs . 41 and 42 for $E_z = 0$ and $E_y = 0$ respectively. For $E_z = 0$, Eq. 41 gives

$$n_{x,f} = -(n_z^2 - 1),$$

where for $E_y = 0$, Eq. 42 gives

$$n_{x,s} = -\frac{P}{S}(n_z^2 - S) \cong -P(n_z^2 - 1).$$

$n_{x,f}$ and $n_{x,s}$ define the perpendicular refractive index for the two LH wave branches, the fast and slow mode respectively. Since $n_{x,f} < n_{x,s}$ with $n_x = c/v_x$, then $v_{x,f} > v_{x,s}$. The slow wave is electrostatic since for $E_y = 0$, Eq. 38 gives $E_x/n_x = E_z/n_z$ (electrostatic wave has $E \parallel n$).

As a conclusion, the differential equations in E_y and E_z are decoupled, i.e the y and z components of the LH wave are independent, thus depicting two wave branches, the fast and the slow wave. Hence when one branch is excited it propagates independently of the other branch. Due to the slow wave efficiency in driving current in the z direction and since it has a lower cut-off density [9] compared to the fast wave which renders it easier to launch, the antenna is designed to launch slow waves rather than fast waves. Note that the wave $n_\parallel$ refractive index should exceed n_a corresponding to the highest plasma density to avoid slow-fast wave mode conversion as shown in Appendix B. This reduces reflection towards the antenna and validates the assumption that only slow waves are included in coupling equations [51, 52].

---

[8] For $\omega = 2 \times \pi \times 3.7 \times 10^9 rad/s$, $n = (10^{17} - 3 \times 10^{19})m^{-3}$, and $B = 3.5T$ (Tore Supra Tokamak magnetic field)

For $n = 10^{17}$, $D \cong -\omega_{pe}^2/\omega \omega_{c,e} \cong -0.0223$, so for $n = A \times 10^{17}$, $D = -A \times 0.0223$.

Near the antenna, $S \cong 1$ and for $n = (10^{17} - 3 \times 10^{19})$ $P \cong (-175.9147 - 0.4273)$ where $|P|$ is increasing for increasing density.

[9] $n_{cut,fast} \cong 8.4 \times 10^{18} m^{-3} \cong 49.4 \times n_{cut,slow}$

Let's write the equations of the electric and magnetic fields corresponding to the modes that propagate inside a wave guide designed to launch waves that have nonzero E_z component where $E_y \cong 0$.

C. Waveguide Modes

1. Rectangular Waveguides

The Grill depicted in Fig. 14 is made of an array of waveguides juxtaposed in the z direction with a geometric period Δ, and separated by thin walls. It is placed few centimeters from the chamber wall to work in an over dense regime. The Grill or the antenna front surface ($x = 0$) is considered to compute the emitted fields which being continuous at the antenna-plasma interface serve as boundary conditions for the propagating fields inside the plasma.

First consider a rectangular waveguide that has dimensions $y = a$ and $z = b$ as shown in Fig. 12.

The plane waves propagate as TEM waves (transverse electric magnetic) in vacuum. TEM waves have both electric and magnetic fields transverse to the direction of propagation. However, in waveguides the wave could propagate in different forms known as TE (transverse electric) and TM (transverse magnetic) modes. TE modes known also as magnetic waves have zero electric field in the direction of propagation. TM modes known also as electric waves have zero magnetic field in the direction of propagation. In particular, inside a rectangular waveguide the TEM mode does not propagate as shown in Appendix B., while TE_{mn} and TM_{mn} modes exist for some nonnegative integers m, n depending on the dimensions of the wave guide (Fig. 12) and the wave frequency. Appendix B. demonstrates how the dimensions of the waveguide determine the cut-off frequency

$$f_{cmn} = c\sqrt{(\frac{m}{2a})^2 + (\frac{n}{2b})^2} \tag{43}$$

of each of these modes where c is the speed of light.

Knowing that a wave propagates in a specific mode if its frequency is above the cut-off frequency of that mode, the propagating modes for a wave guide having $a = 7.2\,cm$ and $b = 3.4\,cm$ are to be investigated as an example. Using Eq. 43, the lowest TE_{mn} cut-off frequency is for $(m,n) = (1,0)$,

$$f_{c10} \cong 2.083\,GHz.$$

Since the next cut-off frequency obtained for $(m,n) = (2,0)$ is

$$f_{c20} = 4.16\, GHz,$$

and since the wave is excited at 3.7 GHz (Tore Supra LH antennas) it is verified that TE_{10} is the dominant and only propagating mode among TE_{mn} modes.

Similarly, the lowest TM_{mn} cut-off frequency is

$$f_{c11} = 15.152\, GHz$$

obtained for $(m,n) = (1,1)$. Thus all TM_{mn} modes are evanescent with TM_{11} being the mode of lowest cut-off frequency.

Suppose that the wave is propagating in the x direction as shown in Fig. 12. The propagating TE_{mn} mode field equations are derived in Appendix B.,

$$E_y(y,z) = \frac{n\pi}{b} \frac{i\omega\mu_0}{(\frac{m\pi}{a})^2 + (\frac{n\pi}{b})^2} A_{mn} cos(\frac{m\pi}{a}y) sin(\frac{n\pi}{b}z) e^{i(\omega t - \beta x)} V.m^{-1}$$

$$E_z(y,z) = -\frac{m\pi}{a} \frac{i\omega\mu_0}{(\frac{m\pi}{a})^2 + (\frac{n\pi}{b})^2} A_{mn} sin(\frac{m\pi}{a}y) cos(\frac{n\pi}{b}z) e^{i(\omega t - \beta x)} V.m^{-1}$$

$$E_x = 0,$$

and

$$H_x(y,z) = A_{mn} cos(\frac{m\pi}{a}y) cos(\frac{n\pi}{b}z) e^{i(\omega t - \beta x)} A.m^{-1}$$

$$H_y(y,z) = \frac{m\pi}{a} \frac{i\beta}{(\frac{m\pi}{a})^2 + (\frac{n\pi}{b})^2} A_{mn} sin(\frac{m\pi}{a}y) cos(\frac{n\pi}{b}z)_z e^{i(\omega t - \beta x)} A.m^{-1}$$

$$H_z(y,z) = \frac{n\pi}{b} \frac{i\beta}{(\frac{m\pi}{a})^2 + (\frac{n\pi}{b})^2} A_{mn} cos(\frac{m\pi}{a}y) sin(\frac{n\pi}{b}z) e^{i(\omega t - \beta x)} A.m^{-1},$$

where A_{mn} has the same unit as the magnetic field intensity $(A.m^{-1})$, μ_0 is the vacuum permeability[10], $\beta = \sqrt{k^2 - (k_y^2 + k_z^2)}(rad.m^{-1})$, $k = \omega/c$, $k_y = m\pi/a$ and $k_z = n\pi/b$ for $m, n = 0,1,2,\dots$ but $(m,n) \neq (0,0)$.

---

[10] $\mu_0 = 4\pi \times 10^{-7} H.m^{-1}(V.s.A^{-1}.m^{-1})$

The TM_{mn} mode field equations are given by,

$$E_y(y,z) = -\frac{m\pi}{a}\frac{\alpha}{(\frac{m\pi}{a})^2 + (\frac{n\pi}{b})^2}e^{-\alpha x}B_{mn}cos(\frac{m\pi}{a}y)sin(\frac{n\pi}{b}z)e^{i\omega t}V.m^{-1} \qquad (44)$$

$$E_z(y,z) = -\frac{n\pi}{b}\frac{\alpha}{(\frac{m\pi}{a})^2 + (\frac{n\pi}{b})^2}e^{-\alpha x}B_{mn}sin(\frac{m\pi}{a}y)cos(\frac{n\pi}{b}z)e^{i\omega t}V.m^{-1}$$

$$E_x(y,z) = e^{-\alpha x}B_{mn}sin(\frac{m\pi}{a}y)sin(\frac{n\pi}{b}z)e^{i\omega t}V.m^{-1},$$

and

$$H_y(y,z) = \frac{n\pi}{b}\frac{i\omega\varepsilon_0}{(\frac{m\pi}{a})^2 + (\frac{n\pi}{b})^2}e^{-\alpha x}B_{mn}sin(\frac{m\pi}{a}y)cos(\frac{n\pi}{b}z)e^{i\omega t}A.m^{-1}$$

$$H_z(y,z) = -\frac{m\pi}{a}\frac{i\omega\varepsilon_0}{(\frac{m\pi}{a})^2 + (\frac{n\pi}{b})^2}e^{-\alpha x}B_{mn}cos(\frac{m\pi}{a}y)sin(\frac{n\pi}{b}z)e^{i\omega t}A.m^{-1}$$

$$H_x = 0,$$

where B_{mn} has the same unit as the electric field intensity $V.m^{-1}$, ε_0 is the vacuum per-mittivity[11], $\beta = k_x$, $k_y = m\pi/a$ and $k_z = n\pi/b$ for $m, n = 1, 2, \ldots$

The electric and magnetic field functions at the aperture of the first waveguide for both TE_{10} and TM_{11} modes shall be explored. TM_{11} mode being the first TM evanescent mode and gives an example of TM_{mn} modes is considered, though TM_{mn} modes do not propagate inside the antenna, but they can be excited at the antenna mouth and thus have to be included in wave-plasma coupling calculations.

The power spectrum depends on the phase between successive waveguides [50, 57]. Consider N waveguides with a successive phase difference of Φ among adjacent waveguides juxtaposed periodically in the z direction as shown in Fig. 14 with period Δ.

Assuming a zero phase in the first waveguide taken as reference waveguide (Fig. 14), the E_z component of the magnetic field in the pth waveguide is given by

$$E_{z,p}(y,z) = E_{z,ref}(z - (p-1)\Delta)e^{i\Phi_p}, \ (p-1)\Delta \leq z \leq (p-1)\Delta + b$$

---

[11]$\varepsilon_0 \approx 8.854 \times 10^{-12}F.m^{-1}(A.s.V^{-1}.m^{-1})$

where $E_{z,ref}$ is the electric field in the reference waveguide starting at $z = 0$ for $0 \leq z \leq b$, and $e^{i\Phi_p} = e^{-i(p-1)\Phi}$. Hence the total electric field becomes

$$E_{z,tot}(y,z) = \sum_{p=1}^{p=N} \theta_{I_p}(z)E_{z,p}, \tag{45}$$

where $E_{z,tot}$ is the electric field at z for $0 \leq z \leq (N-1)\Delta + b$, and θ_{I_p} is the box car function[12] such that

$$\theta_{I_p}(z) = H(z - (p-1)\Delta) \times H((p-1)\Delta + b - z)$$

where $H(z)$ is the Heaviside function defined by

$$H(z) = \begin{cases} 1 \: if \: z \geq 0 \\ 0 \: if \: z < 0 \end{cases}$$

The TE_{10} mode field equations at the first reference waveguide become after normalizing with respect to the maximum amplitude of the H_x magnetic field : ($k_y = \pi/a$, $k_z = 0$)

$$E_x(y,z) = E_y(y,z) = 0,$$

$$E_z(y,z) = -\frac{i\omega\mu_0 a}{\pi} \times 1(A.m^{-1}) \times sin(\frac{\pi}{a}y)e^{i\omega t}V.m^{-1}, \tag{46}$$

and

$$H_x(y,z) = cos(\frac{\pi}{a}y)e^{i\omega t}A.m^{-1},$$

$$H_y(y,z) = \frac{i\beta a}{\pi}sin(\frac{\pi}{a}y)e^{i\omega t}A.m^{-1},$$

$$H_z(y,z) = 0.$$

Hence, the E_z component at the Grill given by Eqs. 45 and 46 is,

$$E_{z,TE_{10}}(y,z) = \frac{\omega\mu_0 a}{\pi}sin(\frac{\pi}{a}y)\sum_{p=1}^{p=N}\theta_{I_p}(z)sin(\omega t - (p-1)\Phi)V.m^{-1}.$$

---

[12] $\theta_{I_p} = \begin{cases} 1 \: if \: z \in I_p, \: I_p = [(p-1)\Delta, (p-1)\Delta + b] \\ \qquad 0 \qquad otherwise. \end{cases}$

Similarly, the TM_{11} mode field equations at the aperture of the first wave guide are given after normalizing with respect to the maximum amplitude of the E_x magnetic field for the first reference waveguide,

$$E_x(y,z) = sin(\frac{\pi}{a}y)sin(\frac{\pi}{b}z)e^{i\omega t}V.m^{-1},$$

$$E_y(y,z) = -\frac{\pi}{a}\frac{\alpha}{(\frac{\pi}{a})^2 + (\frac{\pi}{b})^2}cos(\frac{\pi}{a}y)sin(\frac{\pi}{b}z)e^{i\omega t}V.m^{-1}$$

$$E_z(y,z) = \frac{\pi}{b}\frac{-\alpha}{(\frac{\pi}{a})^2 + (\frac{\pi}{b})^2}sin(\frac{\pi}{a}y)cos(\frac{\pi}{b}z)e^{i\omega t}V.m^{-1} \qquad (47)$$

and

$$H_x(y,z) = 0,$$

$$H_y(y,z) = \frac{\pi}{a}\frac{i\omega\varepsilon_0}{(\frac{\pi}{a})^2 + (\frac{\pi}{b})^2} \times 1(V.m^{-1}) \times sin(\frac{\pi}{a}y)cos(\frac{\pi}{b}z)e^{i\omega t}A.m^{-1}$$

$$H_z(y,z) = -\frac{\pi}{a}\frac{i\omega\varepsilon_0}{(\frac{\pi}{a})^2 + (\frac{\pi}{b})^2} \times 1(V.m^{-1}) \times cos(\frac{\pi}{a}y)sin(\frac{\pi}{b}z)e^{i\omega t}A.m^{-1}.$$

Hence, the E_z component at the Grill given by Eqs. 45 and 47 is,

$$E_{z,TM_{11}}(y,z) = -\frac{\pi}{b}\frac{\alpha}{(\frac{\pi}{a})^2 + (\frac{\pi}{b})^2}sin(\frac{\pi}{a}y)\sum_{p=1}^{p=N}\theta_{I_p}(z)cos(\frac{\pi}{b}(z-(p-1)\Delta))cos(\omega t-(p-1)\Phi)V.m^{-1}.$$

The patterns of the electric field component E_z corresponding to TE_{10} and TM_{11} modes for different instants of time for $\Phi = \pi/2$ are given in Figs. 15 and 16 respectively. Figs. 15 and 16 show standing waves at a fixed y with a pattern that repeats itself each four waveguides due to taking $\Phi = \pi/2$ and since the modes are harmonic functions in z. Note that

$$\left|\frac{E_{z,TE_{10},max}}{E_{z,TM_{11},max}}\right| = ((\frac{\pi}{a})^2 + (\frac{\pi}{b})^2)\frac{ab\omega\mu_0 \times 1(A.V^{-1})}{\alpha\pi^2} = \frac{\omega\mu_0[a^2+b^2] \times 1(A.V^{-1})}{ab\alpha} = 1.13 \times 10^3$$
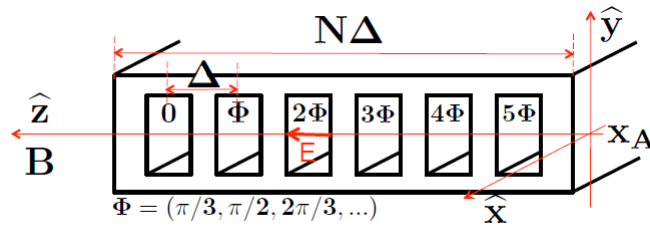
Figure 14: The Grill

where

$$\alpha = \sqrt{[(\frac{\pi}{a})^2 + (\frac{\pi}{b})^2] - k^2} = 66.6 \, rad.m^{-1}.$$

Hence it is verified that the E_z amplitude of the TE_{10} mode is much higher than that of the TM_{11} mode, thus it matches very well with the plasma fields.

2. Parallel Plate Wave Guide

This study mainly deals with a parallel plate waveguide since it models an antenna infinite in one dimension. $0y$ axis is taken as the infinite dimension as shown in Fig. 59 due to assuming plasma homogeneous in the y direction. Consequently, $k_y = 0$. As discussed in Appendix B., the field modes that exist inside this waveguide are the TEM mode which has a zero cut-off frequency, and the TE_n and the TM_n modes ($n > 0$) which have a cut-off frequency

$$f_{cn} = \frac{n \times c}{2b}. \tag{48}$$

Since for $b = 3.4 \, cm$, $f_{cn} = n \times 4.41 \, GHz$, at $3.7 \, GHz$ frequency the TM_n and TE_n modes are evanescent.

The field equations for the TEM mode in the first waveguide with a zero phase, are given by Appendix B.

$$E_y = E_x = H_z = H_x = 0$$

$$E_z(x) = -\frac{A_n}{b} e^{i(\omega t - \beta x)} V.m^{-1} \tag{49}$$
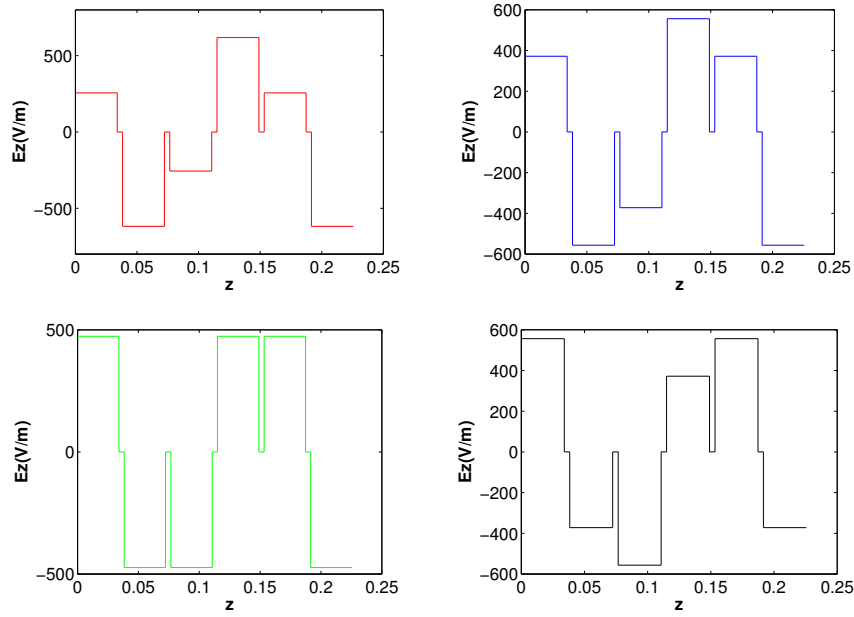
Figure 15: E_z of TE_{10} for $a = 7.2\,cm$, $b = 3.4\,cm$, at $y = 3.6cm$ and for $\Delta = b + 0.4235\,cm$ with 6 output ports evolving in time ($t = \pi/8\omega\,(red)$, $\pi/8\omega + \pi/16\omega\,(blue)$, $\pi/4\omega\,(green)$, $\pi/4\omega + \pi/16\omega\,(black)$ left to right, top to bottom) $(\Phi = \pi/2)$
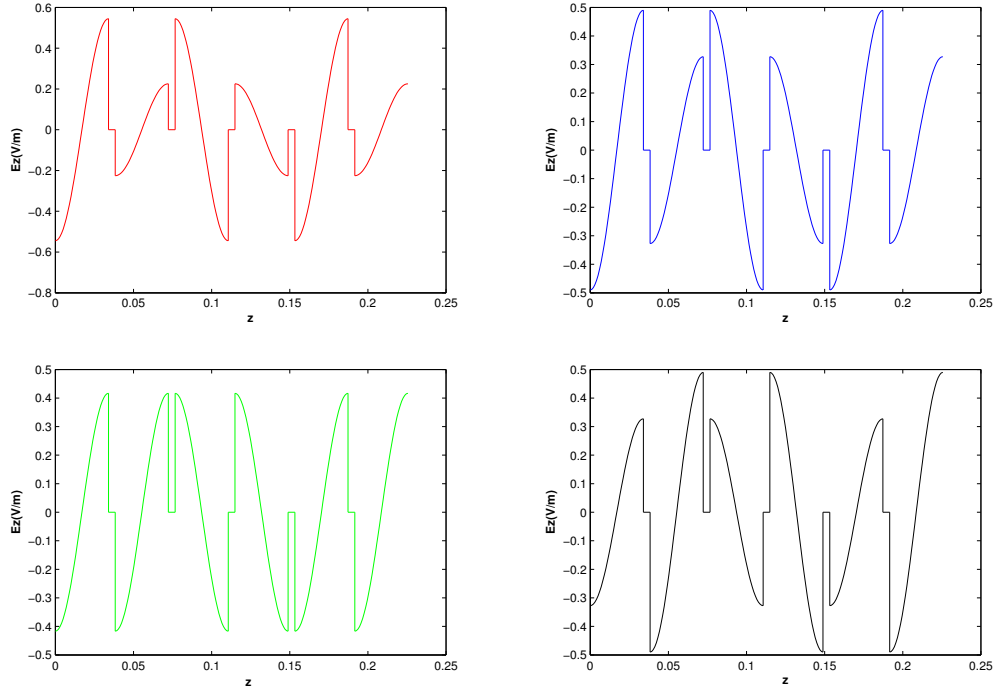
Figure 16: E_z of TM_{11} for $a = 7.2cm$, $b = 3.4\,cm$, at $y = 3.6cm$ and for $\Delta = b + 0.4235\,cm$ with 6 output ports evolving in time ($t = \pi/8\omega\,(red)$, $\pi/8\omega + \pi/16\omega\,(blue)$, $\pi/4\omega\,(green)$, $\pi/4\omega + \pi/16\omega\,(black)$ left to right, top to bottom)$(\Phi = \pi/2)$

$$H_y(x) = \hat{\mathbf{x}} \times \frac{1}{\eta_0}\hat{\mathbf{z}}E_z = \frac{A_n}{bc\mu_0}e^{i(\omega t - \beta x)}A.m^{-1}.$$

where A_n in V is the maximum value of the potential difference between the plates, $\beta = 2\pi/\lambda_0$, η_0 is the wave impedance in vacuum and c is the speed of light in vacuum.

Hence, the E_z component at the Grill given by Eqs. 45 and 49 after normalizing with respect to A_n,

$$E_{z,TEM}(z) = -\frac{1}{b}\sum_{p=1}^{p=N}\theta_{I_p}(z)cos(\omega t - (p-1)\Phi)V.m^{-1}.$$

Referring to Appendix B., the field equations for an evanescent TM_n mode in the first waveguide with a zero phase, are given by

$$E_y = H_x = H_z = 0$$

$$E_x(x,z) = B_n e^{-\alpha x}sin(\frac{n\pi z}{b})e^{i\omega t}V.m^{-1} \tag{50}$$

$$E_z(x,z) = -\frac{\alpha b}{n\pi}e^{-\alpha x}B_n cos(\frac{n\pi z}{b})e^{i\omega t}V.m^{-1} \tag{51}$$

$$H_y(x,z) = \frac{i\omega\varepsilon_0 b}{n\pi}e^{-\alpha x}B_n cos(\frac{n\pi z}{b})e^{i\omega t}A.m^{-1} \tag{52}$$

where B_n is in $V.m^{-1}$ and $\alpha = \sqrt{(\frac{n\pi}{b})^2 - k^2}\ rad.s^{-1}$.

Hence, the E_z component at the Grill given by Eqs. 45 and 51 after normalizing with respect to the maximum amplitude of the E_x electric field for the first reference waveguide,

$$E_{z,TM_1}(x,z) = \frac{-\alpha b}{\pi}\sum_{p=1}^{p=N}\theta_{I_p}(z)cos(\frac{\pi(z-(p-1)\Delta)}{b})cos(\omega t - (p-1)\Phi)V.m^{-1}.$$

The TM_n modes are considered rather than the TE_n modes though both are evanescent, since TE_n modes have zero E_z (Appendix B..) which corresponds to fast waves which are strongly damped in edge plasma.

The dominant TEM mode and the evanescent TM_1 fields are obtained for the adjacent waveguides with a phase difference Φ and periodicity Δ. Figs. 17 and 18 show

the electric field component E_z of the *TEM* and *TM*$_1$ modes in front the Grill ($x > 0$) respectively. These modes show periodic patterns over each four waveguides since Φ is chosen to be $\pi/2$. Comparing the E_z amplitudes of the *TEM* and *TM*$_1$ modes, for

$$\alpha = \sqrt{(\frac{\pi}{b})^2 - k^2} = 50.32\,rad.s^{-1},$$

gives

$$|\frac{E_{z,TEM,max}}{E_{z,TM_1,max}}| = \frac{\pi \times 1m}{\alpha b^2} = 54.$$

Note that the *TEM* mode E_z is one order higher than that of the *TM*$_1$ as shown in Figs. 17 and 18.

Since a parallel plate wave guide characterized by $k_y = 0$, models the assumption that the plasma is homogeneous in the *y* direction (2-D theory), the *TEM* mode is considered for the calculation of the power spectrum being the dominant mode. It is deduced from the above that the electric field corresponding to the dominant *TEM* mode has only E_z component varying as a standing wave independent of *y* with amplitude that is two orders higher than that of the first evanescent *TM*$_1$ (considered since it could be excited a the antenna mouth). In the following chapter, the power spectrum radiated by an array of waveguides at $x = 0$, shall be calculated assuming only *TEM* E_z electric field. The electric field obtained constitutes an initial condition for solving Eq. 40.

D. Radiated Power Spectrum By a Conventional Grill

The antenna is designed to launch a slow wave ($n_z > 1$) characterized by $E_y = 0$. It is placed into the plasma chamber some centimeters away from the wall so that the EM waves are not reflected by the slow wave cut-off and the density satisfies the over dense regime rendering WKB approximation valid .

Assuming that the radiated electric field is the E_z corresponding to the *TEM* mode, the effect of having a progressive phase difference between the excited waves in the adjacent wave guides of the Grill on controlling the power spectrum as a function of n_z will be shown.

Let Φ be the phase difference between the excited fields at the output of each wave guide as shown in Fig. 14. The position of the wave guide z_p, and it's phase are measured with respect to the first wave guide.

Let $z_p = (p-1)\Delta$, and $\Phi_P = -(p-1)\Phi$ for $p = 1,\ldots,N$, where Δ is the periodic
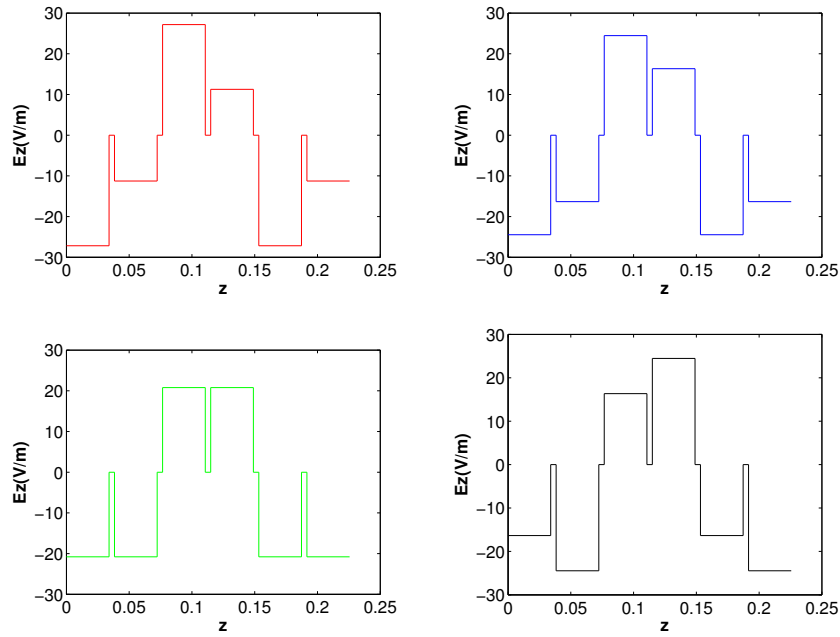
Figure 17: E_z of TEM mode in a parallel wave guide of width $b = 3.4cm$ and $\Delta = b + 0.4235\,cm$ with 6 output ports evolving in time $(t = \pi/8\omega\,(red),\,\pi/8\omega + \pi/16\omega\,(blue),\,\pi/4\omega\,(green),\,\pi/4\omega + \pi/16\omega\,(black)$ left to right, top to bottom$)(\Phi = \pi/2)$
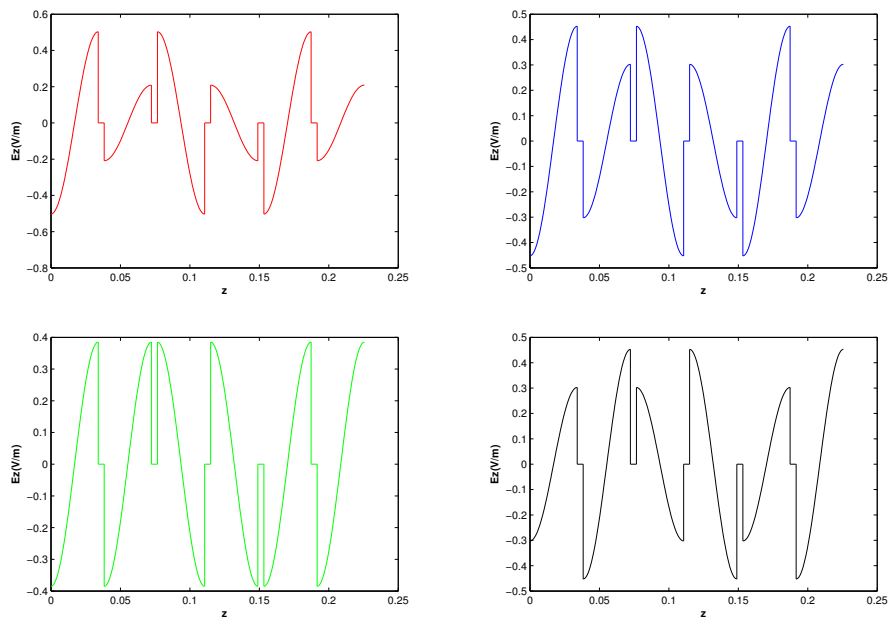
Figure 18: E_z of TM_1 mode of a parallel plate waveguide for $b = 3.4\,cm$ and $\Delta = b + 0.4235\,cm$, $\Phi = \pi/2$ with 6 output ports evolving in time $(t = \pi/8\omega\,(red),\,\pi/8\omega + \pi/16\omega\,(blue),\,\pi/4\omega\,(green),\,\pi/4\omega + \pi/16\omega\,(black)$ left to right, top to bottom$)(\Phi = \pi/2)$

distance between the waveguides in z direction and N is the number of the waveguides. Having the electric field normalized to maximum amplitude, let's take it's Fourier transform along the parallel z dimension of the Grill,

$$\overline{E_z}(0, n_z) = \sum_{p=1}^{N} \int_{z_p}^{z_p+b} E_{zp}(0, z) e^{i n_z k_0 z} [e^{-i n_x k_0 x} + \rho e^{i n_x k_0 x}] dz,$$

where $E_{zp}(0, z) = e^{i\Phi_p}$ due to uniform excitation of the Grill and ρ is the reflection coefficient. Hence at $x = 0$ and neglecting reflections,

$$\overline{E_z}(0, n_z) = b e^{i n_z k_0 b/2} sinc(n_z k_0 b/2) \sum_{p=1}^{N} e^{i\phi}, \tag{53}$$

where $\phi = n_z k_0 \Delta - \Phi$, and

$$sinc(n_z k_0 b/2) = \frac{sin(n_z k_0 b/2)}{n k_0 b/2}.$$

Knowing that

$$\sum_{p=1}^{N} e^{i(p-1)\phi} = \left\{ \begin{matrix} \frac{sin(N\phi/2)}{sin(\phi/2)} e^{i(N-1)\phi/2} \\ N \, for \, \phi = 0, 2\pi, \end{matrix} \right.$$

the module of the radiated power density per unit length becomes,

$$\frac{dP}{dn_z} = \frac{Y_0}{\lambda_0} \overline{|E_z(0, n_z)|^2} = (Y_0/\lambda_0) b^2 sinc^2(n_z k_0 b/2) \left(\frac{sin(N\phi/2)}{sin(\phi/2)} \right)^2 W.m^{-1}. \tag{54}$$

where λ_0 is the wavelength in free space ($\lambda_0 = 2\pi/k_0$). The obtained power density as a function of n_z for a phase difference of $\pi/2$ is shown in Fig. 19. Note that the sinc function describes the envelop where the maxima and minima are given by the sinusoidal functions in ϕ.

Since ϕ is centered at

$$n_{z,0} = \phi/\Delta k_0 = \phi \lambda_0/(\Delta \times 2\pi),$$

(k_0 is the module of the wave vector) the power density attains it's peak at $n_{z,0}$, but it is important to ensure it's not symmetric in n_z, so that the net current is not zero.

The maxima are attained at $\phi/2 = \pi l$, for $l = 0, \pm 1, \pm 2$ etc ... So the first maxima for positive and negative n_z are for $l = 0$, and $l = -1$, that is for $n_{z,0}$ and $n_{z,0^-} = n_{z,0}(1 - 2\pi/\phi)$. For achieving CD, the values of ϕ are chosen to ensure non-symmetric lobes at $n_{z,0}$ and $n_{z,0^-}$.

Regarding the width of the main peak taken at the values at which the power spectrum is half its maximum value. Eq. 54, gives

$$\Delta n_z = \frac{\lambda_0}{L}, \tag{55}$$

where L is the width of the Grill along z.

Also, the zeros of the power spectrum situated around the maxima are given by $N\phi/2 = l\pi \pm \pi = (l \pm 1)\pi$ for $l = mN$ for some integer m.

Therefore $n_z = ((2\pi/N) + \phi)/k_0\Delta$ is a minimum corresponding to the first principal lobe, and the distance between a maximum and a minimum of a lobe is concluded to be $\lambda_0/N\Delta$. The latter is less than Δn_z, since $L < N\Delta$.

Note that Eq. 55 indicates that the width of the n_z spectrum is inversely proportional to the width of the Grill and therefore the toroidal number of waveguides in the Grill. On the other hand, power should be maximized to achieve CD. Consequently, $N\Delta$ is increased by adding more wave guides in the toroidal direction. However the power density cannot be maximized above certain threshold at which deleterious effects appear. These include RF break down in the waveguides and non-linear effects such as density modification due to ponderomotive force [57, 55, 51, 52].

Note that the power amplitude and the number and position of the lobes change with ϕ , the number of the waveguides and Δ. Fig. 19 shows the power spectrum density for $\phi = \pi/2$, $b = 34$ mm, $\Delta = b + 4.235$ mm and for $N = 8$ (solid line) and $N = 24$ (dashed line). The peak is obtained at $n_{z,0} \cong 0.5$ for both values of N; however to obtain a peak at $n_z \cong 2$, $\Delta \simeq 1$ is chosen. Fig. 20 shows how the antenna $n_{z,0}$ and directivity change with Δ and ϕ respectively.

Having given an idea about the dependence of the power spectrum on n_z and the effect of choosing the phase difference between the wave ports on controlling the power spectrum and thus the created current, let's elaborate on the an important parameter that is used to find the n_z spectrum which is the antenna-plasma surface admittance $Y_s(n_z)$.

E. Admittance of Plasma Surface In Front The Antenna

Efficiency of coupling of the electromagnetic waves to plasma is measured by the capacity to transmit the maximum power available at the generators to the plasma without reflection. Matching of the antenna impedance to the plasma could be artificially done from outside but it leads to increasing the electric field and the power density which is not desirable due to causing deleterious effects. Launching slow waves $(n_z > 1)$ is done by introducing a phase difference between the consecutive waveguides, but in this case $N(N + 1)$ parameters are to be controlled due to strong coupling between the N waveguides. This imposes difficulty in controlling the matching system by conventional ways. Hence, it is necessary to derive $Y_s(n_z)$, the plasma surface admittance, in order to
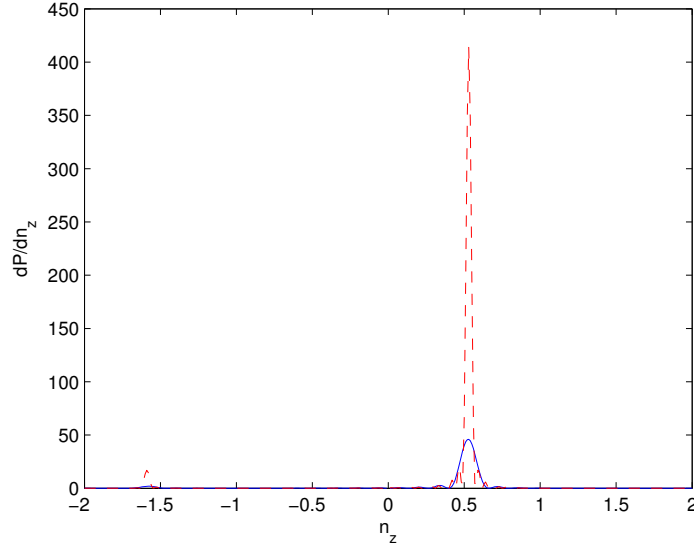
Figure 19: Power Spectrum Density: 8 waveguides (solid line) and 24 waveguides (dashed line)

study antenna-plasma coupling[51, 52]. $Y_s(n_z)$ is a function of edge plasma characteristics including density and density gradient. Suppose that the density increases linearly in front the antenna aperture at $x = 0$, where it is zero for $x < 0$, i.e inside the antenna as shown in Fig. 13. $Y_s(n_z)$ is by definition

$$Y_s(n_z) = -\frac{1}{Y_0}[H_y/E_z]_{\xi=\xi_0}$$

where $\xi_0 = k_0 x|_{x=0} = 0$. $Y_s(n_z)$ shall be developed explicitly.

First Eq. 63 is used since it relates E_z to H_y, thus

$$\frac{E_x}{E_z} = \frac{1}{S}(-iDE_y/E_z + n_z Z_0 H_y/E_z), \tag{56}$$

hence when substituting Eq. 31, Eq. 56 becomes

$$\frac{-1}{jn_z}[\frac{\partial}{\partial \xi}E_z - iZ_0 H_y]\frac{1}{E_z} = (-iD/SE_z)E_y + (n_z Z_0/S)H_y/E_z,$$

therefore

$$\frac{i}{n_z E_z}\frac{\partial}{\partial \xi}E_z - (1/n_z)Y_s = (-iDE_y/SE_z) - (n_z/S)Y_s.$$

In conclusion

$$Y_s = \frac{1}{(n_z^2 - S)}[-in_z D\frac{E_y}{E_z} - i\frac{S}{E_z}\frac{\partial}{\partial \xi}E_z]_{\xi=\xi_0}. \tag{57}$$
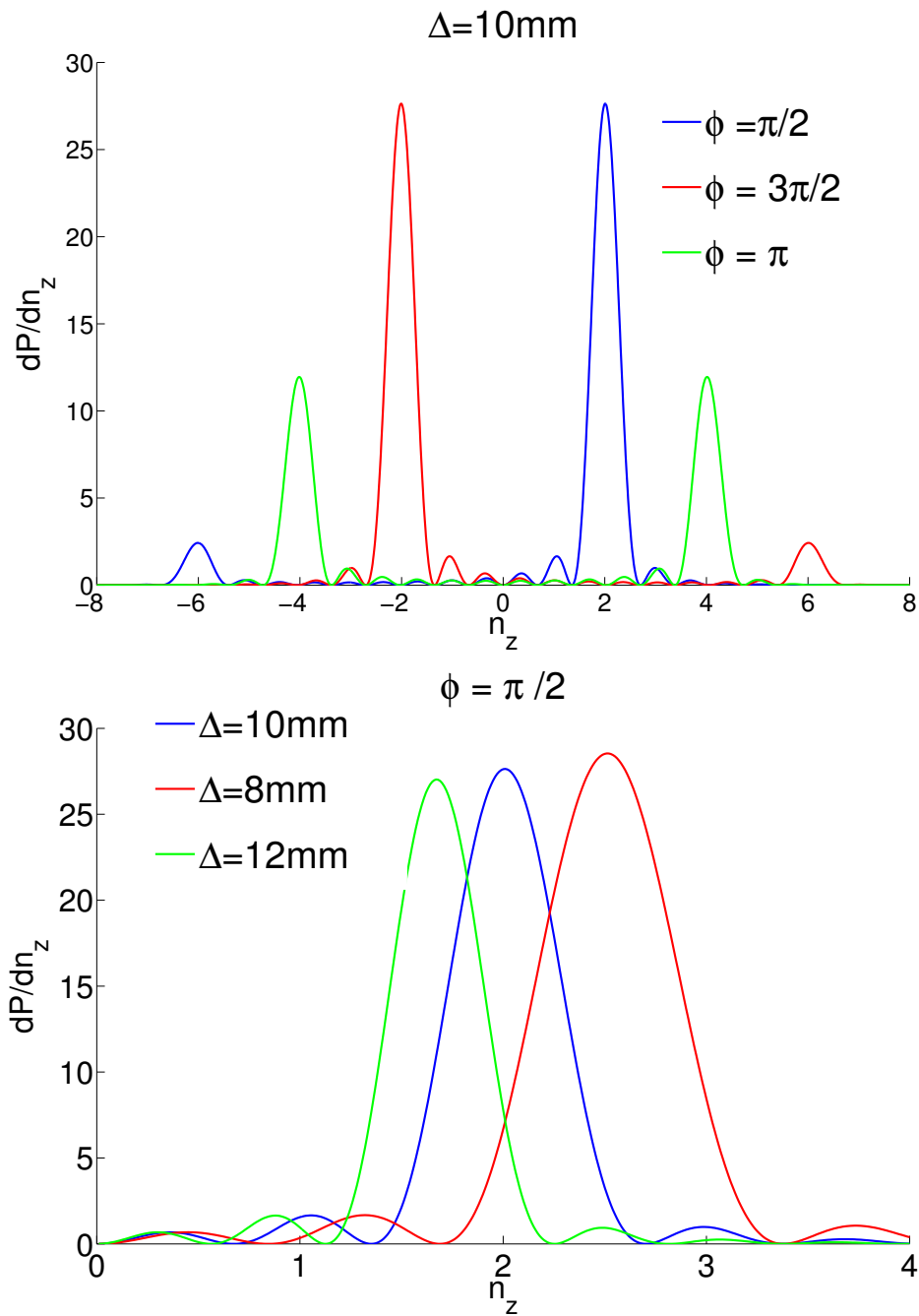
Figure 20: Upper: waveguide phasing ϕ effect on the power spectrum directivity for a waveguide width of $8\,mm$ i.e $\Delta = 10\,mm$ for a FAM antenna. Lower: effect of waveguide width on the antenna peak in $n_{\parallel,0}\,(n_{z,0})$.

In front the antenna the density is close to n_c, hence Eqs. 23, 22, and 24 simplify to $S \approx 1$, $D \approx 0$, and $P = 1 - \omega_{pe}^2/\omega^2$ as shown in Appendix B. Eq. 57 becomes

$$Y_s = \frac{1}{(n_z^2 - 1)}[-i\frac{1}{E_z}\frac{\partial}{\partial \xi}E_z]_{\xi=\xi_0}. \tag{58}$$

Having to find the electric field E_z differential equation of the slow wave, Eqs. 31, 63, and 33 are used to obtain

$$\frac{\partial}{\partial \xi}E_z = iZ_0 H_y - i(n_z^2/S)(Z_0 H_y) = iZ_0 H_y - i(n_z^2)(Z_0 H_y).$$

So,

$$\frac{\partial^2}{\partial \xi^2}E_z = iPY_0 E_z(iZ_0 - i(n_z^2/S)Z_0) = E_z(-P)(\frac{n_z^2}{S} - 1) = E_z(-P)(n_z^2 - 1)$$

Letting $\chi(\xi) = \omega_{pe}^2/\omega^2 = n/n_c$,

$$\frac{\partial^2}{\partial \xi^2}E_z = E_z[\chi(\xi) - 1](n_z^2 - 1). \tag{59}$$

Using Taylor expansion to the first order (linear expansion),

$$\chi(\xi) = \frac{\partial}{\partial \xi}\chi|_{\xi=\xi_0}(\xi - \xi_0) + \chi_0 = \chi_0[\frac{(\xi - \xi_0)}{\Lambda_0} + 1]$$

where

$$\frac{1}{\Lambda_0} = \frac{1}{\chi_0}(\frac{d\chi}{d\xi})_{\xi=\xi_0} = \frac{1}{n_c}\frac{\partial}{\partial \xi}n \times \frac{n_c}{n_0} = \frac{1}{n_0}\frac{\partial}{\partial \xi}n.$$

Hence

$$[\chi(\xi) - 1](n_z^2 - 1) = \frac{\chi_0}{\Lambda_0}(\xi - \xi_0 + \Lambda_0 - \frac{\Lambda_0}{\chi_0})(n_z^2 - 1).$$

Let $\beta_0 = \xi_0 - \Lambda_0(1 - 1/\chi_0) = \xi_0 - \Lambda_0(1 - n_c/n_0)$, then

$$[\chi(\xi) - 1](n_z^2 - 1) = \frac{\chi_0}{\Lambda_0}(n_z^2 - 1)(\xi - \beta_0).$$

Applying a change of variable

$$\eta = [-\frac{\chi_0}{\Lambda_0}(n_z^2 - 1)]^{1/3}(\xi - \beta_0),$$

$$d\xi/d\eta = (\xi - \beta_0)/\eta,$$

thus

$$\frac{\partial}{\partial \eta} E_z = (\frac{\xi - \beta_0}{\eta}) \frac{\partial}{\partial \xi} E_z,$$

Therefore Eq. 59 gives

$$\frac{\partial^2}{\partial \eta^2} E_z = [\frac{\partial}{\partial \eta} (\frac{\xi - \beta_0}{\eta})] \frac{\partial}{\partial \xi} E_z + (\frac{\xi - \beta_0}{\eta})(\frac{\partial}{\partial \eta}) \frac{\partial}{\partial \xi} E_z$$

$$= [\frac{1}{\eta} \frac{\partial \xi}{\partial \eta} + (\xi - \beta_0) \frac{\partial}{\partial \eta} \frac{1}{\eta}] \frac{\partial}{\partial \xi} E_z + (\frac{\xi - \beta_0}{\eta})^2 \frac{\partial^2}{\partial \xi^2} E_z$$

$$= [\frac{\xi - \beta_0}{\eta^2} - (\xi - \beta_0) \frac{1}{\eta^2}] \frac{\partial}{\partial \xi} E_z (\frac{\xi - \beta_0}{\eta})^2 \frac{\partial^2}{\partial \xi^2} E_z$$

$$= (\frac{\xi - \beta_0}{\eta})^2 \frac{\partial^2}{\partial \xi^2} E_z \tag{60}$$

Therefore Eq. 59 becomes

$$\frac{\partial^2}{\partial \eta^2} E_z = \eta E_z,$$

known as Airy differential equation that has Airy functions $A_i(\eta)$ and $B_i(\eta)$ as solutions.[13]

Now, since η and ξ may not have same sign depending on the value of n_z, the solution shall be derived in both regions: $|n_z| < 1$, and $|n_z| > 1$. For $|n_z| < 1$, the wave is evanescent. Also note that as $\xi \to \infty$, $\eta \to \infty$ so $A_i(\eta)$ is chosen as a solution, that is Eq. 58 becomes

$$Y_s = \frac{i}{(1 - n_z^2)^{2/3}} (\frac{A_i'(\eta_0)}{A_i(\eta_0)}) [\frac{\chi_0}{\Lambda_0}]^{1/3},$$

where

$$\eta_0 = [-\frac{\chi_0}{\Lambda_0} (n_z^2 - 1)]^{1/3} (\xi - \beta_0)|_{\xi = \xi_0} = (\frac{(1 - n_z^2)n_0}{n_c})^{1/3} \Lambda_0^{2/3} (1 - \frac{n_c}{n_0}).$$

---

[13]When $\eta > 0$, $A_i(\eta) > 0$ and forms a convex curve that decreases exponentially to zero, while $B_i(\eta) > 0$ and forms a convex curve that increases exponentially.

When $\eta < 0$, both oscillate around zero with increasing frequency and decreasing amplitude.

The fact that for $|n_z| < 1$, Y_s is purely imaginary, means that no power is transmitted to the plasma since the wave does not propagate.

However, for $|n_z| > 1$, there are propagating and evanescent waves hence E_z should be complex. Since for $\xi \to \infty$ ($\eta \to -\infty$) the solution satisfies the condition of having the phase velocity in the positive x direction knowing that radial group velocity $v_{gx} > 0$, we deduce that $E_z \propto A_i(\eta) - iB_i(\eta)$.

$$Y_s = \frac{i}{(n_z^2 - 1)^{2/3}} \left(\frac{A_i'(\eta_0) - iB_i'(\eta_0)}{A_i(\eta_0) - iB_i(\eta_0)}\right) \left[\frac{\chi_0}{\Lambda_0}\right]^{1/3} \tag{61}$$

where

$$\eta_0 = -\left(\frac{(n_z^2 - 1)n_0}{n_c}\right)^{1/3} \Lambda_0^{2/3} \left(1 - \frac{n_c}{n_0}\right).$$

The elementary components for the calculation of the power spectrum in front the antenna are the electric field launched by the waveguides which is a combination of propagating and evanescent modes and the antenna-plasma surface admittance $Y_s(n_z)$. Now, the Multipole theory of the Grill shall be developed. It constructs the scattering matrix that relates the incident and reflected modes taking into account the structure of the Grill. Subsequently, the power spectrum dP/dn_z is calculated more rigorously.

F. Multipole Theory of The Grill

The Grill being the plane formed by the antenna front, constitutes along with the plasma facing it a high frequency (HF) multipole. This multipole is made of N divisions corresponding to the N waveguides that form the antenna (considered active for now). Recall that the antenna waveguides are taken infinite in the y direction. Since only slow waves are considered, existing modes would be the dominant TEM mode and the family of evanescent TM modes as explained in Appendix B. The scattering matrix describes the coupling between the different modes in different waveguides at $x = 0$, and constitutes a key factor in studying the coupling efficiency of the Grill [51, 58].

1. Scattering Matrix

We denote the incident and reflected voltages by V' and V'' respectively. The voltage is a quantity that can be measured thus it is considered. The scattering matrix $\mathscr{L}$

relating the incident and reflected waves voltage is given by $V'' = \mathscr{L}V'$, with

$$V' = \begin{bmatrix} V^{0'} \\ \tilde{V}' \end{bmatrix},$$

where $V^{0'}$ is the voltage corresponding to the fundamental mode, and $\tilde{V}'$ is that corresponding to the first n TM modes and given by

$$\tilde{V}' = \begin{bmatrix} V^{1'} \\ V^{2'} \\ \vdots \\ V^{n'} \end{bmatrix}.$$

Similarly,

$$V'' = \begin{bmatrix} V^{0''} \\ \tilde{V}'' \end{bmatrix},$$

where $V^{0''}$ is the TEM mode reflected voltage and

$$\tilde{V}'' = \begin{bmatrix} V^{1''} \\ V^{2''} \\ \vdots \\ V^{n''} \end{bmatrix}$$

corresponding to the first n reflected TM modes (The total number of modes is $n + 1$).

Note that $V^{0'}$, $V^{n'}$, $V^{0''}$ and $V^{n''}$ are vectors of dimension N corresponding to the N output ports of the Grill. In brief, each mode is considered for the incident wave at the N ports and also in the reflected wave at the N ports.

For the simple case for which the fundamental TEM mode is the only incident wave considered at the N ports,

$$\begin{bmatrix} V^{0''} \\ \tilde{V}'' \end{bmatrix} = \begin{bmatrix} S^{00} \\ \tilde{R}^{n0} \end{bmatrix} . V^{0'}, \tag{62}$$

with S^{00} is the transfer matrix such that S^{00}_{pq} represents the reflected TEM mode electric potential at port p induced by the incident TEM mode electric potential of unit amplitude

at port q, and

$$\tilde{R}^{n0} = \begin{bmatrix} R^{10} \\ R^{20} \\ \vdots \\ R^{n0} \end{bmatrix},$$

where R^{m0} ($1 \leq m \leq n$), are $N \times N$ square matrices such that the entity R^{m0}_{pq} represents the reflected m mode electric potential at port p, induced by the incident electric potential of unit amplitude at port q.

The fundamental TEM mode incident and reflected electric fields at a port p are given in terms of the incident and reflected potential differences across the plates of the first waveguide by the relation

$$V(x) = \int_0^b E_z(x,z).dz$$

where b is the z dimension of a waveguide and the remaining electric field components E_x and E_y are related to the electric potential since they are related to E_z as shown in Appendix B.. Therefore for the TEM mode, $E_x = E_y = 0$, $E_z = \Phi_0 V_0(x)$ with

$$V_0(x) = V^{0'} e^{-ik_0 x} + V^{0''} e^{ik_0 x}$$

where $V^{0'} e^{-ik_0 x}$ represents the incident wave propagating along the $(+)$ $0x$ axis from the antenna towards the plasma and $V^{0''} e^{ik_0 x}$ represents the reflected wave propagating along the $(-)$ $0x$ axis from the plasma towards the antenna. Also, the TEM magnetic field is given by $H_y = -\Phi_0 I_0(x)$ with

$$I_0(x) = Y_0(V^{0'} e^{-ik_0 x} - V^{0''} e^{ik_0 x})$$

where $\Phi_0 = \sqrt{1/b}$ and I_0 is the current created by V_0.

Similarly, the TM_n electric field generated at the waveguide mouth is given by

$$E_x^n = \frac{in\pi}{Y_0 k_0 b} \Phi_n'(z) I_x^n(x) \tag{63}$$

where $\Phi_n'(z) = -\sqrt{\frac{2}{b}} sin(n\pi z/b)$,

$$E_y^n = 0$$

$$E_z^n(x,z) = \Phi_n(z) V_n(x), \tag{64}$$

where $k_0 = 2\pi/\lambda_0$ is the wave vector in vacuum, and $k_n = \sqrt{k_0^2 - n^2\pi^2/b^2}$ is the propagation constant of the TM_n mode.

$$V_n(x) = Y_n(V^{n'}e^{-ik_nx} + V^{n''}e^{ik_nx})$$

and

$$I_x^n(x) = Y_n(V^{n'}e^{-ik_nx} - V^{n''}e^{ik_nx}).$$

Also,

$$\Phi_n = \sqrt{\frac{2}{b}}cos(\frac{n\pi z}{b}) \ (n = 1, 2, \ldots \infty)$$

are the characteristic functions of field variation in the direction transverse to $0x$. Note the characteristic functions are orthogonal

$$\int_{-\infty}^{+\infty} dy \int_0^b dz \Phi_m \Phi_n = \begin{cases} 1 \ if \ m = n \\ 0 \ if \ m \neq n. \end{cases}$$

Y_n is defined as the admittance of the TM_n mode given by

$$Y_n = \frac{k_0 Y_0}{k_n}.$$

The magnetic fields of the TM_n modes are given by $H_x^n = 0$, $H_z^n = 0$ and $H_y^n = -\Phi_n(z)I^n(x)$.

Actually these formulas satisfy the relations for TM_n modes derived in Appendix B..

The total electric field at port p is the sum of all incident and reflected modes at $x = 0$. So,

$$E_{zp} = \Phi_0(V_p^{0'} + V_p^{0''}) + \sum_{n=1}^{\infty} \Phi_n(\xi)(V_p^{n'} + V_p^{n''}) \tag{65}$$

and

$$H_{yp} = -Y_0\Phi_0(V_p^{0'} - V_p^{0''}) - \sum_{n=1}^{\infty} Y_n\Phi_n(\xi)(V_p^{n'} - V_p^{n''}) \tag{66}$$

where $0 \leq \xi \leq b$.

So, the power flux of an m mode going out of a square with dimension 1 in the y direction[14] and b in the z direction is given by

---

[14]The power flux is calculated for a square of dimension 1 in the y direction since the antenna is infinite in this direction.

$$P_m = V_m(x)I_m^*(x).$$

The general case for Eq. 62 is such that all TM_n modes are considered, so

$$\mathscr{L} = \left[\begin{array}{cc} S^{00} & R^{\tilde{0}n} \\ R^{\tilde{n}0} & R^{\tilde{m}n} \end{array} \right], \tag{67}$$

where $S^{00}, R^{\tilde{0}n}, R^{\tilde{n}0}, R^{\tilde{m}n}$ are defined as follows:

1. The scattering matrix among waveguides' ports corresponding to the fundamental mode.

$$\underset{(N \times N)}{S^{00}} = \left[\begin{array}{cccc} S_{11}^{00} & S_{12}^{00} & \cdots & S_{1N}^{00} \\ S_{21}^{00} & S_{22}^{00} & \cdots & S_{2N}^{00} \\ \vdots & & & \\ S_{N1}^{00} & S_{N2}^{00} & \cdots & S_{NN}^{00} \end{array} \right] \tag{68}$$

It is symmetric since S_{pq}^{00} represents the reflected TEM mode electric potential at port p induced by the incident TEM mode electric potential of unit amplitude at port q, and S_{qp}^{00} represents the reflected TEM mode electric potential at port q induced by the incident TEM mode electric potential of unit amplitude at port p.

1. $\underset{(N \times nN)}{R^{\tilde{0}n}} = \left[\begin{array}{cccc} R^{01} & R^{02} & \cdots & R^{0n} \end{array} \right]$ is the scattering (transfer) matrix corresponding to higher modes induced by the fundamental mode excited at the ports, with

$$\underset{(N \times N)}{R^{0m}} = \left[\begin{array}{cccc} R_{11}^{0m} & R_{12}^{0m} & \cdots & R_{1N}^{0m} \\ R_{21}^{0m} & R_{22}^{0m} & & R_{2N}^{0m} \\ \vdots & & & \\ R_{N1}^{0m} & R_{N2}^{0m} & \cdots & R_{NN}^{0m} \end{array} \right]$$

2. $\underset{(nN \times N)}{R^{\tilde{n}0}} = \left[\begin{array}{c} R^{10} \\ R^{20} \\ \vdots \\ R^{n0} \end{array} \right]$ is the scattering (transfer) matrix corresponding to the funda-

mental mode induced by higher modes excited by the ports, with

$$\underset{(N \times N)}{R^{m0}} = \left[\begin{array}{cccc} R_{11}^{m0} & R_{12}^{m0} & \cdots & R_{1N}^{m0} \\ R_{21}^{m0} & R_{22}^{m0} & & R_{2N}^{m0} \\ \vdots & & & \\ R_{N1}^{m0} & R_{N2}^{m0} & \cdots & R_{NN}^{m0} \end{array} \right]$$

3. $\underset{(nN \times nN)}{\tilde{\tilde{R}}} = \begin{bmatrix} R^{11} & R^{12} & \cdots & R^{1n} \\ R^{21} & R^{22} & \cdots & R^{2n} \\ \vdots & & & \\ R^{n1} & R^{n2} & \cdots & R^{nn} \end{bmatrix}$ is the scattering matrix among waveguides' ports

corresponding to the TM_n modes with

$$\underset{(N \times N)}{R^{ms}} = \begin{bmatrix} R^{ms}_{11} & R^{ms}_{12} & \cdots & R^{ms}_{1N} \\ R^{ms}_{21} & R^{ms}_{22} & & R^{ms}_{2N} \\ \vdots & & & \\ R^{ms}_{N1} & R^{ms}_{N2} & \cdots & R^{ms}_{NN} \end{bmatrix}$$

where the entity R^{mn}_{pq} represents the ratio of the induced m mode electric potential at port p, by the incident n mode electric potential of unit amplitude at port q.

So, for N ports, and n modes other than the fundamental mode, the electromagnetic fields could be written in vector form,

$$E_z = \begin{pmatrix} E_{z_1} \\ E_{z_2} \\ \vdots \\ E_{z_p} \\ \vdots \\ E_{z_N} \end{pmatrix}, \text{ which gives using Eq. 65}$$

$$\tilde{E}_z(\xi) = \begin{bmatrix} \Phi_0 I \\ \tilde{\Phi}(\xi) I \end{bmatrix}^T \cdot \begin{bmatrix} V^{0'} + V^{0''} \\ \tilde{V}' + \tilde{V}'' \end{bmatrix} \tag{69}$$

where

$$\tilde{\Phi}(\xi) = \begin{bmatrix} \Phi_1(\xi) I \\ \Phi_2(\xi) I \\ \vdots \\ \Phi_p(\xi) I \\ \vdots \\ \Phi_n(\xi) I \end{bmatrix}$$

and I is the unit square matrix of dimension N. Also

$$H_y = \begin{pmatrix} H_{y_1} \\ H_{y_2} \\ \vdots \\ H_{y_p} \\ \vdots \\ H_{y_N} \end{pmatrix}_{((n+1)N \times 1)},$$

which gives using Eq. 66

$$\tilde{H}_y(\xi) = -Y_0 \begin{bmatrix} \Phi_0 I \\ \tilde{\Phi}(\xi)I \end{bmatrix}^T_{((n+1)N\times 1)} \cdot \begin{bmatrix} I & 0 \\ 0 & \tilde{\tilde{Y}}_b \end{bmatrix} \cdot \begin{bmatrix} V^{0'} - V^{0''} \\ \tilde{V}' - \tilde{V}'' \end{bmatrix}_{((n+1)N\times 1)} \tag{70}$$

where

$$\tilde{\tilde{Y}}_b = \begin{bmatrix} (Y_1/Y_0)I & 0 & 0 & 0 \\ 0 & (Y_2/Y_0)I & 0 & 0 \\ & & \ddots & \\ 0 & 0 & 0 & (Y_n/Y_0)I \end{bmatrix}_{(nN\times nN)}$$

is a diagonal matrix corresponding to the TM_n modes ($n \geq 1$). All terms are pure imaginary when these modes are evanescent, more explicitly when $b > \lambda_0$ all TM_n modes do not propagate.

Recall Lorentz reciprocity theorem explained in [59]

$$\int_S (E_1 \times H_2 - E_2 \times H_1).\hat{\mathbf{n}}dS = 0, \tag{71}$$

where S is in this case an infinite plane along $y0z$, and n is a normal unit vector along x.

So, if E_1 is the incident fundamental mode at port p of unit amplitude ($V_p^{0'} = 1$), E_2 is the incident TM_n mode at port q of unit amplitude ($V_q^{n'} = 1$), H_1 is the reflected TM_n mode at port q induced by the fundamental mode at port p, and H_2 is the reflected fundamental mode at port p induced by TM_n mode at port q, and knowing that

$$R_{pq}^{0n} = \frac{V_p^{0''}(induced\ by\ V_q^{n'})}{V_q^{n'}},$$

and

$$R_{qp}^{n0} = \frac{V_q^{n''}(induced\ by\ V_p^{0'})}{V_p^{0'}},$$

then by Eq. 71

$$R_{pq}^{0n} = R_{qp}^{n0}(\frac{Y_n}{Y_0}).$$

Hence $\tilde{R^{0n}} = \tilde{R^{n0}}^T \tilde{\tilde{Y}}_b$.

Using Eq. 67,

$$V''^0 = S^{00}V'^0 + R^{\tilde{0}n}\tilde{V}',$$

and

$$\tilde{V}'' = R^{\tilde{n}0} + \tilde{\tilde{R}}\tilde{V}''.$$

Thus Eq. 69 becomes

$$\tilde{E}_z(\xi) = \begin{bmatrix} \Phi_0 I \\ \Phi(\xi)I \end{bmatrix}^T \begin{bmatrix} I & Y^{\tilde{0}n} \\ Y^{\tilde{n}0} & \tilde{\tilde{I}} \end{bmatrix} \begin{bmatrix} V^0 \\ \tilde{V} \end{bmatrix}, \tag{72}$$

also Eq. 70 becomes

$$\tilde{H}_y(\xi) = -Y_0 \begin{bmatrix} \Phi_0 I \\ \Phi(\xi)I \end{bmatrix}^T \begin{bmatrix} I & 0 \\ 0 & \tilde{\tilde{Y}} \end{bmatrix} \begin{bmatrix} Y^{00} & -\tilde{Y}^{0n} \\ -\tilde{Y}^{n0} & \tilde{\tilde{Y}} \end{bmatrix} \begin{bmatrix} V^0 \\ \tilde{V} \end{bmatrix}, \tag{73}$$

where the reduced admittance matrices are given by

$$Y^{00} = (I - S^{00})(I + S^{00})^{-1} \qquad \tilde{\tilde{Y}} = (\tilde{\tilde{I}} - \tilde{\tilde{R}})(\tilde{\tilde{I}} + \tilde{\tilde{R}})^{-1} \tag{74}$$

$$Y^{\tilde{n}0} = R^{\tilde{n}0}(I + S^{00})^{-1} \qquad Y^{\tilde{0}n} = R^{\tilde{0}n}(\tilde{\tilde{I}} + \tilde{\tilde{R}})^{-1}. \tag{75}$$

$\tilde{\tilde{I}}$ is $nN \times nN$ unit matrix and V^0 and $\tilde{V}$ are the total electric potentials:

$$V^0 = (I + S^{00})V'^0 \qquad \tilde{V} = (\tilde{\tilde{I}} + \tilde{\tilde{R}})\tilde{V}' \tag{76}$$

2. Radiated Complex Power

The complex power radiated towards the plasma by the Grill per unit length in y direction is calculated

$$\frac{dP}{dy} = Y_0 \int_0^1 dy \int_0^a \tilde{H}_y^{\dagger}(\xi).\tilde{E}_z(\xi)d\xi,$$

Eqs. 72 and 73 are substituted where orthogonality of eigenfunctions Φ_n is used to obtain,

$$P = Y_0 \begin{bmatrix} V^0 \\ \tilde{V} \end{bmatrix}^{\dagger} \begin{bmatrix} Y^{00\dagger} - Y^{\tilde{n}0\dagger}.\tilde{\tilde{Y}}_b^*.Y^{\tilde{n}0} & Y^{00\dagger}.Y^{\tilde{0}n} - Y^{\tilde{n}0\dagger}.\tilde{\tilde{Y}}_b^* \\ -Y^{\tilde{0}n\dagger} + \tilde{\tilde{Y}}^{\dagger}.\tilde{\tilde{Y}}_b^* Y^{\tilde{n}0} & -Y^{\tilde{0}n\dagger}.Y^{\tilde{0}n} + \tilde{\tilde{Y}}^{\dagger}.\tilde{\tilde{Y}}_b^* \end{bmatrix} \begin{bmatrix} V^0 \\ \tilde{V} \end{bmatrix}.$$

3. Electromagnetic Fields Radiated into The Plasma

Beyond the ports of the antenna ($x = 0^+$), the electromagnetic fields are considered as a superposition of infinite continuum of plane waves of indices of propagation n_x in the $0x$ direction and n_z in the z directions. So, the electromagnetic fields could be written as function of n_x by integrating over n_z as follows, $E_y = H_x = H_z = 0$,

$$E_x = -\frac{1}{\lambda_0} \int_{-\infty}^{+\infty} e^{-in_z k_0 z} \frac{V(n_z)}{n_x} [e^{-in_x k_0 x} - \rho_s(n_z) e^{in_x k_0 x}] dn_z,$$

$$E_z = \frac{1}{\lambda_0} \int_{-\infty}^{+\infty} e^{-in_z k_0 z} V(n_z) [e^{-in_x k_0 x} + \rho_s(n_z) e^{in_x k_0 x}] dn_z,$$

and

$$H_y = -\frac{Y_0}{\lambda_0} \int_{-\infty}^{+\infty} e^{-in_z k_0 z} \frac{V(n_z)}{n_x} [e^{-in_x k_0 x} + \rho_s(n_z) e^{in_x k_0 x}] dn_z,$$

where

$$\rho_s(n_z) = \frac{1 - n_x Y_s(n_z)}{1 + n_x Y_s(n_z)},$$

where $Y_s(n_z)$ is defined by Eq. 57.

Using Parseval's theorem, radiated power at $x = 0^+$ is given by

$$P = \frac{Y_0}{\lambda_0} \int_{-\infty}^{+\infty} \bar{E}_z(0, n_z) . \bar{E}^*_z(0, n_z) Y_s^*(n_z) dn_z, \tag{77}$$

knowing that $\bar{E}_z(0, n_z)$ is the Fourier transform of the tangential electric field at at $x = 0$,

$$\bar{E}_z(0, n_z) = V(n_z)[1 + \rho_s(n_z)] = \int_{-\infty}^{+\infty} E_z(0, z) e^{in_z k_0 z} dz \tag{78}$$

4. Continuity of The Electric Field

The fact that the tangential electric is continuous at the interface between the output ports and the plasma, shall be employed to deduce the elements of Grill transfer matrix. First, the E_z Fourier transform in z is used, such that $E_z(0, z)$ integrated between z and z_p in Eq. 78 is written as E_{zp}, i.e E_{zp} is the tangential electric field at port p.

$$\bar{E}_z(0, n_z) = \sum_{p=1}^{N} e^{in_z k_0 z_p} \int_{z_p}^{z_p+b} E_{zp}(z - z_p) e^{in_z k_0 (z - z_p)} dz$$

Apply change of variable $z - z_p = \xi$ with $0 \le \xi \le b$, and rewrite Eq. 72,

$$\bar{E}_z(0, n_z) = (e^{in_z k_0 z_p})^T \begin{bmatrix} \int_0^b \Phi_0 e^{in_z k_0 \xi} d\xi \\ \int_0^b \tilde{\Phi}(\xi) e^{in_z k_0 \xi} d\xi \end{bmatrix}^T \begin{bmatrix} I & Y^{\tilde{0}n} \\ Y^{\tilde{n}0} & \tilde{I} \end{bmatrix} \begin{bmatrix} V^0 \\ \tilde{V} \end{bmatrix},$$

where $e^{in_z k_0 z_p} = \begin{bmatrix} e^{in_z k_0 z_1} \\ e^{in_z k_0 z_2} \\ \vdots \\ e^{in_z k_0 z_N} \end{bmatrix}$ $z_1, z_2, \cdots, z_N$ are the abscissa of the output ports. Let

$$G_0(n_z) = \Phi_0 \int_0^b e^{in_z k_0 \xi} d\xi = \sqrt{\frac{1}{k_0^2 b}} \frac{e^{in_z k_0 b} - 1}{in_z}.$$

Designate $\mathscr{G}_0(n_z) = G_0(n_z) \times I_{(N \times N)}$. Also, let

$$\tilde{G}(n_z)_{(nN \times N)} = \int_0^b \Phi(\tilde{\xi}) e^{in_z k_0 \xi} d\xi = \begin{bmatrix} G_1(n_z).I \\ \vdots \\ G_m(n_z).I \\ \vdots \\ G_n(n_z).I \end{bmatrix},$$

where

$$G_m(n_z) = \sqrt{\frac{2}{k_0^2 b}} \frac{n_z[(-1)^m e^{in_z k_0 b} - 1]}{i(n_z^2 - \frac{m^2 \pi^2}{k_0^2 b^2})}.$$

Therefore,

$$\bar{E}_z(0, n_z) = (e^{in_z k_0 z_p})^T \begin{bmatrix} \mathscr{G}_0(n_z) \\ \tilde{G}(n_z) \end{bmatrix}^T \begin{bmatrix} I & Y^{\tilde{0}n} \\ Y^{\tilde{n}0} & \tilde{I} \end{bmatrix} \begin{bmatrix} V^0 \\ \tilde{V} \end{bmatrix}. \tag{79}$$

5. Complex Power Radiated By Plane Waves

Replacing $\bar{E}_z(0, n_z)$ given by Eq. 79 in the power formula in Eq. 77 yields,

$$P = Y_0 \begin{bmatrix} V^0 \\ \tilde{V} \end{bmatrix}^\dagger \begin{bmatrix} I & Y^{\tilde{n}0\dagger} \\ Y^{\tilde{0}n\dagger} & \tilde{I} \end{bmatrix}$$

$$\begin{bmatrix} \lambda_0^{-1} \int_{-\infty}^{+\infty} Y_s^*(n_z) |\mathscr{G}_0(n_z)|^2 e(n_z) dn_z & \lambda_0^{-1} \int_{-\infty}^{+\infty} Y_s^*(n_z) \mathscr{G}_0^\dagger(n_z) e(n_z) \tilde{G}(n_z)^T dn_z \\ \lambda_0^{-1} \int_{-\infty}^{+\infty} Y_s^*(n_z) \tilde{G}^*(n_z) e(n_z) \mathscr{G}_0(n_z) dn_z & \lambda_0^{-1} \int_{-\infty}^{+\infty} Y_s^*(n_z) \tilde{G}^*(n_z) e(n_z) \tilde{G}(n_z)^T dn_z \end{bmatrix}$$

$$\begin{bmatrix} I & Y^{\tilde{0}n} \\ Y^{\tilde{n}0} & \tilde{\tilde{I}} \end{bmatrix} \begin{bmatrix} V^0 \\ \tilde{V} \end{bmatrix} . \tag{80}$$

where $e(n_z)$ is an Nth order hermitian square matrix with

$$e_{pq}(n_z) = e^{-in_z k_0 (z_p - z_q)},$$

and z_p and z_q are the respective abscissas of the pth and q^{th} waveguides. Now a reduced form of the admittance matrices could be defined.

a. <u>Application of Transfer Matrix Notion</u>

The multipole theory of the Grill simplifies deducing the reflection coefficients as seen by the wave guides for arbitrary amplitude and phase of incident waves. Practically, the generators are connected at a distance from the Grill-plasma interface through long wave guides to assure almost total attenuation of evanescent higher modes. Moreover, the reflection coefficients at the Grill output ports would be seen by the generators as uniquely dependent on S^{00}, the fundamental element of the transfer matrix.

As reported in [51, 52], experiments show that for large number of wave guides ($N \geq 10$), all except the two guides at the extremities have the same intrinsic reflection coefficient ρ_0 (the diagonal elements of S^{00}). However, the internal coupling coefficient t_n ($n = 1, 2, \cdots, N/2$)[15] between any two central guides does not depend on the distance separating them, nevertheless it decays rapidly such that $|t_n| \ll \rho_0$ for $n \geq 4$. For almost all experiments, the guides are fed by equal amplitude, voltages whose phases with arithmetic phase difference ($\Phi_p - \Phi_q = (p-q)\Phi_0$).

In conclusion, all the central guides have the same reflection coefficient ρ,

$$\rho \cong \rho_0 + 2 \sum_{n=1}^{4} t_n cos(n\Phi_0)$$

---

[15]For two ports separated by $n-1$ waveguides, t_n determines the reflection coefficient induced by one port on the other.
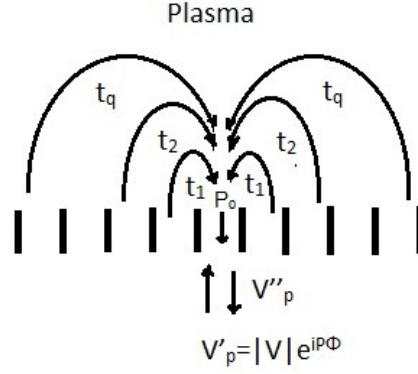
Figure 21: Grill-Plasma reflection coefficients mainly determined experimentally

Φ_0	$\rho \simeq$
$\frac{\pi}{3}$	$\rho_0 + t_1 - t_2 - 2t_3 - t_4$
$\frac{\pi}{2}$	$\rho_0 - 2t_2 + 2t_4$
$\frac{2\pi}{3}$	$\rho_0 - t_1 - t_2 + 2t_3 - t_4$
π	$\rho_0 - 2t_1 + 2t_2 - 2t_3 + 2t$
0	$\rho_0 + 2t_1 + 2t_2 + 2t_3 + 2t_4 \cong -1$

Table 1: Common Reflection Coefficients in The Central Guides for a Network of Large Number of Wave Guides (N>10)

as shown in [51].

For $\Phi_0 = \pi$, the power spectrum would be symmetric in n_z, and results in ions and electrons heating; on the other hand, for smaller values of Φ_0, it is non-symmetric and thus generates current drive. Also, note that for $\Phi_0 = 0$, the plasma acts like a metallic barrier that causes total reflection.

6. Power Spectrum in n_z

The power spectrum of plane waves with n_z index of propagation in the direction of toroidal magnetic field $\vec{B_0}$ (known as the spectrum in n_z) and the LH frequency are the most important parameters in heating and current drive experiments.

On one part, this spectrum should be mostly situated for n_z beyond n_a which is the accessibility value below which slow-fast wave mode conversion may take place. Mode conversion happens indefinitely at between slow and fast wave at a specific density which does not allow the wave to penetrate into the plasma. This certainly plays a major role in minimizing power reflection. The choice of the usable range of n_z is however dependent on wether it is to heat the plasma or to drive current.

Knowing that for $|n_z^2| \leq 1$, the plasma surface admittance $y_s(n_z)$ is imaginary, that is no real power is radiated towards the plasma in this range, and that the width of the wave guides is small enough to ensure the evanescence of TM_n modes ($\tilde{V} = 0$), Eq. 80 gives

$$\triangle P(n_z) = \frac{Y_0}{\lambda_0} \Re[y_s(n_z)] V^{0\dagger}$$

$$\left[|\mathcal{G}_0|^2 e + G_0^* . e . \tilde{G}^T . Y^{\tilde{n}0} + Y^{\tilde{n}0\dagger} . \tilde{G}^* . e . \mathcal{G}_0 + Y^{\tilde{n}0\dagger} . \tilde{G}^* . e . \tilde{G}^T . Y^{\tilde{n}0} \right] V^0 \triangle n_z. \qquad (81)$$

Where $\triangle P(n_z)$ is the real power radiated into the plasma within the interval $(n_z, n_z + \triangle n_z)$.

The multipole theory allows us to separate the input voltages from the Grill part where the incident voltage values are easily measured by non directive probes put inside the wave guides at a distance of $\lambda g/2$ from the Grill-plasma interface. Actually the formula in Eq. 81 serves as a picture of experimental work.

The large factor in Eq. 81 consists of four terms, of which the first term is the main term corresponding to radiation by the fundamental mode, and describes completely the principle lobe of the power spectrum. The remaining three terms represent the contribution of higher modes which take place in the plane of discontinuity between the Guides and the plasma. These terms yield the secondary lobes at higher values of n_z.

Fortunately a small part of these waves (10% of power) are reflected at the plasma edge. The fast ions accelerated by these waves near the plasma edge are not sufficiently confined and thus their energy does not contribute to the core plasma. They hit the limiter or the wall and hence increase the level of impurities.

The n_z spectrum principal lobe is chosen to serve certain targets (ions and electrons heating, CD). Hence the need to determine the characteristics of the antenna including the dimensions of waveguides, N the number of waveguides, and the amplitude and phase of incident electric field.

For simplifying the calculation in Eq. 81, we may neglect the last three terms in the main factor in Eq. 81 to come up with a simple relation,

$$\Delta P(n_z) = Y_0 \frac{b}{\lambda_0} \Re[y_s(n_z)] \left(\frac{sin(\pi n_z b/\lambda_0)}{\pi n_z b/\lambda_0} \right)^2 \Delta n_z$$

$$\left\{ \sum_{p=1}^{N} |v_p|^2 + \sum_{p=1}^{N} \sum_{\substack{q=1 \\ p \neq q}}^{N} |v_p||v_q| cos\left[(p-q)2\pi n_z \frac{\Delta}{\lambda_0} + (\psi_p - \psi_q) \right] \right\} \qquad (82)$$

$|v_p|$, $|v_q|$, ψ_p, ψ_q are the amplitudes and phases of the pth and q^{th} guides respectively.

b : width of of the waveguides

Δ : periodicity of the wave guides along z direction. $\Delta = b + d$ where d is the walls thickness.

The minima and maxima as well as the width of the lobes are determined by the main factor in Eq. 82.

The waveguides are fed by equal amplitude voltage but with a phase difference Φ between consecutive guides.

$$|v_p| = |v_q| = \cdots |v_N| = 1 \qquad (\psi_p - \psi_q) = (q - p)\Phi.$$

Let $\theta = 2\pi n_z \Delta / \lambda_0 - \Phi$, then the main factor in Eq. 82 becomes

$$\{\cdots\} = N + 2 \sum_{p=1}^{N-1} (N - p) cos(p\theta)$$

$$= N(1 + \sum_{p=1}^{N-1} cos(p\theta)) - (1 - cos(N\theta)) \sum_{p=1}^{N-1} pcos(p\theta) + sin(N\theta) \sum_{p=1}^{N-1} psin(p\theta) \quad (83)$$

with
$$1 + \sum_{p=1}^{N-1} pcos(p\theta) = \frac{1}{2} \left(\frac{e^{iN\theta} - 1}{e^{i\theta} - 1} + \frac{e^{-iN\theta} - 1}{e^{-i\theta} - 1} \right) \qquad (84)$$

so,
$$|1 + \sum_{p=1}^{N-1} pcos(p\theta)| = |\frac{sin(N\theta/2)}{sin\theta/2}|$$

Eqs.83 and 84 prove that the expression within parentheses in Eq. 82 has maxima of N^2 at
$$\theta = 2m\pi \quad for \quad m = 0, \pm 1, \pm 2 \ etc \cdots$$

which gives the lobes in the power spectrum. However due to the modulation factor in Eq. 82, these lobes decrease in amplitude with increasing m or equivalently increasing n_z. Each maximum has two minima on both sides. Minima of zero are attained when $N\theta = 2\pi(m \pm 1) \quad for \quad m = 0, \pm 1, \pm 2 \, etc \cdots$

The two main lobes are centered at n_z^+ and n_z^- given by

1. $m = 0$,

$$n_z^+ = \frac{\Phi}{2\pi}\frac{\lambda_0}{\Delta} = \frac{\Phi}{k\Delta}.$$

2. $m = -1$,

$$n_z^- = (\frac{\Phi}{2\pi} - 1)\frac{\lambda_0}{\Delta} = \frac{\Phi - 2\pi}{k\Delta}.$$

These lobes show a half power band width of λ_0/L, where L is the Grill total length in the z direction. However these lobes need not be symmetric, and thus to create a CD the value of Φ should be specified. For $\Phi = \pi$, main lobes are symmetric, but for $\Phi < \pi$, a higher lobe at a specific predetermined value of n_z^+ could be obtained and controlling the half power bandwidth owing to the simple formulas is also possible.

a. Power Spectrum accounting for Reflections

Given Eq. 172 and Eq. 65, and neglecting evanescent TM_n modes and scattering from other waveguide ports, 173 gives The Fourier transfrom of E_z at $x = 0$,

$$\overline{E_z}(0, n_z) = be^{in_z k_0 b/2} sinc(n_z k_0 b/2) \sum_{p=1}^{N} (1 + S_{pp}^{00})e^{i\phi} \tag{85}$$

where S_{pp}^{00} is the scattering coefficient corresponding to the TEM mode at the pth waveguide port, given by: $S_{pp}^{00} = V^{0'}/V^{0''}$, as described in Eq. 68.

Suppose that $S_{pp}^{00} = a_p e^{i\alpha_p \Phi}$ where a_p is the reflection coefficient and $\alpha_p \Phi_p$ is the phase, with (a_p, α_p) are random numbers $]0, 1[$ and Φ is the waveguide phasing. Eq. 174 becomes

$$\overline{E_z}(0, n_z) = be^{in_z k_0 b/2} sinc(n_z k_0 b/2)(\sum_{p=1}^{N} e^{i(p-1)\phi} + \sum_{p=1}^{N} S_{pp}^{00} e^{i(p-1)\phi}) \tag{86}$$

where $\phi = n_z k_0 \Delta - \Phi$ and N is the number of waveguides, but

$$\sum_{p=1}^{N} S_{pp}^{00} e^{i(p-1)\phi} = \sum_{p=1}^{N} a_p e^{i\alpha_p \Phi} e^{i(p-1)\phi} = \sum_{p=1}^{N} a_p e^{i(\alpha_p \Phi + (p-1)\phi)}$$

Thus Eq. 86 becomes

$$\overline{E_z}(0, n_z) = b e^{i n_z k_0 b/2} sinc(n_z k_0 b/2) \left(\sum_{p=1}^{N} e^{i(p-1)\phi} + \sum_{p=1}^{N} a_p e^{i(\alpha_p \Phi + (p-1)\phi)} \right)$$

where

$$dp/dn_z = \frac{Y_0}{\lambda_0} |\overline{E_z}(0, n_z)|^2 \tag{87}$$

which gives using Matlab for $N = 14$, (i.e for two modudels) and assuming two random vectors for a_p and α_p assuming a 100% fluctuating in phase and 70% reflection [60], a perturbed power spectrum. This indicates that a reflection coefficient that varies at the Grill can perturb the power spectrum.

Moreover the toridal variation of the reflection coefficient indictaes a toroidal density fluctuation. This calculation supports the idea the parallel density fluctutions can modify the power spectrum.

Moreover, if only the phase is perturbed randomly at the waveguide phasing,

$$\overline{E_z}(0, n_z) = b e^{i n_z k_0 b/2} sinc(n_z k_0 b/2) \sum_{p=1}^{N} e^{i((p-1)\phi + \alpha_p \Phi)},$$

then the power spectrum in Eq. 87, is perturbed significantly as shown in Fig. 22 for different random phasing cases.
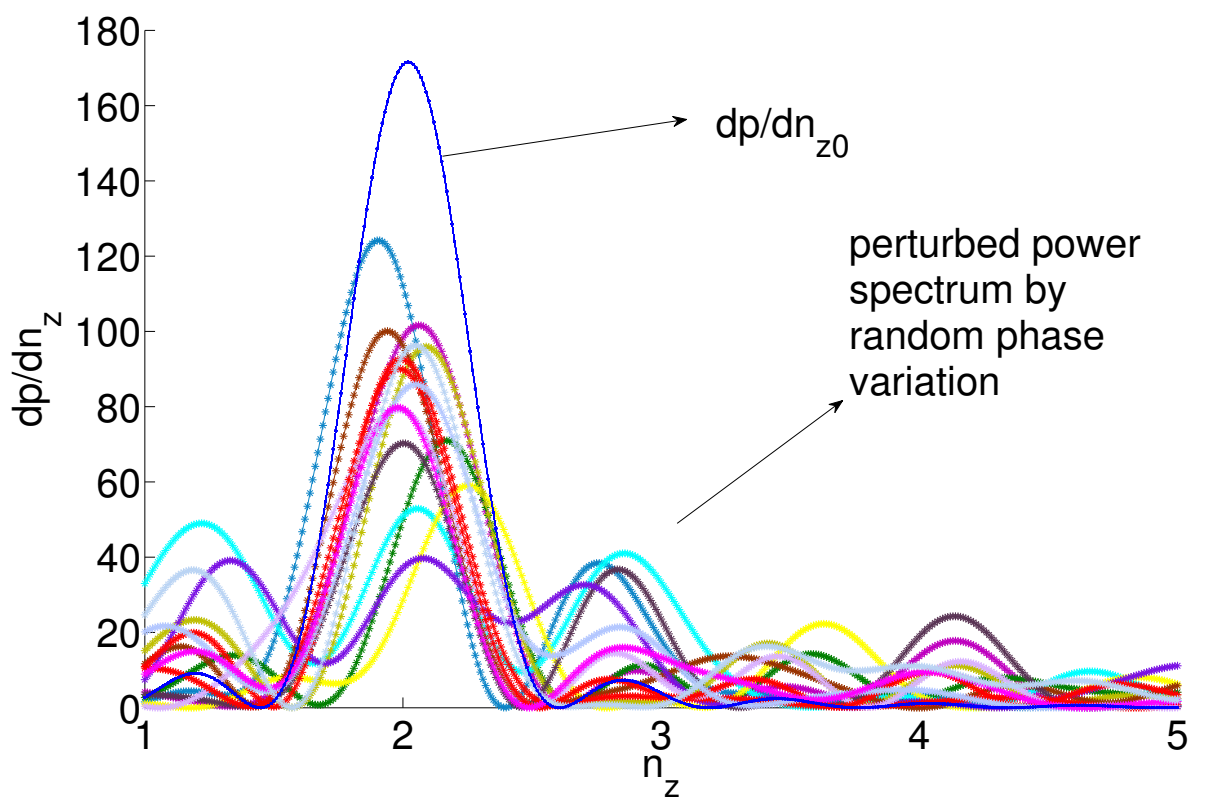
Figure 22: Random phase variation effect on the power spectrum

CHAPTER IV

LOWER HYBRID WAVE SYSTEM

A. Lower hybrid wave antenna

The lower hybrid (LH) wave was initialy assumed convenient for auxiliary heating and current drive of the tokamak plasma by Parker and Hooke in 1971 [61, 62]. The LH antenna based on stacked arrays of phased waveguides (front surface called "Grill") was first proposed in 1974 [63]. The antenna properties were studied by Brambilla [64]. At $n_{\parallel 0} \sim 2$, LH waves were successfully tested on the Japanese tokamak JFT2 [65] and American tokamak PLT [66] and thus drew a lot of attention world wide. Due to its CD efficiency, the LH wave has been efficiently applied in the plasma of the large tokamaks Tore Supra tokamak [67], JET [68] and JT60 [69, 70]. However, scaling to ITER relevant conditions has shown that the LH wave can not sustain a fully non inductive current [71]. It has been recently shown that 20 MW of LH power can provide only 1 MA of the plasma current which is a very small fraction of the needed current in ITER that requires a large percentage of the recycling power [45]. However the LH wave designates a versatile tool for controlling the current density and power deposition profiles in ITER that could play an important role for the achievement of long pulse operation, stabilzing sawteeth, driving significant toroidal plasma rotation, in addition to reducing flux consumption especially during current ramp-up phase[72, 73, 74, 75, 76, 77, 78].

1. LH antenna design

In the last 20 years, two designs of the LH antenna were well developed and tested on different tokamaks such as JET, Tore Supra, JT60, Alcator C-Mod, FTU, HT-7, etc.[1] [72, 74, 78, 39].

In order to launch an asymmetric power spectrum in parallel wave number at $|n_{\parallel}| \approx 2$, the lower hybrid antenna phasing is adjusted either at the level of the transmission

---

[1]Jet (Joint European Torus) is the largest operating tokamak in the world and is built in UK [79]. Tore Supra (torus super conducting tokamak) is one of the largest tokamaks in the world, that operated from 1988 till 2013. It characterized by its super conducting toroidal magnetic coils and actively cooled walls and was built in South of France in Cadarache [80, 81]. TS is being upgraded with a divertor limiter and is named TS WEST in accordance with the EAST (Experimental Advanced Superconducting Tokamak) tokamak situated in eastern China. Both JET and TS have supported the efforts for realizing the ITER project [82, 83], in addition to the other tokamaks around the world such as JT60 (Japan Torus) in Japan, KSTAR (Korea Superconducting Tokamak Advanced Research) in South Korea, Alcator C-Mod (ALto CAmpo TORo, High Field Torus) in U.S., EAST (Experimental Superconducting Tokamak) in China, FTU (Frascati Tokamak Upgrade) in Italy, ASDEX Upgrade (Axially Symmetric Divertor EXperiment) in Germany, COMPASS (COMPact ASSembly) in the Czech Republic, etc.

lines, [84, 85] or at the level of the antenna itself employing multijunction concept system as used in Tore Supra (TS).

Fig. 23 shows FAM (fully active multijunction) and PAM (Passive active multijunction) antennas that constitute the LH system in TS and which are were tested in several discharges including fully non-inductive long discharges [67, 74, 75, 86].

FAM antenna or C3, [87], is an improved design of earlier LH antennas C1 and C2 [88, 89]. Firstly, C3 allows a larger output power of 4 MW instead of 2 MW for C2 due to adding more waveguides with a maximum power density of $25\,MW/m^2$ which is the maximum that allows a steady state operation [37][2]. Secondly, the power in C3 is poloidally divided between three rows of the upper or lower part of the antenna via a TE_{10}-TE_{30} mode converter with 99% conversion efficiency [89, 91]. C2 was operating in TS along side with C3 until 2009 [89], when it was replaced by the passive active multijunction (PAM) antenna. PAM concept was first proposed in 1993 to allow a better cooling of the antenna. Recently it was successfully tested for ITER relevant conditions owing to a water cooling system and a new arrangement of passive and active waveguides which allows it to endure thermal stress and eddy currents for long discharges, in addition to achieving low power reflection coefficients <2% [73, 75, 92]. Fig. 27 shows the reflection coefficient calculated by the LH wave code ALOHA[3], for FAM and PAM antennas, where the density in the SOL is characterized by a decay length $10\,mm$. The FAM and PAM antennas are composed of six rows of waveguide arrays poloidally adjacent while each row is made of eight modules as shown in Fig. 23.

The FAM module along one row is an array of six active waveguides, where passive waveguides (short circuited and have a depth of $\lambda_{LH}/4$) are placed between consecutive modules. However, the PAM module is made of alternating 2 passive and 2 active waveguides as shown in Fig. 24.

The availability of technological advances have allowed to overcome major challenges for building the LH wave system in particular high power generation and efficient transmission [94]. The LH system components include the high power suppliers (multi-MW) provided by 2x8 klystrons (700kW each) for two antennas at TS [41], long transmission lines (6 m), hybrid junctions to divide the power of one klystron between lower and upper parts of the antenna, bi-directional couplers, RF windows, TE_{10}-TE_{30} mode converters that divide the power poloidally between the three rows of a module, and the multijunction antenna made of phase shifters (E-plane bijunction) and of both passive and active waveguides (Fig. 24). Fig. 25 shows the FAM and PAM module description and the various components of the PAM lower hybrid system which weighs 8 tonnes.

---

[2]C3 achieved a 6 min at the 3 MW LHCD power level in Tore Supra [37, 90]

[3]ALOHA stands for 'Advanced Lower Hybrid Antenna coupling code', it is an LH wave coupling code which incorporates the scattering matrix of the LH antenna as specified by another RF software or code such as HFSS and couples it to the SOL plasma via the spectral surface admittance at the plane separating the Grill and the plasma, the output of the code includes the directivity, reflection and the $n_{\parallel}$ power spectrum [93].
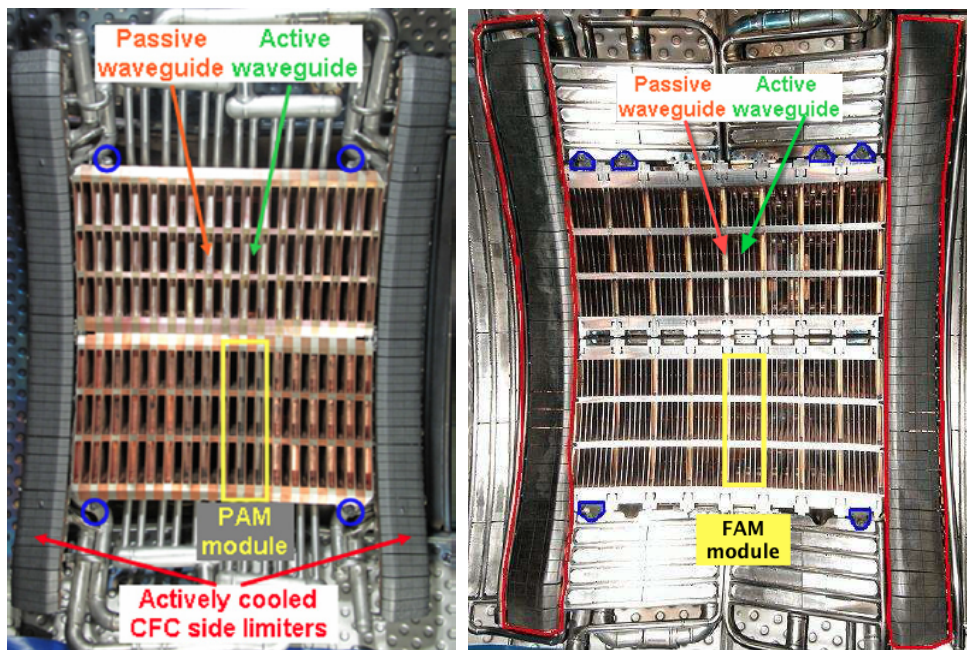
Figure 23: PAM and FAM antennas placed next to each other in Tore Supra, with langmuir probes in blue. One module of the lower part of the antenna, the side limiters and the position of passive and active waveguides are indicated.
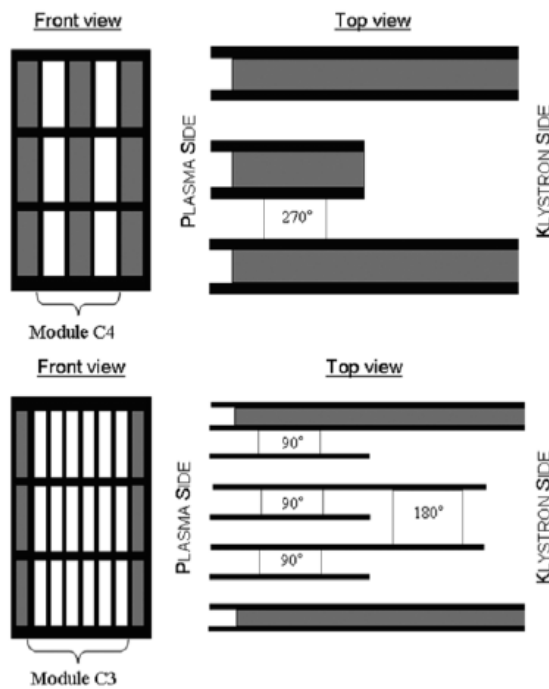
Figure 24: The front face (Grill) structure for one module of FAM (C3) and PAM (C4) (left), and the phase shifters (right)
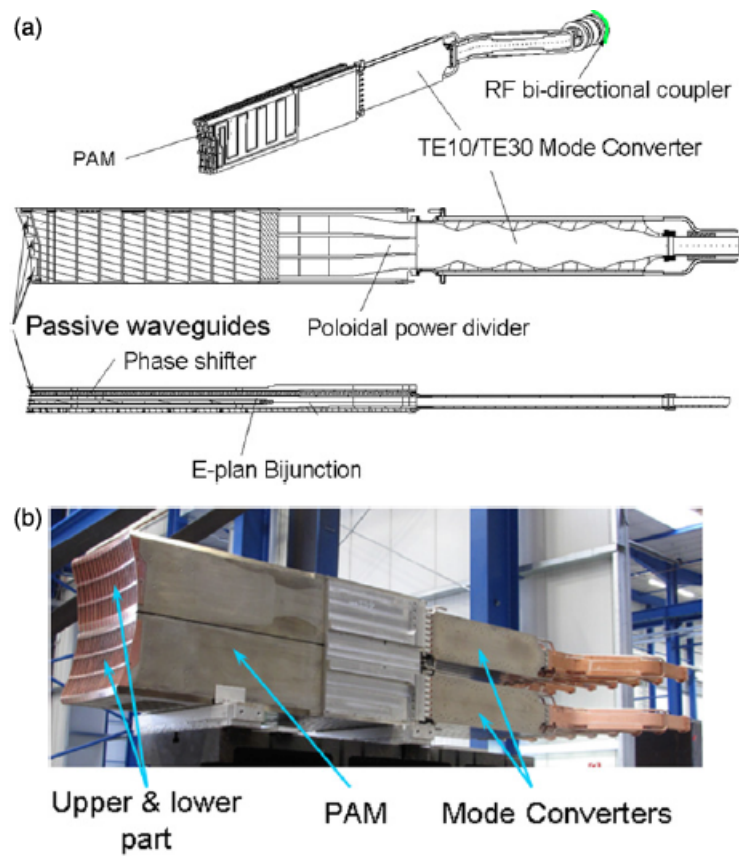
Figure 25: The lower hybrid system components with the PAM antenna structure
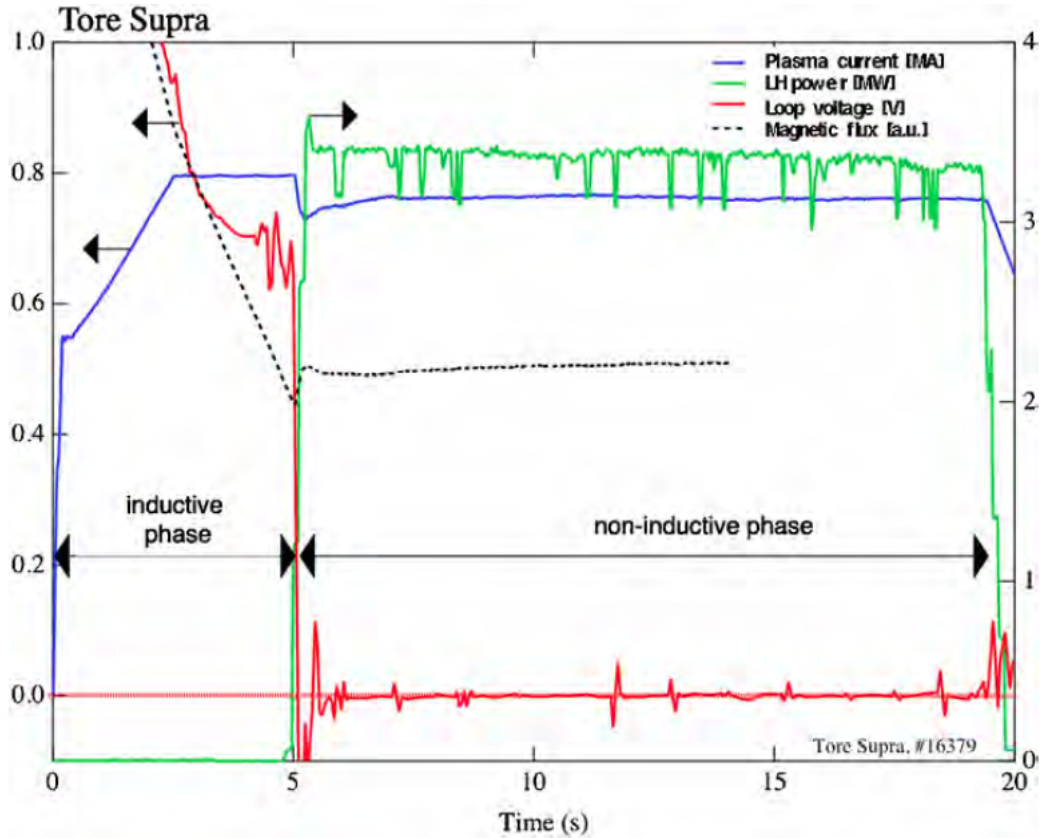
Figure 26: Time evolution of the plasma current with the application of the LH wave at $t = 5s$ for the 6-min TS discharge # 16379 [2]. The decreasing flux sustains the current in the inductive phase. At $t = 5s$ the flux is maintained constant, thus the flux consumption and loop voltage drop to zero, while the current is completely provided non-inductively by an LH power of 3.5 MW.

B. LH wave off-axis current drive efficiency

LHCD efficiency is based on the fact that at high phase velocities energy is deposited on fast electrons which have less Coulomb collision cross section area and thus collide less with other electrons. In particular, at parallel velocities $v_{\|L} \simeq [2.5 - 4]v_{te}$[4] [36], the LH wave transfers momentum to the fast electrons inside the plasma. Consequently, LHCD efficiency given by the ratio $J/P \propto v_{\|}^2$, becomes large due to the high LH parallel phase velocities as argued by Fisch [27, 25].

Tore Supra had been a test bed for long plasma pulses, in which the LH wave has demonstrated successful CD [75, 87, 46]. In particular a 3.5 minutes fully noninductive plasma discharge was recorded on 2002 with 3 MW power equivalent to 600 MJ of thermal energy used to drive current and a longer 6 min discharge was achieved on 1996 [37, 2] with 280 MJ energy exhaust using C2 and C3 antennas. Fig. 26 shows the

---

[4]$v_{\|L}$ is the parallel LH phase velocity at which Landau damping takes place and v_{te} is the thermal phase velocity of the electrons.
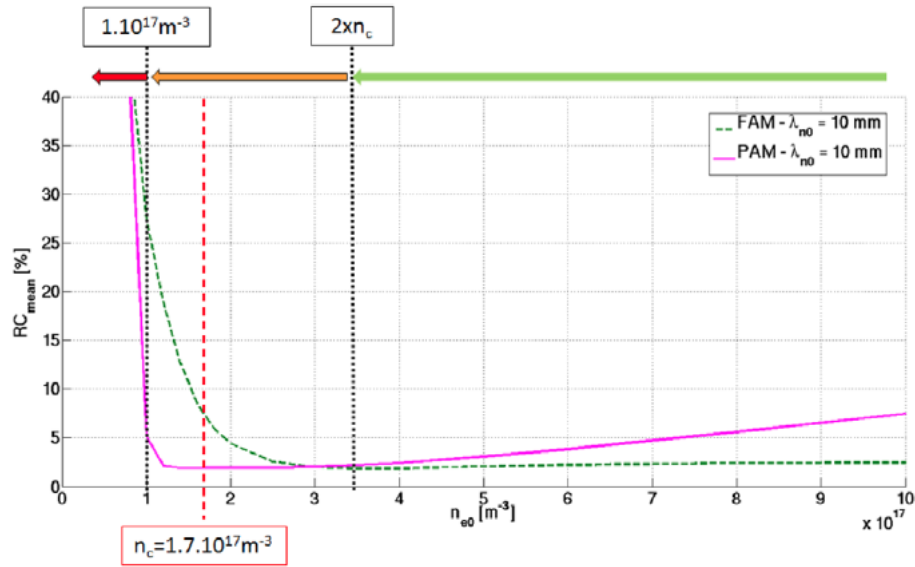
Figure 27: ALOHA coupling code results for the reflection coefficient as a function of the electron density in front the antennas n_{e0} for FAM (green curve) and PAM (magenta curve), where the density profile is increasing with a decay length of 10 *mm*. This figure is extracted from [3].

plasma current time evolution during the inductive phase and upon the application of the LH wave that provides noninductive CD with zero flux consumption. On the other hand, $50\,s$ of fully noninductive discharge was achieved with the PAM antenna alone with the plasma current maintained $I_p = 0.5\,MA$ [75].

For ITER high temperatures, $T_e \geq 10\text{--}12\,keV$, the LH wave deposits energy far from the plasma core at $\rho \sim 0.65 - 0.7$, where ρ is the normalized radius from the plasma center; however its high phase velocity allows electrons to escape trapping which makes it an attractive method for off-axis CD [78]. Consequently, the LH wave is employed in controlling the current density and power deposition profile which is well suited for an accurate control of the safety factor profile which turns out to be critical for improving the performances and stability of the plasma, especially when the pressure gradient becomes high [95, 96, 97]. In fact, tailoring the q profile can change position of the internal transport barrier (ITB) and thus helps to suppress tearing mode instabilities. In addition, the LH wave can help in the first seconds of plasma ignition by saving volts seconds during the current ramp up [75, 76, 72]. Henceforth, the LH wave shall be considered for various plasma scenarios for achieving a steady state in ITER and later in DEMO[5] [72, 40].

---

[5]DEMO is the first plasma reactor to study the possibility of a power plant based on fusion energy, to be implemented after realizing the first fusion reactions in ITER.
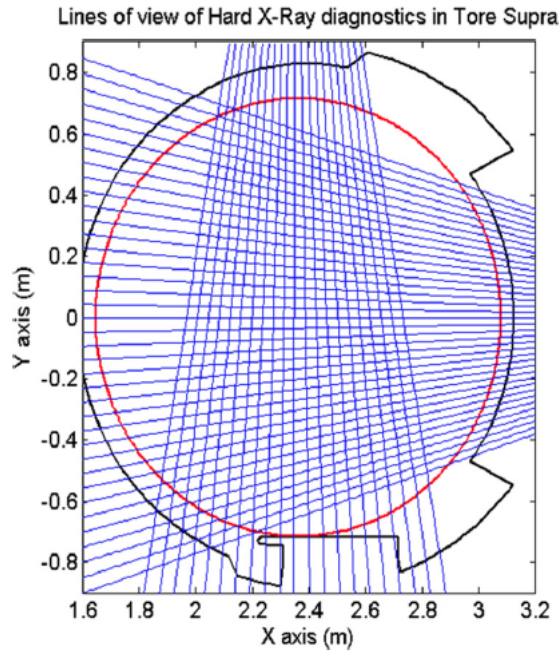
Figure 28: Lines of sight of the HXR system at Tore Supra

C. LH wave modeling and diagnostics

LH modeling has witnessed a breakthrough lately due to the availability of more elaborate technological advances. Firstly, this section gives a brief idea of the diagnostics used in LH wave experiments. These include Langmuir probes, RF probes, Hard X-ray (HXR) cameras, and fast imaging and infrared cameras. The probes are small metallic devices imbedded on the launchers to have measurements at the launchers' mouth. RF probes quantify frequency fluctuation while langmuir probes measure the electron density and temperature and plasma potential (see Fig. 23). Cameras are set on the walls of the tokamak and are of different uses, for example fast imaging cameras used to monitor turbulence and propagating filamentary structures called blobs [98, 99] and infrared camera or visible camera to see striations on the LH antenna that indicate the distribution of the heat flux on the antenna [89, 100]. On the other hand, HXR camera captures bremsstrahlung photon emission energies in the range $[20 - 200]$ keV. Those in the range of $[50 - 110]$ keV result from the collision of the LH accelerated suprathermal electrons via Landau damping with ions or bulk electrons in TS 28, hence HXR spectroscopy determines the spatial, the energy and the temporal characteristics of the LH accelerated electrons[6]with accurate resolution [101, 102]. Only, after Abel inversion of noisy line-integrated HXR signals, power deposition profiles of the accelerated electrons could be spatially determined, a critical issue for reverse shear scenarios [103].

In order to calculate the RF driven current inside plasma, a set of codes has been developed to solve self consistently the equations that describe the wave fields and the

---

[6]Suprathermal tail of electrons generated from the damping of the LH wave has a very low radial diffusivity and thus information on the position of the electron emissivity gives information on the power and consequently the current deposition profiles [101].

plasma. These include a ray tracing code C3PO and the 3D linearized relativistic bounce-averaged electron Fokker-Plank solver LUKE. While the ray tracing method was used to calculate the wave propagation inside plasma [104, 105, 106] such as that of the LH and electron cyclotron waves. C3PO was further improved, [107], so that it can use any coordinate system in particular the magnetic flux coordinates (ψ, θ, ϕ) which in turn have more advantage for an integrated modelling of an axisymmetric plasma equilibrium. On the other hand, LUKE, [108, 18, 109], has been developed for calculating the electron distribution function and thereby deducing the current and power deposition profiles of RF waves , by solving the Fokker-Plank equation given by

$$\frac{df}{dt} = \frac{\partial f}{\partial t} + \dot{x}.\nabla_x f + \dot{p}.\nabla_p f = \mathscr{C}(f) \tag{88}$$

where f is the electron distribution function with variables in space, velocity space and time, x represents a 3D vector in space, p is the momentum and $\mathscr{C}$ is an operator for particle conservation [18]. In order to compare LHCD simulation with HXR signals, fast electron bremsstrahlung (FEB) is reconstructed with LUKE using the numerical code R5-X2 [110] as described in the code suite shown Fig. 30. Note that, the chain of codes used in LHCD calculations have been validated in [111]. As a result, C3PO and LUKE are suitable for integarted tokamak modeling [112, 18]. Fig. 29 shows the LH wave propagation and absorption in plasma beyond LCFS where LCFS stands for the last closed magnetic surface in the plasma which separates the plasma from the scrap-off layer (SOL). Starting with Tore Supra database, METIS (or CRONOS) code uses equilibrium and transport equations to calculate the evolution of the discharge [112], ALOHA code specifies the LH power spectrum at the Grill which is in turn used by C3PO at the LCFL to determine the path of the LH rays in the plasma assuming the power is divided between a finite number of rays; C3PO is coupled to LUKE to resolve the rays absorption inside the plasma and consequently the electron distribution function f is obtained. f is then used to calculate the LH current and power deposition profiles as well as to calculate the line-integrated FEB to be compared with the experimental HXR signals [110].

Note that integrated modeling has achieved a new level via the ITM-TF which the European Integrated Tokamak Modeling Task Force which combines a suite of validated codes and experimental data for a testing the stability of tokamak scenarios. A selection of first physics results applied on ITER and ASDEX Upgrade were presented in [113].
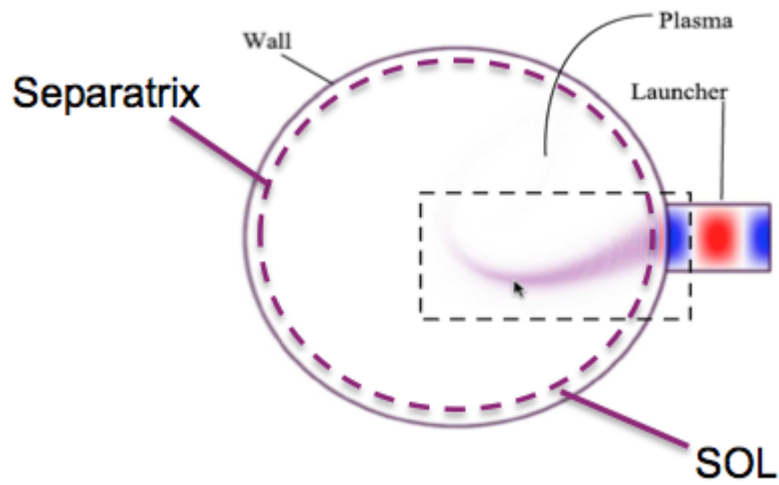
Figure 29: The LH wave propagation path from the antenna through the scrape-off layer (SOL) and across the LCFS (separatrix) into the plasma core where it is absorbed.
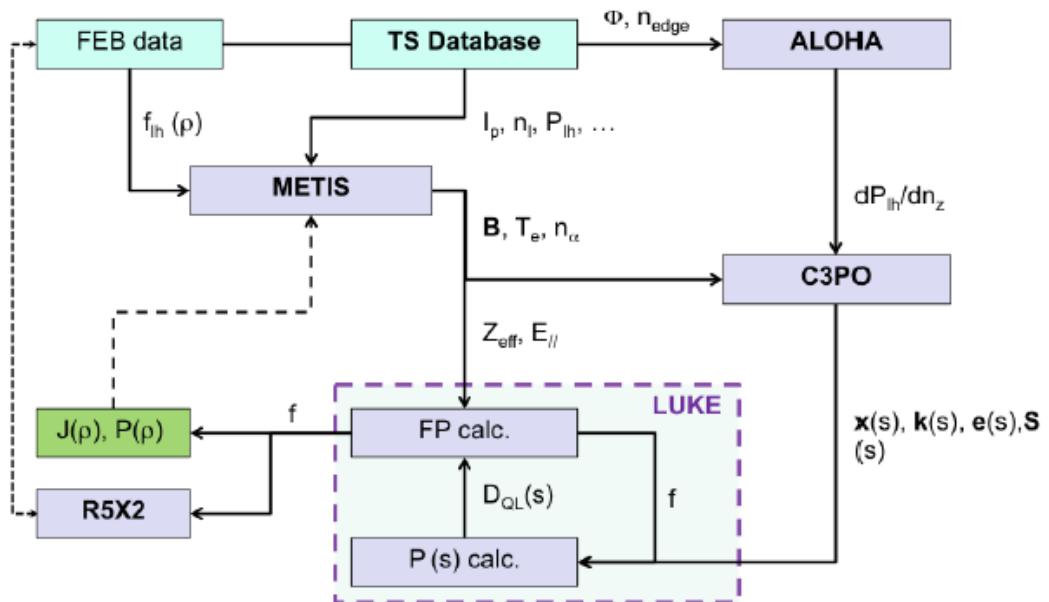
Figure 30: Chain of codes used in LH wave dynamics

CHAPTER V

LH WAVE SPECTRAL GAP PROBLEM

A. Spectral gap problem

The LH wave is absorbed by the usual Landau damping process. The wave is excited at the plasma edge with a frequency ω and a narrow power spectrum which peaks at the parallel refractive index $n_{\|0} = k_{\|0}/\kappa_0$, such that an anisotropic tail of fast resonant electrons can be continuously pulled out from the thermal bulk. Here, $\kappa_0 = \omega/c$, c is the speed of light and $k_{\|0} = \mathbf{k}_0 \cdot \widehat{b}$, where $\mathbf{k}_0$ is the LH wave vector excited by the antenna with $\widehat{b}$ the local magnetic field direction. Since the electron collision frequency scales as v^{-3}, where v is the electron velocity, the smallest possible value of $n_{\|0}$, that fulfills the Stix-Golant accessibility condition, is used, in order to maximize the current drive efficiency [27, 25]. This leads to enlarge the so-called spectral gap, $\delta n_\| \simeq n_{\|L} - n_{\|0}$, where $n_{\|L} \simeq 5.5/\sqrt{T_e\,[keV]}$ is the parallel refractive index at which the linear absorption of the LH wave becomes strong [36]. Consequently, without an efficient physical mechanism that can bridge the spectral gap, the plasma is virtually transparent to the LH wave. The spectral gap problem is illustrated in figure 31 where $n_\| = c/v_\|$; $v_{\|L} \simeq 4v_{the}$ and $n_{\|0}$ is the LH nominal refractive index determined by the antenna.

Since, the LH wave is always fully absorbed experimentally, many mechanisms that could lead to a spectral upshift in the plasma and bridge the spectral gap have been proposed [78]. Among them, the commonly preferred and currently used mechanism in most LH current drive simulations, is the toroidal refraction [114, 115, 116]. Even if it is intrinsic to the tokamak magnetic configuration, its universality is questionable, especially for machines with a high aspect ratio [117]. The spectral upshift, as the LH wave propagates in the plasma, is usually determined by a ray tracing code [1], while the distribution function of the fast electrons that interact resonantly with the wave is calculated by a solver of the Fokker-Planck equation. When the spectral gap is small or moderate[2], $\delta n_\| \leq 2 - 3\Delta n_{\|0}$, where $\Delta n_{\|0}$ is the width of the main lobe in the launched power spectrum, a good quantitative agreement is found between the experimental observations and the numerical predictions [4]. This result represents a remarkable success for the physics of the LH wave and is also an important assessment for the chain of codes that are used for this purpose [111, 18]. Bridging narrow spectral gap via LHCD simulations is shown in figure 33, where the LH waves are fully absorbed in single or few passes around the plasma, the $n_\|$ upshift fills the spectral gap, and the HXR tomography measurements almost coincide with the reconstructed FEB in LUKE simulations. It is noted that CD results are independent of initial conditions such as the positions of the rays and the power spectrum at the separatrix [110]. On the contrary, using same simulation tools and keeping the power spectrum at the separatrix unchanged does not reproduce experi-

---

[1] It has been also calculated by full wave techniques [49, 118, 119]

[2] $\delta n_\| < 0.5$ for $T_e > 5keV$

mental results when the spectral gap is wide as figure 34 shows. Here the $n_\parallel$ upshift due to toroidal refraction is not enough to bridge the spectral gap. The rays undergo multi passes around the plasma such that stochasticity develops well before full absorption of the wave, while the results become unpredictable and sensitive to initial conditions [18], as shown for Tore Supra 6 mins discharge in which both FAM and PAM antennas were operated with a total power of 3 MW [120, 4, 121]. The HXR results for a density scan in figure 34 show smooth evolution for experimental measurements compared to chaotic behavior of the reconstructed FEB. It is concluded that unlike the case of strong damping regime, the codes are rather erratic in the weak damping regime where there spectral gap is large.

Notably, the LH wave efficiently drives current even in presence of a large spectral gap and negligible toroidal upshift as in LH fully driven discharges at TRAIM-1M which is a large aspect ratio tokamak [117]. In particular, a full wave study has suggested that the power spectrum should be already bridged at the separatrix to be able to explain the LH wave dynamics [49]. Same results have been obtained with C3PO and LUKE simulations applied to weak damping regimes at TS which show similarity in LH wave dynamics with TRIAM-1M [4].

Recently, the good agreement between simulations and experiment has been extended to high density and cold plasmas, for which the spectral gap is known to be very large, i.e. $\Delta n_{\parallel 0} \ll \delta n_\parallel$ [7]. In this case, the smooth and progressive parametric dependencies with the plasma parameters or the phasing between antenna waveguides can be reproduced quantitatively, as well as the fast electron bremsstrahlung profile at all photon energies [7]. For such an agreement to be found, the spectral gap must be already bridged as the LH wave passes through the separatrix and penetrates the central region of the plasma. The fraction of the power that is transferred from $n_{\parallel 0}$ to lobes at higher $n_\parallel$ values, thus forming a tail in the interval $n_{\parallel 0} < n_\parallel < n_{\parallel L}$, must exceed 50%, which represents a considerable modification of the narrow power spectrum excited by the LH antenna. From this finding, a statistical picture of the broad power spectrum used for ray tracing calculations has emerged (figure 32), which may be interpreted as the probability distribution function of a

fluctuating narrow spectrum, provided the fluctuation time is much shorter than the collision time of fast electrons [7]. Figure 35 shows how experimental results agree well with the Fokker-Plank and ray tracing simulations that incorporate the tail-model spectrum [7], unlike the results obtained using the initial spectrum as illustrated in figure 34. Since this regime is usually characterized by large amplitude electron density fluctuations in the scrape-off layer (SOL) in front the LH antennas [122, 123], the interaction between the LH wave and the electron density fluctuations is a natural candidate to explain the spectral broadening that must be introduced at the plasma edge to reproduce the observed parametric dependencies and the measured non-thermal bremsstrahlung. An original approach of this problem is presented in this study, the standard model used to describe the scattering of the LH wave by electron density fluctuations being unable to predict a strong modification the power spectrum as it propagates in the scrape-off layer [124, 125, 121]. The numerical model is based on the diffraction of the LH wave by a
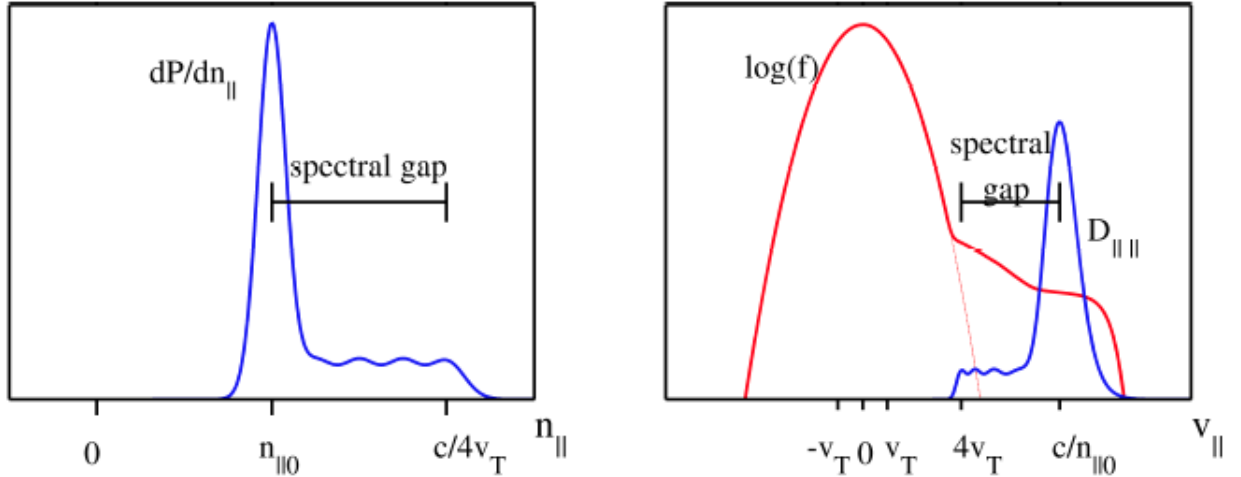
Figure 31: The Maxwellian distrubution function (red) extended so that the LH power spectrum (blue) could be absorbed in the plasma bulk, also a tail is drawn from the power spectrum to show how the spectral gap between $v_{\parallel L} \simeq 4v_T$ and $v_{\parallel 0}$ (left) or equivalently between $n_{\parallel 0} = c/v_{\parallel 0}$ and $n_{\parallel L}$ (right) is roughly bridged, where $v_{\parallel L}$ is the velocity at which the LH wave is absorbed by Landau damping, $v_{\parallel 0}$ is the phase velocity of the emitted wave at the antenna and v_T is the thermal velocity of electrons.The figure is extracted from Ref. [4].

time dependent spatial perturbation of the electron density along the magnetic field line.

B. Interaction of the LH wave with electron density fluctuations in the scrape-off layer

The interaction between the LH wave and the electron density fluctuations at the plasma edge has been first investigated in the framework of the electromagnetic wave scattering theory, assuming that fluctuations are likely driven by the electron drift wave for which $\widetilde{k}_{\parallel} \simeq 0$ [121, 126, 7, 127]. Consequently $k_{\parallel}$ remains unchanged during this process, while $\mathbf{k}_{\perp} = \mathbf{k} \times \widehat{b}$ rotates [3]. The LH wave, once scattered by long wavelength density fluctuations, is still solution of the local cold dispersion relation which depends only of $k_{\perp}^2 = \|\mathbf{k}_{\perp}\|^2$, as the magnetic field direction $\widehat{b}$ is a local axis of symmetry. This physical mechanism cannot bridge itself the spectral gap, but the toroidal refraction between successive scattering events may contribute indirectly to this effect, if their number is large enough. However, with few centimeters thick, the SOL in all tokamaks is far too thin so that fluctuations of the electron density driven by the electron drift wave can modify significantly the power spectrum between the antenna and the separatrix.

Much in the same way, the large and fast shift of the launched power spectrum

---

[3]Fluctuations may contribute to the cold mode conversion between the slow and the fast LH wave, provided the interaction takes place near the conversion layer, which is usually located well inside the separatrix. Therefore, this process is not considered, and wave-wave interaction is supposed to be restricted to wave vector rotation.
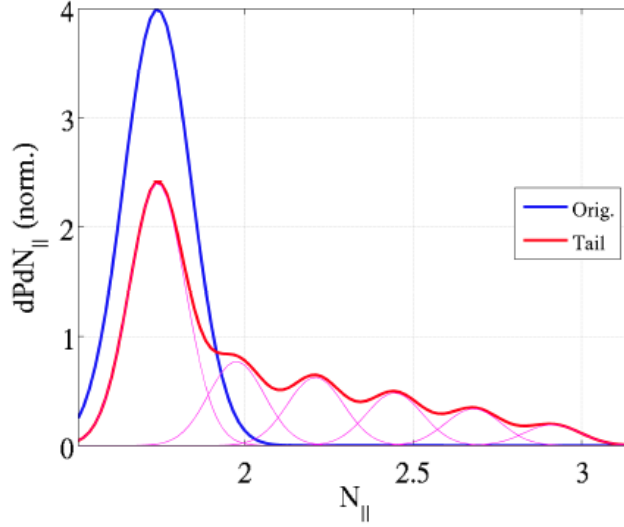
Figure 32: The LH power spectrum (blue) versus the tail model which has heuristically proven to bridge the spectral gap in RFTP simulations which have successfully reproduced experimental observations in TS. The tail model is either static or a PDF with fluctuation time much less than fast electron slowing down time scale. The figure is extracted from Ref. [4].

that is needed to interpret quantitatively the experimental observations during the LH current drive discharges in the Tore Supra tokamak cannot be the consequence of the non-linear ponderomotive force, which is well known to modify the coupling conditions of the LH antenna at high power, by creating a density depletion almost transverse to the magnetic field lines [3, 100]. Full wave calculations in the SOL have shown that this effect leads principally to a modification of the antenna directivity by changing the relative amplitudes between the various lobes which form the launched power spectrum [3]. The main lobe remains always centered at $n_{\|0}$ and is never shifted significantly to higher $n_\|$ values, as required according to Ref. [7]. In addition, there is no evidence that increasing the LH power has any effect on the spectral gap problem from measurements of the fast electron bremsstralung [90].

In this context, for fluctuations of the LH power spectrum suggested in Ref. [7] to be effectively caused by fluctuations of the electron density in the SOL implies the following assumptions: (i) the electron density fluctuates along the magnetic field lines with a time scale shorter than the fast electron slowing down time, (ii) the fluctuating LH parallel power spectrum [4] must reach higher $k_\|$ values of the order of at least $k_{\|L}$, (iii) the LH wave must be diffracted in the SOL between the antenna and the separatrix.

The lack of homogeneity of the electron density along the magnetic field line at the space-scale of the LH wavelength is in contrast with the commonly accepted statement that the parallel transport is high even in the SOL as it is supposed to scale as $\nabla_\| \sim (Rq)^{-1}$ where $q \gg 1$ is the local safety factor and R the major radius [123]. How-

---

[4]The correlation time of the fluctuations must be shorter than the fast electron slowing down time as discussed in Ref. [7].

ever, some experimental observations may indicate that such an effect likely exists near the antenna mouth. Indeed, measurements of the reflection coefficients (RC) show that they fluctuate from one waveguide to the other, with a dispersion of about 30% around the mean value over a given row, whatever the input power or the antenna phasing [5] as shown in Fig. 36. Since the RC depends principaly upon the electron density in front of each waveguide, this result suggests that the electron density itself is perturbed along the toroidal direction in a thin plasma layer. Given that the excited LH parallel wavelength is about four times the waveguide width for most LH antennas, the upper bound $\tilde{k}_{\parallel}^{\mathrm{max}}$ for the wave vector fluctuation spectrum $\tilde{k}_{\parallel}$ of the electron density perturbation in the toroidal direction may reach $4k_{\parallel 0}$, which is enough to fill the spectral gap in typical tokamak plasmas. An indirect signature of the density perturbation may be also given by the glow in front of the antenna, that is always observed when the antenna is powered [89, 5, 6, 128]. As shown in Fig. 37, the up/down poloidal asymmetry is well connected to a convective cell in front of the antenna related to the $E \times B$ force which leads to an excess in density and a slight corresponding increase of the reflection coefficients from a poloidal row to another, depending upon the magnetic field direction. Whereas the radiation emission involves several complex coupled physical processes, it gives some insight into the electron density pattern in front of the antenna and its time evolution. The lack of toroidal uniformity is clearly visible in general, which support the assumption made in the present study [89, 5, 6, 128]. Recent accurate measurements have shown that the perturbations of the striations take place on a fast time scale that less than $1\,ms$ for the LH wave in C-MOD tokamak [6], which is much less than the fast electron slowing down, as stated from Ref. [7]. The observed phenomenology suggests that the fluctuation of the electron density is a local process in the vicinity of each waveguide, which is always present, whatever the plasma regime. Several physical mechanisms may potentialy contribute, like local ionization of neutrals [129], by the LH wave electric field itself, LH driven fast electron flux [128], edge particle recycling, ponderomotive force and local turbulence, all of them being able to change on a short time scale the local electron density at the mouth of the antenna [5, 6, 128]. In fact, calculations in Chapter 3, show that random phase fluctuations at the waveguides mouth lead to perturbing the power spectrum. Actually this can be a consequence of varying reflection coefficient in front the Grill and thus is related to toroidal density variation.

Moreover, measurements of the radial electron density profiles by Langmuir probes have shown that the decay length from the separatrix is much larger in front of the antenna than far away from it, as if the density was locally self-sustained by the LH power. As a consequence, the coupling of the LH wave remains very good even if the antenna is placed at a very long distance,$\sim 15\,cm$, from the last closed magnetic flux surface [89, 130, 131]. This result obtained during a fully non-inductive L-mode discharge could indicate an enhanced radial turbulence in front of the antenna by the LH wave, leading to an apparent local flattening of the electron density, while this effect disappears outside, at another toroidal position. In addition, the limiters of the LH antenna act as a sink and modify the parallel mach number $M_{\parallel}$ resulting in density drop by 50% at the limiters along the toroidal direction [16].

It is important to recall that experimental measurements have shown unambigu-
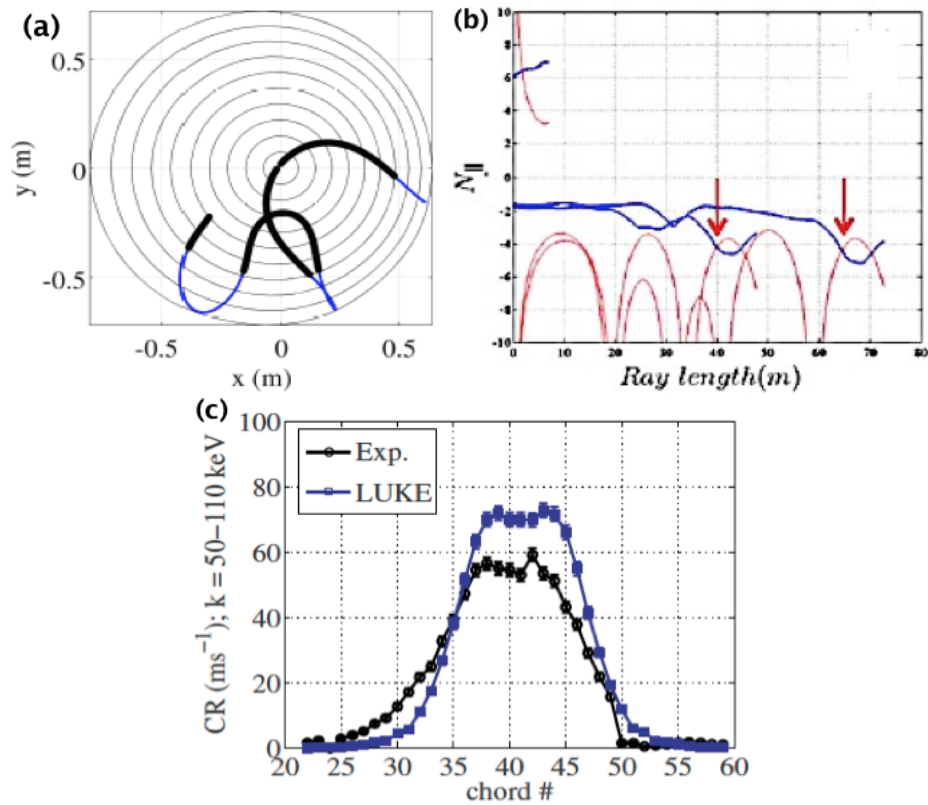
Figure 33: Narrow spectral gap corresponding to a strong damping regime. (a) Propagation of LH ray corresponding to the main lobe for TS shot #45525. (b) Evolution of $n_\parallel$ along the ray trajectory where the thick lines denote absorption. (c) Comparison of HXR count rate between experiment and LUKE simulations showing good agreement.

ously the correlation between the amplitude of the density fluctuations in the SOL and the current drive performances of the LH in the core region of the plasma [132, 133].
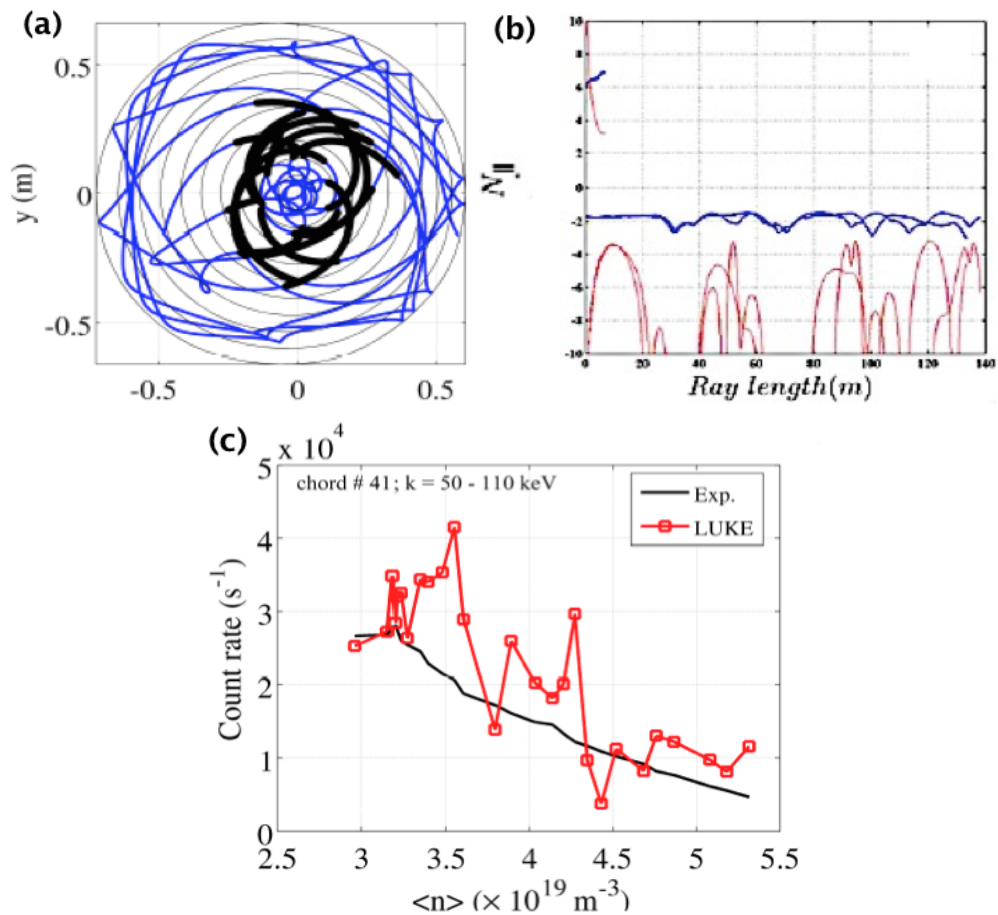
Figure 34: Wide spectral gap corresponding to a weak damping regime. (a) Propagation of LH ray corresponding to the main lobe for TS shot #45155 bouncing between the plasma edge due to cut-off and the core plasma due to (b) Evolution of $n_\parallel$ along the ray trajectory doesn't achieve absorption except after a long time which is explained as accumulation of numerical error. (c) Comparison of HXR count rate between experiment and LUKE simulations for a density scan showing chaotic simulation results
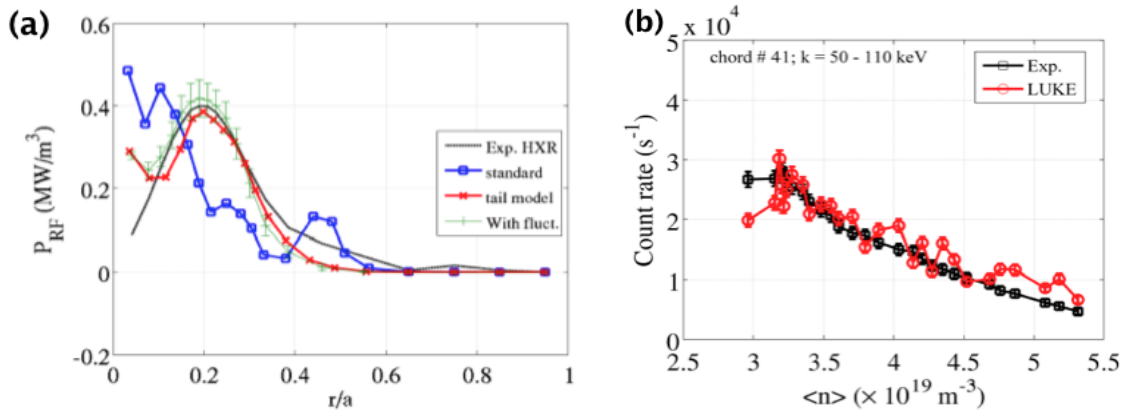
Figure 35: Modeling results using tail-model of the power spectrum at the separatrix with 50% of the power in the tail and $n_\parallel \leq n_{\parallel L}$. (a) Power deposition profile of original power spectrum and tail-model of the power spectrum obtained from simulations compared to the experimental profile obtained by Abel inversion of the HXR signal. (b) Comparison of HXR count rate between experiment and LUKE simulations for a density scan (TS shot #45155) showing good agreement.
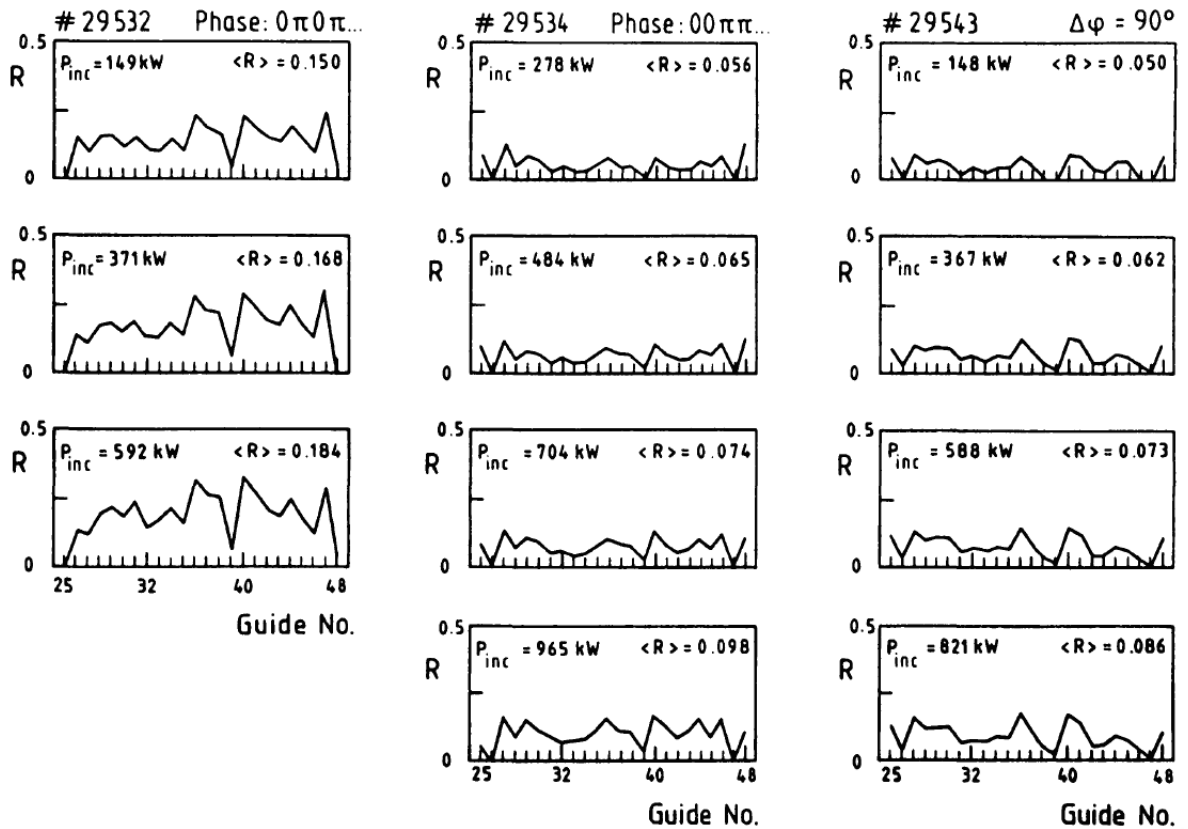
Figure 36: The reflection coefficient along the LH antenna mouth in Ref. [5], indicates a density variation in front the Grill for different phasing cases and differnt LH power values. The density variation parallel wavelength ranges between a minimum $\sim 1\,cm$ which is the width of a waveguide and may reach a maximum equal to the toroidal width of the Grill showing the effect of the LH antenna. 30% density variation is observed.
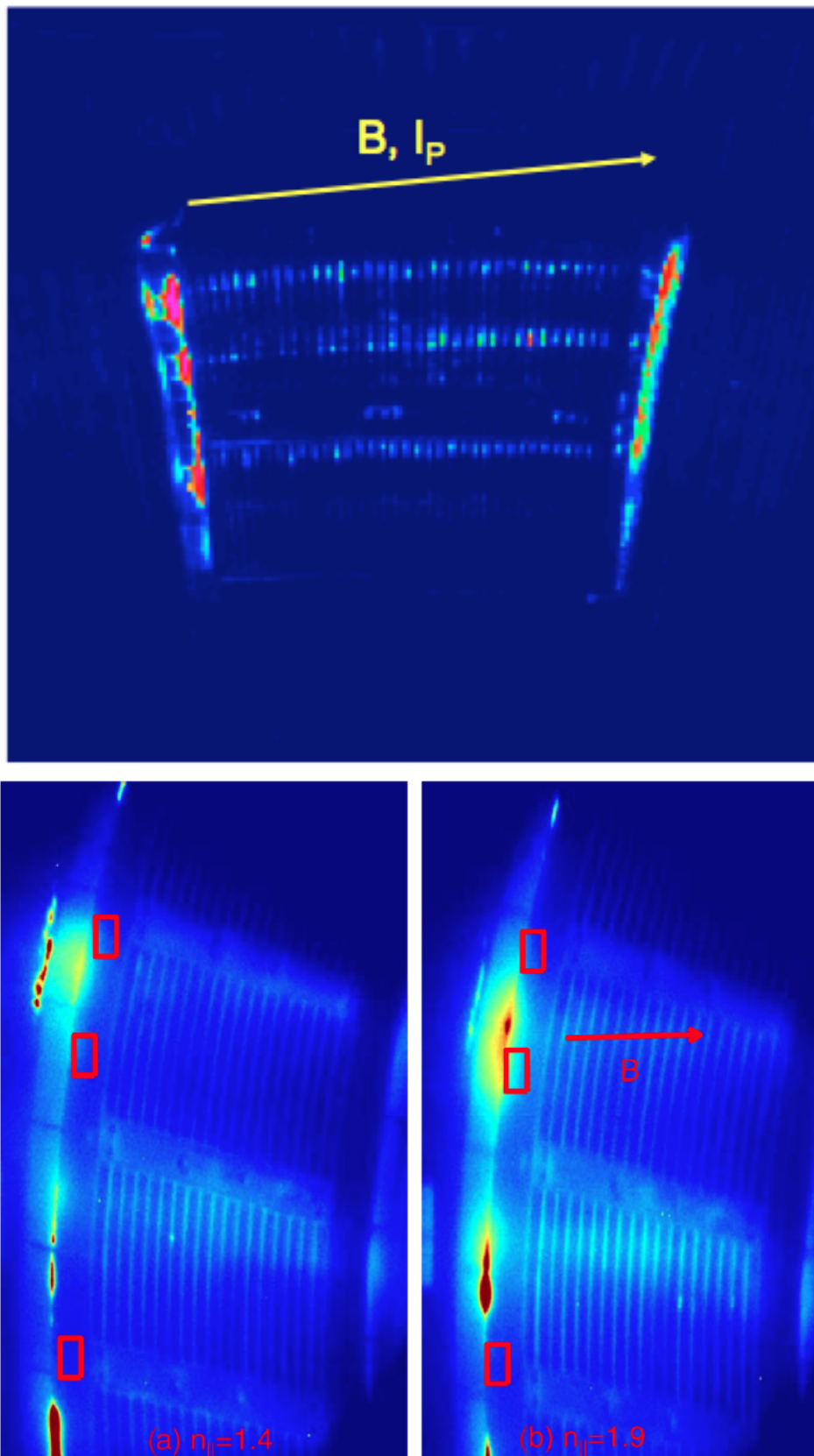
Figure 37: Camera shots of the Grill of the LH launcher while it is powered. Upper: FAM antenna snapshot during Tore Supra shot 34116 taken from presentation by Annika Ekedahl at Tore Supra scientific meeting in 2004, lower: LH launcher at Alcator C-Mod for different phasing cases from Ref. [6]. Both figures show striations due to the formation of a vortex by $E \times B$ drift. Obviously, striations change toroidaly and poloidaly thus breaking density uniformity in front at the LH launcher mouth with up to 100% density fluctuation rate.

CHAPTER VI

DESCRIPTION OF DENSITY FLUCTUATION MODEL

A. Introduction

COMSOL Multiphysics® software [134] is a finite element solver used to model physics and engineering problems with an interactie environment and several modules designed for different applications. The radio frequency module is chosen to simulate the Grill of the LH antenna and the scrape-off layer (SOL) in Tore Supra (TS). The electron density fluctuations are incorporated as a thin layer along the parallel to magnetic field direction in the SOL. Using COMSOL, the evolution of the $n_\parallel$ power spectrum[1] at different distances from the antenna is investigated by calculating the electric and magnetic fields according to the plasma wave. In particular, the dielectric permittivity is expressed in COMSOL as tensor which allows the modelling of the anisotropic plasma medium. Since the plasma under study is a cold plasma, thermal effects are neglected and thus not taken into account. Thus the propagation of the LH wave in the SOL in front of the antenna is performed by solving the usual propagation equation for the wave electric field $\mathbf{E}$

$$\nabla \times (\nabla \times \mathbf{E}) - \kappa_0^2 (1 - \frac{i\overline{\overline{\sigma}}}{\varepsilon_0 \omega})\mathbf{E} = 0 \tag{89}$$

where ε_0 is the vacuum permittivity and $\overline{\overline{\sigma}}$ is the conductivity tensor. In COMSOL Multiphysics®, Eq. 89 is expressed in a slightly different mathematical form

$$\nabla \times \mu_r^{-1}(\nabla \times \mathbf{E}) - \kappa_0^2(\overline{\overline{\varepsilon}} - \frac{i\sigma'}{\omega\varepsilon_0})\mathbf{E} = 0, \tag{90}$$

where μ_r is the relative permeability, $\overline{\overline{\varepsilon}}$ the dielectric tensor,

$$\overline{\overline{\varepsilon}} = \begin{bmatrix} S & iD & 0 \\ -iD & S & 0 \\ 0 & 0 & P \end{bmatrix} \tag{91}$$

is the cold dielectric tensor of the plasma using Stix notation [135], and $i\sigma'/\omega\varepsilon_0$ is used to model an isotropic RF power dissipation with a scalar conductivity σ'. Therefore $\mu_r = 1$ and $\overline{\overline{\varepsilon}} = 1 - i\overline{\overline{\sigma}}/\varepsilon_0\omega$ in the COMSOL solver, while σ' is used as a free parameter to force the full absorption of the LH wave at the boundaries of the integration domain and avoid possible spurious non-physical solutions. In the propagating area, σ' is set to negligible value. Physically, the expression (90) with $\sigma' \neq 0$ at the boundary implies that the wave is assumed to be fully absorbed in the plasma core.

A 2-D slab geometry is considered where the toroidal direction is assumed to match the magnetic field one, $\widehat{z} = \widehat{b}$, since the safety factor $q \gg 1$ at the plasma edge. The

---

[1]$n_\parallel$ power spectrum is the power density versus $n_\parallel$ the LH parallel refractive index.

	FAM	PAM
number of rows and modules/row	6 rows, 8 modules/row	
number of active/passive waveguides per module	6 / 1	2/ 1
active waveguides: length, width, thickness (*mm*)	70, 8 , 2	76, 14.65, 4.325
passive waveguides: length, width, thickness (*mm*)	$\lambda_g/4$, 6.5,3	$\lambda_g/4$, 12, 4.325
phase shift between consecutive modules	$3\pi/2$ *rad*	π *rad*
phase shift between active waveguides	$\pi/2$ *rad*	$3\pi/2$ *rad*
power injected	4 *MW*	3 *MW*
$n_{\parallel 0}$	2.03	1.72

Table 2: Characteristics of FAM and PAM

poloidal direction, $\widehat{y}$, is taken infinite and therefore this dimension is not considered in the calculations. The radial one, $\widehat{x}$, is along the direction of the density gradient. The size Δ_x of the integration domain along $\widehat{x}$ is corresponding to the thickness of the scrape-off layer. For the calculations, $\Delta_x = 11\,cm$. The lower limit of the width Δ_z along $\widehat{z}$ depends approximately of the number of modules N_m used in the simulation, their width Δ_z^m but also of the cone angle θ which characterizes the propagation of the LH wave from the antenna. Therefore, Δ_z is approximately given by the relation

$$\Delta_z \geq N_m\Delta_z^m + \delta_z + 2\Delta_x \tan\theta \qquad (92)$$

taking into account that the LH wave has propagating components in both toroidal directions. In Eq. 92, δ_z is the width of a passive waveguide added at one end of the antenna[2]. Usually, $\delta_z \ll N_m\Delta_z^m$ and its contribution for estimating the minimum value of Δ_z for the full wave calculations may be neglected. For the plasma parameters of the scrape-off layer that are considered, $\theta \approx \pi/4$, while $\Delta_z^m \simeq 7\,cm$ as shown in Tab. 2. The upper limit of Δ_z is fixed by numerical constraints related to the computer on which the COMSOL solver is installed. For standard LH wave calculations with a quiescent plasma in the scrape-off layer, all the modules of the LH antennas are considered, but for simulations with density fluctuations, the number of modules is reduced to two only (see Fig. 38), and in the latter, the size of the integration domain along $\widehat{z}$ is about $45\,cm$ as shown in Fig. 39.

The meshing must be performed carefully in order to catch the correct physics, while keeping the computational effort at a reasonable level. It is set from the ratio of the LH wavelength to the size of the integration domain, and the number of nodes that must be used to describe accurately a wave period. For the full wave calculations of the LH wave, the numerical difficulty arises principaly from the small size of the perpendicular component of the wavelength, $\lambda_\perp$, which can be estimated from the cold dispersion relation expressed in the usual form

$$P_4(n_\parallel)n_\perp^4 + P_2(n_\parallel)n_\perp^2 + P_0(n_\parallel) = 0, \qquad (93)$$

where the coefficients P_4, P_2 and P_0 are functions of the elements S, P and D of the dielectric tensor in the Stix notation [135]. The parallel and perpendicular wavelengths

---

[2]The antenna has $N_m + 1$ passive waveguides placed between modules and at each end of the antenna with each module including one passive waveguide.
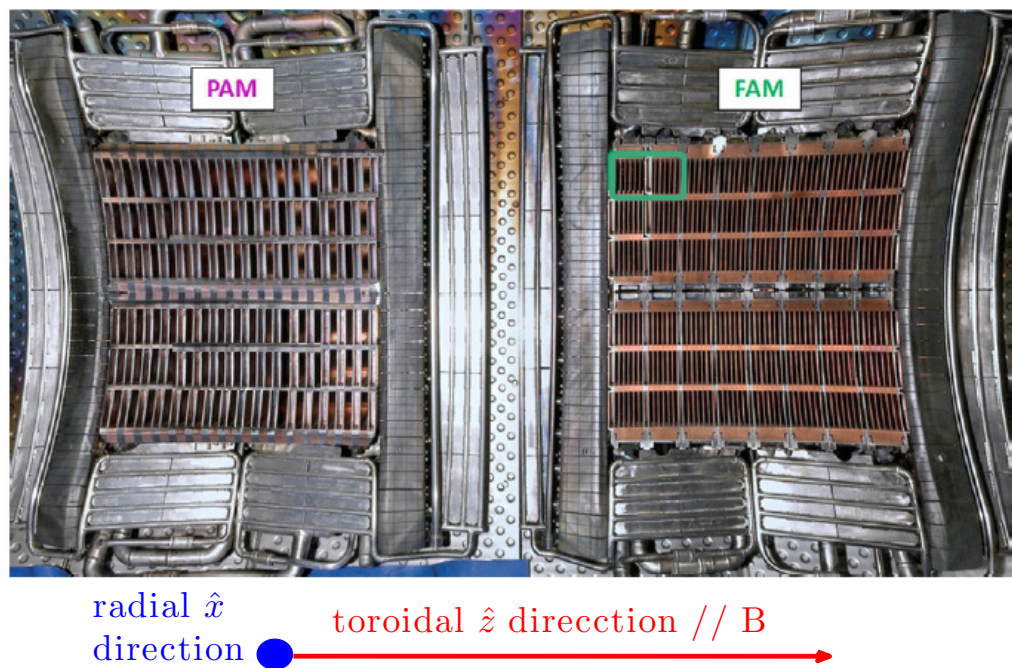
Figure 38: Front image of FAM (right) and PAM (left). The green box encloses two modules per row of the FAM antenna to show the part incorporated in the fluctuation model constructed in COMSOL Multiphysics®. Radial direction, $\hat{\mathbf{x}}$, and toroidal one, $\hat{\mathbf{z}}$ parallel to B the magnetic field in the SOL, are illustrated.
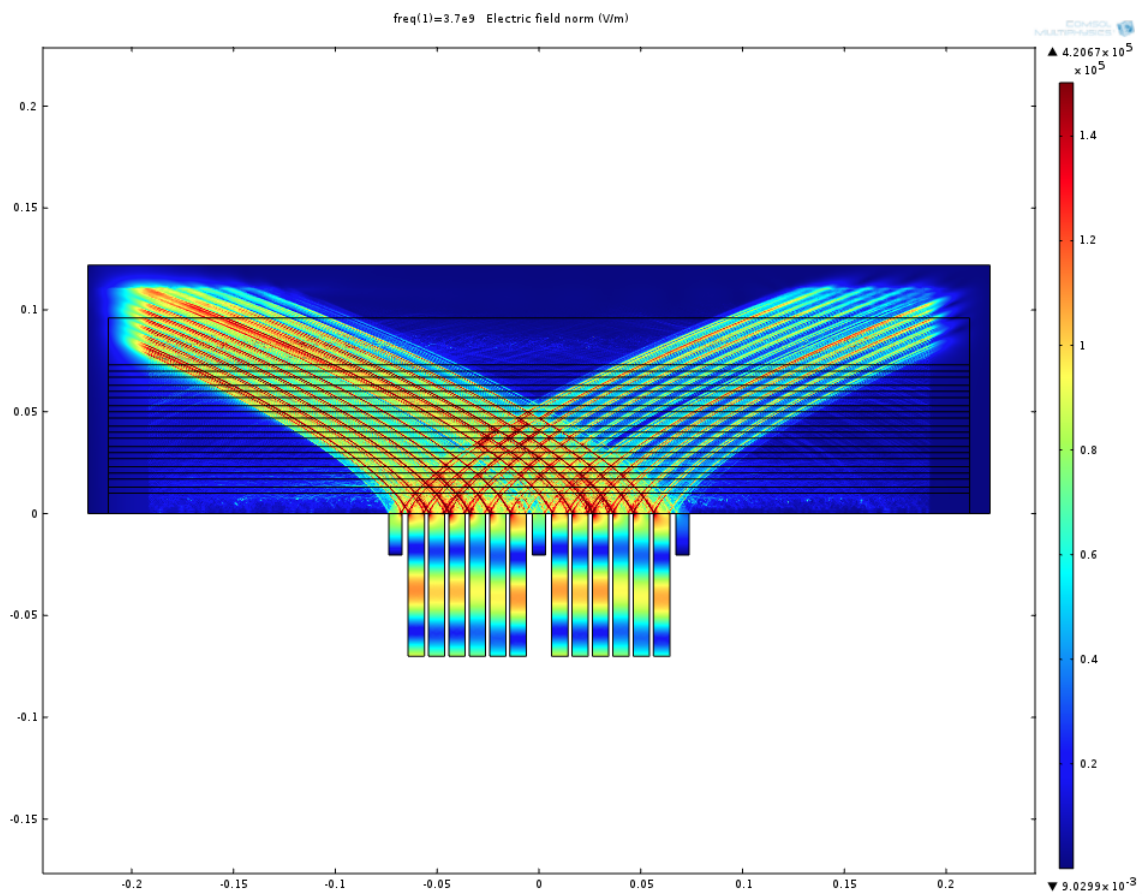
Figure 39: Lower hybrid wave propagation for a two modules antenna, (upper) $n_{e0} = 2 \times 10^{17} \, m^{-3}$ and a density decay length $2 \, cm$.

$\lambda_{\|,\perp}$ may be deduced from the corresponding components of the refractive index $n_{\|,\perp}$ by the relation $\lambda_{\|,\perp} = c/\left(f_{LH}n_{\|,\perp}\right) = \lambda_0/n_{\|,\perp}$, where $f_{LH} = \omega/2\pi$, and $\lambda_0 = 2\pi/\kappa_0$ is the theoretical LH wavelength in vacuum used here as a reference. For $f_{LH} = 3.7\,GHz$, $\lambda_0 \approx 8.1\,cm$.

At the antenna mouth, $n_\| = n_{\|0}$ is determined by the antenna arrangement made of arrays of waveguides that are grouped in modules. For the FAM, $n_{\|0} = \phi_0/\left(\kappa_0 d\right) = \left(\phi_0/2\pi\right)\left(\lambda_0/d\right)$ where d is the periodicity of the waveguides along $\widehat{z}$ and ϕ_0 the phasing between consecutive waveguides. For the phasing $\phi_0 = \pi/2$ corresponding to the maximum of the antenna directivity [57], $n_{\|0} \simeq 2.0$, since $d = 1\,cm$ and therefore $\lambda_{\|0}^{FAM} \approx 4.0\,cm$. The estimate for the PAM is more approximative, since d cannot be defined unambiguously, because the antenna is a complex array made of active and passive waveguides with slightly different widths. With $\phi_0 = 3\pi/2$ and an averaged value $d \approx 3.5\,cm$, $n_{\|0} \simeq 1.7$ for the PAM and $\lambda_{\|0}^{PAM} = 4.7\,cm$. Another parameter is also used in order to have an $n_{\|0}$ scan, which is ϕ_{mod} the phasing between consecutive modules. $N_\|$ is given by $n_\| = n_{\|0}[1 + (\phi_{mod} - \phi_{mod,0})/N\phi_0]$, with $\phi_{mod,0}$ is the module phasing that achieves $n_\| = n_{\|0}$ where $\phi_{mod,0} = 3\pi/2$ for FAM and π for PAM, and N is the number of modules [57, 46].

Note that the electric field in COMSOL is excited at the input port of each active waveguide as follows:

the electric field in the ith active waveguide of the first module is

$$e^{i(k.x-\omega t-(i-1)\phi)}V/m$$

and in the ith waveguide of the jth module it has the form

$$e^{i(k.x-\omega t-[(i-1)\phi+(j-1)\phi_m])}V/m$$

where ϕ and ϕ_m are the phase difference between adjacent waveguides and the feeding phase between adjacent modules respectively.

The value of $\lambda_\perp$ may be easily obtained by taking the electrostatic limit of Eq. 93, $n_\perp^2 = -Pn_\|^2$ [3] since $S \sim 1$ or $n_\perp \approx (\omega_{pe}/\omega)n_\|$ where ω_{pe} is the local electron plasma frequency and $\lambda_\perp \approx (\omega/\omega_{pe})\lambda_\| \approx (f_{LH}/f_{pe})\lambda_\|$ with $f_{pe} = \omega_{pe}/2\pi$. For $f_{LH} = 3.7\,GHz$ and $f_{pe} = 89.8\sqrt{n_e\left[10^{+20}m^{-3}\right]}\,GHz$, $\lambda_{\perp 0}^{FAM} \approx 2.6\,cm$ and $\lambda_{\perp 0}^{PAM} \approx 3\,cm$ for an electron density $n_{e0} = 4 \times 10^{17}\,m^{-3}$ in front of the antenna close to the cut-off density $n_c = 1.7 \times 10^{17}m^{-3}$. However, the density in the scrape-off can increase by a factor ten from the antenna to the separatrix, and $\lambda_\perp$ may drop down to $5\,mm$, [4] assuming that $n_\|$ has not evolved significantly in the SOL. Note that $|P|$ increases as density n_e becomes larger, and consequently $\lambda_\perp$ decreases. For example, for $n_{e0} = 4 \times 10^{17}\,m^{-3}$ i.e $\lambda_\perp = 10\,mm$, an increase in n_e by a factor of 10 results in a decrease by a factor of 4 in $\lambda_\perp$, as shown

---

[3] P is negative for densities greater than the cut-off density n_c.

[4] 5 mm corresponds to 2 cm decay length at the separatrix with $ne0 = 2e17/m^3$ and separatrix at 8 cm from antenna

in Fig. 40; consequently, $k_\perp \in [628, 2616] \, m^{-1}$. Taking the shortest length characteristic $\lambda_\perp$ at the separatrix as the reference whatever the direction and 10 nodes per wavelength, the minimum requirement for accurate calculations, the mesh size along $\widehat{x}$ is $N_x > 140$, while it is $N_z > 500$ along $\widehat{z}$, which corresponds to a reasonably small memory size of the order of $\sim 0.5 \, MBytes$. Therefore, in order to improve the accuracy of the calculations, 20 nodes per wavelength have been considered, which corresponds to an acceptable trade-off between performances and memory consumption.

The above estimate must be significantly revisited in presence of electron density fluctuations, since wavelengths as small as one tenth of $\lambda_\perp$ at the separatrix have to be considered in the parametric studies. Therefore, the required memory size may increase up a much larger value of $250 \, MB$. However, it is possible to reduce the memory consumption by using a non-uniform meshing, reducing the mesh size in areas where the plasma is quiescent.

Besides, calculations concern also the electric field pattern in the waveguides, which must be calculated consistently with its evolution in the SOL. The meshing technique that is used is detailed in [134] and the additional amount of memory that is required reaches about $12 \, GB$.

In conclusion, in order to ensure accurate meshing at different radial positions in the SOL, a uniform mesh over the perturbed domain is chosen. Moreover, the largest mesh element size in the main SOL including the Grill is taken as $\lambda_{m,\perp}/20$ where $\lambda_{m,\perp}$ is the minimum size of $\lambda_\perp$ as density varies. In this manner, a lower bound of 20 mesh points per wavelength is retrieved at different positions which minimizes the error in the results and optimizes the total number of mesh elements.

Fig. 41 shows the radial mesh evolution where:

1 - Antenna domain, mesh size: $0.4 \, mm$, since $\lambda_{LH} \cong 8 \, cm$.

2 - Nonfluctuating plasma domain (blue) has constant density, $n_{e0} = 2.6 \times n_c$, mesh size: $\lambda_\perp(n_{e0})/20 \simeq 0.045 \, mm$.

3 - SOL domain (red), n_e fluctuates around the mean density n_{e0}, mesh size: $\lambda_\perp(n_{e,max})/20 \simeq 0.034 \, mm$, where $n_{e,max}$ is the highest density attained in the SOL when 50% density fluctuations are considered.

1. Wave damping

The conductivity σ' in Eq. 90, which is a scalar function, is employed to control the wave damping. Actually, the imaginary term $i\sigma'/\omega\varepsilon_0$ represents power dissipation.
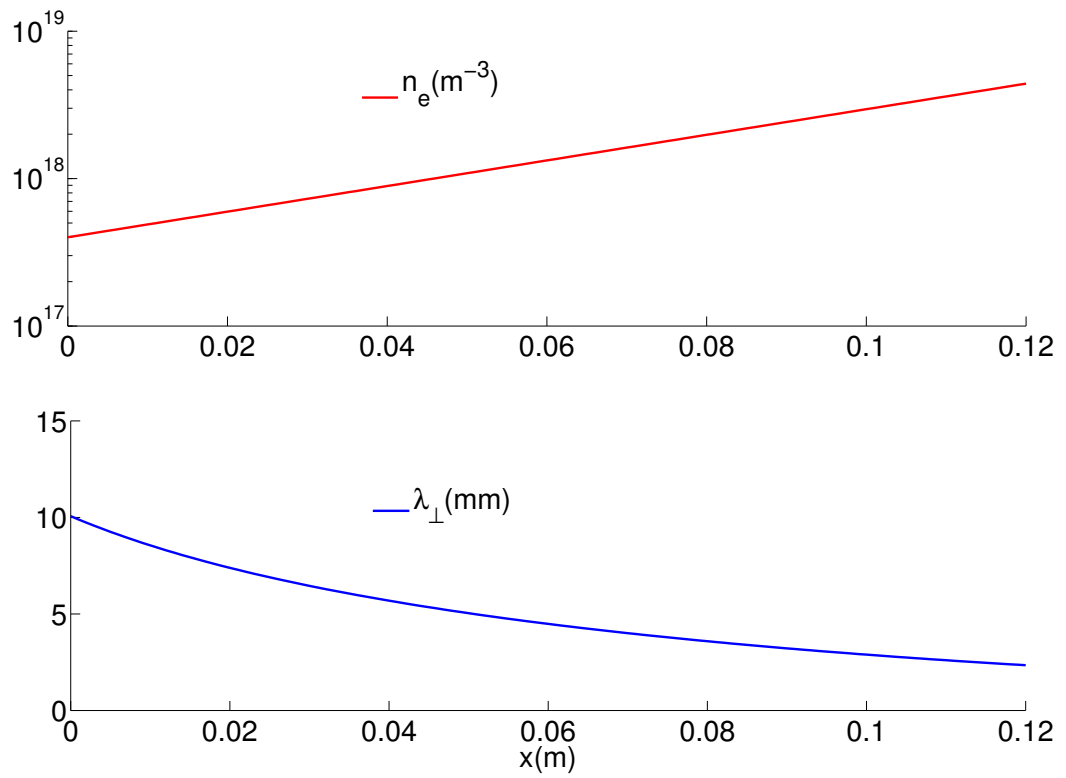
Figure 40: The magnitude of the LH wavelength perpendicular to magnetic field lines $\lambda_\perp$ plotted as a function of x, the radial distance from the antenna, shows how $\lambda_\perp$ decreases when the density n_e increases.
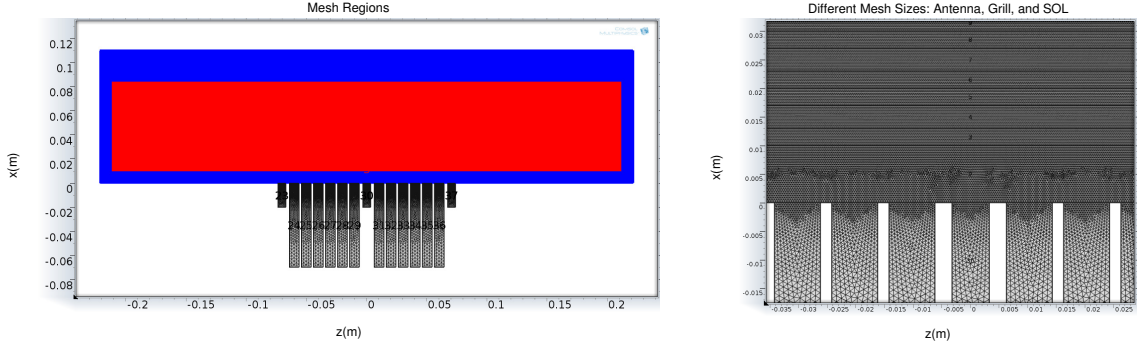
Figure 41: Meshing layers (unit is m). (left)The plasma antenna model is divided into three regions: the antenna (black) where plasma density is zero and thus LH wavelength is that in vacuum, the grill (blue) which is the region just in front the antenna and the outer boundaries (blue) added to damp the wave and have constant density and thus the mesh size is set according to the corresponding $\lambda_\perp$ value being less than $\lambda_\parallel$ at the densities used, and the fluctuating SOL plasma (red) where density fluctuates and thus the mesh size is set according to the smallest $\lambda_\perp$ value given by the maximum attainable density resulting from fluctuations. Note that the mesh size is 20 points per $\lambda_\perp$ (wavelength) in the SOL (antenna) domain. (right) The corresponding mesh size distribution in the antenna, grill and SOL.

Knowing that the wave propagates without absorption in the SOL and is damped inside the plasma, $i\sigma'/\omega\varepsilon_0$ is set to a negligible value in the SOL ($i\sigma'/\omega\varepsilon_0 \approx 5 \times 10^{-5} \ll (S, P)$ where $S \simeq 1$, $P \gg 1$) and it is increased smoothly beyond the propagation area where the wave is absorbed as shown in Fig. 42. Consequently, the wave is fully damped at the boundaries and thus no spurious reflection occurs.

Actually, the walls adjacent to the antenna are the only walls that exist realistically and thus the wave is damped along the remaining outermost boundaries, which are the toroidal wall in front the antenna and the two lateral walls on the sides. A constant negligible damping inside the SOL is maintained so that it continuously increases in the damping layer added around the SOL region. It is crucial to adjust the damping function σ' as well as the mesh between the SOL and the outer damping region to enhance the continuity of the wave as it crosses the SOL without being reflected by an abrupt change in the meshing or damping. First, the damping function σ' is constructed such that it imposes a constant negligible damping (dp_{cstin}) in the SOL, constant damping outside the SOL (dp_{cstr}, dp_{cstt}) and an exponentially increasing damping around the SOL. More explicitly, σ' is the sum of a radial, toroidal and inner components i.e.

$$\sigma' = \sigma'_r + \sigma'_t + \sigma'_{in} \tag{94}$$

with

$$
\begin{aligned}
\sigma'_r &= dp_{cstr} \times H(y, d_{cstr}) + dp_{expr} \times H(y, d_{expr}) \times exp(v(y - d_{expr})) \times (y - d_{expr}) \\
\sigma'_t &= dp_{cstt} \times H(x, d_{cstt}) + dp_{exp} \times H(x, d_{expt}) \times exp(v(x - d_{expt})) \times (x - d_{expt}) \\
&\quad + dp_{cstt} \times H(-x, d_{cstt}) + dp_{exp} \times H(-x, d_{expt}) \times exp(v(-x - d_{expt})) \times (-x - d_{expt}) \\
\sigma'_{in} &= dp_{cstin} \times H(-x, -d_{cstin}) \times H(x, -d_{cstin}) \times H(y, d_{cstr})
\end{aligned}
$$
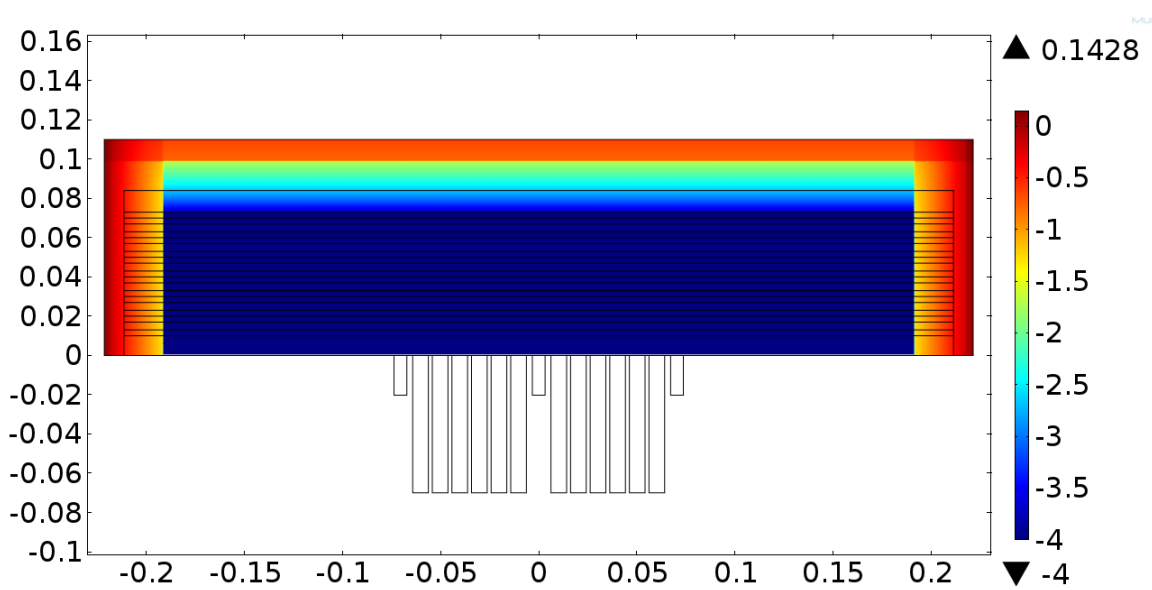
Figure 42: A log scale sketch of the magnitude of the damping function given by σ' in Eq. 90 where σ' is employed in the plasma wave equation to damp the LH wave at the walls to mimic an infinite medium and avoid spurious reflection.

where H is the Heaviside function,

dp_{cstr} is the coefficient of constant damping outside the SOL starting from radial distance $x = d_{cstr}$,

dp_{cstt} is the coefficient of constant damping outside the SOL starting at toroidal positions $z = d_{cstt}$ and $z = -d_{cstt}$,

dp_{exp} is the coefficient of exponential damping outside the SOL both radially and toroidally starting at a radial distance $x = d_{expr}$ and at toroidal positions $z = -d_{expt}$ and $z = d_{expt}$,

dp_{cstin} is the coefficient of constant damping within the SOL starting between toroidal positions $z = -d_{cstin}$ and $z = d_{cstin}$,

d_{cstt} , d_{expr}, d_{expt}, d_{cstin} are described in the above definitions, and ν is fixed.

Fig. 43 shows the distribution of damping within the model geometry.

Tab. 3 displays the damping coefficients in the damping function σ' which are tuned to obtain the optimized model.

Note that dp_{cstin} is optimized to 1×10^{-4} so that more than 93% of the power launched at the Grill is retrieved 8 cm away from the antenna as shown in Tab. 4.
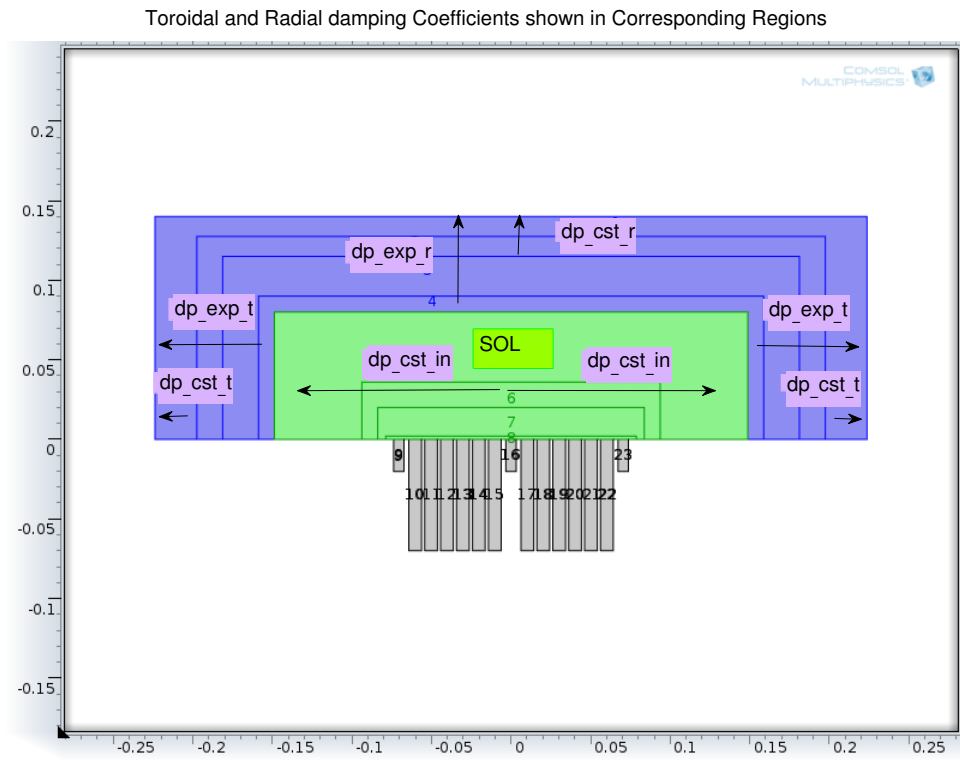
Figure 43: Damping distribution with enlarged vertical dimension

dp_{cstr}	dp_{cstt}	dp_{exp}	dp_{cstin}
0.15	0.15	0.05	0.0001

Table 3: Damping power coefficients

x (cm)	input	1	3	5	7	8	9	10	11	11.8
$P_x(10^5 W/m)$	4.46	4.45	4.39	4.34	4.28	4.2	3.94	3.25	2	0.13

Table 4: Evolution of power time average P_x integrated along $\hat{\mathbf{z}}$

The optimal damping values are shown in Fig. 42, indicating almost zero values in the SOL and highest values on the boundaries. The extended domain of the exponential damping along the radial direction damps the power gradually especially that the power is stronger in this direction, and should not be suppressed abruptly. Fig. 39 shows the electric field magnitude distribution in the antenna and plasma after optimizing damping coefficients, so that the model area and thus calculation memory requirements are optimized.

B. Validation

Before studying the effect of electron density fluctuations on the LH wave propagation in the SOL, the simulations performed with the COMSOL solver of the full wave equation (89) have been validated for a quiescent plasma against results obtained in similar conditions with the ALOHA 1-D LH coupling code [93]. Both FAM and PAM like antenna structures have been considered with a full row of 8 modules, and the input powers are $3\,MW$ and $4\,MW$ respectively. Fig. 44 shows a COMSOL simulation for FAM and PAM where the wave is damped only one centimeter in front the antenna to reduce calculation stress.

Once the solution of the full wave equation has been calculated, the LH power spectra dP/dn_z is determined by applying a fast Fourier transform to the 2-D power density along $\hat{z}$ and at different radial positions along $\hat{x}$. The density in the SOL is almost linearly decreasing from the separatrix to the antenna with a decay length $n_e/\nabla n_e = 2\,cm$, the electron density being $n_{e0} = 1.2n_c$ for the FAM and $n_{e0} = n_c$ for the PAM. As shown in Fig. 45 the results obtained by the two codes are in excellent agreement either for both the negative and positive parts of dP/dn_z and whatever the applied phasing values. The comparison is performed for three module phasing values with 0 and $\pm\pi/6$ differences respectively from $\phi_{mod,0} = \pi/2$ for the FAM and $3\pi/2$ for the PAM as shown in Tab. 5. Fig. 45 shows the position of the LH power spectrum main lobe while the module phasing increases, such that dP/dn_z peaks at $n_z = 1.92, 2.01, 2.11$ for FAM and at $n_z = 1.63$, 1.72, 1.81 for PAM. For the positive part of the LH power spectrum, the main lobes are centered at the correct theoretical n_z values and their widths are also well determined, such that the total input power for each antenna is well retrieved.
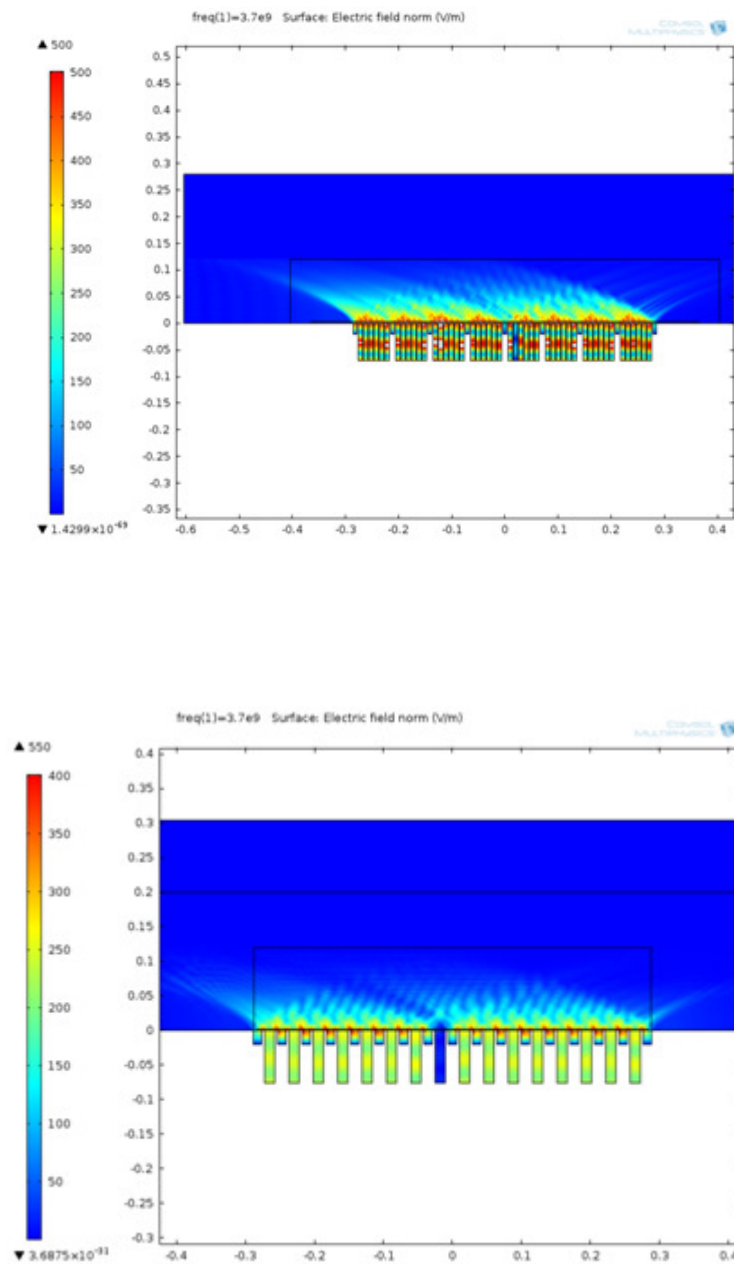
Figure 44: 2-D simulation of one row in FAM (top) and PAM (bottom) emphasizing the Grill structure and the propagating LH wave which is damped close to the antenna to reduce calculation effort resulting from having a radial density gradient in the SOL and a full row of the antennas. length unit is meter.

	$n_{e0}(10^{17}m^{-3})$	$\phi_{mod,0}$	ϕ_{mod}		
			$\phi_{mod,0} - \pi/6$	$\phi_{mod,0}$	$\phi_{mod,0} + \pi/6$
FAM	2.0	$\pi/2$	$n_{z0} \simeq 1.9$	$n_{z0} \simeq 2.0$	$n_{z0} \simeq 2.1$
PAM	1.7	π	$n_{z0} \simeq 1.6$	$n_{z0} \simeq 1.7$	$n_{z0} \simeq 1.8$

Table 5: Parameters used in validating the COMSOL model, with the n_{z0} values relative to three module phasing cases, expressed in terms of $\phi_{mod,0}$ which achieves highest directivity
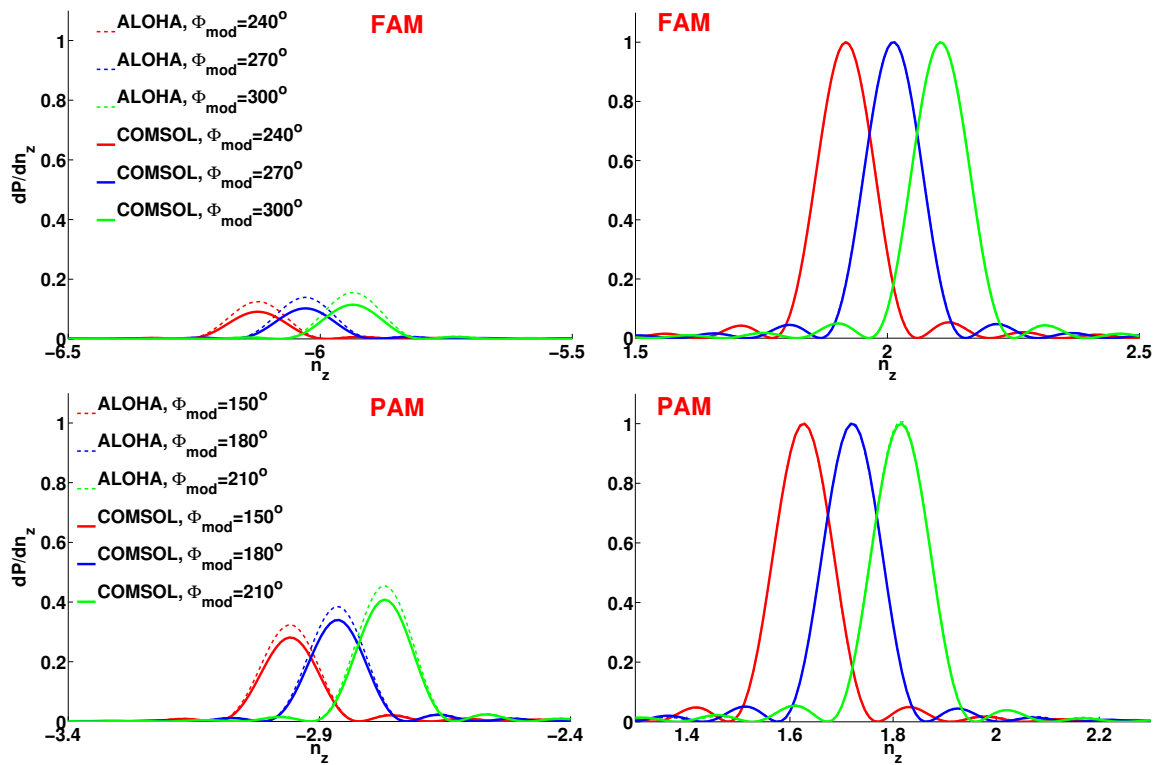
Figure 45: Comparison of LH n_z (equivalently $n_{\parallel}$) power spectra for FAM and PAM like LH antennas based on power values calculated in COMSOL Multiphysics® (solid) against power spectra calculated in ALOHA 1D coupling code (dashed) for three module phasing values: $\phi_{mod} = \phi_{mod0} - \pi/6\,(red), \phi_{mod0}\,(blue), \phi_{mod0} + \pi/6\,(green)$ where $\phi_{mod0} = (3\pi/2, \pi)$ for (FAM,PAM) is the module phasing that achieves highest directivity.
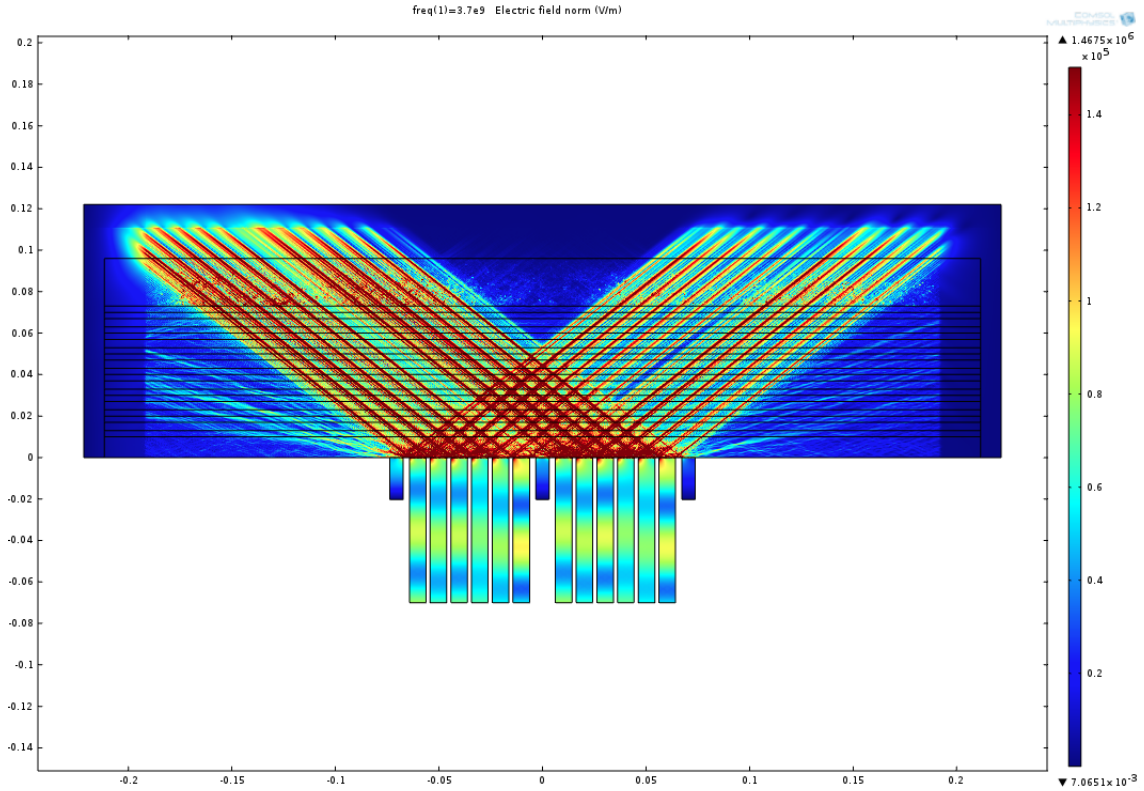
Figure 46: Lower hybrid wave propagation for a two modules antenna with a flat density with $n_{e0} = 4.4x10^{17} m^{-3}$

C. Fluctuation Model

As density fluctuates at high rates above 50%, meshing becomes extremely fine and calculation stress increases beyond the capabilities of the computer on which COMSOL is installed and which has 24 *Gbytes* of cache memory. Hence, in order to reduce the calculation stress a flat density is assumed in the SOL for the fluctuation model with $n_{e0} = 4.4 \times 10^{17} m^{-3}$. Though the electric field propagation is different for a flat density SOL as the comparison between Fig. 39 and Fig. 46 shows, the power spectrum obtained using COMSOL is the same (shown in Fig. 47). Note that the spectral width is four times larger than that of a full row of the antenna since only two modules are assumed knowing that $\Delta n_{\parallel} \propto 1/L$ where L is the $\hat{z}$ dimension of the antenna.
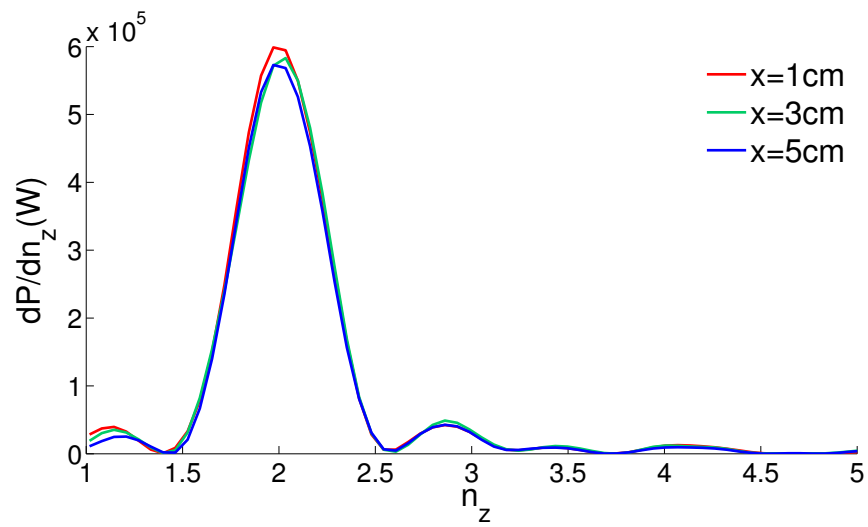
Figure 47: Power spectrum of 2 module FAM like antenna at different distances from the antenna for a quiescent plasma and flat density.

CHAPTER VII

SIMULATIONS RESULTS

A. Fluctuation Model

Electron density fluctuations in the SOL are incorporated in front of a FAM like antenna using the model discussed in Ref. [121]. The background density is set to $n_0 = 2.6 \times n_c$ to avoid reflections due to densities nearing cut-off in the presence of high fluctuation amplitudes up to 50%. The SOL size is set to $\Delta_x = 8$ cm and is representative to the Tore Supra tokamak. The module phasing is assumed to be $\phi_{mod,0} = \pi/2$ and the total input power of the two modules is set to 0.5 MW. The electron density is $n = n_0 + \tilde{n}$, where the average over the toroidal direction is $\bar{\tilde{n}} = 0$. In accordance with the model discussed in Chap. 4, fluctuations are represented by a thin perturbed layer varying along $\hat{\mathbf{z}}$, assuming a monochromatic wave-like parallel dependence with a random phase as shown in Fig. 48.

$$\tilde{n} = \sigma_n n_0 \sin(\tilde{k}_z z + \tilde{\phi}) \exp\left(-\frac{(x-\tilde{x})^2}{\Delta\tilde{x}}\right) \tag{95}$$

where $\tilde{k}_z$ is the fluctuation parallel wave number, $\sigma_n \in [0,1]$ is the relative amplitude of perturbations, $\tilde{\phi} \in [0, 2\pi]$ is the perturbation phase, $\tilde{x}$ is the radial position of the fluctuating layer assuming a Gaussian radial dependence, and $\Delta\tilde{x}$ is the corresponding FWHM[1].

More explicitly, Fig. 48 shows a perturbation layer centered at $\tilde{x} = 0.375$ and extending by $\Delta\tilde{x} = 0.125$ in both $\hat{\mathbf{x}}$ directions, with a 50% density fluctuation amplitude. Also, $\tilde{k}_z = 0.5k_{\|0}$ where $k_{\|0}$ (also denoted k_{z0}) is the LH parallel wavenumber ($k_{\|0} = \kappa_0 \times n_{\|0} \simeq 1.58\,\mathrm{cm}^{-1}$). The fluctuating layer in the simulations is positioned in the middle of the SOL. Even though physical arguments lead to consider it closer to the antenna mouth, positioning the perturbation in the middle of the simulation box makes it possible to identify clearly the effect of fluctuations between the antenna and the perturbed layer. It is found that the results obtained are almost independent of its position.

The effect of density fluctuations on the LH electric field and power spectrum is investigated in the presence of the perturbed layer described in Fig. 48 with $\tilde{\phi}/\pi \simeq 1.6$ and $\tilde{k}_z = k_{\|0}$. The LH electric field shown in Fig. 49 indicates that the LH beam is diffracted along the perturbed layer, and then continues to propagate towards the separatrix.

---

[1]$\tilde{x}$ and $\Delta\tilde{x}$ are scaled to the SOL depth of 8 cm, hence $\tilde{x} = 0$ and $\tilde{x} = 1$ correspond to the antenna and the separatrix respectively.
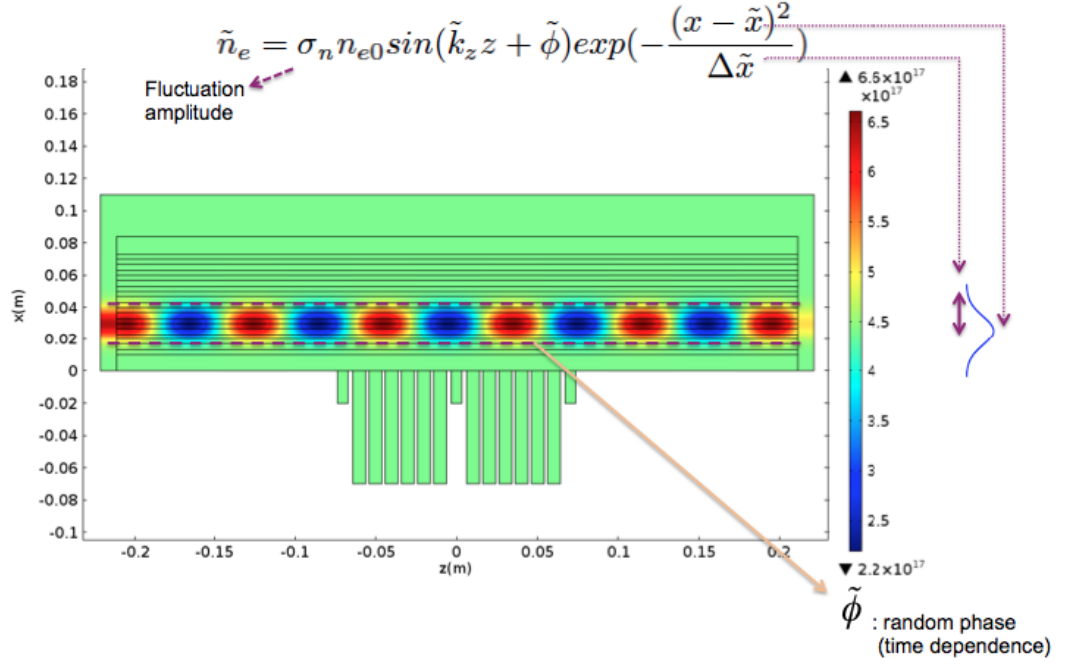
Figure 48: COMSOL model of two modules FAM like antenna and a thin density fluctuating layer in the SOL for $\tilde{x} = 3\ cm$, $\Delta\tilde{x} = 1\ cm$, $\sigma_n = 0.5$, $\tilde{k}_z = 0.5k_{z0}$, $\tilde{\phi}$ random

In a quiescent plasma, the LH power spectrum, which is peaked at $n_{z0} \simeq 2.0$ with negligible amount of power in the tail, remains unchanged from the antenna to the separatrix. A significant fraction of the LH power in the main peak is transferred to multiple satellite peaks in dP/dn_z once the wave propagates through the perturbed region, an irreversible process until the separatrix is reached. As shown in Fig. 50, the LH power spectrum exhibits large fluctuations depending upon the perturbation phase, a result which is consistent with the heuristic quantitative analysis of LHCD TS discharges with a large spectral gap [7]. Interestingly, the density fluctuations in the SOL have no effect on the power spectrum in front of the antenna, and the coefficients of the scattering matrix must remain consistent with the theory based on a quiescent local plasma, as observed experimentally.

B. Density perturbation effect on the power spectrum at the separatrix

The main effect of the density perturbation layer is the appearance of new lobes in the LH power spectrum, whose positions and amplitudes could change considerably depending upon the phase $\tilde{\phi}$ and the wavevector $\tilde{k}_z$. The perturbed power spectrum is fitted by two lobes with a Gaussian shape. The first one is located at n_{z0} and corresponds to the main lobe calculated for a quiescent plasma with fixed mean and standard
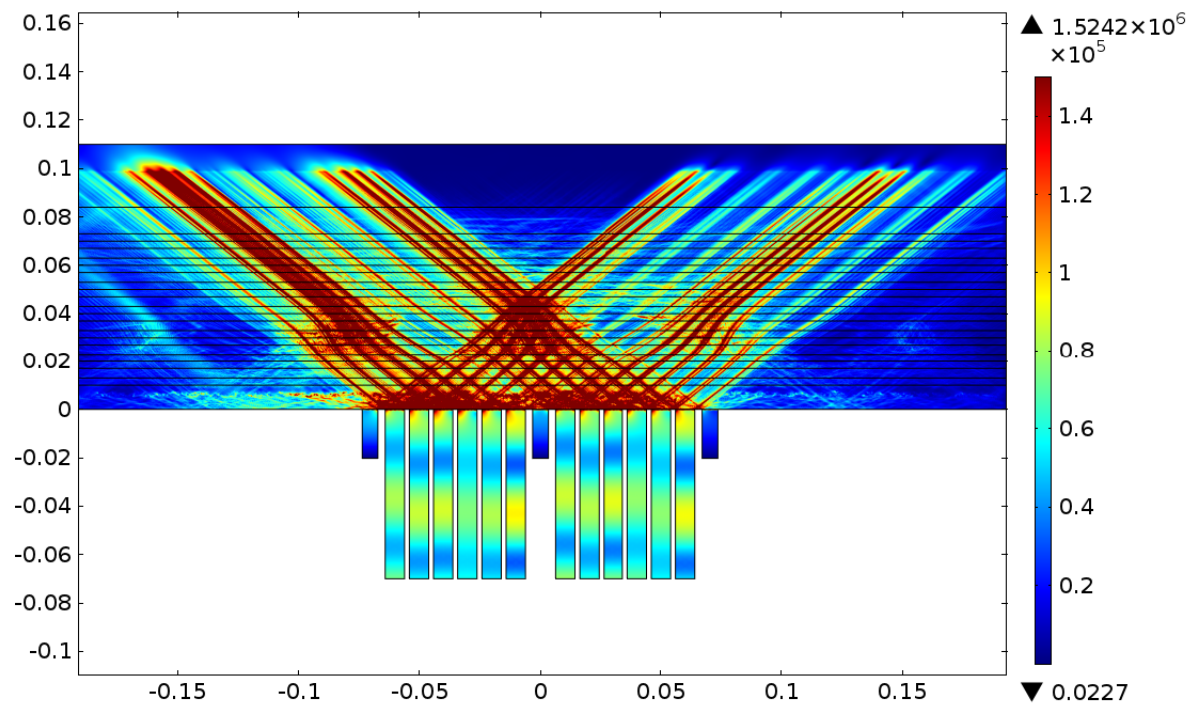
Figure 49: Electric field distribution resulting from the fluctuating ayer described in Fig. 48. Diffraction of the electric field is observed.
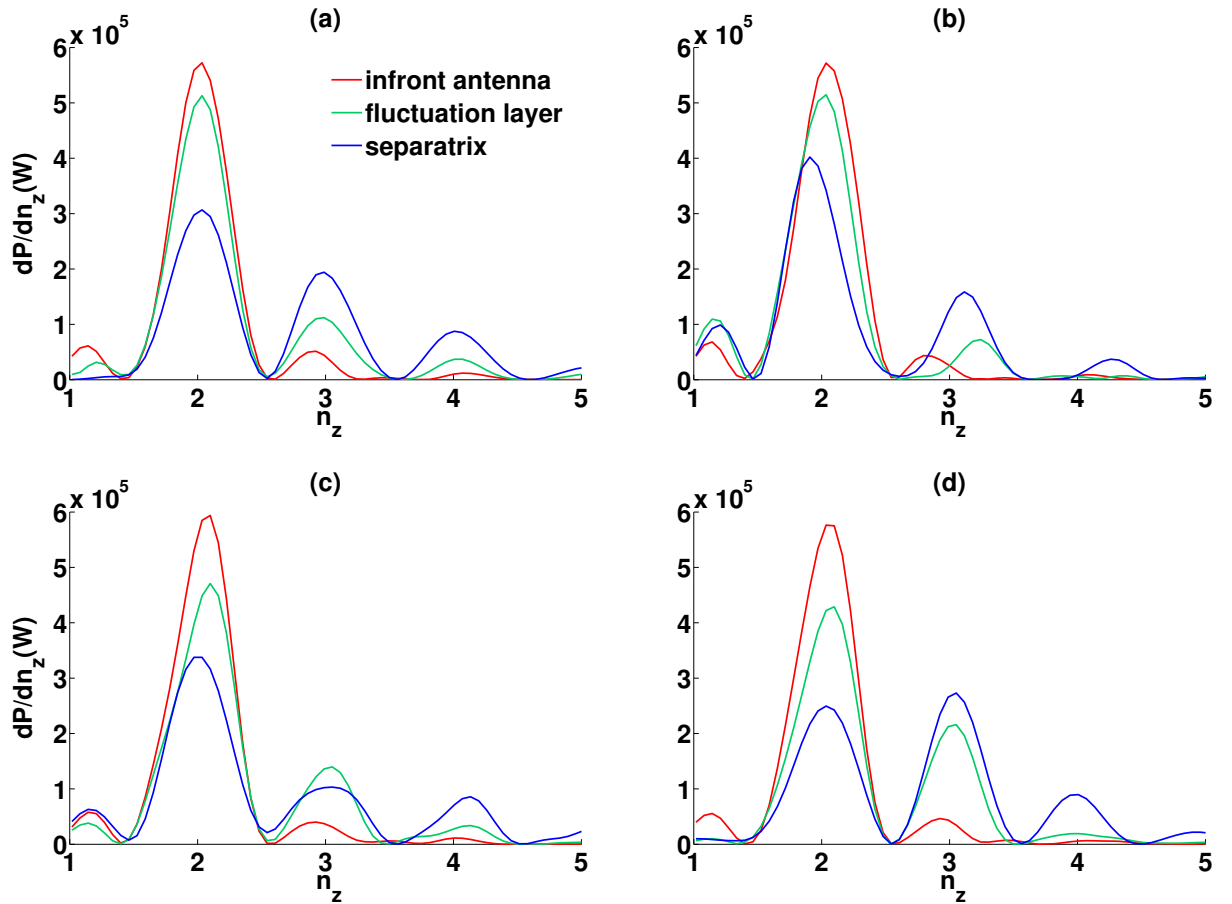
Figure 50: (a), (b), (c), (d) : Instantaneous power spectra for different phases $\tilde{\phi}(\pi)$ $= 0.28, 1.9, 0.97, 1.5$ and at different positions in the SOL. Here $\tilde{k}_z = 0.5 k_{z0}$ $\tilde{x} = 3\ cm$, $\Delta\tilde{x} = 1\ cm$, $\sigma_n = 0.5$. The figures show satellite peaks that change position and amplitude with in the domain $1 < n_{z0} < 5$ which corresponds to a large spectral gap.

deviation given by $\mu(n_{z0}) \cong 2$, and $\sigma(n_{z0}) = 0.21$. Its position and width are found to remain almost unchanged by the fluctuations whereas its amplitude changes due to power transfered to the tail. The second lobe, which characterizes the spectral tail, is centered at $\mu(n_z)$ corresponding to the equivalent mean value of all new satellite lobes, with a standard deviation $\sigma(n_z)$ such that the total power in the spectrum remains unchanged. In order to find the equivalent Gaussian curve of the tail, all tail lobes are fitted by a Gaussian and consequently the mean, standard deviation and power amplitude of the tail $\mu(n_z)$, $\sigma(n_z)$ and $P(n_z)$ are derived from those of the lobes that form the tail according to the formulas:

$$\mu(n_z) = \sum_{i=1}^{4} p_i \times \mu_i(n_z) \tag{96}$$

$$\sigma(n_z) = (\sum_{i=1}^{4} p_i \times [\mu_i(n_z)^2 + \sigma_i(n_z)^2])^{1/2} - \mu(n_z)^2 \tag{97}$$

$$P(n_z) = \frac{1}{\sigma(n_z)} \sum_{i=1}^{4} p_i \sigma_i(n_z) \tag{98}$$

where $i = 1,...,4$ corresponds to the index of a lobe that constitutes the tail with a maximum of 4 lobes and p_i, $\mu_i(n_z)$ and $\sigma_i(n_z)$ are the power amplitude, mean, and standard deviation of the ith lobe deduced using a Gaussian fit. Note that $P(n_z)$ is calculated by conserving the area of the lobes that form the tail, knowing that the area of a Gaussian curve with amplitude p and standard deviation σ is $p\sigma\sqrt{2\pi}$.

The time averaged power spectrum is calculated by summing over a large number of random phases, assuming that the correlation time of the fluctuations is much shorter than the sampling time [121]. Such approach is consistent with the prescription discussed in Ref. [7] that fluctuations of the LH power spectrum must be much shorter than the fast electron slowing down time, in order to reproduce the experimental observations. The number of phases is chosen such that the statistical noise is almost negligible. It is shown that the phase (or time) averaged quantities $\overline{\mu}$, $\overline{\sigma}$, $\overline{P_{tail}/P_{tot}}$ and $\overline{P_{main}/P_{tot}}$ are independent of the number of phases when it exceeds 20, whatever the ratio $\tilde{k}_z/k_{\parallel 0}$, knowing that $\overline{\mu}$, $\overline{\sigma}$, $\overline{P_{tail}/P_{tot}}$ and $\overline{P_{main}/P_{tot}}$ are obtained by applying the two-Gaussian fit described above on the phase averaged power spectrum.

Fig. 51 illustrates the fitting procedure by showing the basic Gaussian curves that fit the main lobe and the tail lobes, in addition to tail equivalent Gaussian (dashed). Though such a description is simplified regarding the complexity of the tail in the power spectrum, it allows to characterize easily the fraction of power that is transfered from the main peak to the tail, the mean position of the tail and its width. This approach is particularly convenient for identifying general trends from parametric studies.

$\tilde{k}_z$	$0.1k_{z0}$	$0.34k_{z0}$	$0.95k_{z0}$
$\mu(n_z)$	2.3	2.8	3.8
$\sigma(n_z)$	0.33	0.73	0.64

Table 6: This table corresponds to the power spectra in Fig. 51. It shows the characteristics of the tail, $\mu(n_z)$ (mean) and $\sigma(n_z)$ (standard deviation), as the fluctuation parallel wave number $\tilde{k}_z$ varies.

An example is given for three wavevector values $\tilde{k}_z/k_{z0} = [0.1, 0.34, 0.95]$ in Fig. 51 where the main lobe corresponds to $\mu(n_{z0}) \cong 2$, and $\sigma(n_{z0}) = 0.21$. The other parameters in the calculations are $\tilde{x} = 0.375$, $\Delta\tilde{x} = 0.125$, $n_0 = 2.6n_c$, and $\sigma_n = 0.5$. For $\tilde{k}_z/k_{\parallel 0} = 0.1$, the fluctuations lead to an apparent broadening and a small shift of the main lobe; hence the main lobe and the tail overlap resulting in tail with a mean $\mu(n_z) = 2.3$ and standard deviation $\sigma(n_z) = 0.33$. Increasing $\tilde{k}_z$ to $\tilde{k}_z = 0.34k_{\parallel 0}$ leads to the appearance of four satellite lobes, one with $n_\parallel < n_{\parallel 0}$ and three with $n_\parallel > n_{\parallel 0}$. The equivalent lobe is then centered at $\mu(n_z) = 2.8$ with the corresponding standard deviation $\sigma(n_z) = 0.73$ as shown in Tab. 6. In this case, 50% of the power in the main lobe is transfered to the satellite lobes. Moreover, the satellite lobes have gradually decreasing power amplitude values in n_z showing a resonance condition in consistence with the model described in Fig. 32, [4]. By increasing $\tilde{k}_z$ to $\tilde{k}_z = 0.95k_{\parallel 0}$, the satellite lobes resulting from the fluctuations are shifted to higher $n_\parallel$ values, while their amplitudes are decreasing. Consequently, the fraction of the power transfered to the tail is lower. The case $\tilde{k}_z = 0.95k_{z0}$, results in a power spectrum in which the main lobe is back to be very similar to the quiescent plasma one and a tail with much less power, showing that the perturbation effect on the power spectrum is fading away. Remarkably, the tail center of gravity shift upwards with $\mu(n_z) = 3.8$, and due to having less number of lobes $\sigma(n_z)$ decreases to 0.64.

1. $\tilde{k}_z$ Scan

The spectral broadening of the LH wave by the fluctuations of the electron density strongly depends of the ratio $\tilde{k}_z/k_{\parallel 0}$ as shown in Sec. B.. Using the simplified two-Gaussian description for the power spectrum, and averaging over multiple phases, it is possible to identify the range of wavevectors for which density fluctuations lead to significant modifications of the excited LH power spectrum. The parameters of reference for all simulations are those used for the calculations presented in Sec. A. given by $\tilde{x} = 0.375$, $\Delta\tilde{x} = 0.125$, $\sigma_n = 0.5$, and $n_{e0} = 2.6n_c$. Since the simulations indicate a significant perturbation of the LH power spectrum for a Fourier component of the fluctuating density layer comparable to the LH wavelength, the $\tilde{k}_z$ scan is performed over the range $[0.1, 1]k_{z0}$ in which fluctuations can contribute to filling the spectral gap.

Based on the changes in $\mu(n_z)$, $\sigma(n_z)$, and power fraction of the main lobe and the tail shown in Fig. 60, a substantial understanding of the fluctuation parallel wavelength $\tilde{k}_z$
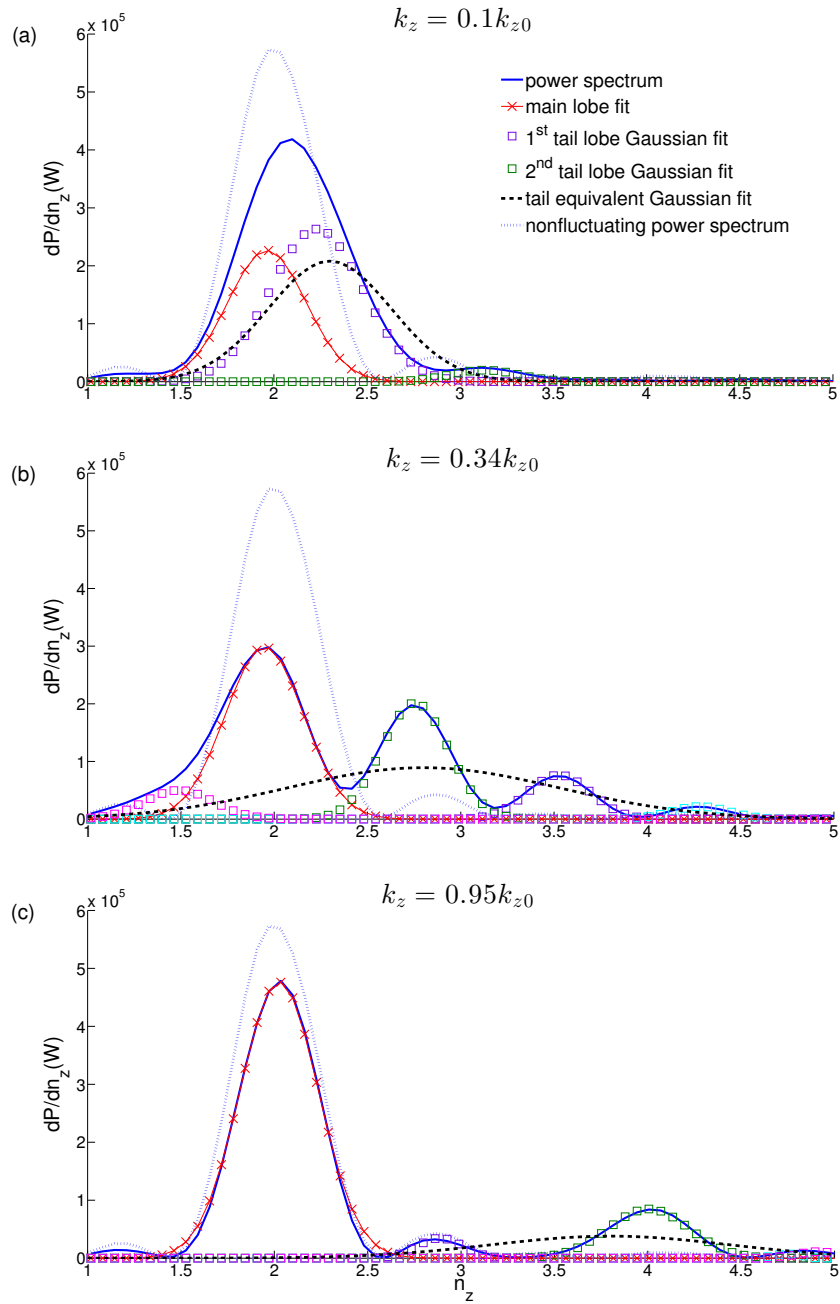
Figure 51: Power spectrum resulting from fluctuation layer given by: $\tilde{x} = 0.375$, $\Delta \tilde{x} = 0.125$, $n_{e0} = 2.6 n_c$, $\sigma_n = 0.5$. Fitting the power spectrum, main lobe and tail using Gaussian fit: power spectrum (solid), Gaussian fit of main lobe (x marker) and tail lobes (square markers). Dashed curve is the Gaussian equivalent of the tail lobes since its mean and standard deviation are calculated from the mean and standard deviation of the Gaussian lobes fitting the tail, while its amplitude is chosen so that the area of the tail is conserved. Dotted curve shows the nonfluctuating power spectrum as reference. Three $\tilde{k}_z$ values are taken: (a) $\tilde{k}_z = 0.1 k_{z0}$, (b) $\tilde{k}_z = 0.34 k_{z0}$, (c) $\tilde{k}_z = 0.95 k_{z0}$.

role in modifying the LH power spectrum is drawn. In particular, the different $\tilde{k}_z$ cases in Fig. 51 point out the main stages of the evolution of the power spectra as $\tilde{k}_z$ varies. First, the power spectrum at the separatrix that propagates through density fluctuations of large parallel wavelength of $\tilde{\lambda}_z = 40\,cm$ i.e $\tilde{k}_z = 0.1k_{z0}$, is widened at the level of the main lobe as shown in Fig. 51. This explains the large power fraction in the tail against low $\mu(n_z)$ and $\sigma(n_z)$ at $\tilde{k}_z = 0.1k_{z0}$ as given in Fig. 60. As $\tilde{k}_z/k_{\|0}$ is increased, the tail lobe becomes progressively resolved from the main lobe. The broadening and the spectral upshift of the tail lobe increase almost linearly with $\tilde{k}_z/k_{\|0}$ up to $\tilde{k}_z/k_{\|0} = 0.35$, but its fraction of power remains constant, at about 70%. For $\tilde{k}_z/k_{\|0} > 0.35$, the spectral upshift is still proportional to $\tilde{k}_z/k_{\|0}$, but the fraction of power carried by the tail lobe decreases linearly, while its width remains almost constant. Finally, when $\tilde{k}_z/k_{\|0} > 1$, the effect of density fluctuations fades out, and the power spectrum is identical to that obtained with a quiescent plasma.

The study clearly shows that density fluctuations in the toroidal direction over a rather wide range of $\tilde{k}_z/k_{z0}$ values $[0.1, 1]$ can contribute to fill the spectral gap by an upshift and a broadening of the tail lobe. In particular for $\tilde{k}_z \in [0.2, 0.5]k_{z0}$, i.e at fluctuation wavelengths in the range $[8 - 20]\,cm$, the tail is reasonably consistent with the tail model in Fig. 32 with $\mu(n_z) \in [2.3, 3.4]$ and $\sigma(n_z) \in [0.5, 0.74]$ and with large power transfer that exceeds 50% as required by calculations done in Ref. [7] in order to reproduce the experimental observations.

2. *Effect of increasing x̃ and Δx̃*

Monitoring the increase of $\tilde{x}$ and $\Delta\tilde{x}$ aims at looking for the impact of the positioning of the fluctuating layer at different distances from the antenna as well as increasing the fluctuation layer radial width, on modifying the LH power spectrum at the separatrix.

This study compares two plots that independently display the results for three $\Delta\tilde{x}$ values; each corresponding to a different position of the fluctuating layer with $\sigma_n = 0.5$ and $n_{e0} = 2.6n_c$.

Consistent results were obtained when applying $\tilde{k}_z$ scan for the two $\tilde{x}$ values $\tilde{x} \in \{0.375, 0.5\}$, as shown in Figs. 64(a) and 64(b) for $\tilde{x} = 0.375$ and $\tilde{x} = 0.5$ respectively. This observation shows that varying the position of the fluctuating layer doesn't affect the results in terms of the characteristics of the perturbed LH power spectrum at the separatrix.

Conversely, the radial width of the fluctuation layer contributes slightly to the variations of $\overline{\mu}$, $\overline{\sigma}$, $\overline{P_{tail}/P_{tot}}$ and $\overline{P_{main}/P_{tot}}$ as shown in Fig. 64, for both $\tilde{x}$ values. The power transferred to the tail is larger up to 20% in the interval $0.1k_{z0} < \tilde{k}_z < 0.5k_{z0}$ as $\Delta\tilde{x}$ is increased to double its value. On the contrary, in the interval $0.5k_{z0} < \tilde{k}_z < 1.0k_{z0}$, a
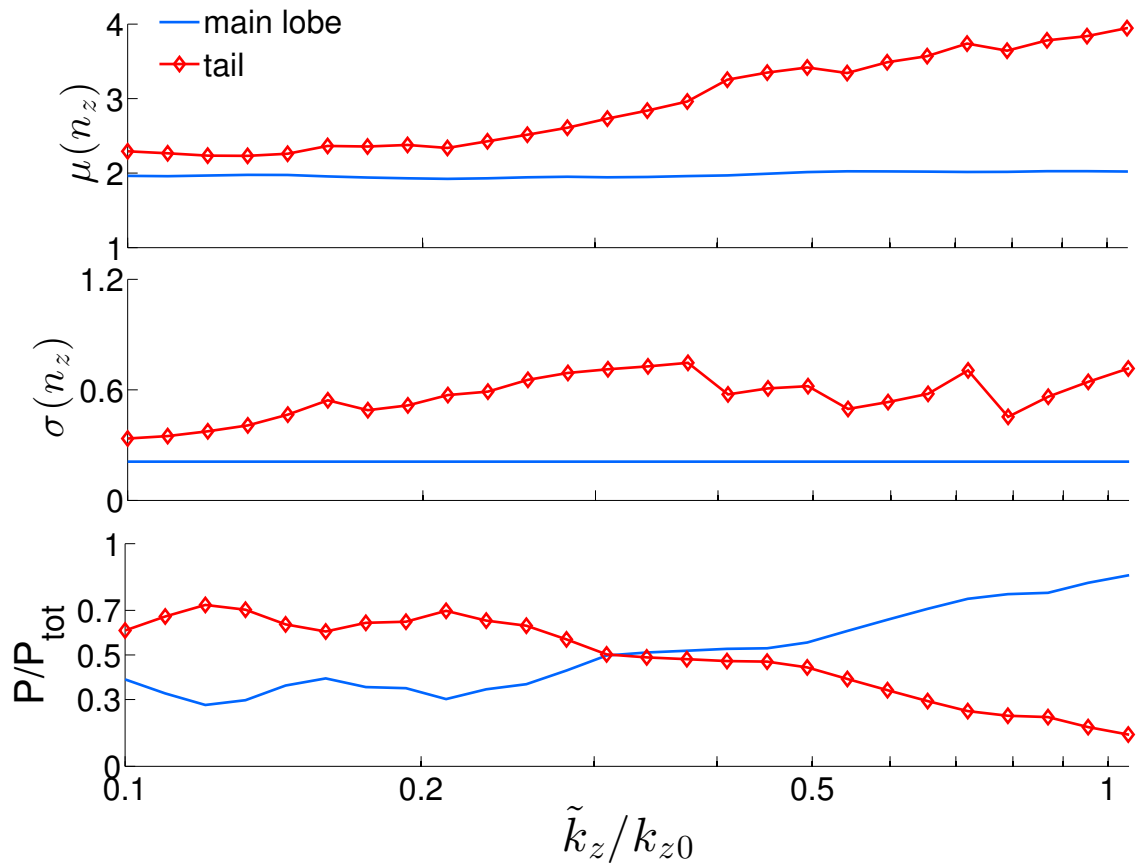
Figure 52: Phase averaged $\tilde{k}_z$ sweep used as a reference for upcoming parameter scans comparison. The fluctuation layer is characterized by: $\tilde{x} = 0.375$, $\Delta\tilde{x} = 0.125$, $n_{e0} = 2.6n_c$, $\sigma_n = 0.5$.

reverse effect is obtained; as $\tilde{k}_z$ increases a decreased power transfer to the tail is obtained at larger $\Delta\tilde{x}$. Hence enlarging the radial width of a fluctuating layer for $\tilde{\lambda}_z > \lambda_{LH}$, increases the power transfered to the tail.

3. Effect of the amplitude of density fluctuations $\sigma_\mathbf{n}$ and its relation to the fluctuation width

The effect of density fluctuations amplitude (σ_n) on the LH power spectrum is addressed independently and in relation to increasing the fluctuation radial width (Δx_{tot}). First, $\tilde{k}_z$ scans for density perturbations at different fluctuation amplitude values given by $\sigma_n \in \{0, 0.2, 0.35, 0.5\}$ for $\tilde{x} = 0.375$, $\Delta\tilde{x} = 0.125$, $n_{e0} = 2.6n_c$, show that decreasing the density fluctuation amplitude decreases the power transferred to the tail for $\tilde{k}_z$ values in the interval $\tilde{k}_z \in [0.1 - 1]k_{z0}$ as shown in Fig. 67(a). The observation of $\mu(n_z)$ and $\sigma(n_z)$ evolution for the different σ_n cases, points out that as σ_n decreases, the tail form develops at higher values of $\tilde{k}_z$, and is maintained over a smaller $\tilde{k}_z$ interval, given by $\tilde{k}_z \in [0.3 - 0.5]k_{z0}$ for the case $\sigma_n = 0.35$ and $\tilde{k}_z \in [0.33 - 0.45]k_{z0}$ for the case $\sigma_n = 0.2$ compared to larger interval $\tilde{k}_z \in [0.2 - 1]k_{z0}$ for the case $\sigma_n = 0.5$.

Though high density fluctuation amplitude of more than 50% is observed in the SOL in most tokamaks, [123], the following study aims at looking for other parameters effect in presence of low density fluctuation amplitude, in particular the radial width of the fluctuating layer. The fluctuating layer radial dependence is assumed as a box car function with total width Δx_{tot} in place of Gaussian radial dependence, to increase the impact of the perturbations. Fig. 67(b) shows a $\tilde{k}_z$ scan comparison for $\Delta x_{tot} \in \{0.413, 0.625, 0.8\}$ with 20% fluctuations amplitude. In addition, Fig. 67(b) includes $\tilde{k}_z$ scans with Gaussian radial dependence given by $\Delta\tilde{x} = 0.125$ for 50% and 20% fluctuation amplitude cases with $\tilde{x} = 0.375$, where n_{e0} is fixed, $n_{e0} = 2.6n_c$ for all cases, to clarify the difference between low fluctuation amplitude cases with increasing radial width Δx_{tot}, and previous scans with Gaussian radial dependence $\Delta\tilde{x}$.

The 20% fluctuation amplitude case for $\Delta\tilde{x} = 0.125$ shows a slightly varying mean and very low power in the tail; however, for increasing Δx_{tot} the tail power also increases such that it is possible to recover the effects obtained with $\sigma_n = 0.5$ and $\Delta\tilde{x} = 0.125$ as shown in Fig. 67(b). This is due to main lobe widening that occurs for all values of $\tilde{k}_z$, demonstrated by the low values of the mean $\mu(n_z)$. For $\Delta x_{tot} = 0.79$, the tail separates from the main lobe at $\tilde{k}_z > 0.2k_{z0}$, attaining a maximum in mean at $\tilde{k}_z = 0.34k_{z0}$.

As a conclusion, increasing the fluctuation width with a box car radial dependence increases the power in the tail up to 80% at low $\tilde{k}_z$ values. This entails a strong widening effect on the main lobe, and complies with the tail model over determined interval of $\tilde{k}_z$ over $[0.25 - 0.4]k_{z0}$ with a 40% of the total power for large enough radial width.
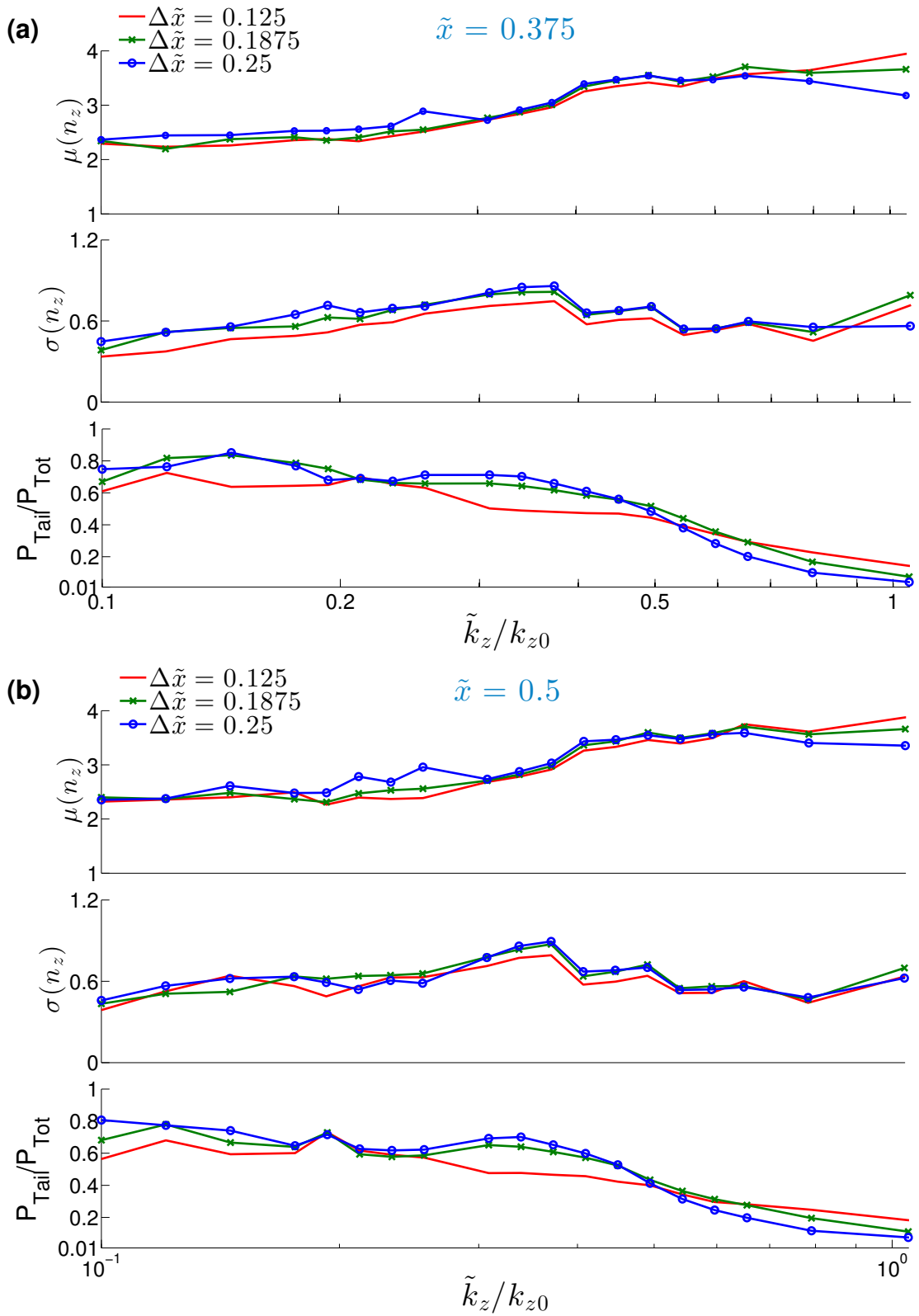
Figure 53: Phase averaged $\tilde{k}_z$ sweep for evaluating the effect of increasing the fluctuation layer radial width $\Delta\tilde{x} = [0.125, 0.1875, 025]$ for two $\tilde{x}$ cases : (a) $\tilde{x} = 0.375$, (b) $\tilde{x} = 5$ where $n_{e0} = 2.6 n_c$ and $\sigma_n = 0.5$.
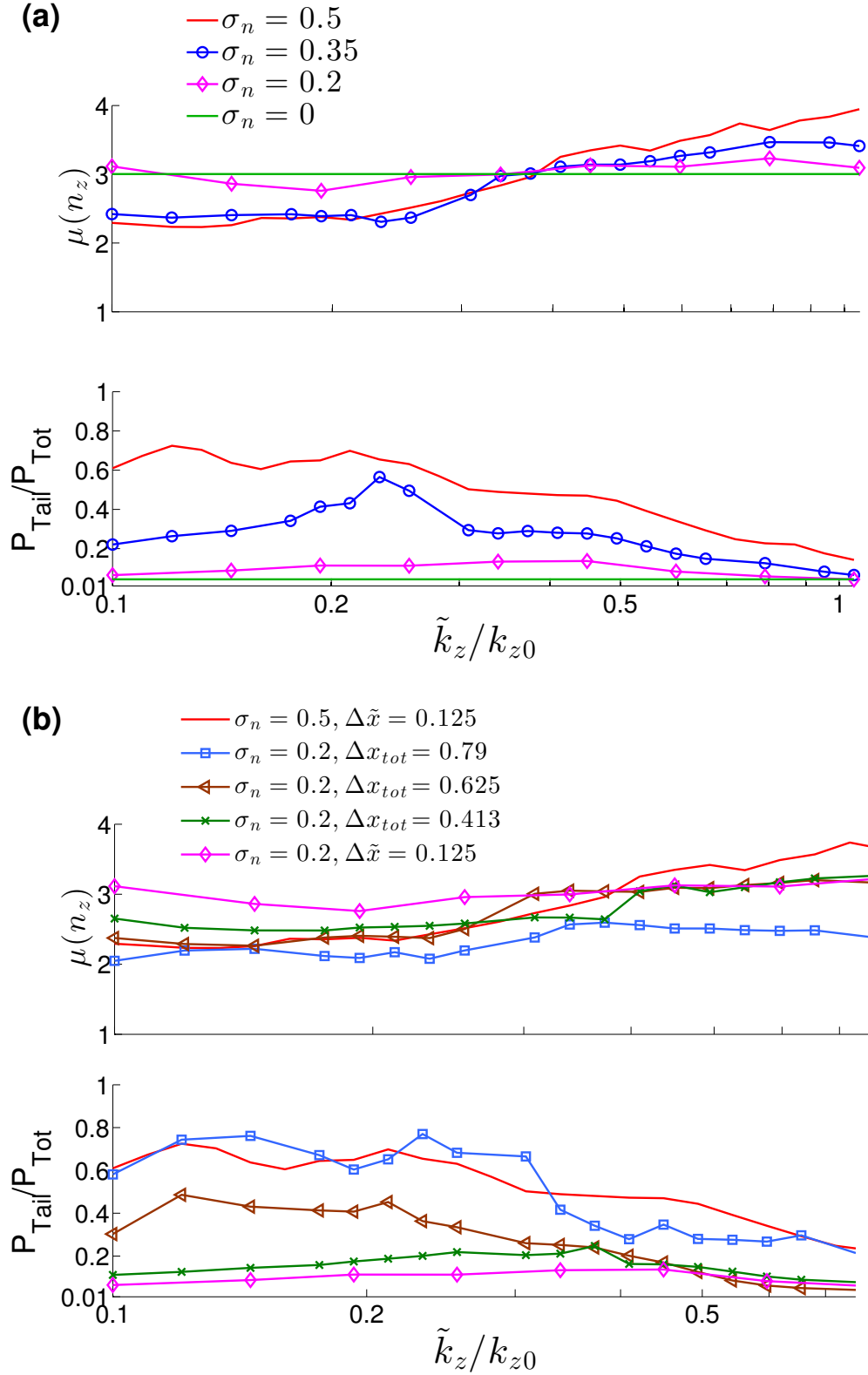
Figure 54: (*a*) Phase averaged $\tilde{k}_z$ sweep for evaluating the effect of changing the fluctuation density amplitude where $\tilde{x} = 0.375$, $\Delta \tilde{x} = 0.125$, $n_{e0} = 2.6 n_c$, $\sigma_n = [0, 0.2, 0.35, 0.5]$. (*b*) Radial box dependence of the density fluctuation layer with total radial width $\Delta x_{tot} = [0.413, 0.625, 0.79]$, $n_{e0} = 2.6 n_c$, $\sigma_n = 0.2$, compared to Gaussian radial dependence with $\tilde{x} = 0.375$, $\Delta \tilde{x} = 0.125$, $n_{e0} = 2.6 n_c$, $\sigma_n = [0.2, 0.5]$ shows that at low density fluctuation amplitude of 20%, high fraction of the power is transferred to the tail when the radial width of the fluctuation is increased and is assumed to be a box car function.
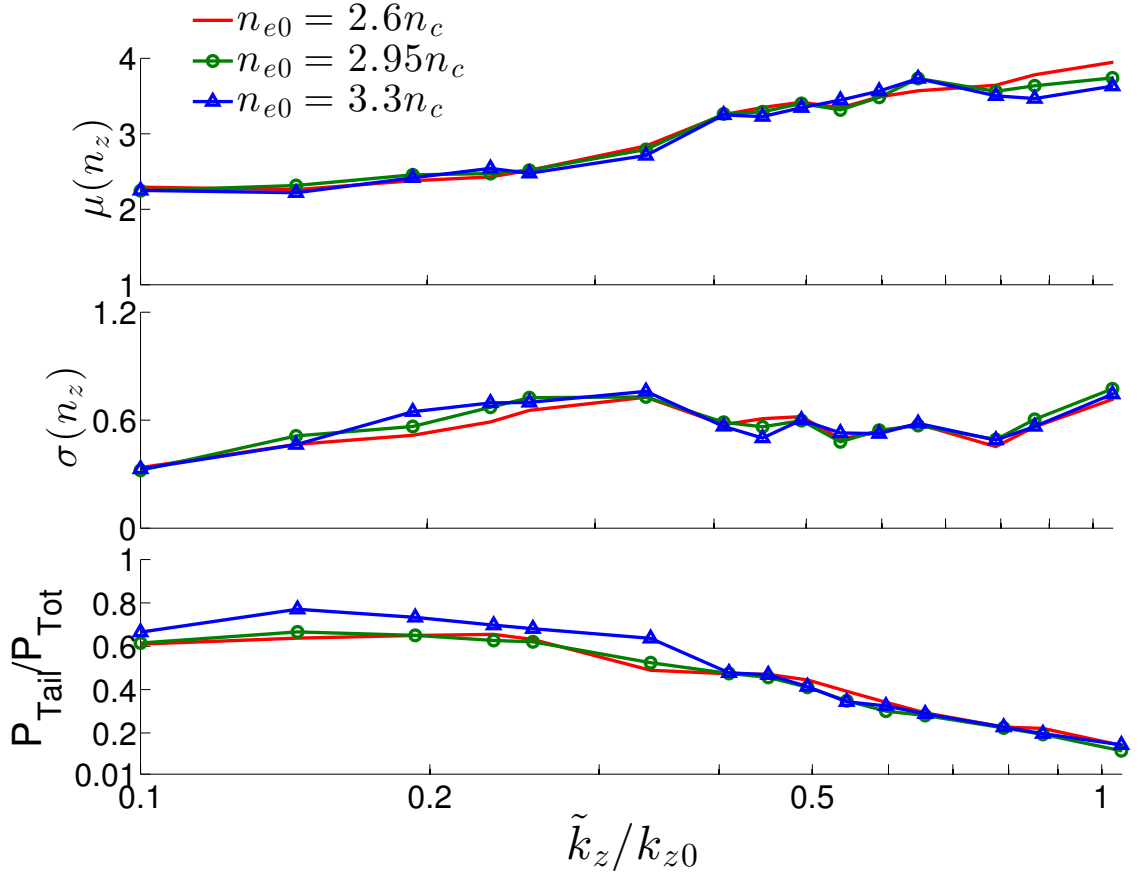
Figure 55: Phase averaged $\tilde{k}_z$ sweep for evaluating the effect of changing the reference density n_{e0}, where $\tilde{x} = 0.375$, $\Delta\tilde{x} = 0.125$, $n_{e0} = [2.6, 2.95, 3.3]n_c$, $\sigma_n = 0.5$.

4. Reference density n_{e0} and phase average comparison

The reference density n_{e0} is also varied up to 30%, $n_{e0} \in \{2.6, 2.95, 3.3\}n_c$, as given by Fig. 55 where $\tilde{x} = 0.375$, $\Delta\tilde{x} = 0.125$, $\sigma_n = 0.5$. The $\tilde{k}_z$ scan comparison for the three density cases for the tail power, $\mu(n_z)$ and $\sigma(n_z)$ are negligible. Therefore, changing the value of the reference density n_{e0} has no effect on the fluctuation results as long as the density in the SOL is not close to the cut-off density value.

In order to figure out the effect of averaging over a different number of phases (initially 20 phases were taken), a $\tilde{k}_z$ scan is repeated for the fluctuation parameters $\tilde{x} = 0.375$, $\Delta\tilde{x} = 0.125$, $n_{e0} = 2.6n_c$, $\sigma_n = 0.5$ while averaging over independent sets of phases of different numbers. Simulations are done for 10, 15 and 25 phases chosen randomly and uniformly distributed over $[0.2\pi[$. The phase averaged power spectra for each case are compared to the basic scan shown in Fig. 60.

Fig. 56 shows minimal differences in power transferred to the tail for the different phase average cases, in particular for a smaller perturbation wavelength that corresponds to $\tilde{k}_z > 0.14k_{z0}$, where the maximum power difference is 8%. Conversely, due to having a
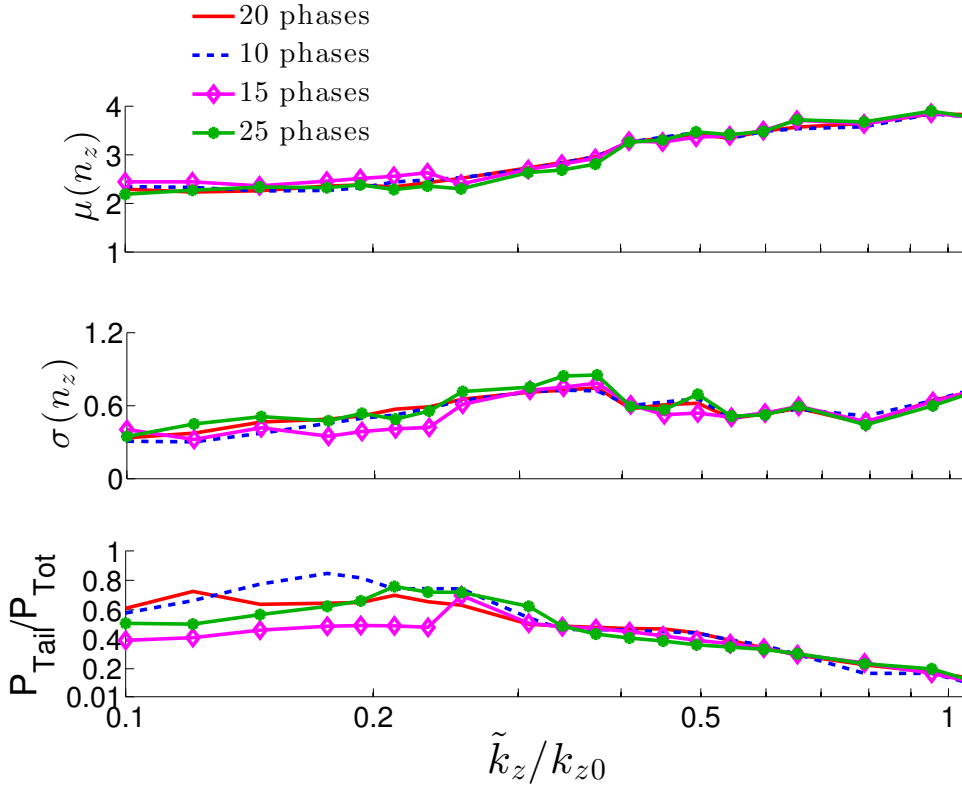
Figure 56: Phase average Comparison for different number of phases where $\tilde{x} = 0.375$, $\Delta\tilde{x} = 0.125$, $n_{e0} = 2.6n$, $\sigma_n = 0.5$.

larger perturbation parallel wavelength at lower values of $\tilde{k}_z$, the difference in the power fraction transferred to the tail attains a maximum of 20% between the 25 phases average and the 20 phases average over the interval $\tilde{k}_z < 0.14k_{z0}$. The tail mean and standard deviation are consistent for all phase averaging cases showing that the tail evolves in a similar manner under the effect of changing $\tilde{k}_z$. In conclusion, 20 phases average is a good estimate of the pdf of perturbed LH power spectrum at the separatrix.

C. Full density model: $\tilde{k}_x$ dependence for a combination of $\tilde{k}_z$ modes

A 30% density fluctuation is introduced over the SOL by including multiple fluctuation layers at many radial positions and dividing the fluctuation energy over many $\tilde{k}_z$ values chosen in the vicinity of the LH wavelength. The density distribution for two sets of $\tilde{k}_z$ values is considered, one given by $\tilde{k}_z \in [0.3 - 0.5]k_{z0}$ and the other by $[0.1 - 0.7]k_z0$, while the phases are chosen randomly and independently for each wavenumber and each layer. $\tilde{n}_e$ takes the form

$$\tilde{n}_e = \sum_{l=1}^{L} \sum_{n=1}^{N} \frac{1}{\sqrt{N}} \sigma_n n_{e0} \sin(\tilde{k}_{z,n} z + \tilde{\phi}_{l,n}) \exp(-\frac{x - \tilde{x}_l}{\Delta \tilde{x}}) \tag{99}$$

where L is the number of layers and N is the number of $\tilde{k}_z$ modes. In the calculation, $\Delta \tilde{x}$ is uniform over all layers and $|\tilde{x}_l - \tilde{x}_{l+1}|$ is constant. Based on the radial positions and $\Delta \tilde{x}$, the radial Fourier component of the fluctuation $\tilde{k}_x$ is calculated. Fig. 57(a) shows the density distribution over the SOL upon introducing 7 fluctuation layers having same fluctuation radial width ($\Delta \tilde{x} = 0.053$) and uniformly separated along the radial direction, while the Fourier modes $[0.1 - 0.7]k_{z0}$ are superposed along each layer.

For a total fluctuation radial width of 0.75 (normalized to the SOL depth), $\sigma_n = 0.3$ and $n_{e0} = 2.6 n_c$, the power spectrum at the separatrix averaged over 20 phasing cases for $\tilde{k}_x \in [1 - 11.1]$ ($\tilde{k}_x$ is scaled to κ_0, the LH wavenumber), and $\tilde{k}_z \in [0.3 - 0.5]k_{z0}$ or $\tilde{k}_z \in [0.1 - 0.7]kz0$ with equal fluctuation energy over all modes, has one peak at n_{z0} and a tail occupying up to 25% of the total power as shown in Fig. 57(b). Conversely, the tail mean and power vary largely in time as shown in Fig. 57(c), which indicates that even when the density fluctuation amplitude is lower, a combination of modes in the vicinity of the LH wavelength extending over the SOL have a large instantaneous effect on the power spectrum for which the tail mean and power could oscillate between large values.

1. Example of long fluctuation wavelength effect as fluctuation radial width increases

Turbulence observations in the plasma edge suggest long wavelength fluctuations along the parallel to magnetic field lines direction, [123], while parallel fluctuations in the SOL in front the LH antenna require more experimental effort. Hence, the following example aims at showing that even at large fluctuation parallel wavelength of $1.0 m$, the power spectrum undergoes a significant widening if the radial width $\Delta \tilde{x}$ is increased. Fig. 58 displays the power spectra evolution for three $\Delta \tilde{x}$ values 0.31, 0.38, and 0.44 for which the main lobe spectral width increases as $\Delta \tilde{x}$ increases. The power spectra fit shows both the red and yellow Gaussian lobes that fit the main lobe and they correspond to the original lobe at fixed standard deviation, and the tail respectively. As a result, the power spectrum main lobe spreads over a large interval given by $n_z \in [1.3 - 3]$ for $\Delta \tilde{x} = 0.31, 0.38, 0.44$.
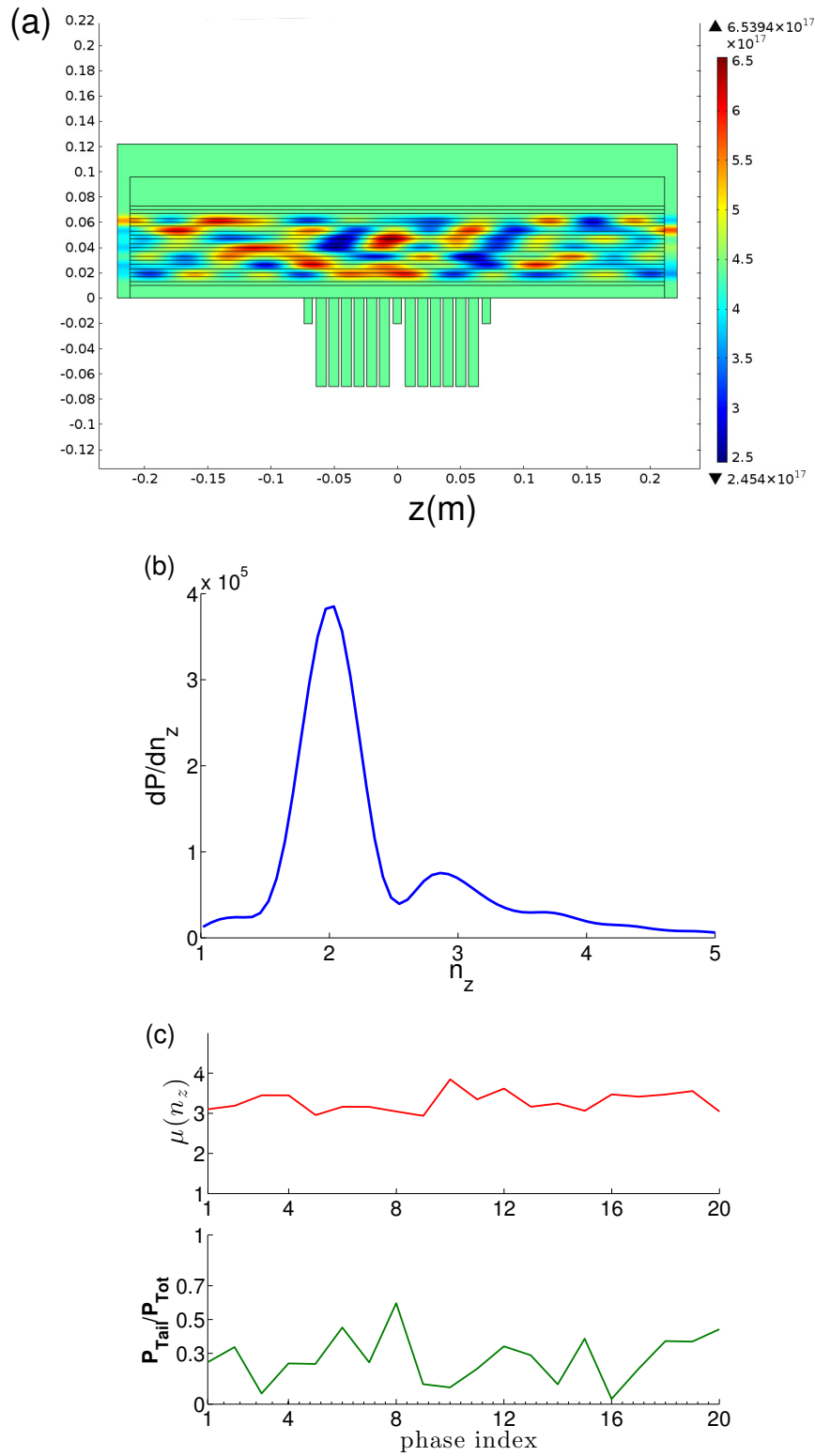
Figure 57: 7 radial fluctuation layers with total density fluctuation energy of 30% distributed equally over $\tilde{k}_z$ values: $\tilde{k}_z = [0.1, 0.2, ..., 0.7]k_{z0}$ for $n_{e0} = 2.6n_c$. (a) Density plot (unit is m^{-3}) for a random phasing case with $\tilde{k}_x(k_0) = 11.1$ where $\tilde{k}_x$ is the radial fluctuation wave number calculated from the width of the fluctuation layers and the distance between two consecutive layers. (b) Phase averaged power spectrum at the separatrix for $\tilde{k}_x(k_0) = 7.2$. (c) Phase dependent power and mean of the tail for 20 randomly chosen phasing cases where $\tilde{k}_x(k_0) = 7.2$.
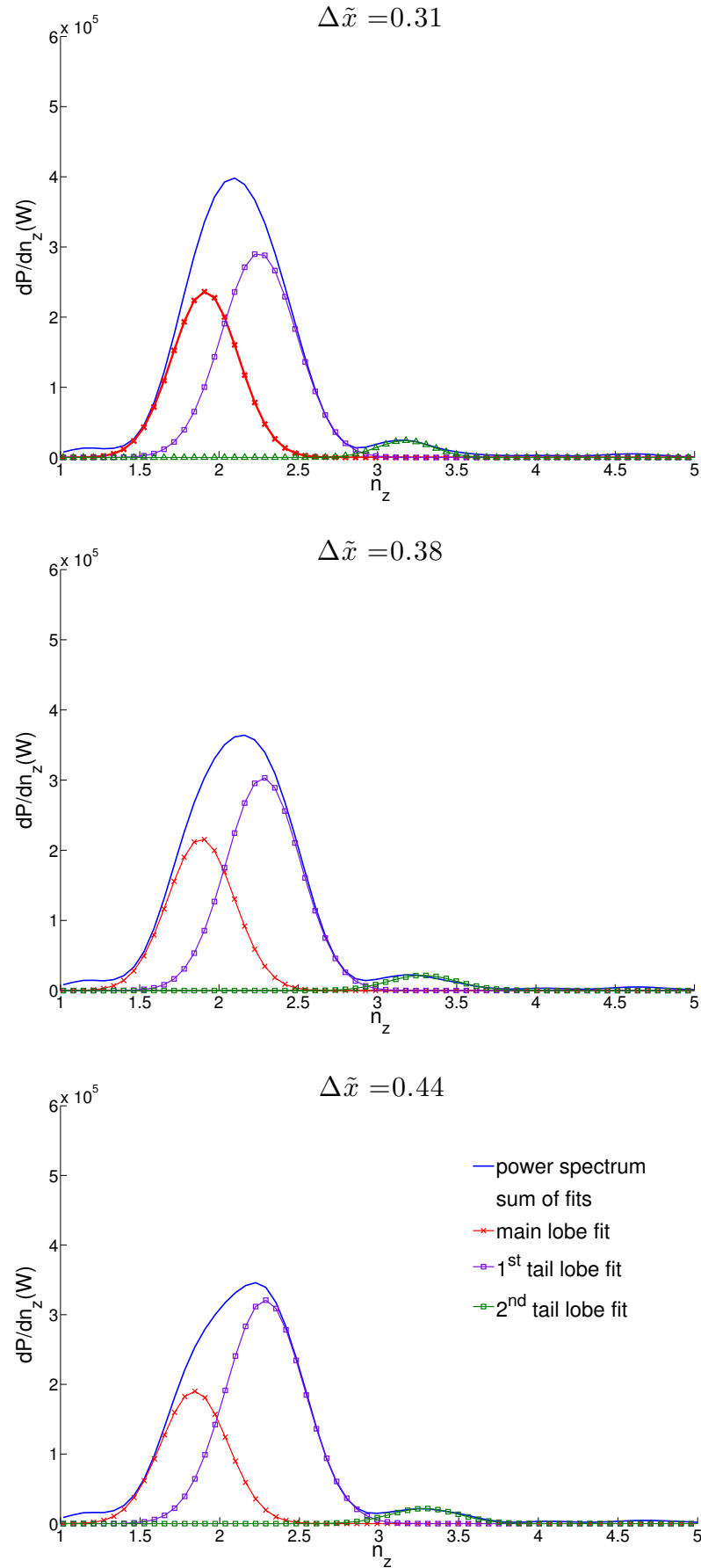
Figure 58: Power spectrum resulting from a fluctuation layer with a large parallel wavelength: $\tilde{\lambda}_z = 12.5 \times \lambda_{LH}$, where $\Delta\tilde{x} = 0.31, 0.38, 0.44$.

CHAPTER VIII

CONCLUSION

A 2-D slab model of the SOL and a FAM like antenna with two modules is simulated in COMSOL Multiphysics® to solve the full plasma wave equation in presence of a thin perturbed electron density layer. Since meshing imposes a challenge due to the very short LH wavelength at higher densities, a constant background density is assumed. When the range of the Fourier component of the density fluctuations parallel to the magnetic field is of the same order of the LH parallel wavelength, the power spectrum is strongly modified by diffraction. As a result, the LH power spectrum at the separatrix exhibits satellite peaks carrying a significant amount of power, as inferred from ray tracing and Fokker-Planck calculations [7]. Other fluctuation parameters are studied, showing that the radial width of the perturbed layer and the relative amplitude of the electron density fluctuations are the main parameters that contribute to broadening the LH power spectrum and increasing the power in the spectral tail. On the other hand, it is found that the average density, radial position of the fluctuating layer, LH input power (see Appendix F), and averaging over larger number of phases have a minimal effect.

While other mechanisms suggested to bridge the LH large spectral gap in weak damping regimes do not fully explain the necessary $n_\parallel$ upshift [78], ray tracing and Fokker-Planck calculations have shown that a fluctuating tail model of the LH power spectrum at the separatrix successfully reproduces experimental observations in TS large spectral gap regimes [7, 18]. Despite its simplicity, the model developed in the present work is able to yield the characteristics of the initial power spectrum at the separatrix required by ray-tracing and Fokker-Planck calculations for reproducing experimental results. This suggests that density variation parallel to the magnetic field in a thin layer in front the LH antenna can break the usual picture given by standard antenna spectrum calculations. A short review of existing experimental data concerning the time-space characteristics of the density in front of the LH antenna may support this analysis. Based on the results presented here, further theoretical studies and experimental measurements are necessary to provide the physical mechanisms at play in the vicinity of the waveguides, and quantify their contribution. In summary, the present study suggests that diffraction by local electron density fluctuations in the SOL in front the LH antenna could modify the LH power spectrum in accordance with Ref. [7], and thus exhibit a plausible mechanism to bridge the large spectral gap at the plasma edge.

APPENDIX A

MODES INSIDE A WAVEGUIDE

Consider a rectangular waveguide that has dimensions $y = a$ and $z = b$. Assume time harmonic fields with $e^{i\omega t}$ time dependence, propagating in the $\hat{\mathbf{x}}$ direction. The electric and magnetic fields have the form,

$$E(x,y,z) = [e(y,z) + \hat{\mathbf{z}}e_x(y,z)]e^{-ik_x x}$$

$$H(x,y,z) = [h(y,z) + \hat{\mathbf{z}}h_x(y,z)]e^{-ik_x x}$$

where $e(y,z)$ and $h(y,z)$ are functions to be determined and k_x is the x component of the wave vector .

Fourier transform in time of Maxwell's equations for source free wave guides gives

$$\nabla \times \mathbf{E} = -i\omega\mu\mathbf{H} \qquad (100)$$

$$\nabla \times \mathbf{H} = i\omega\varepsilon\mathbf{E} \qquad (101)$$

The field components could be written in terms of E_x and H_x and their derivatives [136]. Consequently, solving for the TEM which is characterized by zero electric and magnetic fields in the wave direction of propagation which is the $0x$ axis, renders all other field components zero. Therefore the TEM mode does not propagate inside a rectangular waveguide. Only TE_{mn} and TM_{mn} modes propagate inside rectangular wave guides in which E_x and H_x are respectively zero. Therefore one field should be solved in each case by applying Helmholtz[1] equations and boundary conditions[2].

---

[1]Helmholtz equations are second order differential equations in E or H given by:
$\nabla^2 H + k^2 H = 0,$
$\nabla^2 E + k^2 E = 0.$
These equations result from using both Faraday's and Ampere's laws.
$\nabla \times \nabla \times \mathbf{H} = \nabla \times (i\omega\varepsilon\mathbf{E}) = \mathbf{i}\omega\varepsilon(-\mathbf{i}\omega\mu\mathbf{H}) = (\omega^2/\mathbf{c}^2)\mathbf{H} = k^2\mathbf{H}.$
with $k = \omega\sqrt{\mu_0\varepsilon_0}$ where μ_0 and ε_0 are the vacuum permeability and permittivity respectively.
Also note that $\nabla \times \nabla \times \mathbf{H} = \nabla(\nabla.\mathbf{H}) - \nabla^2\mathbf{H} = \nabla((1/\mu)\nabla.\mathbf{B}) - \nabla^2\mathbf{H} = -\nabla^2\mathbf{H} = -\hat{\mathbf{x}}\nabla^2 H_x - \hat{\mathbf{y}}\nabla^2 H_y - \hat{\mathbf{z}}\nabla^2 H_z.$
Thus for $i = x, y, z$
$$(\frac{\partial}{\partial x^2} + \frac{\partial}{\partial y^2} + \frac{\partial}{\partial z^2} + k^2)H_i = 0.$$

[2]For perfect conductor materials, the boundary conditions resulting from having zero fields inside the

For the TE_{mn} mode, $E_x = 0$ since its electric field is transverse to the direction of propagation. Thus Helmholtz wave equation for H_x is given by

$$(\frac{\partial}{\partial x^2} + \frac{\partial}{\partial y^2} + \frac{\partial}{\partial z^2} + k^2)H_x = 0 \qquad (102)$$

which becomes when substituting $\partial/\partial x^2$ by $-k_x^2$,

$$(\frac{\partial}{\partial y^2} + \frac{\partial}{\partial z^2} + k_c^2)H_x = 0 \qquad (103)$$

where $(k_c)_{mn}$ is called the cut-off wave number. $k_c^2 = k^2 - k_x^2 = k_y^2 + k_z^2$ with k_y, k_z unknowns to be solved. Similarly, for the TM_{mn} mode since $H_x = 0$ (TM_{mn} modes are characterized by a magnetic field transverse to the direction of propagation), the Helmholtz wave equation for E_x is solved,

$$(\frac{\partial}{\partial x^2} + \frac{\partial}{\partial y^2} + \frac{\partial}{\partial z^2} + k^2)E_x = 0 \qquad (104)$$

which becomes when substituting $\partial/\partial x^2$ by $-k_x^2$,

$$(\frac{\partial}{\partial y^2} + \frac{\partial}{\partial z^2} + k_c^2)E_x = 0. \qquad (105)$$

A. Rectangular Waveguides Modes

Applying boundary conditions given by zero tangential electric field $E_t = 0$ at the walls of the waveguide. For the TE_{mn} modes, Eq. (103) is solved by method of separation of variables [137] which gives $k_y = m\pi/a$ and $k_z = n\pi/b$, $m, n = 0, 1, 2, \ldots$

$$E_y(y,z) = i\frac{n\pi}{b} \frac{\omega\mu_0}{(\frac{m\pi}{a})^2 + (\frac{n\pi}{b})^2}A_{mn}cos(\frac{m\pi}{a}y)sin(\frac{n\pi}{b}z)e^{i(\omega t - k_x x)} V.m^{-1} \qquad (106)$$

$$E_z(y,z) = -\frac{m\pi}{a} \frac{i\omega\mu_0}{(\frac{m\pi}{a})^2 + (\frac{n\pi}{b})^2}A_{mn}sin(\frac{m\pi}{a}y)cos(\frac{n\pi}{b}z)e^{i(\omega t - k_x x)} V.m^{-1} \qquad (107)$$

$$E_x = 0, \qquad (108)$$

material are: $\hat{n}.\vec{D} = \rho_s, \quad \hat{n}.\vec{B} = 0, \hat{n} \times \vec{E} = 0, \quad \hat{n} \times \vec{H} = \vec{J_s}$, where ρ_s and J_s are the surface charge and current density distributions respectively.

and

$$H_x(y,z) = A_{mn}cos(\frac{m\pi}{a}y)cos(\frac{n\pi}{b}z)e^{i(\omega t - k_x x)} A.m^{-1} \tag{109}$$

$$H_y(y,z) = \frac{m\pi}{a}\frac{ik_x}{(\frac{m\pi}{a})^2 + (\frac{n\pi}{b})^2}A_{mn}sin(\frac{m\pi}{a}y)cos(\frac{n\pi}{b}z)e^{i(\omega t - k_x x)} A.m^{-1} \tag{110}$$

$$H_z(y,z) = \frac{n\pi}{b}\frac{ik_x}{(\frac{m\pi}{a})^2 + (\frac{n\pi}{b})^2}A_{mn}cos(\frac{m\pi}{a}y)sin(\frac{n\pi}{b}z)e^{i(\omega t - k_x x)} A.m^{-1} \tag{111}$$

where A_{mn} has the same unit as the magnetic field intensity ($A.m^{-1}$), μ_0 is the vacuum permeability ($H.m^{-1}\,or\,V.s.A^{-1}.m^{-1}$) and

$$(\frac{m\pi}{a})^2 + (\frac{n\pi}{b})^2 + k_x^2 = k^2. \tag{112}$$

Similarly, the TM_{mn} mode field equations are obtained by solving Eq. (105),

$$E_y(y,z) = -\frac{m\pi}{a}\frac{ik_x}{(\frac{m\pi}{a})^2 + (\frac{n\pi}{b})^2}B_{mn}cos(\frac{m\pi}{a}y)sin(\frac{n\pi}{b}z)e^{i(\omega t - k_x x)} V.m^{-1} \tag{113}$$

$$E_z(y,z) = -\frac{n\pi}{b}\frac{ik_x}{(\frac{m\pi}{a})^2 + (\frac{n\pi}{b})^2}B_{mn}sin(\frac{m\pi}{a}y)cos(\frac{n\pi}{b}z)e^{i(\omega t - k_x x)} V.m^{-1} \tag{114}$$

$$E_x(y,z) = B_{mn}sin(\frac{m\pi}{a}y)sin(\frac{n\pi}{b}z)e^{i(\omega t - k_x x)} V.m^{-1}, \tag{115}$$

and

$$H_y(y,z) = \frac{n\pi}{b}\frac{i\omega\varepsilon_0}{(\frac{m\pi}{a})^2 + (\frac{n\pi}{b})^2}B_{mn}sin(\frac{m\pi}{a}y)cos(\frac{n\pi}{b}z)e^{i(\omega t - k_x x)} A.m^{-1} \tag{116}$$

$$H_z(y,z) = -\frac{m\pi}{a}\frac{i\omega\varepsilon_0}{(\frac{m\pi}{a})^2 + (\frac{n\pi}{b})^2}B_{mn}cos(\frac{m\pi}{a}y)sin(\frac{n\pi}{b}z)e^{i(\omega t - k_x x)} A.m^{-1} \tag{117}$$

$$H_x = 0 \tag{118}$$

where B_{mn} has the same unit as the electric field intensity $V.m^{-1}$, ε_0 is the vacuum permittivity ($F.m^{-1}$ or $A.s.V^{-1}.m^{-1}$). Now

$$k_x = \begin{cases} \beta = \sqrt{k^2 - [(\frac{m\pi}{a})^2 + (\frac{n\pi}{b})^2]} \; if \, k^2 > (\frac{m\pi}{a})^2 + (\frac{n\pi}{b})^2 \\ -i\alpha = -i\sqrt{(\frac{m\pi}{a})^2 + (\frac{n\pi}{b})^2 - k^2} \; if \, k^2 < (\frac{m\pi}{a})^2 + (\frac{n\pi}{b})^2 \end{cases} \tag{119}$$

where $k = \omega/c$ is real since vacuum is a loss free dielectric medium, β is the phase constant which defines the guide wavelength by $\beta 2\pi = \lambda_g$ and α is the attenuation constant. Thus a mode propagates ($k_x = \beta$) if

$$k^2 > (\frac{m\pi}{a})^2 + (\frac{n\pi}{b})^2,$$

which gives

$$\frac{\omega^2}{c^2} > (\frac{m\pi}{a})^2 + (\frac{n\pi}{b})^2,$$

equating both sides gives the cut-off frequency of both TE_{mn} and TM_{mn} modes is obtained

$$f_{cmn} = c\sqrt{(\frac{m}{2a})^2 + (\frac{n}{2b})^2}, \tag{120}$$

with the lowest cut-off frequency determining the dominant propagating mode.

Consequently, a launched wave propagates in a specific mode if it's frequency is above the cut-off frequency of that mode.

B. Parallel Plates Waveguide Modes

The modes that propagate in a parallel plate waveguide shall be studied. A parallel plate waveguide models an antenna that is infinite in the $\hat{\mathbf{y}}$ direction.

The fields for the TEM mode ($E_x = H_x = 0$), where the wave propagates in the $\hat{\mathbf{x}}$ direction as in the left sketch in Fig. 59 are obtained by solving Laplace's equation: $\nabla^2 \phi(y,z) = 0$ to find the electrostatic potential between the two plates $\phi = V_0 z/b$ where the potential is assumed zero on one plate takes the value V_0 on the other one. E_z is then deduced $E_z = -\nabla \phi = -V_0/b$. So the total electric field is

$$E_z = -\left(\frac{V_0}{b}\right)e^{i(\omega t - \beta x)} \tag{121}$$

where

$$H_y = \frac{Y_0}{b}\hat{\mathbf{x}} \times E_z\hat{\mathbf{z}} = \frac{V_0\sqrt{\varepsilon_0}}{b\sqrt{\mu_0}}e^{i(\omega t - \beta x)} \tag{122}$$

where $\beta = k$, and

$$E_x = E_y = H_x = H_z = 0. \tag{123}$$

The TE_n mode field equations are obtained by solving the Helmholtz equation for H_x where $E_x = 0$ and $\partial/\partial y = 0$ (Fig. 59),

$$E_z = E_x = H_y = 0 \tag{124}$$

$$H_x = A_n cos\left(\frac{n\pi z}{a}\right)e^{i(\omega t - \beta x)} \tag{125}$$

$$E_y = \frac{i\omega\mu_0 b}{n\pi}A_n sin\left(\frac{n\pi z}{b}\right)e^{i(\omega t - \beta x)} \tag{126}$$

$$H_z = \frac{i\beta b}{n\pi}A_n sin\left(\frac{n\pi z}{b}\right)e^{i(\omega t - \beta x)} \tag{127}$$

where $\beta = \sqrt{k^2 - \left(\frac{n\pi}{b}\right)^2}$ is real (i.e the TE_n mode propagates) if $n\pi/b$. Thus the cut-off frequency is concluded by

$$\frac{\omega}{c} > \frac{n\pi}{b}$$

hence

$$f_{c,n} = \frac{n \times c}{2b}.$$

Also Refering to the model of parallel waveguide given by Fig. 59, the TM_n mode field equations for a wave propagating in the $\hat{\mathbf{x}}$ direction are obtained. For $H_x = 0$, Helmholtz equation is solved for E_x, where the other field components are obtained using Maxwell's equations,

$$E_y = H_z = H_x = 0 \tag{128}$$

$$E_x = B_n sin\left(\frac{n\pi z}{b}\right)e^{i(\omega t - \beta x)} \tag{129}$$
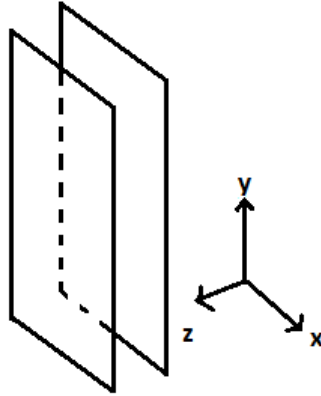
Figure 59: parallel plate waveguide

$$E_z = -i\frac{\beta b}{n\pi}B_n cos(\frac{n\pi z}{b})e^{i(\omega t - \beta x)} \tag{130}$$

$$H_y = \frac{i\omega\varepsilon_0 b}{n\pi}B_n cos(\frac{n\pi z}{b})e^{i(\omega t - \beta x)}. \tag{131}$$

APPENDIX B

ELECTROMAGNETIC DISPERSION RELATION IN COLD PLASMA

The electromagnetic dispersion relation is analyzed and the characteristics of the lower hybrid wave propagation inside plasma are studied. Assume that the density has a gradient in the $\hat{\mathbf{x}}$ direction such that $|k| \gg |\frac{\nabla n}{n}|$, and that k has projections in the $\perp$ and $\parallel$ directions only.

First start with Maxwell's equations for the electric and magnetic fields,

$$\nabla \times \mathbf{E} = -\partial_t \mathbf{B} \tag{132}$$

$$\nabla \times \mathbf{B} = \mu_0 \mathbf{J} + \frac{1}{c^2} \partial_t \mathbf{E} \tag{133}$$

Consider variations in the form,

$$\mathbf{E}(\mathbf{x},t) = \widetilde{\mathbf{E}}(\mathbf{x},t) e^{i(\mathbf{k}\cdot\mathbf{r} - \omega t)}, \tag{134}$$

where, the envelope $\widetilde{\mathbf{E}}(\mathbf{x},t)$ is slowly varying in time and space. Using Eqs. 132 and 133, and neglecting higher orders in Eq. 134 that is considering the zero order plane wave only, the wave equation in E becomes,

$$\nabla \times (\nabla \times \mathbf{E}) + \frac{1}{c^2} \partial_t^2 \mathbf{E} + \mu_0 \partial_t \mathbf{J} = 0. \tag{135}$$

Apply spatial and time Fourier transform and substitute $J = \sigma E$ where σ is the local conductivity tensor,

$$ik \times ik \times \mathbf{E} - \frac{\omega^2}{c^2} \mathbf{E} - i\omega \mu_0 \mathbf{J} = 0$$

$$\iff -k \times k \times \mathbf{E} - \frac{\omega^2}{c^2} \mathbf{E} - i\omega \mu_0 \sigma \mathbf{E} = 0$$

$$\iff (k \times k \times \mathbb{I} + \frac{\omega^2}{c^2} \mathbb{I} + i\omega \mu_0 \sigma) \mathbf{E} = 0$$

$$\iff (k \times k \times \mathbb{I} + \frac{\omega^2}{c^2} (\mathbb{I} + \frac{i}{\omega \varepsilon_0} \sigma)) \mathbf{E} = 0. \tag{136}$$

Let

$$\mathbb{K} = \mathbb{I} + \frac{i}{\varepsilon_0 \omega} \sigma. \tag{137}$$

where $\sigma/\omega\varepsilon_0$ is the susceptibility tensor. σ is obtained by identifying the *x, y, and z* components of equations:

$$\mathbf{J} = \sigma \mathbf{E} \tag{138}$$

and

$$\mathbf{J} = nqv = ne \sum_{i=x,y,z} (v_{s,i} - v_{e,i}). \tag{139}$$

The particle equation of motion is used to write the velocity components of the ions and electrons as a function of the components of the electric field,

$$m_s \partial_t v_s = q_s (E + v_s \times B_0), \tag{140}$$

where v_s and E are the perturbed quantities inside plasma where s stands for different ion species inside plasma and v_0 and E_0 are both assumed zero. Also $B_0 = B_0 \hat{\mathbf{z}}$ is the static magnetic field. Decomposing Eq. 140 gives,

$$-i\omega v_{\alpha,x} = \frac{q_\alpha}{m_\alpha}(E_x + v_{\alpha,y} \times B_0)$$

$$-i\omega v_{\alpha,y} = \frac{q_\alpha}{m_\alpha}(E_y - v_{\alpha,x} \times B_0)$$

$$-i\omega v_{\alpha,z} = \frac{q_\alpha}{m_\alpha}(E_z),$$

where α stands for electrons and ions species. Let's find $v_{e,x}, v_{e,y}, v_{s,x}$ and $v_{s,y}$ explicitly.

$$v_{e,x}\left[1 - \frac{\omega_{c,e}^2}{\omega^2}\right] = \frac{e}{i\omega m_e}E_x - \frac{\omega_{c,e}}{\omega^2}\frac{e}{m_e}E_y.$$

Therefore,

$$v_{e,x} = \frac{e}{im_e}\frac{\omega}{\omega^2 - \omega_{c,e}^2}E_x - \frac{\omega_{c,e}}{\omega^2 - \omega_{c,e}^2}\frac{e}{m_e}E_y. \tag{141}$$

Subsequently,

$$v_{e,y} = \frac{e}{m_e}\frac{\omega_{c,e}}{\omega^2 - \omega_{c,e}^2}E_x + \frac{e}{i\omega m_e}\frac{\omega^2}{\omega^2 - \omega_{c,e}^2}E_y \tag{142}$$

Similarly,

$$v_{s,x} = \frac{-e}{i\omega m_s}(E_x) - \frac{\omega_{c,s}}{i\omega}\left[\frac{-e}{i\omega m_s}(E_y) + \frac{\omega_{c,s}}{i\omega}v_{s,x}\right]$$

which gives

$$v_{s,x} = -\frac{\omega}{\omega^2 - \omega_{c,s}^2}\frac{e}{im_s}(E_x) - \frac{\omega_{c,s}}{\omega^2 - \omega_{c,s}^2}\frac{e}{m_s}(E_y). \tag{143}$$

Also

$$v_{s,y} = \frac{e}{m_s}\frac{\omega_{c,s}}{\omega^2 - \omega_{c,s}^2}E_x - \frac{e}{i\omega m_s}\frac{\omega^2}{\omega^2 - \omega_{c,s}^2}E_y. \tag{144}$$

Now

$$J_x = ne(\sum_s v_{s,x} - v_{e,x})$$

$$= ne^2\left[-\sum_s(\frac{\omega}{\omega^2 - \omega_{c,s}^2}\frac{1}{im_s} + \frac{\omega}{\omega^2 - \omega_{c,s}^2}\frac{1}{im_s})E_x + (\frac{\omega_{c,e}}{\omega^2 - \omega_{c,e}^2}\frac{1}{m_e} - \frac{\omega_{c,s}}{\omega^2 - \omega_{c,s}^2}\frac{1}{m_s})E_y\right].$$

But Eq. 138, gives $J_x = \sigma_{xx}E_x + \sigma_{xy}E_y + \sigma_{xz}E_z$, hence

$$\sigma_{xx} = -ne^2(\frac{\omega}{\omega^2 - \omega_{c,e}^2}\frac{1}{im_e} + \sum_s\frac{\omega}{\omega^2 - \omega_{c,s}^2}\frac{1}{im_s}),$$

$$\sigma_{xy} = ne^2(\frac{\omega_{c,e}}{\omega^2 - \omega_{c,e}^2}\frac{1}{m_e} - \sum_s\frac{\omega_{c,s}}{\omega^2 - \omega_{c,s}^2}\frac{1}{m_s}),$$

$$\sigma_{xz} = 0.$$

Similarly

$$J_y = \sigma_{yx}E_x + \sigma_{yy}E_y + \sigma_{yz}E_z = ne(\sum_s v_{s,y} - v_{e,y})$$

$$= ne\left[\sum_s\frac{e}{m_s}\frac{\omega_{c,s}}{\omega^2 - \omega_{c,s}^2}E_x - \sum_s\frac{e}{i\omega m_s}\frac{\omega^2}{\omega^2 - \omega_{c,s}^2}E_y - \frac{e}{m_e}\frac{\omega_{c,e}}{\omega^2 - \omega_{c,e}^2}E_x - \frac{e}{i\omega m_e}\frac{\omega^2}{\omega^2 - \omega_{c,e}^2}E_y\right]$$

Then

$$\sigma_{yx} = ne^2(\sum_s\frac{1}{m_s}\frac{\omega_{c,s}}{\omega^2 - \omega_{c,s}^2} - \frac{1}{m_e}\frac{\omega_{c,e}}{\omega^2 - \omega_{c,e}^2}),$$

$$\sigma_{yy} = -ne^2 \left(\sum_s \frac{1}{i\omega m_s} \frac{\omega^2}{\omega^2 - \omega_{c,s}^2} + \frac{1}{i\omega m_e} \frac{\omega^2}{\omega^2 - \omega_{c,e}^2} \right),$$

$$\sigma_{yz} = 0.$$

Also

$$J_z = \sigma_{zx}E_x + \sigma_{zy}E_y + \sigma_{zz}E_z = ne\left(\sum_s v_{s,z} - v_{e,z} \right) = -ne^2 \left(\sum_s \frac{1}{i\omega m_s} + \frac{1}{i\omega m_e} \right) E_z.$$

then

$$\sigma_{zx} = \sigma_{zy} = 0,$$

and

$$\sigma_{zz} = -ne^2 \left(\sum_s \frac{1}{i\omega m_s} + \frac{1}{i\omega m_e} \right).$$

$\mathbb{K}$ in Eq. 137 is obtained,

$$\mathbb{K} = \begin{bmatrix} 1 & 0 & 0 \\ 0 & 1 & 0 \\ 0 & 0 & 1 \end{bmatrix} + \frac{i}{\varepsilon_0 \omega} \sigma$$

Using Stix notation:

$$\mathbb{K} = \begin{bmatrix} \varepsilon_\perp & -i\varepsilon_{xy} & 0 \\ i\varepsilon_{xy} & \varepsilon_\perp & 0 \\ 0 & 0 & \varepsilon_\parallel \end{bmatrix} = \begin{bmatrix} S & -iD & 0 \\ iD & S & 0 \\ 0 & 0 & P \end{bmatrix},$$

where,

$$\varepsilon_\perp = S = 1 + \frac{\omega_{pe}^2}{\omega_{ce}^2 - \omega^2} + \sum_s \frac{\omega_{ps}^2}{\omega_{c,s}^2 - \omega^2} \cong 1 + \frac{\omega_{pe}^2}{\omega_{ce}^2} - \sum_s \frac{\omega_{ps}^2}{\omega^2},$$

$$\varepsilon_\parallel = P = 1 - \left(\frac{\omega_{pe}}{\omega} \right)^2 - \sum_s \left(\frac{\omega_{pe}}{\omega} \right)^2,$$

$$\varepsilon_{xy} = D = \frac{\omega_{pe}^2}{\omega} \frac{\omega_{c,e}}{\omega_{c,e}^2 - \omega^2} - \sum_s \frac{\omega_{ps}^2}{\omega} \frac{\omega_{c,s}}{\omega_{c,s}^2 - \omega^2} \cong \frac{\omega_{pe}^2}{\omega \omega_{c,e}}.$$

Since

$$k \times k \times \mathbb{I} = (k.\mathbb{I})k - k^2\mathbb{I} = kk - k^2\mathbb{I} = \begin{bmatrix} k_x^2 - k^2 & 0 & k_xk_z \\ 0 & -k^2 & 0 \\ k_xk_z & 0 & K_z^2 - k^2 \end{bmatrix},$$

Eq. 136 can be written as

$$\mathbf{D}.\mathbf{E} = 0, \tag{145}$$

where

$$\mathbf{D} = k \times k \times \mathbb{I} + \frac{\omega^2}{c^2} \left(\mathbb{I} + \frac{i}{\omega \varepsilon_0} \sigma \right) = \begin{bmatrix} k_x^2 - k^2 & 0 & k_xk_z \\ 0 & -k^2 & 0 \\ k_xk_z & 0 & -k_x^2 \end{bmatrix} + \frac{\omega^2}{c^2} \mathbb{K}$$

$$= \begin{bmatrix} -k_z^2 & 0 & k_xk_z \\ 0 & -k^2 & 0 \\ k_xk_z & 0 & -k_x^2 \end{bmatrix} + \frac{\omega^2}{c^2} \begin{bmatrix} S & -iD & 0 \\ iD & S & 0 \\ 0 & 0 & P \end{bmatrix} = \frac{\omega^2}{c^2} \begin{bmatrix} S-n_\parallel^2 & -iD & n_\perp n_\parallel \\ iD & S-n^2 & 0 \\ n_\perp n_\parallel & 0 & P-n_\perp^2 \end{bmatrix},$$

(146)

The solution for Eq. 145 excluding the trivial solution, is obtained by setting

$$|\mathbf{D}| = 0.$$

i.e.

$$P_4(n_\parallel)n_\perp^4 + P_2(n_\parallel)n_\perp^2 + P_0(n_\parallel) = 0. \tag{147}$$

where

$$P_4 = \varepsilon_\perp = S,$$

$$P_2 = (\varepsilon_\parallel + \varepsilon_\perp)(n_\parallel^2 - \varepsilon_\perp) + \varepsilon_{xy}^2,$$

$$P_0 = \varepsilon_\parallel[(n_\parallel^2 - \varepsilon_\perp)^2 - \varepsilon_{xy}^2].$$

Now let's estimate $\varepsilon_\parallel$, $\varepsilon_\perp$, ε_{xy} for $\omega = 2 \times \pi \times 3.7 \times 10^9 rad/s$, $n_{s,e} = (10^{17} - 3 \times 10^{19})m^{-3}$, and $B = 3.5\,T$. Since $\varepsilon_\perp \cong (1.0008 - 1.1553)$ and $\varepsilon_\parallel \cong (-175.9147 - 0.4273)$ where $\varepsilon_\parallel$ is decreasing for increasing density, and $\varepsilon_{xy} \cong (0.02162 - 6.6764)$.[1]

Now P_0 and P_2 shall be calculated for $n = 10^{17}\,m^{-3}$,

$$P_0 = \varepsilon_\parallel[(n_\parallel^2 - \varepsilon_\perp)^2 - \varepsilon_{xy}^2] \cong 1.8$$

$$P_2 = (\varepsilon_\parallel + \varepsilon_\perp)(n_\parallel^2 - \varepsilon_\perp) + \varepsilon_{xy}^2 \cong 3.6,$$

---

[1]

For hydrogen plasma with $n = 10^{17}m^{-3}$,
$\varepsilon_\perp \cong 1 + \omega_{pe}^2/\omega_{ce}^2 - \omega_{ps}^2/\omega^2 \cong 1.0008$, $\varepsilon_\parallel \cong 1 - (\omega_{pe}/\omega)^2 - (\omega_{ps}/\omega)^2 \cong 0.4273$,
$\varepsilon_{xy} \cong \omega_{pe}^2/\omega\omega_{c,e} \cong 0.02162$,
For $n = 3 \times 10^{19}m^{-3}$,
$\varepsilon_\perp \cong 1.1553$, $\varepsilon_\parallel \cong -175.9147$, $\varepsilon_{xy} \cong \frac{\omega_{pe}^2}{\omega\omega_{c,e}} \cong 6.6764$,
To make sure $\varepsilon_\parallel$ is sufficiently negative, $n = 10^{18}\,m^{-3}$ is taken

$$\varepsilon_\parallel \cong 1 - (\omega_{pe}/\omega)^2 - (\omega_{ps}/\omega)^2 \cong 1 - 10(\frac{2.8}{3.7})^2 - 10(\frac{0.0664}{3.7})^2 \cong -4.7271,$$

while for $n = 3 \times 10^{19}$, $P_0 \cong -19953$, $P_2 \cong -452$. Note that since $P_4 \cong 1$, and $|\varepsilon_\parallel| \gg \varepsilon_\perp$, ε_{xy} then $P_0 > 0$, $P_2 < 0$. Solving for the roots of Eq. 147.

$$n_\perp^2 = \frac{-P_2 \pm \sqrt{\triangle}}{2P_4}, \tag{148}$$

where $\triangle = P_2^2 - 4P_4P_0$ is always nonnegative in the lower hybrid range. The root with (+) sign is the slow wave branch, since it has lower $v_\perp$, and the root with the (−) sign is the fast wave branch. For $\Delta = 0$, it has a cold confluence that is the double root solution signifies a slow-fast wave mode conversion at a specific value of n_a (n accessibility) which is density dependent [35]. Thus the wave $n_\parallel$ refractive index should exceed n_a corresponding to the highest plasma density to avoid mode conversion into a fast wave.

Let's study the slow wave branch, characterized by [2]

$$n_\perp^2 \cong -(n_\parallel^2 - S)(\frac{P}{S}). \tag{149}$$

Resonance occurs for $n_\perp = 0$ that is for $S = 0$, which gives

$$\omega^{-1} = \omega_{LH}^{-1} = \sqrt{(\omega_{cs}\omega_{ce})^{-2} + \omega_{ps}^{-2}}. \tag{150}$$

Cut-off takes place at $P = 0$, which is when the wave frequency matches the natural frequency of the plasma hence at cut-off $\omega_{LH} = \omega_{pe}$. Hence $n_{cut,slow} = 1.6 \times 10^{17}\, m^{-3}$. [3]

The fast wave is given by

$$n_\perp^2 = \frac{-P_2 - \sqrt{\triangle}}{2P_4}.$$

Since $P_0 = 0$, gives $n_\perp = 0$ and $P_0 = 0$ gives $(n_\parallel^2 - \varepsilon_\perp)^2 - \varepsilon_{xy}^2 = 0$, then $n_\parallel^2 - \varepsilon_\perp = \varepsilon_{xy}$ describes cut-off. As a result, $n_{cut,fast} \cong 8.4 \times 10^{18}\, m^{-3}$.

4

2

$$n_\perp^2 = \frac{-P_2 + \sqrt{\triangle}}{2P_4} \cong -(n_\parallel^2 - S)(\frac{P}{S}) \left[\frac{(S+P)(-1 + (1 - 4SP(-D^2/(S+P)^2(n_\parallel^2 - S)^2))^{1/2}}{2P} \right]$$

3

$$n_{cut,slow} = \frac{\omega_{LH}^2 \varepsilon_0 m}{e^2} = \omega_{LH}^2 (\frac{8.8 \times 10^{-12} \times 9.1 \times 10^{-31}}{1.6^2 \times 10^{-38}}) = 16862 \times 10^{13} \cong 1.6 \times 10^{17}\, m^{-3}.$$

4

$$n_\parallel^2 - \varepsilon_\perp = \varepsilon_{xy} \iff n_\parallel^2 - (1 + \frac{\omega_{pe}^2}{\omega_{ce}^2} - \frac{\omega_{ps}^2}{\omega^2}) = \frac{\omega_{pe}^2}{\omega\omega_{c,e}}$$

$$\implies n_{cut,fast} = \frac{3}{35.67} \times 10^{20} \cong 8.4 \times 10^{18} m^{-3}.$$

Note that $n_{cut,fast} \gg n_{slow,fast}$, thus it is more difficult to launch.

Now using Eqs. 145 and 146, $E_{x,y}/E_z$ is to be compared for slow and fast waves. Eq. 145 gives

$$(S - n_\parallel^2)E_x - iDE_y + n_\perp n_\parallel E_z = 0$$

but $E_y = 0$ for the slow wave, thus

$$\left(\frac{E_x}{E_z}\right)_{slow} = \frac{n_\perp n_\parallel}{(S - n_\parallel^2)} = \frac{n_\parallel}{(S - n_\parallel^2)}\sqrt{-(n_\parallel^2 - S)(\frac{P}{S})} \sim \sqrt{P/S} \tag{151}$$

$$\left(\frac{E_x}{E_z}\right)_{fast} = \frac{P - n_\perp^2}{n_\perp n_\parallel} \sim P/S, \tag{152}$$

So

$$\frac{E_{z,slow}}{E_{z,fast}} \sim \sqrt{P/S} \sim 10. \tag{153}$$

Hence slow wave is more efficient for Landau damping since it has larger parallel electric field.

APPENDIX C

REFLECTION COEFFICIENT CALCULATION

The electric field along a cross section of a waveguide ($x = constant$) is the sum of the incident and reflected parts:

$$E1 = E_i exp(-ikx) + E_r exp(+ikx)$$

where at $x + \lambda/4$,

$$E2 = E_i exp(-ik(x + \lambda/4)) + E_r exp(+ik(x + \lambda/4)),$$

Hence

$$E_i = \frac{1}{2}(E1 + iE2)e^{ikx}$$

and

$$E_r = \frac{1}{2}(E1 - iE2)e^{-ikx}$$

The reflection coefficient is given by $\Gamma = (E_r/E_i)^2$.

APPENDIX D

COMPARING THE POWER BETWEEN COMSOL SIMULATIONS AND ALOHA FOR FAM AND PAM

In order to compare the power spectra obtained in Aloha with those obtained using the electric field calculated by Comsol, it is necessary to figure out which are the dominant modes in the 2 D configuration used in Comsol and modes description used in Aloha. Actually, Aloha takes the TE_{10} mode as the pricipal mode since it considers the antenna as rectangular waveguides array. However; in Comsol the TEM mode is the principal mode, since the antenna is modelled as a parallel plate waveguide. Thus

$$E_{max}(rect) = E_{max}(parallel\ plate) \times \sqrt{\frac{2k_0}{a \times \beta_{10}}}$$

where k_0 the wave number in vacuum and β_{10} is the TE_{10} mode wave number.

Thus

$$Power(Aloha) = Power(Comsol)\frac{2k_0}{a \times \beta_{10}}$$

However, for simple comparison the power spectra were normalized to maximum power.

APPENDIX E

THE LH WAVE PARALLEL PHASE VELOCITY AND THE LANDAU DAMPING PHASE VELOCITY

Let the electron temperature T_e in a tokamak be $T_e = [3 - 10] \, KeV$. Note that $n_\parallel = c/v_\parallel$, where $n_\parallel$ is the refractive index of the Lower hybrid wave parallel to the magnetic field lines and c is the velocity of light.

For the FAM antenna, $n_\parallel \simeq 2$, hence $v_\parallel = c/2$. Therefore

$$v_{the} = \sqrt{T_e/m_e} \in c \times [0.045 - 0.14], \tag{154}$$

where v_{the} is the electron phase velocity, thus $v_\parallel = [3.57 - 11.1] \, v_{the}$.

On the other hand, $n_{\parallel,L} \simeq 5.5/\sqrt{T[KeV]} \in [1.74 - 3.17]$ where $n_{\parallel,L}$ is the parallel refractive index corresponding to Landau damping. Therefore,

$$v_{\parallel,L} = c/n_{\parallel,L} \simeq [4.1 - 7]v_{the} \equiv [0.32 - 0.57]c. \tag{155}$$

In particular, for $T_e = 5KeV$, $v_\parallel \simeq 5v_{the}$, while $v_{\parallel,L} \equiv 0.4c$ which is lower than $v_\parallel$ thus describes the spectral gap problem in low temperature plasmas.

APPENDIX F

CALCULATING THE SPECTRUM OF DENSITY FLUCTUAIONS

A. Introduction

In order to formulate the plasma electron density perturbation in the SOL heuristically, the mathematical background that describes the fluctuations is presented. A stochastic description is used based on the large difference of fast fluctuations correlation time and that of the fast LH electrons slowing down time scale.

B. Statistical Description of Plasma Fluctuations

1. Reynold's Decomposition

First, the plasma density fluctuations are considered in the parallel $\hat{\mathbf{z}}$ dimension. Let $n_e(z,t)$ be a continuous density function dependent on space component z and time t. The fluctuating part with a zero time average $\widetilde{n}_e(z,t)$ could be seperated from the slowly evolving part $n_{e0}(z,t)$ using Reynold's decomposition. Thus

$$n_e(z,t) = n_{e0}(z,t) + \widetilde{n}_e(z,t). \tag{156}$$

Notice that $n_{e0}(z,t)$ is the average of $n_e(z,t)$ over a time δt,

$$n_{e0}(z,t) = \overline{n_e(z,t)} = \frac{1}{\delta t} \int_t^{t+\delta t} n_e(z,t')dt' \tag{157}$$

where δt is chosen such that

$$(\hat{\widetilde{\omega}} - \Delta\widetilde{\omega}/2)^{-1} \ll \delta t \ll (\hat{\bar{\omega}} + \Delta\bar{\omega}/2)^{-1} \tag{158}$$

with $\hat{\widetilde{\omega}}$, $\Delta\widetilde{\omega}$ and $\hat{\bar{\omega}}$, $\Delta\bar{\omega}$ being the central frequency and the bandwidth of the high frequency and low frequency bands distinguished in the spectrum of $n_e(z,t)$ respectively.

Note that, Eq. 157 gives, $\overline{\widetilde{n}_e(z,t)} = 0$, but a zero mean does not imply that the fluctuations are small. And (158) indicates that $n_{e0}(z,t)$ is almost constant on the time interval δt, thus $n_{e0}(z,t) \simeq n_{e0}(z)$, where δt is taken as the slowing down time scale

of fast electrons. Also, in this study, the density background is flat and therefore low frequency is taken to be zero and n_{e0} is fixed in space and time.

2. Fourier Transform and Random Phase Approximation

Lets designate n_e , n_{e0}, and $\tilde{n}_e$ by a, A, and $\tilde{a}$ to simplify the notation. The time and space autocorrelation functions measure the self similarity over specified space and time intervals respectively which allows the determination of the limits beyond which an event is nondeterministic and thus is dealt with as a random variable. Moreover, they provide a tool to measure the loss of information with respect to the considered scales in space and time. The single space Eulerian time correlation function is given by

$$\mathscr{R}_{aa}^t(z,t,z,t-\Delta t) = \overline{\tilde{a}(z,t)\tilde{a}^*(z,t-\Delta t)}, \tag{159}$$

and the single time autocorrelation function is given by

$$\mathscr{R}_{aa}^t(z,t,z-\Delta z,t) = <\tilde{a}(z,t),\tilde{a}^*(z-\Delta z,t)>, \tag{160}$$

where

$$<\tilde{a}(z,t),\tilde{a}^*(z-\Delta z,t)> = \frac{1}{L}\int_{-L/2}^{+L/2} \tilde{a}(z,t)\tilde{a}^*(z-\Delta z,t)dz. \tag{161}$$

An important property is to have $\mathscr{R}_{aa}^t$ independent of the choice of time but rather dependent on the time difference Δt. This is applicable by assuming stationary fluctuations over δt. Thus

$$\mathscr{R}_{aa}^t = \mathscr{R}_{aa}^t(\Delta t). \tag{162}$$

Similarily, assuming homogeneous fluctuations in space gives

$$\mathscr{R}_{aa}^z = \mathscr{R}_{aa}^z(\Delta z). \tag{163}$$

Let's designate by τ_f and ξ_f the time and space correlations respectively. Thus $\mathscr{R}_{aa}^t$ is a random variable of time if $\Delta t \gg \tau_f$ and similarily, $\mathscr{R}_{aa}^z$ is a random variabe of space if $\Delta z \gg \xi_f$.

Now using the fourier transform, $\tilde{a}(z,t)$ is written as a superposition of plane waves,

$$\tilde{a}(z,t) = \int_{-\infty}^{+\infty} d\tilde{\omega} \int_{-\infty}^{+\infty} \tilde{a}_{\tilde{k},\tilde{\omega}} e^{i\tilde{S}_{\tilde{k},\tilde{\omega}}} d\tilde{k}, \tag{164}$$

where the phase $S_{\widetilde{k},\widetilde{\omega}} = \widetilde{k}.z - \widetilde{\omega}(\widetilde{k})t$, knowing that

$$\widetilde{k} = \frac{2\pi}{\widetilde{\lambda}}$$

is the fluctaution wave vector, $\widetilde{\lambda}$ is the corresponding fluctuation wave length and $\widetilde{\omega}(\widetilde{k})$ is the dispersion relation. Eq. 164 sums over many wavelengths which form a wavepacket traveling at a groug velocity $v_g = d\widetilde{\omega}/d\widetilde{k}$. The fluctuation period relative to a wave with a wavelength $\widetilde{\lambda}$, $\widetilde{\tau}(\widetilde{k})$ is given by

$$\widetilde{\tau}(\widetilde{\lambda}) = \frac{2\pi}{\widetilde{\omega}(\widetilde{k})} = \frac{1}{\widetilde{f}(\widetilde{k})}.$$

For the case of $\Delta t \ll \tau_f$ and $\Delta z \ll \xi_f$, a deterministic evolution allows approximating the phase in (164) by $\Delta S \simeq 0$, hence

$$\frac{\Delta z}{\widetilde{\lambda}} - \frac{\Delta t}{\widetilde{\tau}(\widetilde{\lambda})} = 0. \tag{165}$$

A linear dispersion relation $\widetilde{\omega}(\widetilde{k}) = \widetilde{v}\widetilde{k}$ or $\widetilde{\tau}(\widetilde{\lambda}) = \widetilde{\lambda}/\widetilde{v}$, gives $\Delta z = \widetilde{v}\Delta t$, which is valid for the low frequency fluctuations.[1]

The loss of space coherence is accompanied by a loss in time coherence. Consequently, the criterion for statistical description is based on the following equation,

$$\xi_f \simeq \widetilde{v}\tau_f. \tag{166}$$

When Δt exceeds τ_f, $\Delta\widetilde{S}_{\widetilde{k},\widetilde{\omega}}$ assumes any value and the term $\Delta t\widetilde{v}/\widetilde{\lambda}$ is mapped to a random phase

$$-\Delta t\widetilde{v}/\widetilde{\lambda} \longrightarrow \chi_{\widetilde{k}}$$

for each mode $\widetilde{k}$ with uniform distribution over $[0,1]$.

Thus the phase increment becomes

$$\Delta\widetilde{S}_{\widetilde{k},\widetilde{\omega}} = 2\pi(\frac{\Delta z}{\widetilde{\lambda}} + \chi_{\widetilde{k}}), \tag{167}$$

so that $\tilde{a}(z,t)$ describes discrete events in time while continuity in space is maintained. Now, linear dispersion relation gives $\widetilde{a}_{\widetilde{k},\widetilde{\omega}} = \widetilde{a}_{\widetilde{k}}\delta(\widetilde{\omega} - \widetilde{v}\widetilde{k})$, hence

$$\tilde{a}(z,t) = \int_{-\infty}^{+\infty} d\widetilde{\omega} \int_{-\infty}^{+\infty} \widetilde{a}_{\widetilde{k},\widetilde{\omega}} e^{i(\widetilde{k}.z - \widetilde{\omega}t)} d\widetilde{k}$$

---

[1] $\widetilde{v}$ is the phase velocity.

$$= \int_{-\infty}^{+\infty} d\widetilde{\omega} \int_{-\infty}^{+\infty} \widetilde{a}_{\widetilde{k}} \delta(\widetilde{\omega} - \widetilde{v}\widetilde{k}) e^{i(\widetilde{k}.z - \widetilde{\omega}t)} d\widetilde{k}$$

$$= \int_{-\infty}^{+\infty} \widetilde{a}_{\widetilde{k}} e^{i(\widetilde{k}.z - \widetilde{v}\widetilde{k}t)} d\widetilde{k}. \qquad (168)$$

Now for a given time step t_j, where $t_j = \sum_{j'=1}^{j'=j} \Delta t_{j'}$ for $\Delta t_{j'} \gg \tau_f$, the discretized phase term $-\widetilde{v}\widetilde{k}t_j$ could be reformulated as a uniform random variable $\phi_{\widetilde{k}}^{(j)}$ having values in $[0, 2\pi]$,

$$\widetilde{a}(z, t_j) = \widetilde{a}_{(j)}(z) = \int_{-\infty}^{+\infty} \widetilde{a}_{\widetilde{k}} e^{i(\widetilde{k}.z - \phi_{\widetilde{k}}^{(j)})} d\widetilde{k}. \qquad (169)$$

A genralization to the multidimensional case is obtained by neglecting the cross correlations between various dimesions,

$$\widetilde{a}(z, t_j) = \widetilde{a}_{(j)}(z) = \int \cdots \int \widetilde{a}_{\widetilde{\mathbf{k}}} e^{i(\widetilde{\mathbf{k}}.x - \phi_{\widetilde{\mathbf{k}}}^{(j)})} d\widetilde{\mathbf{k}} \qquad (170)$$

where $\phi_{\widetilde{\mathbf{k}}}^{(j)}$ is a uniform random variable between 0 and 2π. For further simplification,

$$\widetilde{a}_{(j)}(x) = \int_{0}^{+\infty} \widetilde{a}_{\widetilde{k}} \left[e^{i(\widetilde{k}.x + \phi_{\widetilde{k}}^{(j)})} + e^{-i(\widetilde{k}.x - \phi_{-\widetilde{k}}^{(j)})} \right] d\widetilde{k}, \qquad (171)$$

also since $\widetilde{a}_{(j)}(z)$ is a real function of x, the condition $\phi_{\widetilde{\mathbf{k}}}^{(j)} = -\phi_{-\widetilde{\mathbf{k}}}^{(j)}$ must be satisfied and hence,

$$\widetilde{a}_{(j)}(z) = 2 \int_{0}^{+\infty} \widetilde{a}_{\widetilde{k}} cos(\widetilde{k}.z + \phi_{\widetilde{k}}^{(j)}) d\widetilde{k}, \qquad (172)$$

which could be written as

$$\widetilde{a}_{(j)}(z) = 2 \int_{0}^{+\infty} \widetilde{a}_{\widetilde{k}} sin(\widetilde{k}.z + \phi_{\widetilde{k}}^{(j)}) d\widetilde{k}, \qquad (173)$$

since $\phi_{\widetilde{\mathbf{k}}}^{(j)}$ and $\phi_{\widetilde{\mathbf{k}}}^{(j)} - \pi/2$ have same probability distribution functions (pdf). The discrete sum of Eq. 173 gives,

$$\widetilde{a}_{(j)}(z) = 2 \lim_{\Delta\widetilde{k} \longrightarrow 0} \Delta\widetilde{k} \sum_{l=0}^{l=\infty} \widetilde{a}_{\widetilde{k}}(\widetilde{k} = l\Delta\widetilde{k}) sin(l\Delta\widetilde{k}.z + \phi_{l}^{(j)}), \qquad (174)$$

where $\widetilde{K} = l\Delta\widetilde{k}$. Let's assume $\widetilde{a}_j(z)$ to be periodic in x with a period L, then

$$\widetilde{k}L = 0 \, mod(2\pi) \qquad (175)$$

i.e.

$$\widetilde{k} = \frac{2\pi}{L}l. \tag{176}$$

thus

$$\Delta\widetilde{k} = \frac{2\pi}{L}. \tag{177}$$

(incrementing $\widetilde{k}$ by $\Delta\widetilde{k}$, is obtained by increasing l by 1).

Replacing Eq. 177 in Eq. 174,

$$\widetilde{a}_{(j)}(z) = \frac{4\pi}{L}\sum_{l=0}^{l=\infty}\widetilde{a}_{\widetilde{k}}(\widetilde{k}=l\Delta\widetilde{k})sin(2\pi(\frac{lz}{L}+\chi_l^{(j)})), \tag{178}$$

since $\phi_l^{(j)} = 2\pi\chi_l^{(j)}$ and putting

$$\widetilde{a}_l \equiv \frac{4\pi}{L}\widetilde{a}_{\widetilde{k}}(\widetilde{k}=\frac{2\pi}{L}l) \tag{179}$$

or for a unitary definition of the fourier transform (let $\widetilde{\kappa} = \widetilde{k}/2\pi$)

$$\widetilde{a}_l \equiv \frac{2}{L}\widetilde{a}_{\widetilde{\kappa}}(\widetilde{\kappa}=\frac{l}{L}). \tag{180}$$

Therefore Eq. 178 becomes,

$$\widetilde{a}_{(j)}(x) = \sum_{l=0}^{l=\infty}\widetilde{a}_l sin(2\pi(\frac{lx}{L}+\chi_l^{(j)})), \tag{181}$$

But $\overline{\widetilde{a}(z,t)} = 0$ at any z, and ergodicity gives $<\widetilde{a}_{(j)}(z)>= 0$ at any time t,

$$<\widetilde{a}_{(j)}(z)>= \frac{1}{L}\int_{-L/2}^{+L/2}\sum_{l\geq 0}\widetilde{a}_l sin(\frac{2\pi}{L}lz+\phi_l^{(j)})dz$$

$$= \widetilde{a}_0 sin(\phi_0^{(j)}) + \frac{1}{L}\int_{-L/2}^{+L/2}\sum_{l\geq 1}\widetilde{a}_l sin(\frac{2\pi}{L}lz+\phi_l^{(j)}))dz$$

$$= \widetilde{a}_0 sin(\phi_0^{(j)}),$$

hence $\widetilde{a}_0 = 0$ since $\phi_0^{(j)}$ can take any value between 0 and 2π. Finally,

$$\widetilde{a}_{(j)}(z) = \sum_{l\geq 1}\widetilde{a}_l sin(2\pi(\frac{lz}{L}+\chi_l^{(j)})), \tag{182}$$

is the starting point of fluctuations.

3. Fluctuations Level and Time Average

Having discretized time; the number of time realizations in relation to the fluctuation level should be well determined for calculating the mean value $A(z)$. Let δt be decomposed into equal time steps $\Delta t_j = \Delta t$

$$\delta t = \sum_{j=1}^{j=N} \Delta t_j \tag{183}$$

then

$$A(z) = \overline{a(z,t)} = \frac{1}{\delta t} \int_t^{t+\delta t} a(z,t')dt'$$

$$= \frac{1}{\delta t} \sum_{j=1}^{j=N} \int_{t_j}^{t_j+\Delta t} a(z,t')dt'$$

$$= \frac{1}{\delta t} \sum_{j=1}^{j=N} \left(\int_{t_j}^{t_j+\Delta t} A(z,t')dt' + \int_{t_j}^{t_j+\Delta t} \widetilde{a}(z,t')dt' \right)$$

$$= A(z) + \frac{1}{\delta t} \sum_{j=1}^{j=N} \int_{t_j}^{t_j+\Delta t} \widetilde{a}(z,t')dt' \tag{184}$$

where by Eq. 158 and since $\Delta t \ll \delta t$ for $N \gg 1$, $A(z,t)$ is taken constant on the interval $[t_j, t_j + \Delta t]$. Regarding the fast fluctuations term

$$\int_{t_j}^{t_j+\Delta t} \widetilde{a}(z,t')dt' = \widetilde{a}(z,t_j)\Delta t + \mathcal{O}(\Delta t^2) \tag{185}$$

thus

$$\overline{\widetilde{a}(z,t)} = \frac{1}{\delta t} \sum_{j=1}^{j=N} \int_{t_j}^{t_j+\Delta t} \widetilde{a}(z,t')dt' = \frac{1}{N} \sum_{j=1}^{j=N} \widetilde{a}_j(z) + \mathcal{O}(\Delta t^2) \tag{186}$$

Let $\mathbb{E}_N(\widetilde{a}(z,t)) = \frac{1}{N}\sum_{j=1}^{j=N} \widetilde{a}_j(z)$, be the mean of $\widetilde{a}_j(z)$ taken at N instants of time, where each value has been assigned equal probability of $1/N$ due to having $\Delta t \gg \tau_f$ (time step is well beyond correlation time)

$$\overline{\widetilde{a}(z,t)} = \mathbb{E}_N(\widetilde{a}(z,t)) + \mathcal{O}(\Delta t^2) \tag{187}$$

Henceforth, an unbiased estimator of $A(x)$ could be valid

$$A_N(z) = \mathbb{E}_N(a(z,t)).$$

$$A_N(z) = A(z) + \mathbb{E}_N(\widetilde{a}(z,t))$$

with

$$\mathbb{E}_N(A_N(z)) = \mathbb{E}_N(A(z)) + \mathbb{E}_N(\widetilde{a}(z,t)) = A(x) + \mathbb{E}_N(\widetilde{a}(z,t))$$

if convergence is obtained in the statistical sense

$$\lim_{N \longrightarrow \infty} \mathbb{E}_N(\widetilde{a}(z,t)) = \overline{\widetilde{a}(z,t)} = 0.$$

Since the amplitude of $\widetilde{a}(z,t)$ need not be small relative to $A(z)$, N should be large enough to uncover the fluctuations effect shown by the ratio $\widetilde{a}(z,t)/A(z)$. If $A(z)$ is not known, one woul have to determine N especially if $\widetilde{a}(z,t)/A(z)$ is large. Moreover, if the auto-correlation function is assumed as gaussian in time,

$$R_{aa}^t(0,\Delta t) = \sigma_a^2 e^{-\Delta t^2/\tau_f^2}, \tag{188}$$

where $\sigma_a^2 = \lim_{N \to \infty} \sigma_{a,N}^2$, with $\sigma_{a,N}^2$ is the variance of $a(z,t)$ after N realizations, then for $\alpha = 0.01$ chosen as a reasonable level of decorrelation at Δt, i.e

$$\frac{R_{aa}^t(\Delta t)}{R_{aa}^t(0)} \leq \alpha, \tag{189}$$

$$\Delta t_\alpha \geq \tau_f \sqrt{-ln\alpha} = 2.14\,\tau_f \tag{190}$$

Therefore

$$N_\alpha = \delta t/\tau_f \sqrt{-ln\alpha} \tag{191}$$

4. Determining the coefficients $\widetilde{a}_l$ from Power spectrum and auto correlation function

Fourier decomposition of density fluctuation spectrum helps deducing the coefficients from the autocorrelation function.

$$R_{aa}^z(\Delta z,t_j) = \frac{1}{L}\int_{-L/2}^{L/2} dz \sum_{l \geq 1}\widetilde{a}_l sin(2\pi(\frac{lz}{L} + \chi_l^{(j)})) \sum_{l' \geq 1}\widetilde{a}_{l'} sin(2\pi(l'\frac{z-\Delta z}{L} + \chi_{l'}^{(j)}))$$

$$= \sum_{l\geq 1}\widetilde{a}_l \sum_{l'\geq 1}\widetilde{a}_{l'} \frac{1}{L}\int_{-L/2}^{L/2} sin(2\pi(\frac{lz}{L}+\chi_l^{(j)}))sin(2\pi(l'\frac{z-\Delta z}{L}+\chi_{l'}^{(j)}))dz$$

$$=\frac{1}{2}\sum_{l\geq 1}\widetilde{a}_l \sum_{l'\geq 1}\widetilde{a}_{l'}\frac{1}{L}\int_{-L/2}^{L/2} cos(2\pi(\frac{lz}{L}+\chi_l^{(j)}-(l'\frac{z-\Delta z}{L}+\chi_{l'}^{(j)})))-cos(2\pi(\frac{lz}{L}+\chi_l^{(j)}+(l'\frac{z-\Delta z}{L}+\chi_{l'}^{(j)})))dz$$

if $l \neq l'$, both terms in the integrand vanish, and if $l = l'$, second term of the integrand vanish, by the rule: $sin(a\pm b) = sin(a)cos(b)\pm sin(b)cos(a)$. Thus,

$$R_{aa}^z(\Delta z, t_j) = \sum_{l\geq 1}\widetilde{a}_l \sum_{l'\geq 1}\widetilde{a}_{l'}\frac{1}{2}cos(2\pi l'\frac{\Delta z}{L})\delta_{ll'}$$

$$= \sum_{l\geq 1}\frac{\widetilde{a}_l^2}{2}cos(2\pi\frac{l}{L}\Delta z) \tag{192}$$

Hence

$$\tilde{a}_l = \frac{2}{L}\int_{-L/2}^{L/2}R_{aa}^z(z')cos(2\pi\frac{l}{L}z')dz'$$

By change of variable $y = \frac{2\pi}{L}z$,

$$\tilde{a}_l = \frac{1}{\pi}\int_{-\pi}^{\pi}R_{aa}^z(\frac{L}{2\pi}y)cos(ly')dy \tag{193}$$

The variance of the signal is given by

$$R_{aa}^z(0) = \frac{1}{L}\int_{-L/2}^{L/2}\widetilde{a}^2(z,t_j)dz = \sigma_a^2$$

which is the square of the ampliude of density fluctuations.

Now for large values of $\tilde{\kappa}$ given in eq. 180, an interval $\Delta\tilde{\kappa}$ contains an increasingly higher number of plane waves. Hence, a density of plane waves is defined as follows,

$$\sum_{\kappa\leq\kappa_l\leq\kappa+\Delta\kappa}\frac{\widetilde{a}_l^2}{2} \simeq 2\Gamma(\kappa)\Delta\kappa \tag{194}$$

and equivalently,

$$\Gamma(\kappa) = \frac{1}{4} \sum_{l \geq 1} \widetilde{a_l}^2 \delta(\kappa - \frac{l}{L}).$$

Therefore for $l \gg 1$, by eq. 192

$$R_{aa}^z(\Delta z) = \int_0^{+\infty} 2\Gamma(\kappa) cos(2\pi\kappa\Delta z) d\kappa \tag{195}$$

thus

$$R_{aa}^z(\Delta z) = \int_{-\infty}^{+\infty} \Gamma(\kappa) exp(2\pi i \kappa \Delta z) d\kappa \tag{196}$$

by Weiner -Kintchine theorem. In order to express $\widetilde{a_l}$ in terms of $\Gamma(\kappa)$, $\Gamma(\kappa)$ is integrated over a narrow interval of κ. In the interval $[l/L - \Delta\kappa/2, l/L + \Delta\kappa/2]$ with $\Delta\kappa \ll 2/L$, $\Gamma(\kappa)$ is almost constant since $l-1$ and $l+1$ are outside the interval, so

$$\int_{-l/L-\Delta\kappa/2}^{l/L+\Delta\kappa/2} \Gamma(\kappa) d\kappa = \frac{1}{4} \sum_{l \geq 1} \widetilde{a_{l'}}^2 \int_{-l'/L-\Delta\kappa/2}^{l'/L+\Delta\kappa/2} \delta(\kappa - \frac{l'}{L}) d\kappa$$

$$= \frac{1}{4} \widetilde{a_l}^2 \tag{197}$$

and hence

$$\widetilde{a_l} \simeq 2\sqrt{\kappa(\frac{l}{L})\Delta\kappa}. \tag{198}$$

By Eq.192, $\sum_{l \geq 1} \widetilde{a_l}^2 = 2\sigma_a^2$, thus for $\widetilde{a_l} \simeq \alpha\sqrt{\Gamma_l}$ where $\Gamma_l = \Gamma(l/L)$,

$$\alpha^2 \sum_{l \geq 1} \Gamma_l = 2\sigma_a^2, \tag{199}$$

therefore eq.(182) becomes

$$\widetilde{a}_{(j)}(z) = \sqrt{2}\sigma_a \sum_{l \geq 1} \sqrt{\frac{\Gamma_l}{\sum_{l \geq 1}\Gamma_l}} sin(2\pi(\frac{lz}{L} + \chi_l^{(j)})) \tag{200}$$

which is independent of the units of Γ_l. Note that l is bounded since L the width of the plasma box is finite, and is considered as the period of the density fluctuation modes, eq.(177).

5. *Uniform Gaussian Autocorrelation*

The Autocorrelation function is spacially gaussian such that

$$\sum_{l\geq 1}\frac{\tilde{a}_l^2}{2}cos(2\pi\frac{l}{L}\Delta z) = R_{aa}^z(0)e^{\frac{\Delta z^2}{\xi_f^2}} \tag{201}$$

Hence

$$\frac{\tilde{a}_l^2}{2} = \frac{2}{L}\int_{-L/2}^{+L/2} R_{aa}^z(0)e^{-\frac{z^2}{\xi_f^2}}cos(-\frac{2\pi}{L}lz)dz$$

$$= R_{aa}^z(0)\frac{2}{L}\int_{-L/2}^{+L/2} e^{-\frac{z^2}{\xi_f^2}}cos(-\frac{2\pi}{L}lz)dz$$

$$= \frac{2R_{aa}^z(0)}{2\pi L}\int_{-l\pi}^{+l\pi} e^{-\alpha_l^2 y^2}cos(y)dy$$

$$= \frac{2R_{aa}^z(0)}{\pi L}\int_{0}^{+l\pi} e^{-\alpha_l^2 y^2}cos(y)dy \tag{202}$$

where $2\pi lz/L = y$ and

$$\alpha_l = \frac{L}{2\pi l}\xi_f = \frac{1}{2\pi l\varepsilon} \tag{203}$$

with $\varepsilon = \xi_f/L$ is the ration of density parallel correlation length to the plasma box parallel width. Hence

$$\frac{\tilde{a}_l^2}{2} = \frac{2R_{aa}^z(0)}{\pi l}\{\frac{i\sqrt{\pi}}{4\alpha_l}e^{-\frac{1}{4\alpha_l^2}}(Erfi[\frac{1}{2\alpha_l} - il\pi\alpha_l] - Erfi[\frac{1}{2\alpha_l} + il\pi\alpha_l])\}$$

$$= R_{aa}^z(0)\varepsilon i\sqrt{\pi}e^{-\pi^2 l^2\varepsilon^2}(Erfi[\pi l\varepsilon - \frac{i}{2\varepsilon}] - Erfi[\pi l\varepsilon + \frac{i}{2\varepsilon}]) \tag{204}$$

knowing that $Erfi(z)$ is the imaginary error function defined as

$$Erfi(z) = -iErf(iz) = \frac{Erf(iz)}{i} \tag{205}$$

where z is complex, and Erf is the error function. Assume

$$\pi l\varepsilon \ll \frac{1}{2\varepsilon} \tag{206}$$

i.e

$$l \ll \frac{1}{2\pi\varepsilon^2} \tag{207}$$

then, the appoximation

$$\pi l \varepsilon \pm \frac{i}{2\varepsilon} \simeq \frac{i}{2\varepsilon}, \tag{208}$$

is valid, thus

$$\frac{\tilde{a}_l^2}{2} = R_{aa}^z(0)\varepsilon i \sqrt{\pi} e^{-\pi^2 l^2 \varepsilon^2} (Erfi[\pi l \varepsilon - \frac{i}{2\varepsilon}] - Erfi[\pi l \varepsilon + \frac{i}{2\varepsilon}]) \tag{209}$$

But in the limit $z \to \infty$, asypmtotic expansion gives

$$\lim_{z\to\infty} (Erfi[-iz] - Erfi[iz]) = -2i(1 - e^{-x^2}(\frac{1}{\sqrt{\pi}z} + O[\frac{1}{z^2}])) \tag{210}$$

Substituting by the leading term,

$$\tilde{a}_l^2 \simeq 4\sqrt{\pi} R_{aa}^z(0)\varepsilon e^{-\pi^2 l^2 \varepsilon^2} \tag{211}$$

i.e

$$\tilde{a}_l \simeq 2(\sqrt{\pi}\varepsilon)^{1/2} \sqrt{R_{aa}^z(0)} e^{-\frac{\pi^2 l^2 \varepsilon^2}{2}} \tag{212}$$

With the condition $l_{max} \leq (2\pi\varepsilon^2)^{-1}$, and since $R_{aa}^z(0) = \sigma_a^2$, Eqs. 197 and 212 give

$$\Gamma_l \equiv \frac{\tilde{a}_l^2}{4} = \sqrt{\pi}\varepsilon\sigma_a^2 e^{-\pi^2 l^2 \varepsilon^2} \tag{213}$$

Thus Eq. 200 becomes

$$\tilde{a}_{(j)}(z) = \sqrt{2}\sigma_a \sum_{l\geq 1} \sqrt{\frac{e^{-\pi^2 l^2 \varepsilon^2}}{\sum_{l\geq 1} e^{-\pi^2 l^2 \varepsilon^2}}} sin(2\pi(\frac{lz}{L} + \chi_l^{(j)}))$$

$$= \frac{\sqrt{2}\sigma_a}{(\sum_{l\geq 1} e^{-\pi^2 l^2 \varepsilon^2})^{1/2}} \sum_{l\geq 1} e^{-\frac{\pi^2 l^2 \varepsilon^2}{2}} sin(2\pi(\frac{lz}{L} + \chi_l^{(j)})) \tag{214}$$

But since $\sum_{l \geq 1} \sqrt{\frac{e^{-\pi^2 l^2 \varepsilon^2}}{\sum_{l \geq 1} e^{-\pi^2 l^2 \varepsilon^2}}} > 1$, this leads to going beyond cut-off. Hence to ensure the

wave propagation, the term $\sum_{l \geq 1} \sqrt{\frac{e^{-\pi^2 l^2 \varepsilon^2}}{\sum_{l \geq 1} e^{-\pi^2 l^2 \varepsilon^2}}}$ has to be normalized. Therefore,

$$\widetilde{a}_{(j)}(z) = \sqrt{2} \sigma_a \frac{1}{\sum_{l \geq 1} e^{-\pi^2 l^2 \varepsilon^2 / 2}} \sum_{l \geq 1} e^{-\pi^2 l^2 \varepsilon^2 / 2} sin(2\pi(\frac{lz}{L} + \chi_l^{(j)})) \qquad (215)$$

APPENDIX G

PRIMARY EVALUATION OF THE PERTURBED LH POWER SPECTRUM

A. Parametric Scan Results: Systematic Comparison of Power Spectrum at Three Radial Positions for The Fluctuations Parameters : $\tilde{k}_z$, σ_n, $\tilde{x}$, $\Delta\tilde{x}$, n_{e0}

This chapter shows the primary scan results of the fluctuation parameters $\tilde{k}_z$, σ_n, $\tilde{x}$, $\Delta\tilde{x}$ and n_{e0} which are the fluctuation parallel wave number, amplitude, radial position, radial extent and background density respectively. Since evaluating how the electron density fluctuations modify the n_z power spectrum at the separatrix can be done in different methods; a rather basic way is first used in which the mean and standard deviation of the power spectrum, denoted μ and σ respectively, are calculated in order to account for the weight of n_z values in the interval $n_z \in [1,5]$. n_z is considered as a random variable with probability distribution function P_z, which is the n_z Fourier value of the power known as the power density spectrum value of n_z. Therefore, the statistical mean of the n_z Power spectrum function is given by

$$\mu = (\sum_{1 \le n_z \le 5} P_z)^{-1} \sum_{1 \le n_z \le 5} n_z * P_z, \tag{216}$$

and the standard deviation is given by

$$\sigma = ((\sum_{1 \le n_z \le 5} P_z)^{-1} \sum_{1 \le n_z \le 5} (n_z - \mu)^2 * P_z)^{1/2}. \tag{217}$$

Henceforth, additional emerging lobes, with variable n_z positions could be pinpointed in the parameter scan results. Note that $\tilde{x}$ and $\Delta\tilde{x}$ will be normalized to the SOL width which is 8 *cm* and all results are phase averaged over 20 phases equiprobable over $[0, 2\pi]$.

1. $\tilde{k}_z$ scan

For $n_{e0} = 4.4 \times 10^{17}/m^3$, $\sigma_n = 0.5$, $\tilde{x} = 0.375$, $\Delta\tilde{x} = 0.125$, and an input total power 0.5 *MW*, a scan over $\tilde{k}_z$ with 50 points between 0.1 and 10 is done.

Fig. 60 shows the change in μ and σ upon varying the wavelength of the density fluctuations. The increase in μ for $0.2k_{z0} < \tilde{k}_z < 0.5k_{z0}$ (k_{z0} is the parallel wavevector $K_{z0} = \kappa_0 \times n_{z0}$) indicates a upshift in the averaged peak of the n_z power spectrum at the
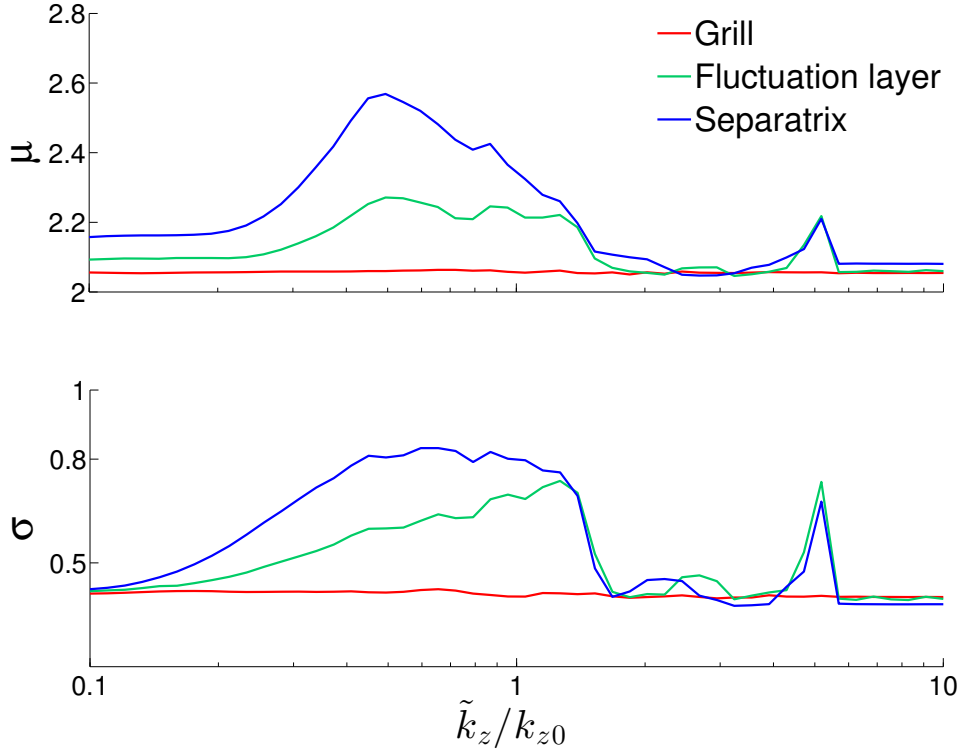
Figure 60: $\tilde{k}_z$ scan for $\sigma_n = 0.5$, $\Delta\tilde{x} = 0.125$, $\tilde{x} = 0.375$

separatrix. A maximum value of 2.57 is attained by μ at 0.49 compared to 2.06 for nonfluctuating plasma. Note that $\mu = 2.16$ for $\tilde{k}_z = 0.1k_{z0}$, due to the side lobes that appear for n_z values greater than those of the main lobe as demonstrated in Fig. 61. σ increases by 200% on the interval $\tilde{k}_z \simeq (0.45, 1.3)k_{z0}$, which shows a widening of the power spectrum main lobe or the appearance of new satellite lobes. Also, the value of σ drops sharply from 0.69 at $\tilde{k}_z = 1.4k_{z0}$ to 0.4 at $\tilde{k}_z = 1.7k_{z0}$.

The phase averaged power spectrum at the peaks $\tilde{k}_z = [0.5, 1.3, 5.2]k_{z0}$ is given in Fig. 62. At $\tilde{k}_z = 0.5k_{z0}$, the power is distributed over three lobes at the separatrix. However, for $\tilde{k}_z = 1.3k_{z0}$, which seems to be beyond the resonant region in $\tilde{k}_z$, the power is again concentrated around the main lobe at $n_z = 2.2$, with secondary lobe emerging at $n_z = 4.7$, which is also noticed for the case $\tilde{k}_z = 5.2k_{z0}$. The peak at $\tilde{k}_z = 5.2k_{z0}$ (Fig. 60) could be due to the fact that $\tilde{\lambda}_z \simeq$ *waveguide parallel width*. Though it is not important due to its negligible amplitude, the electric field and power spectra at $\tilde{k}_z = 4.4k_{z0}$ and $\tilde{k}_z = 5.2k_{z0}$ were investigated. Fig. 63 shows that power is transferred from the negative side of the power spectrum to the positive side for $\tilde{k}_z = 5.2k_{z0}$, where the electric field shows as well a slight energy transfer from the wave secondary propagative part to main one.
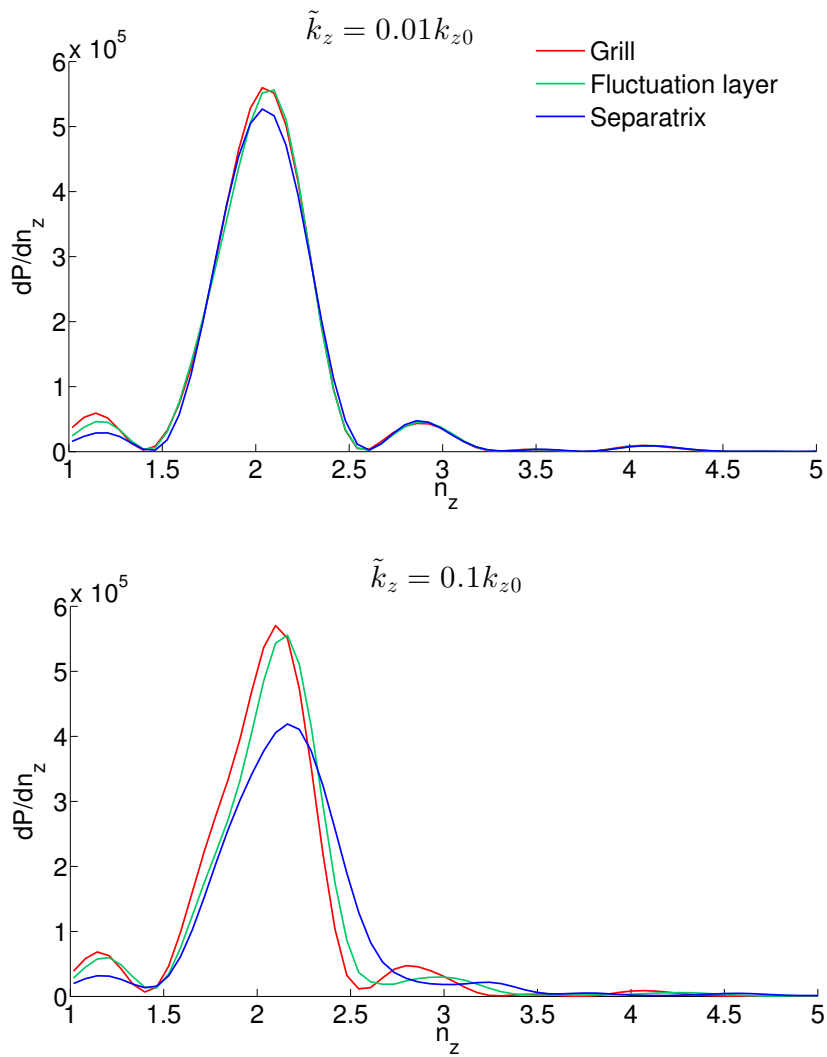
Figure 61: $\tilde{k}_z = [0.01, 0.1]k_{z0}$ shows the power spectrum at low low fluctuation wave number, in particular the initial power spectrum is retrieved at vary large fluctuation wavelength
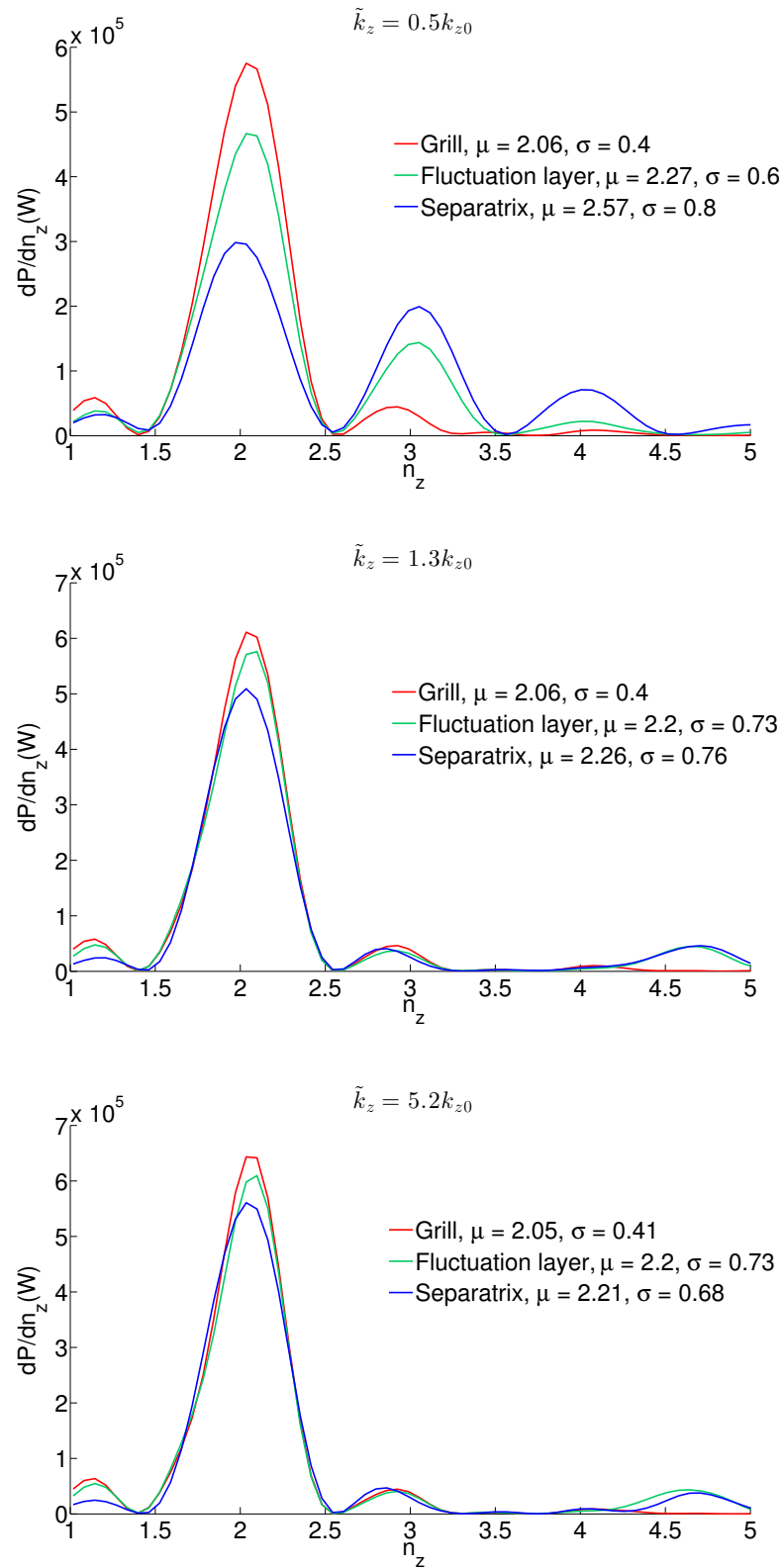
Figure 62: Comparison of the Power Spectra at 3 different peaks in $\tilde{k}_z$ scan Analysis
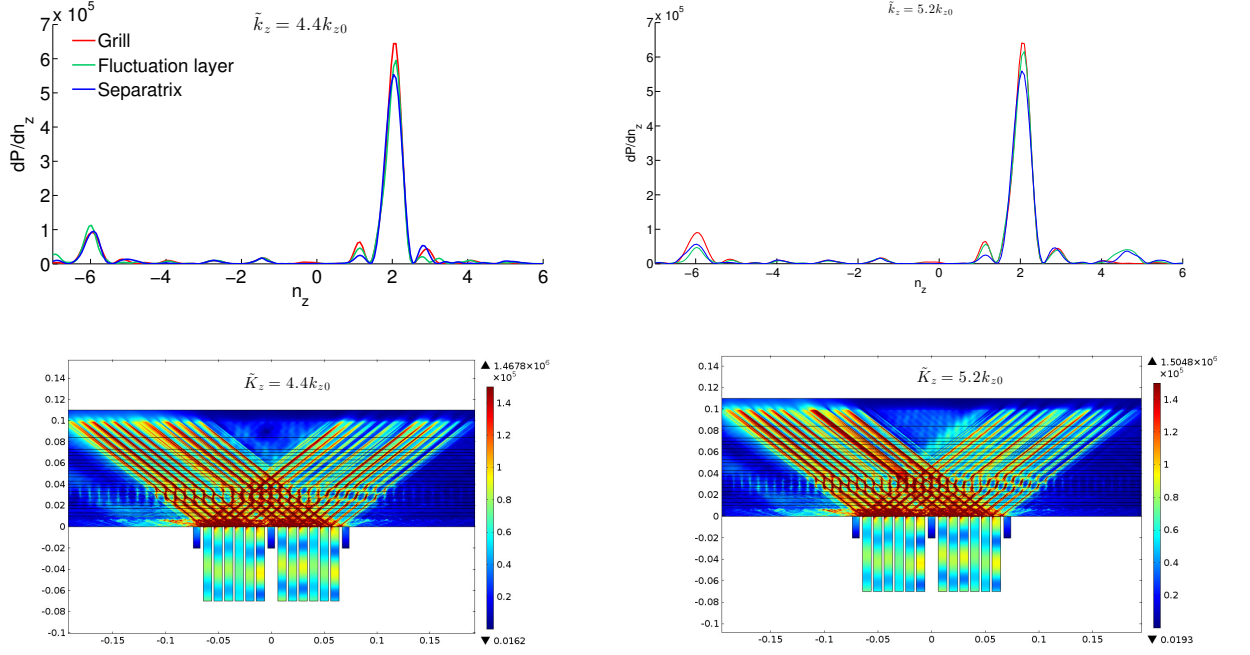
Figure 63: Comparison of electric field and power spectra for $\tilde{k}_z = 4.4k_{z0}$ and $\tilde{k}_z = 5.2k_{z0}$

2. *Effect of increasing $\Delta\tilde{x}$ and changing $\tilde{x}$*

A comparison between three values of $\Delta\tilde{x}$ is done to investigate the effect of enlarging the radial extent of fluctuations. Fig. 64 shows the obtained results for 17 points of $\tilde{k}_z$ for both values of $\tilde{x} = [0.375, 0.5]$. The strongest effect at the separatrix is attained at $\tilde{k}_z \simeq 0.5k_{z0}$, where as $\Delta\tilde{x}$ increases the peaks in μ and σ attain higher values given by $\mu_{max} = [2.48, 2.51, 2.67]$ and $\sigma_{max} = 0.83, 0.91, 0.945$ for $\Delta\tilde{x} \in [0.125, 0.1875, 0.25]$ respectively. This indicates that increasing $\Delta\tilde{x}$ induces more broadening in the n_z power spectrum.

Note that for the LH wave, $\lambda_\perp \simeq 0.09$ when the density is highest i.e for $n_e = n_{e0}(1 + \sigma_n)$ and $\sigma_n = 0.5$. Hence, $\Delta\tilde{x} = 0.09$ is explored. Fig. 65 shows a similar evolution of the μ and σ curves as in Fig. 60 in which $\Delta\tilde{x} = 0.125$. Fig. 60 also shows that for a very small value of $\Delta\tilde{x}$ given by the example $\Delta\tilde{x} = 0.02$, there is no effect.

The similar results obtained for both values $\tilde{x} = [0.375, 0.5]$ as observed in Fig. 64 , shows that the position of the fluctuation layer has no effect on the power spectrum at the separatrix.
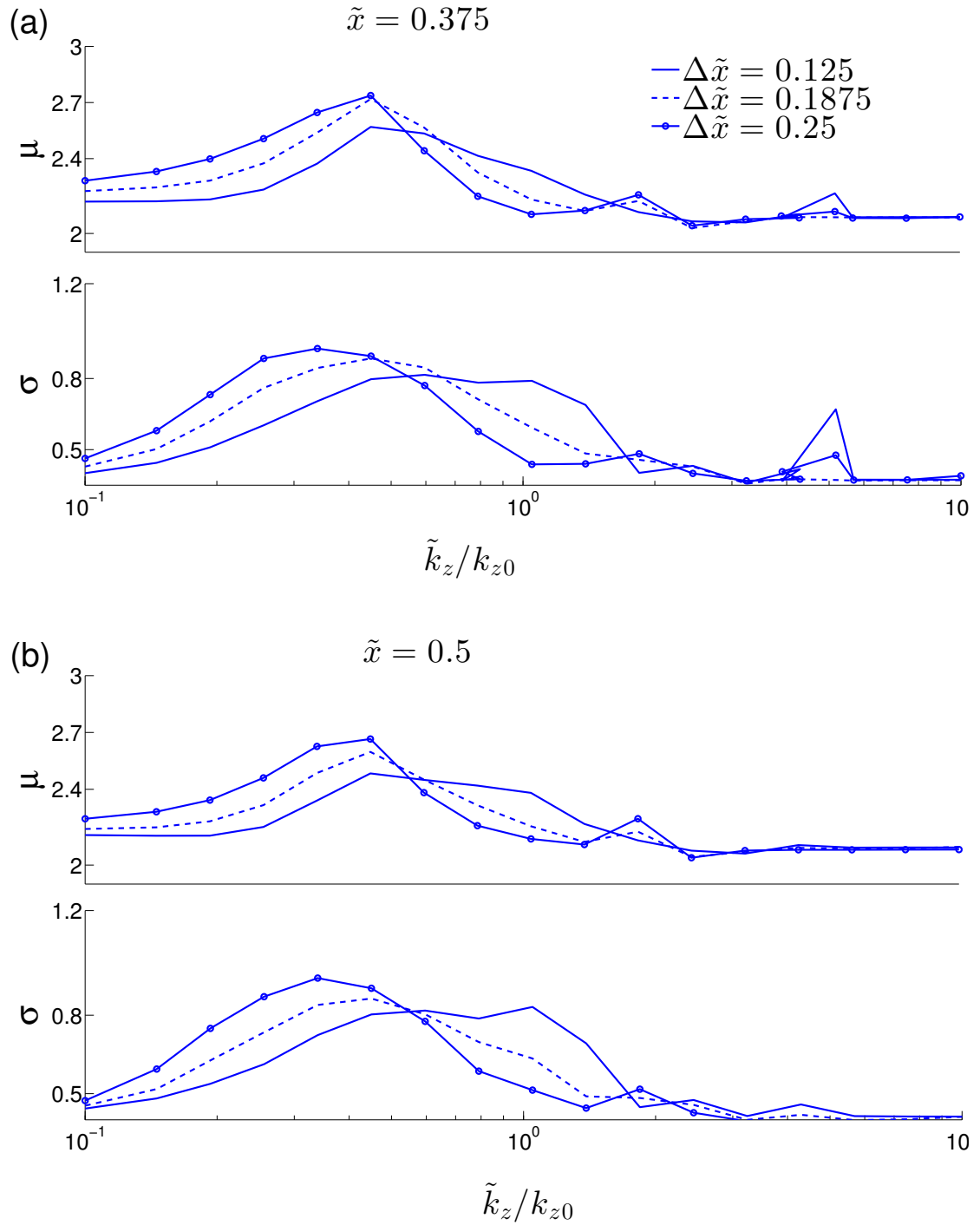
Figure 64: Effect of Increasing $\Delta\tilde{x}$ on $\tilde{k}_z$ scan for $\sigma_n = 0.5$, $\Delta\tilde{x} = [0.125, 0.185, 0.25]$, (a) $\tilde{x} = 0.375$, (b) $\tilde{x} = 0.5$.
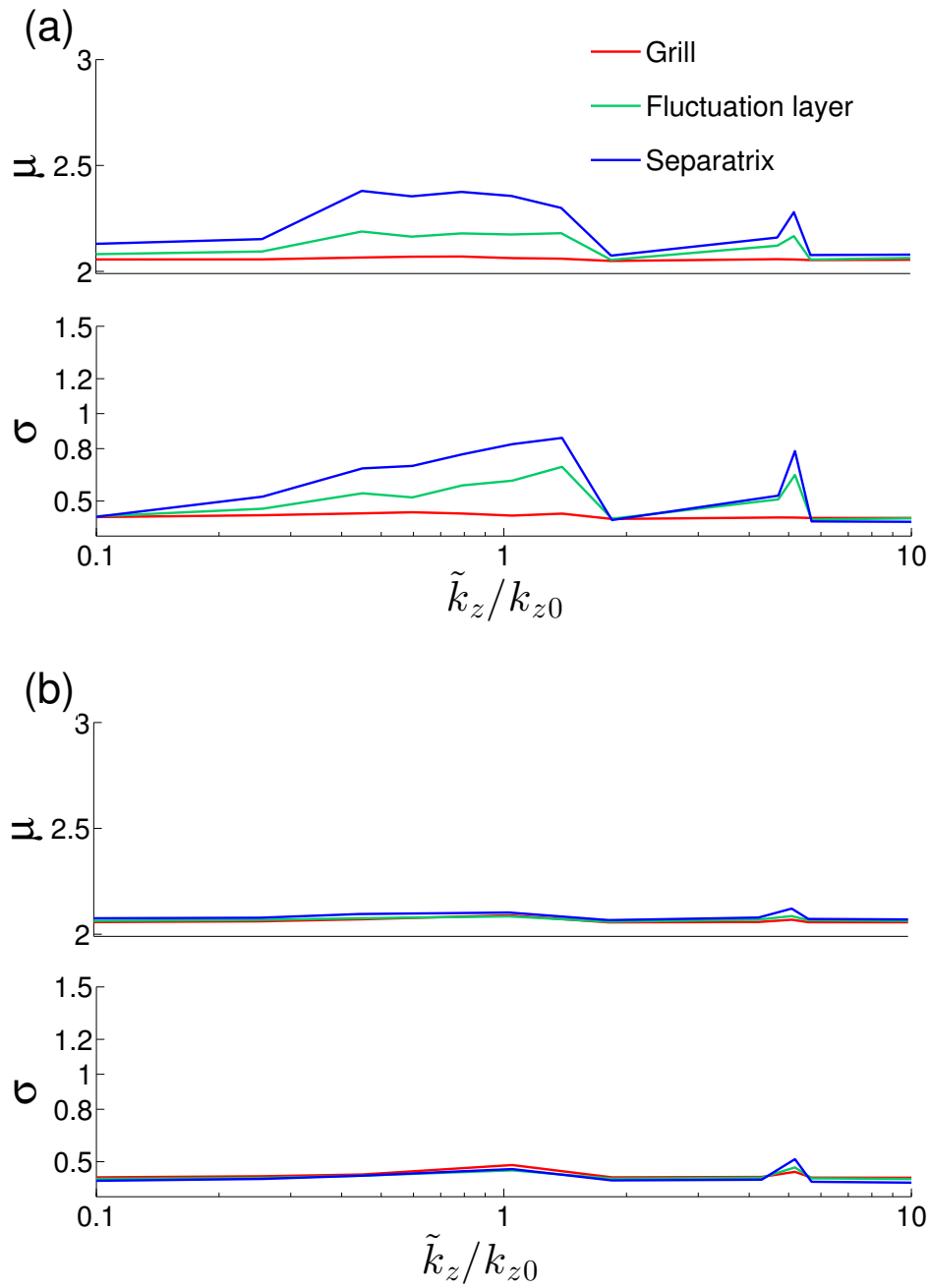
Figure 65: Effect of decreasing $\Delta\tilde{x}$ on $\tilde{k}_z$ scan for $\sigma_n = 0.5$, $\tilde{x} = 0.375$, (a)$\Delta\tilde{x} = 0.09$, (b) $\Delta\tilde{x} = 0.02$.

$\sigma_n = 0.5, \tilde{x} = 3cm, \Delta\tilde{x} = 1cm$, average over 20 phases, $x = 5cm$
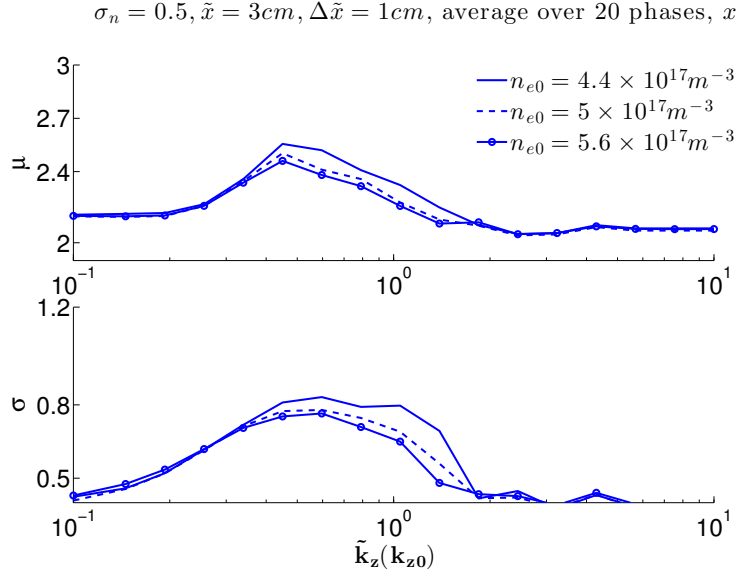
Figure 66: Effect of Increasing n_{e0} on $\tilde{k}_z$ scan

3. Effect of Increasing the Reference Density n_{e0}

The reference density n_{e0} effect is also investigated. Fig. 66 compares $\tilde{k}_z$ scan (17 points in $[0.1 - 10]k_{z0}$) for $n_{e0} \in [4.4, 5, 5.6] \times 10^{17}m^{-3}$, where $\sigma_n = 0.5, \Delta\tilde{x} = 0.125, \tilde{x} = 0.375$. It shows as a primary conclusion that as density increases, the n_z power spectrum shift and broadening at the separatrix slightly decreases. However, another study shows no effect in changing the fluctuation background density given by adding $0.5n_{e0}$ and $1.6n_{e0}$ to the fluctuating layer as shown in Fig. 68, indicating no effect of background density. Note that only 6 points of $\tilde{k}_z$ are used in Fig. 68 which are $\tilde{k}_z = [0.1, 0.5, 1, 1.7, 5.2, 10]k_{z0}$.

4. Effect of Changing the Amplitude of Density Fluctuations σ_n

A low fluctuation amplitude given by $\sigma_n = 0.2$ has negligible effect on the power spectrum as shown in Fig. 67.

a. Linearity in Power

The Linearity of the power effect is checked at three points of $\tilde{k}_z$ ($\tilde{k}_z \simeq [0.5, 0.6, 0.8]k_{z0}$). Fig. 69 shows that the fluctuations effect doesn't depend on power since μ and σ curves coincide for three different power values given by $P_{in} = [1, 0.5, 0.25]MW$.
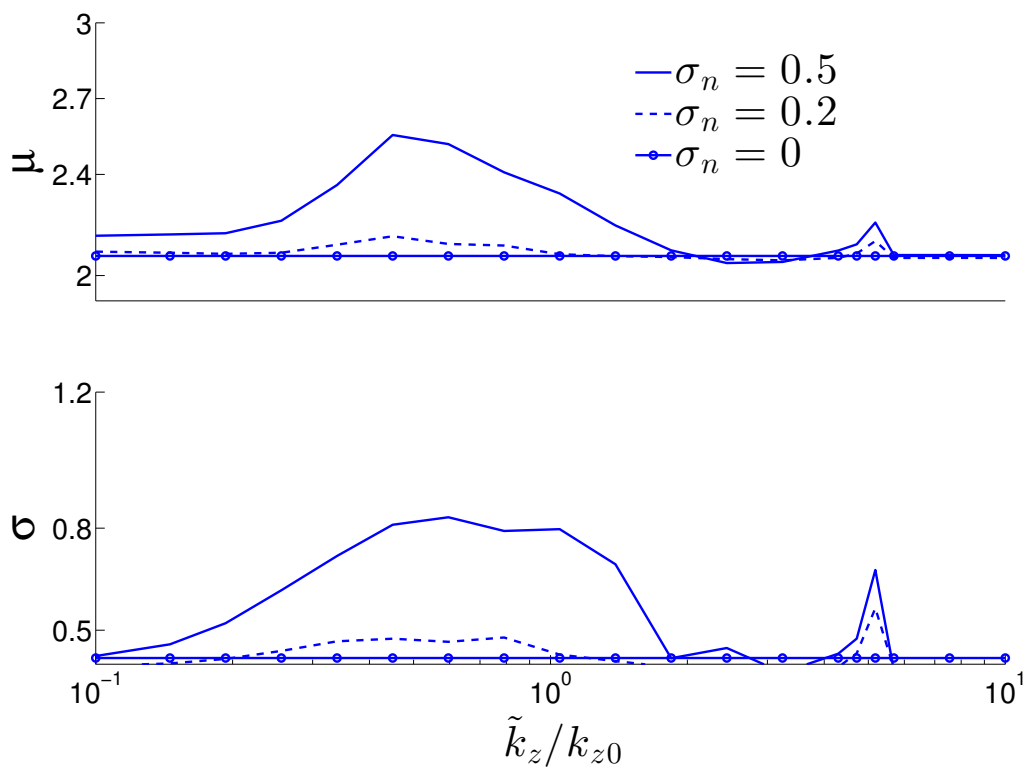
Figure 67: Effectt of decreasing σ_n on $\tilde{k}_z$ scan for $\sigma_n = 0.5$, $\Delta\tilde{x} = 0.125$, $\tilde{x} = 0.375$, $n_{e0} = 4.4 \times 10^{17} m^{-3}$.
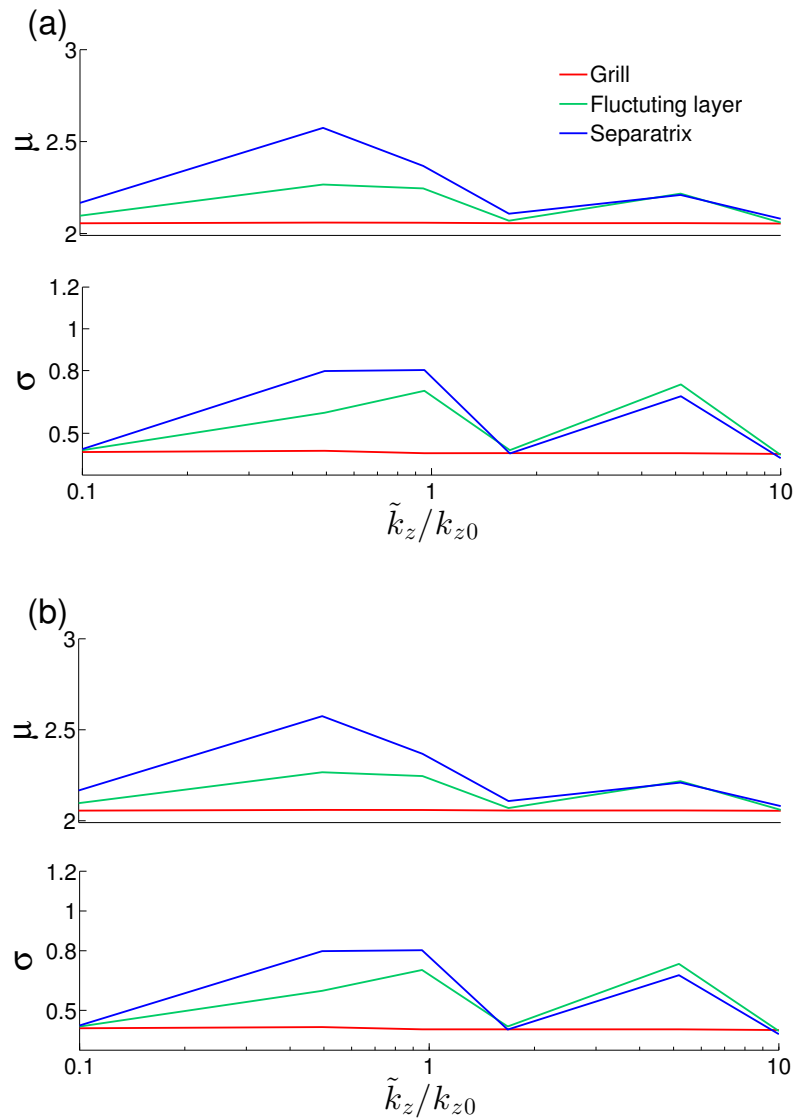
Figure 68: Effect of changing background density $n_{e0} = 4.4 \times 10^{17} m^{-3}$ by adding a constant density value to the fluctuating layer (a) $0.5 n_{e0}$ is added , (b) $1.6 n_{e0}$ is added, same results are obtained indicating no effect of the background density
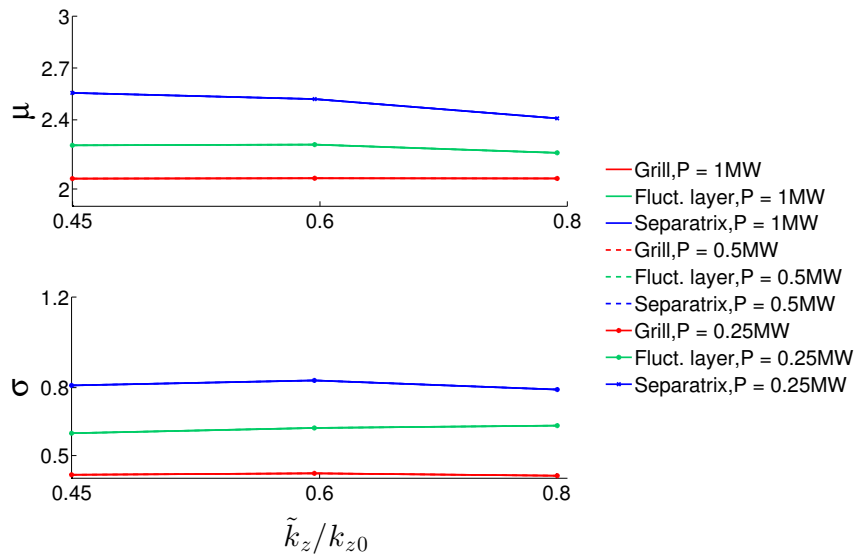
Figure 69: Power effect for three values of $\tilde{k}_z$ phase averaged for $\sigma_n = 0.5$, $\Delta \tilde{x} = 0.125$, $\tilde{x} = 0.375$, $n_{e0} = 4.4 \times 10^{17} m^{-3}$.

BIBLIOGRAPHY

[1] "http://www.efda.org/fusion/focus-on/plasma-heating-current-drive/neutral-beam-injection/."

[2] D. V. Houtte, G. Martin, A. Becoulet, J. Bucalossi, G. Giruzzi, G. T. Hoang, T. Loarer, and B. S. on behalf of the Tore Supra Team, "Recent fully non-inductive operation results in tore supra with 6 min, 1 gj plasma discharges," *Nucl. Fusion*, vol. 44, no. 5, pp. L11–L15, 2004.

[3] M. Preynas, M. Goniche, J. Hillairet, X. Litaudon, A. Ekedahl, and L. Colas, "Experimental characterization and modelling of non-linear coupling of the lower hybrid current drive power on tore supra," *Nuclear Fusion*, vol. 53, no. 1, p. 013012, 2013.

[4] J. Decker, Y. Peysson, J.-F. Artaud, E. Nilsson, A. Ekedahl, M. Goniche, J. Hillairet, and D. Mazon, "Damping of lower hybrid waves in large spectral gap configurations," in *20th Topical Conference on Radio Frequency Power in Plasmas, Sorrento, Italy, June 25-28* (AIP, ed.), 2013.

[5] V. PETRZILKA, "Non-linear coupling of the lower hybrid grill in asdex," *Nucl. Fusion*, vol. 31, pp. 1758–1767, 1991.

[6] C. Lau, G. R. Hanson, B. Labombard, Y. Lin, O. Meneghini, R. Ochoukov, R. Parker, S. Shiraiwa, J. Terry, G. Wallace, J. Wilgen, and S. Wukitch *Plasma Phys. Control. Fusion*, vol. 55, p. 02500, 2013.

[7] J. Decker, Y. Peysson, J.-F. Artaud, E. Nilsson, A. Ekedahl, M. Goniche, J. Hillairet, and D. Mazon, "Damping of lower hybrid waves in large spectral gap configurations," *Phys. Plasmas*, vol. 21, p. 092504, 2014.

[8] M. Verrall, "Climate group rejects criticisim of warnings," *Nature*, vol. 371, no. 274, 1994.

[9] "http://www.iter.org/sci/beyonditer."

[10] "http://www.iter.org/mach."

[11] P. Rebut, P. Lallia, and M. Watkins, "The critical temperature gradient model of plasma transport: applications to jet and future tokamaks," *Plasma Physics and Controlled Nuclear Fusion Research*, vol. 2, p. 191, 1988.

[12] W. Hogan. International Atomic Energy Agency, Vienna, Austria, 1995.

[13] Y. Lin-Liu and R. Miller, "Upper and lower bounds of the effective trapped particle fraction in general tokamak equilibria," *Phys. Plasmas*, vol. 2, no. 5, pp. 1666–1668, 1995.

[14] L. Spitzer, *The Physics of fully Ionized Gases*. Interscience, NY, 1956.

[15] L. Chen, R. B. White, and M. N. Rosenbluth, "Excitation of internal kink modes by trapped energetic beam ions," *Phys. Rev. Lett.*, vol. 52, pp. 1122–1125, Mar 1984.

[16] P. C. Stangeby, *The Plasma Boundary of Magnetic Fusion Devices*. IOP Publishing, Bristol and Philadelphia, 2000.

[17] F. Kazarian-Vibert, X. Litaudon, D. Moreau, R. Arslanbekov, G. T. Hoang, and Y. Peysson, "Full steady-state operation in tore supra," *Plasma Phys. Control. Fusion*, vol. 38, pp. 2113–2131, 1996.

[18] Y. PEYSSON and J. DECKER, "Numerical simulations of the radio-frequency driven toroidal current in tokamaks," *Fusion Science and Technology*, vol. 65, pp. 22–42, 2014.

[19] S. Meschino, S. Ceccuzzi, F. Mirizzi, L. Pajewski, G. Schettini, J. F. Artaud, Y. S. Bae, J. H. Belo, G. Berger-By, J. M. Bernard, A. Cardinali, C. Castaldo, R. Cesario, J. Decker, L. Delpech, A. Ekedahl, J. Garcia, P. Garibaldi, M. Goniche, D. Guilhem, H. Jia, Q. Y. Huang, J. Hillairet, G. T. Hoang, F. Imbeaux, F. Kazarian, S. H. Kim, X. Litaudon, R. Maggiora, R. Magne, L. Marfisi, D. Milanesio, W. Namkung, L. Panaccione, Y. Peysson, P. K. Sharma, M. Schneider, A. A. Tuccillo, O. Tudisco, G. Vecchi, R. Villari, and K. Vulliez, "Bends in oversized rectangular waveguide," *FUSION ENGINEERING AND DESIGN*, vol. 86, pp. 746–749, OCT 2011. 26th Symposium on Fusion Technology (SOFT), Porto, PORTUGAL, SEP 27-OCT 01, 2010.

[20] D. Guilhem, A. Argouarch, J.-M. Bernard, F. Bouquey, L. Colas, L. Delpech, F. Durodie, A. Ekedahl, J. Van Helvoirt, J. Hillairet, *et al.*, "Implications of the tore-supra west-project on radio-frequency additionnal heating systems," *Plasma Science, IEEE Transactions on*, vol. 42, no. 3, pp. 600–605, 2014.

[21] E. Lerche, D. Van Eester, J. Ongena, M. Mayoral, M. Laxaback, F. Rimini, A. Argouarch, P. Beaumont, T. Blackman, V. Bobkov, *et al.*, "Optimizing ion-cyclotron resonance frequency heating for iter: dedicated jet experiments," *Plasma Physics and Controlled Fusion*, vol. 53, no. 12, p. 124019, 2011.

[22] X. Litaudon, I. Voitsekhovitch, J. Artaud, P. Belo, J. P. Bizarro, T. Casper, J. Citrin, E. Fable, J. Ferreira, J. Garcia, L. Garzotti, G. Giruzzi, J. Hobirk, G. Hogeweij, F. Imbeaux, E. Joffrin, F. Koechl, F. Liu, J. Lonnroth, D. Moreau, V. Parail, M. Schneider, P. Snyder, the ASDEX-Upgrade Team, J.-E. Contributors, and the EU-ITM ITER Scenario Modelling Group, "Modelling of hybrid scenario: from present-day experiments towards iter," *Nucl. Fusion*, vol. 53, p. 073024, 2013.

[23] L. Colas, A. Argouarch, S. Brémond, M. Chantant, Y. Corre, M. Firdaouss, M. Goniche, D. Guilhem, J.-P. Gunn, J. Jacquot, *et al.*, "Rf-sheath patterns modification via novel faraday screen and strap voltage imbalance on tore supra ion cyclotron antennae," *Journal of Nuclear Materials*, vol. 438, pp. S330–S333, 2013.

[24] A. Becoulet, "Heating and current drive regimes in the ion cyclotron range of frequency," *Plasma Physics and Controlled Fusion*, vol. 38, no. 12A, p. A1, 1996.

[25] N. Fisch, "Theory of current drive in plasmas," *Rev. Mod. Phys.*, vol. 59, no. 1, pp. 175–234, 1987.

[26] R. Prater, "Heating and current drive by electron cyclotron waves," *Phys. Plasmas*, vol. 11, pp. 2349–2376, 2004.

[27] N. Fisch, "Confining a tokamak plasma with RF-driven currents," *Phys. Rev. Lett.*, vol. 41, no. 13, pp. 873–876, 1978.

[28] "Iter physics basis," *Chapter 6: Nucl. Fusion*, vol. 39, no. 2495, 1999.

[29] J. Wesson, *Tokamaks*. The International Series of Monographs on Physics, Clarendon Press, third ed., 2004.

[30] C. Kessel, "Bootstrap current in a tokamak," *Nucl. Fusion*, vol. 34, no. 9, pp. 1221–1238, 1994.

[31] T. S. Taylor, "Physics of advanced tokamak," *Plasma Phys. Control. Fusion*, vol. 39, no. 12B, pp. B47–B73, 1997.

[32] K. Y. S. T. O. T. T. S. S. Y. K. Y. I. A. H. T. K. H. H. S. N. O. S. H. F. T. I. S. K. Y. S. T. O. T. T. S. S. Y. K. Y. I. A. H. T. K. H. H. S. N. O. S. H. F. T. Fujita T, Ide S, "Quasisteady high-confinement reversed shear plasma with large bootstrap current fraction under full noninductive current drive condition in jt-60u," *Phys Rev Lett.*, vol. 87, p. 085001, AUG 2001.

[33] T. OHKAWA, "New methods of driving plasma current in fusion devices," *Nucl. Fusion*, vol. 10, no. 2, pp. 185–188, 1970.

[34] "http://www.efda.org/newsletter/efficient-high-power-plasma-heating/."

[35] P. Bonoli, "Linear theory of lower hybrid heating," *IEEE Trans. on Plasma Sci.*, vol. PS-12, no. 2, pp. 95–107, 1984.

[36] M. Brambilla, *Kinetic Theory of Plasma Waves*. Oxford Science Publications, 1998.

[37] Y. Peysson, G. Rey, R. Arslanbekov, V. Basiuk, B. beaumont, G. Berger-By, P. Bibet, J. J. Capitain, J. Carrasco, J. P. Crenn, P. Froissard, P. Garin, M. Goniche, L. Ladurelle, X. Litaudon, D. Moreau, M. Pain, M. Tareb, J. Tonon, J. P. Bizarro, J. S. Ferreira, and P. Rodrigues, "Long pulse rf experiments on tore supra : results and simulations," *IAEA*, vol. 3, pp. 279–294, 1996.

[38] K. Kupfer, D. Moreau, and X. Litaudon, "Statistical theory of wave propagation and multipass absorption for current drive in tokamaks," *Phys. Fluids B*, vol. 5, no. 12, pp. 4391–4407, 1993.

[39] X. Litaudon, F. Crisanti, B. Alper, J. F. Artaud, Y. F. Baranov, E. Barbato, V. Basiuk, A. Becoulet, M. Becoulet, C. Castaldo, C. D. Challis, G. D. Conway, R. Dux, L. G. Eriksson, B. Esposito, C. Fourment, D. Frigione, X. Garbet, C. Giroud, N. C. Hawkes, P. Hennequin, G. T. A. Huysmans, F. Imbeaux, E. Joffrin, P. J. Lomas, P. Lotte, P. Maget, M. Mantsinen, J. Mailloux, D. Mazon, F. Milani, D. Moreau, V. Parail, E. Pohn, F. G. Rimini, Y. Sarazin, G. Tresset, K. D. Zastrow, M. Zerbini, and contributors to the EFDA-JET Workprogramme, "Towards fully non-inductive current drive operation in jet," *Plasma Phys. Control. Fusion*, vol. 44, pp. 1057–1086, 2002.

[40] C. Gormezano, A. C. C. Sips, T. C. Luce, S. Ide, A. Bécoulet, X. Litaudon, A. Isayama, J. Hobirk, M. R. Wade, T. Oikawa, R. Prater, A. Zvonkov, B. Lloyd, T. Suzuki, E. Barbato, P. Bonoli, and C. K. P. an, "Iter review. chapter 6: Steady state operation," *Nuc. Fusion*, vol. 47, pp. S285–S336, 2007.

[41] P. Bibet, B. Beaumont, J. Belo, L. Delpech, A. Ekedahl, G. Granucci, F. Kazarian, X. Litaudon, J. Mailloux, F. Mirizzi, V. Pericoli, M. Prou, K. Rantamaki, and A. Tuccillo, "Toward a lhcd system for iter," *Fusion Eng. and Design*, vol. 74, p. 419, 2005.

[42] N. Fisch and A. Boozer, "Creating an asymmetric plasma resistivity with waves," *Phys. Rev. Lett.*, vol. 45, no. 9, pp. 720–722, 1980.

[43] D. Purohit, T. Bigelow, D. Billava, T. Bonicelli, J. Caughman, C. Darbos, G. Denisov, F. Gandini, T. Gassmann, M. Henderson, *et al.*, "An overview of control system for the iter electron cyclotron system," *Fusion Engineering and Design*, vol. 86, no. 6, pp. 959–962, 2011.

[44] L. Urso, H. Zohm, A. Isayama, M. Maraschek, E. Poli, A. U. Team, *et al.*, "Asdex upgrade—jt-60u comparison and ecrh power requirements for ntm stabilization in iter," *Nuclear Fusion*, vol. 50, no. 2, p. 025010, 2010.

[45] J. Decker, Y. Peysson, J. Hillairet, J.-F. Artaud, V. Basiuk, A. Becoulet, A. Ekedahl, M. Goniche, G. Hoang, F. Imbeaux, A. Ram, and M. Schneider, "Calculations of lower hybrid current drive in iter," *Nucl. Fusion*, vol. 51, p. 073025, 2011.

[46] M. Preynas, A. Ekedahl, N. Fedorczak, M. Goniche, D. Guilhem, J. Gunn, J. Hillairet, X. Litaudon, J. Achard, G. Berger-By, J. Belo, E. Corbel, L. Delpech, T. Ohsako, and M. Prou, "Coupling characteristics of the iter-relevant lower hybrid antenna in tore supra:experiments and modelling," *Nuclear Fusion*, vol. 51, no. 2, p. 023001, 2011.

[47] B. P. B. J. B. B. C. R. C. M. F. P. K. A. L. F. L. A. M. J. M. F. O. J. P. C. T. P. T. A. V. J.-C. W. B. W. R. Jorge H., Bibet B. and W. D.J., "An iter-relevant passive active multijunction launcher for lower hybrid current drive in jet-grade plasmas," *Nucl. Fusion*, vol. 51, no. 08301, 2011.

[48] J. K. P. P. N. S. P. P. P. J. S. J. Zácek F., Klíma R. and K. L., "Spectrum broadening and fluctuations of lower hybrid waves observed in the castor tokamak," *Plasma Phys. Control. Fusion*, vol. 41, no. 1221, 1999.

[49] Y. Peysson, E. Sébelin, X. Litaudon, D. Moreau, J. C. Miellou, M. Shoucri, and I. P. Shkarofsky, "Full wave modelling of the lower hybrid current drive in tokamaks," *Nucl. Fusion*, vol. 38, no. 6, pp. 939–944, 1998.

[50] M. Brambilla, "Propagation and absorption of waves at the lower hybrid resonance," *Plasma Phys.*, vol. 18, pp. 669–674, 1976.

[51] N. T.K., 1986.

[52] D. M. D. and T. Nguyen, "Couplage de l'onde lente au voisinage de la fréquence hybride basse dans les grands tokamaks," 1984.

[53] G. M. D. Moreau, C. Gormezano and T. Nguyen, "Density regimes for lower hybrid wave coupling in tokamak plasmas," *Radiation in Plasmas B. McNamara (Ed.), World Scientific, Singapour*, vol. 1, no. 331, 1984.

[54] C. Gormezano and D. Moreau, "Lower hybrid wave coupling in the wega tokamak," *Plasma Phys. Control. Fusion*, vol. 26, no. 553, 1984.

[55] A. ENGLAND, O. ELDRIDGE, S. KNOWLTON, M. PORKOLAB, and J. WILSON, "Power transmission and coupling for radiofrequency heating of plasmas," *Nucl. Fusion*, vol. 29, pp. 1527–1633, 1989.

[56] R. Cairns, *Radiofrequency Heating of Plasmas.* Adam Hilger, 1991.

[57] X. Litaudon and D. Moreau, "Coupling of slow waves near the lower hybrid frequency in jet," *Nucl. Fusion*, vol. 30, p. 471, 1990.

[58] X. Litaudon, G. Berger-by, P. Bibet, J. Bizarro, J. Capitain, J. Carrasco, M. Goniche, G. Hoang, K. Kupfer, R. Magne, D. Moreau, Y. Peysson, J.-M. Rax, G. Rey, D. Rigaud, and G. Tonon, "Lower hybrid wave coupling in tore supra through multijunction launchers," *Nucl. Fusion*, vol. 32, p. 1883, 1992.

[59] C. A. Balanis, *Antenna theory analysis and design.* 2005.

[60] P. Jacquet, Y. Demers, G. A. Chaudron, V. Glaude, A. C. ÌĄ, A. D. ÌĄ, R. Mireault, A. Robert, and L. Vachon, "Microwave probe diagnostic for the lower hybrid multijunction antenna on tdev," *Rev. Sci. Instrum.*, vol. 68, no. 2, pp. 1176–1182, 1997.

[61] R. R. Parker *Massachusetts Inst. Technology, Research Laboratory of Electronics*, vol. 97, 1971.

[62] W. Hooke, "Course on instabilities and confinement in toroidal plasmas," *International School of Plasma Physics, Varenna, Italy*, p. 269, 1971.

[63] p. C. 2nd Top. Conf. Lubbok, Texas, ed., *RF Plasma Heating*, 1974.

[64] M. BRAMBILLA, "Slow-wave launching at the lower hybrid frequency using a phased waveguide array," *Nucl. Fusion*, vol. 16, pp. 47–54, 1976.

[65] T. Yamamoto, T. Imai, M. Shimada, N. Suzuki, M. Maeno, S. Konoshima, T. Fujii, K. Uehara, T. Nagashima, A. Funahashi, and N. Fujisawa, "Experimental observation of the rf-driven current by the lower-hybrid wave in a tokamak," *Phys. Rev. Lett.*, vol. 45, pp. 716–719, Sep 1980.

[66] K. BERNHARDI and K. WIESEMANN, "X-ray bremsstrahlung measurements on an ecr-discharge in a magnetic mirror," *Plasma Physics*, vol. 24, pp. 867–884, 1982.

[67] D. Moreau and the Tore Supra Team, "Lower-hybrid current drive experiments in tore supra," *Phys. Fluids B*, vol. 4, no. 7, pp. 2165–2175, 1992.

[68] C. GORMEZANO, G. BOSIA, and M. BRUSATI *Control. Fusion and Plasma Physics (Proc. 18th Eur. Conf. Berlin)*, vol. 15C, 1991.

[69] T. Imai and the JT-60 Team *Plasma Physics and Controlled Fusion Research*, vol. 1, 1990.

[70] T. WATARI, "Review of japanese results on heating and current drive," *PLASMA PHYSICS AND CONTROLLED FUSION*, vol. 35, pp. A181–A198, FEB 1993. EUROPHYSICS TOPICAL CONF ON RADIOFREQUENCY HEATING AND CURRENT DRIVE OF FUSION DEVICES, BRUSSELS, BELGIUM, JUL 08-10, 1992.

[71] P. H. Rebut, D. Boucher, C. Gormezano, B. E. Keen, and M. L. Watkins, "A fusion reactor: continuous or semi-continuous," *Plasma Phys. Control. Fusion*, vol. 35, pp. A3–A14, 1993.

[72] A. A. Tuccillo, E. Barbato, Y. S. Bae, A. Bécoulet, S. Bernabei, P. Bibet, G. Calabrò, A. Cardinali, C. Castaldo, R. Cesario, M. H. Cho, S. Cirant, F. Crisanti, A. Ekedahl, L. G. Eriksson, and D. F. and, "Progress in lhcd: a tool for advanced regimes on iter," *Plasma Phys. Control. Fusion*, vol. 47, no. 12B, pp. B363–B377, 2005.

[73] G. T. Hoang, A. Bécoulet, J. Jacquinot, J. F. Artaud, Y. S. Bae, B. Beaumont, J. H. Belo, G. Berger-By, J. P. S. Bizarro, P. Bonoli, M. H. Cho, J. Decker, L. Delpech, A. Ekedahl, J. Garcia, and G, "A lower hybrid current drive system for ITER," *Nucl. Fusion*, vol. 49, no. 7, p. 075001, 2009.

[74] J. Hillairet, A. Ekedahl, M. Goniche, Y. S. Bae, J. Achard, A. Armitano, B. Beckett, J. Belo, G. Berger-By, J. M. Bernard, E. Corbel, L. Delpech, J. Decker, R. Dumont, D. Guilhem, G. T. Hoang, F. Kazarian, H. J. Kim, X. Litaudon, R. Magne, L. Marfisi, P. Mollard, W. Namkung, E. Nilsson, S. Park, Y. Peysson, M. Preynas, P. K. Sharma, M. Prou, and T. S. Team, "Recent progress on lower hybrid current drive and implications for ITER," *NUCLEAR FUSION*, vol. 53, p. 073004, JUL 2013.

[75] A. Ekedahl, L. Delpech, M. Goniche, D. Guilhem, J. Hillairet, M. Preynas, P. K. Sharma, J. Achard, Y. S. Bae, X. Bai, C. Balorin, Y. Baranov, V. Basiuk, A. Becoulet, J. Belo, G. Berger-By, S. Bremond, C. Castaldo, S. Ceccuzzi, R. Cesario, E. Corbel, X. Courtois, J. Decker, E. Delmas, X. Ding, D. Douai, C. Goletto, J. P. Gunn, P. Hertout, G. T. Hoang, F. Imbeaux, K. K. Kirov, X. Litaudon, R. Magne, J. Mailloux, D. Mazon, F. Mirizzi, P. Mollard, P. Moreau, T. Oosako, V. Petrzilka, Y. Peysson, S. Poli, M. Prou, F. Saint-Laurent, F. Samaille, and B. Saoutic, "Validation of the iter-relevant passive-active-multijunction lhcd launcher on long pulses in tore supra," *Nuclear Fusion*, vol. 50, no. 11, p. 112002, 2010.

[76] Y. Peysson, "Status of lower hybrid current drive," in *13th Topical Conference on Radio Frequency Power in Plasmas* (S. Bernabei and F. Paoletti, eds.), vol. 485 of *AIP Conference Proceedings*, (New York), pp. 183–192, American Institute of Physics, 1999.

[77] S. Shiraiwa, G. Baek, P. T. Bonoli, I. C. Faust, A. E. Hubbard, O. Meneghini, R. R. Parker, G. M. Wallace, J. R. W. R. W., H. A. P., Smirnov, D. Brunner, B. LaBombard, C. Lau, R. Mumgaard, S. Scott, N. Tsujii, S. Wolfe, and A. C.-M. Team, "Progress towards steady-state regimes in alcator c-mod," *Nucl. Fusion*, vol. 53, NOV 2013.

[78] P. T. Bonoli, "Review of recent experimental and modeling progress in the lower hybrid range of frequencies at iter relevant parameters," *Phys. Plasmas*, vol. 21, p. 061508, 2014.

[79] "https://www.euro-fusion.org/?faqtags=jet."

[80] "http://www-fusion-magnetique.cea.fr/gb/cea/ts/ts.htm."

[81] E. T. SUPRA *in Proceedings of the 15th Confer- ence on Plasma Physics and Controlled Nuclear Fusion Research, Seville (International Atomic Energy Agency, Vienna, 1995), Vienna, 1995 Vol. 1, IAEA-CN-60/A1-5 Institute of Physics, Bristol, U.K.,*, p. 105, 1995.

[82] F. Romanelli and J. E. Contributors, "Overview of the jet results with the iter-like wall," *Nucl. Fusion*, vol. 53, p. 104002, 2013.

[83] B. Saoutic, J. Abiteboul, L. Allegretti, S. Allfrey, J. M. Ane, T. Aniel, A. Argouarch, J. F. Artaud, M. H. Aumenier, S. Balme, V. Basiuk, O. Baulaigue, P. Bayetti, A. Becoulet, M. Becoulet, M. S. Benkadda, F. Benoit, G. Berger-by, J. M. Bernard, B. Bertrand, P. Beyer, A. Bigand, J. Blum, D. Boilson, G. Bonhomme, H. Bottollier-Curtet, C. Bouchand, F. Bouquey, C. Bourdelle, S. Bourmaud, C. Brault, S. Bremond, C. Brosset, J. Bucalossi, Y. Buravand, P. Cara, V. Catherine-Dumont, A. Casati, M. Chantant, M. Chatelier, G. Chevet, D. Ciazynski, G. Ciraolo, F. Clairet, M. Coatanea-Gouachet, L. Colas, L. Commin, E. Corbel, Y. Corre, X. Courtois, R. Dachicourt, M. D. Febrer, M. D. Joanny, R. Daviot, H. De Esch, J. Decker, P. Decool, P. Delaporte, E. Delchambre, E. Delmas, L. Delpech, C. Desgranges, P. Devynck, T. Dittmar, L. Doceul, D. Douai, H. Dougnac, J. L. Duchateau, B. Dugue, N. Dumas, R. Dumont, A. Durocher,

F. X. Duthoit, A. Ekedahl, D. Elbeze, M. El Khaldi, F. Escourbiac, F. Faisse, G. Falchetto, M. Farge, J. L. Farjon, M. Faury, N. Fedorczak, C. Fenzi-Bonizec, M. Firdaouss, Y. Frauel, X. Garbet, J. Garcia, J. L. Gardarein, L. Gargiulo, P. Garibaldi, E. Gauthier, O. Gaye, A. Geraud, M. Geynet, P. Ghendrih, I. Giacalone, S. Gibert, C. Gil, G. Giruzzi, M. Goniche, V. Grandgirard, C. Grisolia, G. Gros, A. Grosman, R. Guigon, D. Guilhem, B. Guillerminet, R. Guirlet, J. Gunn, O. Gurcan, S. Hacquin, J. C. Hatchressian, P. Hennequin, C. Hernandez, P. Hertout, S. Heuraux, J. Hillairet, G. T. Hoang, C. Honore, M. Houry, T. Hutter, P. Huynh, G. Huysmans, F. Imbeaux, E. Joffrin, J. Johner, L. Jourd'Heuil, Y. S. Katharria, D. Keller, S. H. Kim, M. Kocan, M. Kubic, B. Lacroix, V. Lamaison, G. Latu, Y. Lausenaz, C. Laviron, F. Leroux, L. Letellier, M. Lipa, X. Litaudon, T. Loarer, P. Lotte, S. Madeleine, P. Magaud, P. Maget, R. Magne, L. Manenc, Y. Marandet, G. Marbach, J. L. Marechal, L. M. Si, C. Martin, G. Martin, V. Martin, A. Martinez, J. P. Martins, R. Masset, D. Mazon, N. Mellet, L. Mercadier, A. Merle, D. Meshcheriakov, O. Meyer, L. Million, M. Missirlian, P. Mollard, V. Moncada, P. Monier-Garbet, D. Moreau, P. Moreau, L. Morini, M. Nannini, M. N. Habib, E. Nardon, H. Nehme, C. Nguyen, S. Nicollet, R. Nouilletas, T. Ohsako, M. Ottaviani, S. Pamela, H. Parrat, P. Pastor, A. L. Pecquet, B. Pegourie, Y. Peysson, I. Porchy, C. Portafaix, M. Preynas, M. Prou, J. M. Raharijaona, N. Ravenel, C. Reux, P. Reynaud, M. Richou, H. Roche, P. Roubin, R. Sabot, F. Saint-Laurent, S. Salasca, F. Samaille, A. Santagiustina, Y. Sarazin, A. Semerok, J. Schlosser, M. Schneider, M. Schubert, F. Schwander, J. L. Segui, G. Selig, P. Sharma, J. Signoret, A. Simonin, S. Song, E. Sonnendruker, F. Sourbier, P. Spuig, P. Tamain, M. Tena, J. M. Theis, D. Thouvenin, A. Torre, J. M. Travere, E. Tsitrone, J. C. Vallet, E. Van der Plas, A. Vatry, J. M. Verger, L. Vermare, F. Villecroze, D. Villegas, R. Volpe, K. Vulliez, J. Wagrez, T. Wauters, L. Zani, D. Zarzoso, and X. L. Zou, "Contribution of Tore Supra in preparation of ITER," *NUCLEAR FUSION*, vol. 51, p. 094014, SEP 2011.

[84] S. Bernabei, J. C. Hosea, C. C. Kung, G. D. Loesser, J. Rushinski, J. R. Wilson, R. R. Parker, and M. Porkolab, "Design of a compact lower hybrid coupler for alcator c-mod," *Fusion science and technology*, vol. 43, no. 2, pp. 145–152, 2003.

[85] S. Park, H. Do, and J. Jeong, "Development status of kstar 5 ghz lhcd system," *Fusion Eng. Des.*, vol. 85, pp. 197–204, 2010.

[86] A. Becoulet, G. T. Hoang, J. F. Artaud, Y. S. Bae, J. Belo, G. Berger-By, J. M. Bernard, P. Cara, A. Cardinali, C. Castaldo, S. Ceccuzzi, R. Cesario, M. H. Cho, J. Decker, L. Delpech, H. J. Do, A. Ekedahl, J. Garcia, P. Garibaldi, M. Goniche, D. Guilhem, C. Hamlyn-Harris, J. Hillairet, Q. Y. Huang, F. Imbeaux, H. Jia, F. Kazarian, S. H. Kim, Y. Lausenaz, X. Litaudon, R. Maggiora, R. Magne, L. Marfisi, S. Meschino, D. Milanesio, F. Mirizzi, P. Mollard, W. Namkung, L. Pajewski, L. Panaccione, S. Park, H. Park, Y. Peysson, A. Saille, F. Samaille, G. Schettini, M. Schneider, P. K. Sharma, A. Tuccillo, O. Tudisco, G. Vecchi, R. Villari, K. Vulliez, Y. Wu, H. L. Yang, and Q. Zeng, "Steady state long pulse tokamak operation using Lower Hybrid Current Drive," *FUSION ENGINEERING AND DESIGN*, vol. 86, pp. 490–496, OCT 2011. 26th Symposium on Fusion Technology (SOFT), Porto, PORTUGAL, SEP 27-OCT 01, 2010.

[87] P. Bibet, G. Agarici, M. Chantant, J. J. Cordier, C. Deck, L. Doceul, A. Durocher, A. Ekedahl, P. Froissard, L. Garguiolo, L. Garampon, M. Goniche, P. Hertou, F. Kazarian, D. Lafon, C. Portafaix, G. Rey, F. Samaille, F. Surle, and G. Tonon, "New advanced launcher for lower hybrid current drive on tore supra," *Fusion engineering and design*, vol. 51-52, pp. 741–746., 2000.

[88] G. Rey, R. Aymar, and G. Berger-By *Proc. 15th Symp. on Fusion Technol.*, vol. 1, p. 514, 1988.

[89] A. EKEDAHL, M. GONICHE, D. GUILHEM, F. KAZARIAN, Y. PEYSSON, and T. S. TEAM, "Lower hybrid current drive in tore supra," *Fus. Science Technology*, vol. 56, no. 1150-1172, 2009.

[90] Y. Peysson and the Tore Supra Team, "High power lower hybrid current drive experiments in the tore supra tokamak," *Nucl. Fusion*, vol. 41, no. 11, pp. 1703–1713, 2001.

[91] R. J. Dumont, M. Goniche, J.-F. Artaud, V. Basiuk, C. Bourdelle, Y. Corre, J. Decker, A. Ekedahl, D. Elbèze, G. Giruzzi, G.-T. Hoang, F. Imbeaux, X. Litaudon, P. Lotte, P. Maget, D. Mazon, E. Nilsson, B. Saoutic, and the Tore Supra Team, "Advances in multi-megawatt, long pulse operation in tore supra," in *39th European Physical Society Conference on Plasma Physics and Controlled Fusion, Stockholm, Sweden, 2-6 July 2012*, 2012.

[92] D. Guilhem, J. Achard, J. Belo, B. Bertrand, Z. Bej, P. Bibet, C. Brun, M. Chantant, E. Delmas, L. Delpech, Y. Doceul, A. Ekedahl, C. Goletto, M. Goniche, J. Hatchressian, J. Hillairet, M. Houry, P. Joubert, M. Lipa, S. Madeleine, A. Martinez, M. Missirlian, S. Poli, C. Portafaix, D. Raulin, A. Saille, B. Soler, D. Thouvenin, J. Verger, K. VuUiez, and B. Zago, "Passive active multi-junction 3,7 ghz launcher for tore-supra long pulse experiments. manufacturing process and tests," *AIP Conference Proceedings*, vol. 1187, no. 1, pp. 435–438, 2009.

[93] J. Hillairet, D. Voyer, A. Ekedahl, M. Goniche, M. Kazda, O. Meneghini, D. Milanesio, and M. Preynas, "Aloha: an advanced lower hybrid antenna coupling code," *Nuclear Fusion*, vol. 50, no. 12, p. 125010, 2010.

[94] L. Delpech, J.Achard, A. Armitano, J. Artaud, Y. Bae, J. Belo, G. Berger-By, F. Bouquey, M. Cho, E. Corbel, J. Decker, H.Do, R. Dumont, A. Ekedahl, P. Garibaldi, M. Goniche, D. Guilhem, J. Hillairet, G. Hoang, H. Kim, J. Kim, H.Kim, J. Kwak, R.Magne, P. Mollard, Y. Na, W. Namkung, Y. Oh, S.Park, H.Park, Y. P. andS.Poli, M. Prou, F. Samaille, H. Yang, and T. T. S. Team, "Advances in multi-megawatt lower hybrid technology in support of steady-state tokamak operation," *Nucl. Fusion*, vol. 54, p. 103004, 2014.

[95] W. Houlberg, C. Gormezano, J. Artaud, E. Barbato, V. Basiuk, A. Bécoulet, P. Bonoli, R. Budny, L. Eriksson, D. Farina, Y. Gribov, R. Harvey, J. Hobirk, F. Imbeaux, C. Kessel, V. Leonov, and M. Mur, "Integrated modelling of the current profile in steady-state and hybrid iter scenarios," *Nucl. Fusion*, vol. 45, p. 1309, 2005.

[96] G. Garcia, G. Giruzzi, J. F. Artaud, V. Basiuk, J. Decker, F. Imbeaux, Y. Peysson, and M. Schneider, "Critical threshold behavior for steady-state internal transport barriers in burning plasmas," *Phys. Rev. Lett.*, vol. 100, no. 25, p. 255004, 2008.

[97] R. L. Haye, "Neoclassical tearing modes and their control," *Phys. Plasmas*, vol. 13, p. 055501, 2006.

[98] N. Fedorczak, J. Gunn, P. Ghendrih, G. Ciraolo, H. Bufferand, L. Isoardi, P. Tamain, and P. Monier-Garbet, "Experimental investigation on the poloidal extent of the turbulent radial flux in tokamak scrape-off layer," *Journal of Nuclear Materials*, vol. 415, pp. S467–S470, 2011.

[99] D. Iraji, A. Diallo, A. Fasoli, I. Furno, and S. Shibaev, "Fast visible imaging of turbulent plasma in torpexa," *Review of Scientific Instruments*, vol. 79, no. 10, p. 10F508, 2008.

[100] O. Meneghini, *Full-wave modeling of lower hybrid waves on Alcator C-Mod*. PhD thesis, M.I.T., 2012.

[101] O. Barana, D. Mazon, G. Caulier, D. Garnier, M. Jouve, L. Laborde, and Y. Peysson, "Real-time determination of suprathermal electron local emission profile from hard x-ray measurements on tore supra," *IEEE Trans. on Nuclear Sci.*, vol. 53, no. 3, pp. 1051–1055, 2006.

[102] Y. Peysson and F. Imbeaux, "Tomography of the fast electron bremsstrahlung emission during lower hybrid current drive on TORE SUPRA," *Rev. Sci. Instr.*, vol. 70, no. 10, pp. 3987–4007, 1999.

[103] ï. Peysson and R. Arslanbekov, "Measurement of the non-thermal bremsstrahlung emission between 30 and 200 kev with a high time-space resolution on the tokamak tore supra," *Nuclear Instruments and Methods in Physics Research A*, vol. 380, pp. 423–426, 1996.

[104] J. P. Bizarro, Y. Peysson, P. Bonoli, J. Carrasco, T. D. de Wit, V. Fuchs, G. T. Hoang, X. Litaudon, D. Moreau, C. Pocheau, and I. P. Shkarofsky, "On self-consistent ray-tracing and fokker-planck modeling of the hard x-ray emission during lower hybrid current drive in tokamaks," *Phys. Fluids B*, vol. 5, no. 9, pp. 3276–3283, 1993.

[105] Y. Peysson, R. Arslanbekov, V. Basiuk, J. Carrasco, X. Litaudon, and J. P. Bizarro, "Magnetic ripple and the modeling of the lower-hybrid curent drive in tokamaks," *Phys. Plasmas*, vol. 3, no. 10, pp. 3668–3688, 1996.

[106] F. Imbeaux and Y. Peysson, "Ray-tracing and fokker–planck modelling of the effect of plasma current on the propagation and absorption of lower hybrid waves," *Plasma Phys. Control. Fusion*, vol. 47, no. 11, pp. 2041–2065, 2005.

[107] Y. Peysson, J.Decker, and L. Morini, "A versatile ray-tracing code for studying rf wave propagation in toroidal magnetized plasmas," *Plasma Phys. Control. Fusion*, vol. 54, p. 045003 (16pp), 2012.

[108] J. Decker, A. Ram, A. Bers, Y. Peysson, C. Lashmore-Davies, R. Cairns, G. Taylor, and P. Efthimion, "Current drive by electron Bernstein waves in spherical tokamaks," in *31st EPS Conference on Plasma Phys., London, 28 June - 2 July 2004*, vol. 28G, p. 2.166, Europhysics Conference Abstracts, 2004.

[109] A. J. Brizard, J. Decker, Y. Peysson, and F. X. Duthoit, "Orbit-averaged guiding-center fokker-planck operator," *Phys. Plasmas*, vol. 16, p. 102304, OCT 2009.

[110] Y. Peysson and J. Decker, "Fast electron bremsstrahlung in axisymmetric magnetic configuration," *Phys. Plasmas*, vol. 15, no. 9, p. 092509, 2008.

[111] E. Nilsson, J. Decker, Y. Peysson, J.-F. Artaud, A. Ekedahl, J. Hillairet, T. Aniel, V. Basiuk, M. Goniche, F. Imbeaux, D. Mazon, and P. Sharma, "Comparative modelling of lower hybrid current drive with two launcher designs in the tore supra tokamak," *Nucl. Fusion*, vol. 53, p. 083018, 2013.

[112] J. F. Artaud, V. Basiuk, F. Imbeaux, M. Schneider, J. Garcia, G. Giruzzi, P. Huynh, T. Aniel, F. Albajar, J. M. Ane, A. Bécoulet, C. Bourdelle, A. Casati, L. Colas, J. Decker, R. Dumont, L. Eriksson, X. Garbet, R. Guirlet, P. Hertout, G. T. Hoang, W. Houlberg, G. Huysmans, E. Joffrin, S. Kim, F. Köchl, J. Lister, X. Litaudon, P. Maget, R. Masset, B. Pégourié, Y. Peysson, P. Thomas, E. Tsitrone, and F. Turco, "The CRONOS suite of codes for integrated tokamak modelling," *Nucl. Fusion*, vol. 50, no. 4, p. 043001, 2010.

[113] G. L. Falchetto, D. Coster, R. Coelho, B. D. Scott, L. Figini, D. Kalupin, E. Nardon, S. Nowak, L. L. Alves, J. F. Artaud, V. Basiuk, J. P. S. Bizarro, C. Boulbe, A. Dinklage, D. Farina, B. Faugeras, J. Ferreira, A. Figueiredo, P. Huynh, F. Imbeaux, I. Ivanova-Stanik, T. Jonsson, H. J. Klingshirn, C. Konz, A. Kus, N. B. Marushchenko, G. Pereverzev, M. Owsiak, E. Poli, Y. Peysson, R. Reimer, J. Signoret, O. Sauter, R. Stankiewicz, P. Strand, I. Voitsekhovitch, E. Westerhof, T. Zok, W. Zwingmann, I.-T. Contributors, A. U. Team, and J.-E. Contributors, "The european integrated tokamak modelling (itm) effort: achievements and first physics results (vol 54, 043018, 2014)," *Nucl. Fusion*, vol. 54, SEP 2014.

[114] P. Bonoli and R. Englade, "Simulation model for lower hybrid current drive," *Phys. Fluids*, vol. 29, no. 9, pp. 2937–2950, 1986.

[115] D. Ignat, "Toroidal effects on propagation, damping, and linear mode conversion of lower hybrid waves," *Phys. Fluids*, vol. 24, no. 6, pp. 1110–1114, 1981.

[116] M. Brambilla and A. Cardinali, "Eikonal description of h.f. waves in toroidal plasmas," *Plasma Phys.*, vol. 24, p. 1187, 1982.

[117] H. Takahashi, "The generalized accessibility and spectral gap of lower hybrid waves in tokamaks," *Phys. Plasmas*, vol. 1, no. 7, pp. 2254–2276, 1994.

[118] J. C. Wright, P. T. Bonoli, A. E. Schmidt, C. K. Phillips, E. J. Valeo, R. W. Harvey, and M. A. Brambilla, "An assessment of full wave effects on the propagation and absorption of lower hybrid waves," *PHYSICS OF PLASMAS*, vol. 16, no. 7, 2009.

[119] S. Shiraiwa, O. Meneghini, R. Parker, P. Bonoli, M. Garrett, M. Kaufman, J. Wright, and S. Wukitch, "Plasma wave simulation based on a versatile finite element method solver," *Phys. Plasmas*, vol. 17, p. 056119, 2010.

[120] D. van Houtte, G. Martin, A. Bécoulet, J. Bucalossi, F. Saint-Laurent, B. Saoutic, and X. T. supra team, "Real time control of fully non-inductive operation in tore supra leading to 6 min, 1 gj plasma discharges," *Fusion Eng. and Design*, vol. 74, pp. 651–658, 2005.

[121] Y. Peysson, J. Decker, L. Morini, and S. Coda, "Rf current drive and plasma fluctuations," *Plasma Phys. Control. Fusion*, vol. 53, p. 124028, 2011.

[122] T. Oosako, A. Ekedahl, M. Goniche, J. Achard, J. Decker, Y. Peysson, and T. S. Team, "Characterisation of sol density fluctuations in front of the lhcd pam launcher in tore," *AIP Conference Proceedings*, vol. 1406, no. 1, pp. 239–242, 2011.

[123] S. J. Zweben, J. A. Boedo, O. Grulke, C. Hidalgo, B. LaBombard, R. J. Maqueda, P. Scarin, and J. L. Terry, "Edge turbulence measurements in toroidal fusion devices," *Plasma Phys. Control. Fusion*, vol. 49, pp. 1–23, 2007.

[124] P. L. Andrews and F. W. Perkins, "Scattering of lower-hybrid waves by drift-wave density fluctuations: Solutions of the radiative transfer equation," *Phys. Fluids*, vol. 26, no. 9, pp. 2537–2545, 1983. fluctuations.

[125] G. Vahala, L. Vahala, and P. Bonoli, "Effect of magnetic and density fluctuations of the propagation of lower-hybrid waves in tokamaks," *Phys. Fluids B*, vol. 4, no. 12, pp. 4033–4045, 1992.

[126] V. P. Ridolfini, M. Apicella, G. Calabro, C. Cianfarani, E. Giovannozzi, and L. Panaccione, "Lower hybrid current drive efficiency in tokamaks and wave scattering by density fluctuations at the plasma edge," *Nucl. Fusion*, vol. 51, pp. 113023–113035, 2011.

[127] K. Hizanidis, A. Ram, Y. Kominis, and C. Tsironis, "Fokker-planck description of the scattering of radio frequency waves at the plasma edge," *Phys. Plasmas*, vol. 17, no. 1, pp. 1–10, 2010. fluctuations.

[128] H. Q. W. C. X. B. N. W. Z. G. R. C. L. W. K. F. G. J. H. Y. X. J. Z. S. C. L. M. H. L. S. D. N. Y. W. Z. G. H. H. Y. L. L. L. M. S. J. L. L. C. N. Z. J. C. X. Q. Q. Y. H. L. Y. L. Li, G. S. Xu and Y. Ye, "Fast electron flux driven by lower hybrid wave in the scrape-off layer," *PHYS. PLASMAS*, vol. 22, no. 022510, p. 9, 2015.

[129] E. H. Kong, B. J. Ding, M. H. Li, Y. C. Li, Z. G. Wu, L. Zhang, F. K. Liu, J. F. Shan, X. J. Zhang, C. M. Qin, G. S. Xu, H. Q. Wang, X. Z. Gong, K. F. Gan, M. Wang, and J. Q. Feng, "Density modification in the scrape-off-layer during lhw coupling at east," *Plasma Physics and Controlled Fusion*, vol. 56, no. 7, 2014.

[130] A. Ekedahl, V. Petrzilka, Y. Baranov, T. M. Biewer, M. Brix, M. Goniche, P. Jacquet, K. K. Kirov, C. C. Klepper, J. Mailloux, M.-L. Mayoral, M. F. F. Nave,

J. Ongena, E. Rachlew, and J.-E. contributors, "Influence of gas puff location on the coupling of lower hybrid waves in jet elmy h-mode plasmas," *Plasma Phys. Control. Fusion*, vol. 54, p. 074004, 2012.

[131] J. H. Belo, P. Bibet, J. P. S. Bizarro, B. Bertrand, R. Cesario, M. Corona, P. Finburg, A. S. Kaye, F. Leguern, A. Lioure, J. Mailloux, F. Mirizzi, J. Ongena, and C. Portafaix, "An iter-relevant passive active multijunction launcher for lower hybrid current drive in jet-grade plasmas," *Nucl. Fusion*, vol. 51, AUG 2011.

[132] M. Goniche, P. Sharma, V. Basiuk, Y. Baranov, C. Castaldo, R. Cesario, J. Decker, L. Delpech, A. Ekedahl, K.Kirov, D. Mazon, T. Oosako, Y. Peysson, and M. Prou., "Lower hybrid current drive efficiency at high density on tore supra," in *19 Topical Conference on Radio Frequency Power in Plasmas, Newport, RI, June 1-3 2011* (T. editor field must be built in the standard Latex way : editors must be separated by a and , eds.), 2011.

[133] G. M. Wallace, *Behavior of lower hybrid waves in the scrape off layer of a diverted tokamak*. PhD thesis, Massachusetts Institute of Technology, 2010.

[134] R. W. Pryor, *Multiphysics Modeling Using COMSOL: A First Principles Approach*. Jones Bartlett Publishers, Inc., 2009.

[135] T. Stix, *Waves in Plasmas*. American Institute of Physics, 1992.

[136] D. M. Pozar, *Microwave Engineering*. John Wiley and Sons Inc., 2005.

[137] R. F. Harrington, *Time-Harmonic Electromagnetic Fields*. John Wiley and Sons Inc., New York, 1961.